

Philipps



Universität  
Marburg

# **Photoconductive THz emitters and detectors on the basis of InGaAs/InP for terahertz time domain spectroscopy**

Dissertation

zur

Erlangung des Doktorgrades  
der Naturwissenschaften  
(Dr. rer. nat.)

dem

Fachbereich Physik  
der Philipps-Universität Marburg

vorgelegt von

**Roman Jürgen Bruno Dietz**

aus Heilbronn-Neckargartach

Marburg/Lahn, 2015

Vom Fachbereich Physik der Philipps-Universität Marburg

als Dissertation angenommen am: 08.01.2015

Erstgutachter: Prof. Dr. Martin Koch

Zweitgutachter: Prof. Dr. Martin Schell

Tag der mündlichen Prüfung: 19.01.2015

Hochschulkennziffer: 1180





## Abstract

The topic of the present thesis is the development and investigation of photoconductive semiconductor structures for the opto-electronic generation and detection of terahertz (THz) radiation by the use of femtosecond fiber lasers at emission wavelengths of 1550 nm and 1030 nm. Aside from investigating fundamental physical questions, the main motivation for the development of such semiconductor structures is to satisfy the rising demand for compact, cost-efficient and rapid THz measurement systems. The goal of this thesis is to expand the field of application of THz measurement beyond scientific research towards industrial process control by developing optimized devices and systems.

For the fabrication of the photoconductive semiconductor structures, several approaches are tested. These approaches are based on either ternary indium gallium arsenide/indium aluminum arsenide (InGaAs/InAlAs) heterostructures or quaternary indium aluminum gallium arsenide (InAlGaAs) and realized via molecular beam epitaxy (MBE). The choice of the material system originates from the demand for efficient optical absorption at the aforementioned wavelengths.

The first improvement in the performance of the photoconductive semiconductor structures discussed in this work is obtained by micro-structuring the THz antennas, a technique which was first demonstrated in this work. The micro-structuring leads to significant improvements in field homogeneity and electrical contact to the semiconductor. This results in an enhancement of the THz measurement signals by more than one order of magnitude and an accompanying increase of the spectral bandwidth from 2.5 THz to 4 THz.

A core conclusion concerning the development of the semiconductors is the necessity of differentiation between emitter and detector structures in order to further improve the performance of THz measurement systems. This is for the most part due to an inherent antagonism between high carrier mobility and short carrier lifetimes due to defect incorporation. In the case of THz emitters, the performed investigations show that ultra-short carrier lifetimes are not mandatory and that the emphasis has to be put on high carrier mobility. Therefore a new approach is investigated, where regions with high defect densities are spatially separated from absorption regions that exhibit high carrier mobility. This can be achieved in InGaAs/InAlAs heterostructures by taking advantage of a special characteristic of MBE growth of InAlAs at growth temperatures around 400°C. The insight obtained from these investigations allows for THz emitter structures with THz powers that are increased by two orders of magnitude as compared to un-optimized emitter structures.

On the other hand, the evaluation of semiconductor structures for application as THz detectors, leads to the finding that short carrier lifetimes and hence high defect densities are preferable over carrier mobility. Carrier lifetimes of a few hundred femtoseconds are realized by the incorporation of arsenide-related defects via non-stoichiometric low temperature growth of InGaAs/InAlAs heterostructures and additional beryllium doping. Furthermore, to describe the carrier capture and recombination processes on arsenic defects and beryllium acceptors, a detailed rate equation model is derived and validated by pump-power-dependent differential transmission measurements. The accordingly obtained detectors in combination with the aforementioned emitters allow for THz measurements with a spectral bandwidth of up to 6 THz and a dynamic range of 90 dB.

The investigations so far are all performed for an excitation wavelength of 1550 nm. However, Ytterbium doped fiber lasers with a central wavelength of 1030 nm can have significantly higher output powers than erbium-doped fiber lasers emitting at 1550 nm. This plus in output power becomes interesting for certain THz system designs. Therefore two different approaches of semiconductor growth are tested to improve the device performance at this excitation wavelength.

Concerning THz measurement systems, two new approaches are developed and tested in a joint effort with external partners:

The first approach is based on high power ytterbium fiber lasers which allow for the simultaneous excitation of several detector channels on a line-detector with a single laser. By this a THz system for imaging applications with enhanced measurement speed is realized.

The second approach is based on electronically controlled optical sampling (ECOPS). Here, the repetition rate of two lasers is tuned with respect to each other in a controlled manner, to dispose of the need for slow mechanical delay stages for scanning the THz pulse trace. With this system approach and the previous developments for THz emitters and detectors, it is possible to construct THz measurement systems with measurement speeds of up to 8 kHz.

In conclusion, within the frame work of this thesis an improvement of the measurement signals of fiber coupled THz systems by up to three orders of magnitude is achieved by targeted semiconductor development and thorough investigation of the involved carrier dynamics. As a consequence thereof the detectable THz bandwidth is increased from 2.5 THz to 6 THz. Furthermore, it comprises the first demonstration of a multichannel imaging system based on Ytterbium fiber lasers as well as the first realization of an all fiber coupled THz measurement system with kilohertz measurement rates while maintaining sufficient THz bandwidth and dynamic range.

## Zusammenfassung

Das Thema der vorliegenden Dissertation umfasst die Herstellung und Untersuchung von photoleitenden Halbleiterstrukturen zur opto-elektronischen Erzeugung und Detektion von kohärenter Terahertz (THz) Strahlung unter Verwendung von gepulsten Femtosekunden-Faserlasern mit Zentralwellenlängen von 1550 nm und 1030 nm. Neben der Untersuchung von grundlegenden physikalischen Fragestellungen ergibt sich die Motivation zur Entwicklung derartiger Halbleiterstrukturen aus dem steigenden Bedarf nach kompakten, kosteneffizienten und schnellen THz-Messsystemen. Ziel der durchgeführten Arbeit ist es, durch verbesserte Komponenten und Systeme eine Ausweitung des Anwendungsbereichs der THz-Messtechnik, über wissenschaftliche Anwendung hinaus, auf die industrielle Prozesskontrolle zu ermöglichen.

Für die Herstellung der photoleitenden Halbleiterstrukturen werden mehrere Ansätze untersucht, welche sämtlich auf einem molekularstrahl-epitaktischen Wachstum von ternären Indium-Gallium-Arsenid/Indium-Aluminium-Arsenid (InGaAs/InAlAs) Heterostrukturen oder quaternärem Indium-Aluminium-Gallium-Arsenid (InAlGaAs) beruhen. Die Wahl des Materialsystems ergibt sich aus der Anforderung einer effizienten Absorption der obengenannten Emissionswellenlängen der Faserlaser.

Eine erste Verbesserung in Bezug auf die Leistungscharakteristik der photoleitenden Halbleiterstrukturen wird durch eine Mikrostrukturierung der THz-Antennen erreicht, die im Rahmen dieser Arbeit erstmals umgesetzt wird. Durch erhebliche Verbesserungen bezüglich Feldhomogenität und Halbleiterkontaktierung kann eine Steigerung der THz-Messsignale um mehr als eine Größenordnung erreicht werden, sowie eine damit einhergehende Steigerung der spektralen Bandbreite des kohärenten Systems von anfänglich 2,5 THz auf 4 THz.

Ein zentrales Ergebnis im Bereich der Halbleiterentwicklung ist, dass eine Differenzierung zwischen Emittlern und Detektoren erforderlich ist, um die Leistungsfähigkeit der THz-Messsysteme weiter zu steigern. Dies ist hauptsächlich dem inhärenten Antagonismus zwischen hoher Ladungsträgermobilität und kurzen Ladungsträgerlebensdauern im Halbleiter durch Defekteinbau geschuldet.

Die durchgeführten Untersuchungen zeigen, dass im Falle von Halbleiterstrukturen für THz Emittler auf kurze Ladungsträgerlebensdauern weitestgehend verzichtet werden kann und der Schwerpunkt auf eine hohe Ladungsträgermobilität zu legen ist. Hierzu wird ein neuartiger Wachstumsansatz untersucht, bei dem defektreiche Regionen von Absorptionsregionen mit hoher Ladungsträgermobilität räumlich getrennt werden. Dies lässt sich durch das Wachstum von InGaAs/InAlAs Heterostrukturen bei Wachstumstemperaturen um 400°C erreichen, bei

dem eine spezielle Wachstumscharakteristik von InAlAs ausgenutzt wird. Die daraus gewonnenen Erkenntnisse ermöglichen die Realisierung von Emittierstrukturen, welche eine Steigerung der abgestrahlten THz-Leitung von bis zu zwei Größenordnungen gegenüber nichtoptimierten Emittiern aufweisen.

Die Analyse der Halbleiterstrukturen für Detektoren ergibt hingegen, dass eine ausreichend hohe Defektdichte und somit eine sehr kurze Ladungsträgerlebensdauer zu bevorzugen ist. Extrem kurze Lebensdauern, von wenigen hundert Femtosekunden, werden hierbei durch den Einbau von Arsendefekten durch nicht-stöchiometrisches Tieftemperaturwachstum von InGaAs/InAlAs Heterostrukturen bei gleichzeitiger Berylliumdotierung realisiert. Zudem wird ein detailliertes Ratengleichungsmodell zu Ladungsträgereinfang und Rekombination an Arsendefekten sowie Beryllium Akzeptoren entwickelt und mittels leistungsabhängiger differentieller Transmissionsmessungen validiert. Mit Detektoren aus diesen Halbleiterschichten lassen sich so, in Kombination mit den zuvor entwickelten Emittiern, THz-Signale mit einer spektralen Bandbreite von bis zu 6 THz bei einem Dynamikbereich von 90 dB erreichen.

Die obengenannten Untersuchungen werden alle für eine Anregungswellenlänge von 1550 nm durchgeführt. Mit Ytterbium-Faserlasern mit einer Zentralwellenlänge von 1030 nm lassen sich jedoch wesentlich höhere optischen Leistungen als mit Erbium-Faserlasern bei 1550 nm erreichen, was für einige THz-Systemansätze interessant ist. Daher wurden zwei unterschiedliche Wachstumsansätze untersucht, um photoleitende Halbleiterstrukturen für diese Anregungswellenlängen zu optimieren.

Bezüglich der Messsysteme wurden zwei weiterführende Ansätze von Zeitbereichsspektrometern mit externen Partnern entwickelt und gemeinsam untersucht:

Der erste Ansatz beruht auf der Ausnutzung der hohen Leistungen von Ytterbium-Faserlasern, durch welche es möglich ist, mit einem Laser mehrere Kanäle auf einem THz-Zeilendetektor gleichzeitig zu betreiben. Auf diese Weise wird ein Zeitbereichsspektrometer für bildgebende THz-Messungen mit erhöhter Messgeschwindigkeit demonstriert.

Der zweite untersuchte Ansatz beruht auf dem Verfahren des elektro-optisch kontrollierten optischen Abtastens (engl. electronically controlled optical sampling, ECOPS). Hierbei wird die Repetitionsrate zweier Laser kontrolliert zueinander verstimmt, um ein zeitliches Abrastern der THz-Pulse ohne langsame mechanische Verzögerungsstrecken zu ermöglichen. In Kombination mit der vorangegangenen Leitungssteigerung aus der Halbleiterentwicklungen wird es mit diesem Verfahren möglich, ein vollständig fasergekoppeltes THz-Messsystem zu konstruieren, mit welchem sich Messraten von

mehreren Kilohertz bei gleichzeitiger spektraler Bandbreite von 2 THz mit 50 dB Dynamikbereich erzielen lassen.

Zusammenfassend wird im Rahmen der vorliegenden Arbeit durch gezielte Halbleiterentwicklungen und eingehende Untersuchung der Ladungsträgerdynamik eine Steigerung der THz-Messsignale von fasergekoppelten THz-Systemen von bis zu drei Größenordnungen erreicht. Damit einhergehend ergibt sich eine Steigerung der THz-Bandbreite von 2,5 THz auf 6 THz. Weiterführend wird erstmalig ein bildgebendes Mehrkanal-Messsystem auf Basis von Ytterbium Faserlasern demonstriert als auch ein fasergekoppeltes THz-Messsystem mit Kilohertz Messraten und gleichzeitig hinreichender THz Bandbreite sowie Dynamikbereich realisiert.



## **Acknowledgements**

There are many persons, without whom this work would not have been possible and whom I would like to express my gratitude.

First and foremost I would like to thank Prof. Dr. Martin Schell and Dr. Bernd Sartorius for giving me the opportunity to work at the Fraunhofer Heinrich-Hertz-Institute and conduct my research in the field of photoconductive material and THz spectroscopy, as well as the opportunity to visit numerous conferences and doing a research stay abroad.

With the same gratitude I would like to thank Prof. Dr. Martin Koch for agreeing to be my doctorate supervisor, giving me the opportunity to use facilities at the University of Marburg and for all the fruitful advice and discussions concerning my research and beyond.

Furthermore, I would like to thank Dr. Thorsten Göbel for the continuity in support for my work as the successor of Dr. Sartorius as the THz group leader, for his advice and discussions concerning my work and for proof-reading this manuscript.

I owe a lot of thanks to Björn Globisch for being a great padawan and colleague as well as for all the joint work and the endless discussions on carrier dynamics in photoconductors.

I am very grateful for the support in technical matters from Dr. Dennis Stanze and Dr. Helmut Roehle as well as to Dr. Harald Künzel and Jutta Böttcher, for being the good souls of the molecular beam epitaxy and the discussions concerning growth parameters.

I would also like to address many thanks to Dr. Rafal Wilk, Dr. Nico Vieweg, Dr. Maik Scheller, Anika Brahm, Dr. Christian Jansen, Norman Born, Tillman Jung, and Ajanth Velauthapillai for the great collaborations in our respective joint research projects.

Thanks also to Souni Breil for proof-reading this manuscript with the eye of a native speaker.

Last but not least, I would like to express my gratitude to my family for their support and love, without which I would never have come this far.



## **Table of Contents**

<b>Abstract</b>	<b>5</b>
<b>Zusammenfassung</b>	<b>7</b>
<b>Acknowledgements</b>	<b>11</b>
<b>Table of Contents</b>	<b>13</b>
<b>Preface</b>	<b>15</b>
<b>1. Introduction</b>	<b>15</b>
1.1 Photoconductive generation and detection of pulsed THz radiation	17
1.2 Recombination mechanisms in semiconductors	21
1.3 Low-temperature growth of photoconductive materials	23
<b>2. Micro structuring of photoconductive antennas: The mesa structure</b>	<b>27</b>
<b>3. High mobility photoconductive THz emitters</b>	<b>31</b>
<b>4. Short carrier lifetime photoconductive THz detectors</b>	<b>41</b>
4.1 All-fiber electronically controlled optical sampling THz-TDS system	52
<b>5. Photoconductors for 1030 nm pulsed laser excitation</b>	<b>55</b>
5.1 Ytterbium fiber-laser based multichannel THz-TDS system	64
<b>6. Conclusion and Outlook</b>	<b>66</b>
<b>7. Publications</b>	<b>69</b>
<b>I. Bibliography</b>	<b>72</b>
<b>II. Appendix</b>	<b>81</b>



## **Preface**

This thesis is written in a cumulative form, hence the author's publications in the field of photoconductive terahertz (THz) antennas and THz spectroscopy systems are summarized and combined to form a descriptive presentation on the research field in general and on the insights obtained by this work. Chapter 1 will therefore give a short introduction to the field of THz spectroscopy and its applications as well as the state of the art in device and system technology. In this section, the emphasis will be put on photoconductive pulsed THz generation and detection, which represents the main subject of this work. Additionally, some basic properties of semiconductor materials for photoconductive antennas (PCA) and non-radiative recombination processes in semiconductors will be reviewed, which are necessary for a profound understanding of the later discussed PCA devices. Chapter 2 will discuss results obtained from a micro-structuring process for the improvement of PCAs and which has been employed for all PCA devices investigated within this work [1]. In chapter 3, the growth and characterization of high mobility PCA emitters with increased optical-to-THz conversion efficiencies will be discussed [2]–[4]. Chapter 4 addresses the fabrication of short lifetime PCA detectors for high THz bandwidth and high dynamic range detection as well as the involved semiconductor physics [5], [6]. Furthermore, it will discuss the design of measurement systems with increased measurement speeds [7], [8]. Chapter 5 will present PCA devices and their optimization for an excitation with ytterbium-doped fiber lasers at a center wavelength of 1030 nm, as well as briefly review a multi-channel THz-TDS system based on these PCAs [9]–[11]. Finally, chapter 6 will give a conclusion and an outlook on possible further developments in the field.

## **1. Introduction**

Historically, the field of terahertz science and technology, comprising electro-magnetic waves with frequencies in the range of 100 GHz to 10 THz, equal to energies of 0.4 meV to 40 meV, emerged shortly after the advent of the first femtosecond lasers in the 1980s as a core-enabling element for pulsed THz generation. The reason for this late development is the circumstance that coherent electromagnetic waves with frequencies in the THz range are difficult to generate: Electronic circuits are too slow or at least inefficient for the generation of THz frequencies beyond 1 THz, and optical transitions for stimulated emission in semiconductors, e.g. inter sub-band transitions in quantum cascade lasers, cannot be used at room temperature due to thermal excitation [12]. Therefore, an indirect generation approach combining a laser and semiconductor for an optoelectronic conversion process led to the first successful demonstration of broadband THz generation and detection. The aforesaid demonstration was achieved by employing a femtosecond laser and a photoconductive

antenna to generate and detect pulsed THz radiation, today known as THz time-domain spectroscopy (THz-TDS), which was first shown by Auston et al. [13] and later repeated by Grischkowsky et al. [14]. The convenience of this approach is that the measurement signals are generated by step-by-step scanning the THz pulse in the time domain, which allows for direct current (DC) or very low frequency current measurements of high frequency signals. The first demonstration of a spectroscopic application employing the THz-TDS scheme was the analysis of the absorption of water vapor in the THz frequency range [15]. Since then, THz spectroscopy has flourished into a versatile and prosperous field thanks to the broad variety of physical, chemical and biological phenomena connected with this frequency/energy range. These interactions include the excitation of excitonic resonances [16]–[20] and inter-subband transitions [21], [22] in semiconductors, excitations of vibrational and rotational modes in molecules [23]–[26] as well as interactions of bio-molecules with water [27], [28], just to name a few. Furthermore, applications for medical diagnostics with THz spectroscopy were investigated. Here, the detection of cancer cells [29], [30] or liver cells with cirrhosis [31] has been investigated by monitoring the cell's water content. However, one of the most promising fields for widespread industrial applications (due to the high level of technical feasibility) is non-destructive testing of coatings, polymer products and electronic devices [32]–[34].

For the optoelectronic generation and detection of THz radiation a plurality of methods and materials have been investigated. The first emitters and detectors used were photoconductive antennas (PCAs) based on radiation-damaged silicon-on-sapphire [13], [14]. Shortly thereafter the first PCA [35] and THz-TDS system [36] based on low-temperature grown (LTG) gallium arsenide (GaAs) were demonstrated. Later on, other conversion processes were investigated, such as THz generation in nonlinear crystals [37]–[39] or plasmas [40], [41] as well as other schemes such as continuous wave (cw) THz generation in LTG-GaAs PCAs [42] and photodiodes [43], [44].

However, the combination of Titanium-Sapphire femtosecond lasers and LTG GaAs PCAs remained the solution of choice for THz-TDS systems with frequencies up to 10 THz. The main drawbacks of systems based on Titanium-Sapphire lasers are their relatively high cost, large size and limited stability when subjected to harsh environments. Due to these limitations THz-TDS has long remained a technique used only by specialized research groups, generally for in-the-lab applications. The invention of stable and cost efficient mode-locked fiber lasers based on erbium-doped fibers, emitting at a center wavelength of 1550 nm, thus raised hopes for smaller, more reliable and lower priced THz-TDS setups that could potentially lead to more widespread application. These hopes were further supported by the availability of affordable optical components in this wavelength range made possible by the rise of the optical telecommunications market. In confluence, these spurred the investigation of

photoconductive materials with band gap energies that are suitable for an excitation at this wavelength.

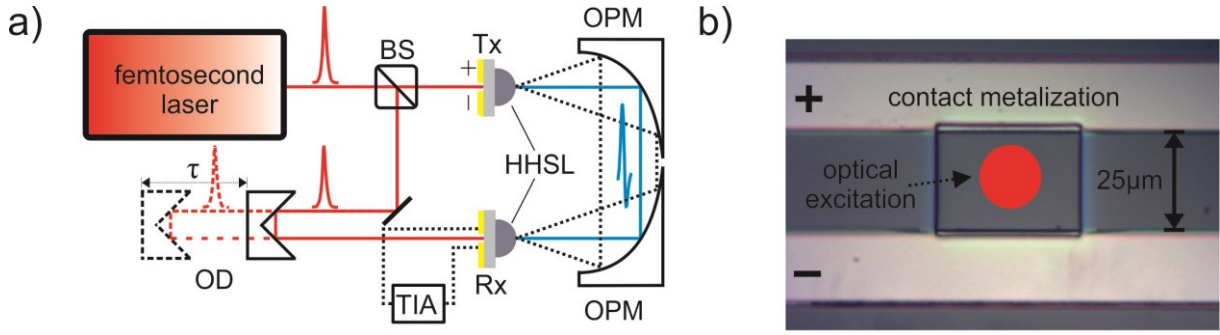
The central goal of this work is the development and fabrication of photoconductive antennas for excitation with mode-locked femtosecond fiber lasers to enable cost-effective, high-performance THz-TDS systems for out-of-lab applications. To achieve this goal, the potential and limitations of molecular beam epitaxial growth of indium gallium arsenide based photoconductors are investigated. Therefore, the interplay of material properties and carrier dynamics in view of the physics of THz emission and detection are reviewed.

### **1.1 Photoconductive generation and detection of pulsed THz radiation**

This section will give a short introduction on the principles of THz-TDS and the fundamental physics of photoconductive generation and detection of pulsed THz radiation.

Photoconductive THz generation is an optoelectronic conversion process of optical light into THz radiation. In the case of pulsed THz radiation the optical light source is a femtosecond pulse laser. In order to ensure sufficient light absorption, the photon energies of the laser are chosen to be equal to or higher than the band gap energy of the semiconductor material of the PCA (or vice versa). The principle of THz-TDS is shown in Fig. 1.1 a). Each laser pulse is split into two parts, one pulse exciting the emitter PCA and one the detector PCA. The detector path contains a variable optical delay, usually a motorized mechanical stage or a shaker with a retro reflector mirror, to delay the arrival of the optical pulse to the THz pulse by a time  $\tau$ . The pulse at the emitter triggers the THz pulse emission at time  $t$ , whereas the pulse in the detector branch gates the conductivity of the detector at a time  $t+\tau$ . By step-by-step variation of the delay  $\tau$ , the amplitude and phase of the electro-magnetic field of the THz pulse incident on the detector can be reconstructed by measuring the DC current induced in the detector by the incident THz field for each time step  $\tau$ . The detector current signal trace as a function of  $\tau$  then resembles the incident THz pulse and the THz spectrum can be obtained by a Fourier transformation of the detector current trace.

Photoconductive THz generation process: A PCA emitter usually features two metal electrodes deposited on top of the semiconductor material to apply a bias voltage to the illuminated part of the semiconductor material [Fig. 1.1 b)]. The incident laser pulse induces a fast-rising carrier density in the semiconductor which is accelerated in the applied electrical bias field. The resulting current density can be described, to a good approximation, by a simple one-dimensional Drude-like model comprising several coupled rate equations as worked out by Jepsen et al. [45].



BS: Beam splitter, Tx: Photoconductive emitter, Rx : Photoconductive detector, OD: Optical delay, HHSL: Hyper-hemispherical Silicon lens, OPM: Off-axis parabolic mirror, TIA: Transimpedance amplifier

Fig. 1.1 a) Schematic drawing of a typical THz-TDS setup with silicon lenses attached to the photoconductive antennas and parabolic mirrors in the THz beam path. b) Top view microscope image of a photoconductive antenna design with a strip-line contact metallization and a 25  $\mu\text{m}$  photoconductive gap.

The model will be discussed here for illustrative purposes and the limits of the model's validity, aside from the general limitations of a non-quantum mechanical approach, will be pointed out when necessary. In this model the electron current density in the PCA is then given by:

$$j(t) = -e \cdot n_{e,CB}(t) \cdot v(t), \quad (1.1)$$

where  $n_{e,CB}(t)$  is the electron density in the conduction band (CB) of the emitter induced by the laser pulse,  $v(t)$  is the velocity of the electron, and  $e$  is the elementary charge. Since the contribution of holes in the valence band (VB) to the emitter current is much smaller, due to their generally higher effective mass, it can safely be omitted for simplicity [45]. The carrier density  $n_{e,CB}(t)$  can be described by the rate equation:

$$\frac{d}{dt} n_{e,CB}(t) = -\frac{n_{e,CB}(t)}{\tau_c} + G(t). \quad (1.2)$$

Here,  $G(t)$  is the generation rate caused by the optical excitation, e.g. a Gaussian pulse, and  $\tau_c$  is the carrier capture time into defect states in the photoconductor.

The carrier acceleration in this model is described by two coupled rate equations. Equation (1.3) describes the change of the carrier velocity  $v(t)$ , i.e. the carrier acceleration in the electric field. Screening of the externally applied bias field  $E_{Bias}$  by free carriers is taken into account via a screening polarization  $P_{Sc}(t)$ . The change of the screening polarization is described by equation (1.4), where the second term of the rhs describes the build-up of the polarization due to the current density in the photoconductor  $j(t)$ , which increases until the electrons are captured (trapped) by a defect state in the band gap on the time scale  $\tau_c$ . The first term on the rhs describes the decline of the static polarization induced by trapped

electrons due to recombination with holes, which is governed by the recombination time  $\tau_r$ . The two rate equations then read:

$$\frac{d}{dt}v(t) = -\frac{v(t)}{\tau_s} + \frac{e}{m^*} \left( E_{Bias} - P_{Sc}(t)/\epsilon\eta \right) \quad (1.3)$$

and

$$\frac{d}{dt}P_{Sc}(t) = -\frac{P_{Sc}(t)}{\tau_r} + j(t) = -\frac{P_{Sc}(t)}{\tau_r} + e \cdot n_{e,CB}(t)v(t). \quad (1.4)$$

Here  $v(t)$  is the electron velocity,  $\tau_s$  is the carrier scattering time which comprises (via Matthiesen's rule) all relevant scattering mechanisms such as electron-phonon scattering, ionized impurity scattering and electron-electron scattering. The elementary charge, electron effective mass, and absolute permittivity are denoted by  $e$ ,  $m^*$  and  $\epsilon$ , respectively. The factor  $\eta$  is a geometrical factor that is equal to three in case of a spherical symmetry [46].

The emitted THz field in the far-field approximation is then proportional to the time derivative of the current [13], [47]:

$$E_{THz}(t) \propto \frac{d}{dt}j(t) \quad (1.5)$$

As visible from Eq. (1.2), the rise time of the carrier density is governed by the laser pulse width, while the decay time is governed by  $\tau_c$ . Regular pulse durations of mode-locked fiber laser are on the order of 100 fs while the carrier lifetimes in the fastest PCAs are on the order of a few hundred femtoseconds. Therefore, the amplitudes of the high frequency components of the emitter current are predominately defined by the laser pulse duration. The carrier capture time merely defines the frequency position of the maximum amplitude, as will be shown in chapter 3. The amplitude of the current pulse is primarily defined by the scattering time in the material  $\tau_s$ . Hence a long scattering time, i.e. a high carrier mobility, is important for emitter materials.

Photoconductive THz detection: On the detection side in general the same set of equations (1.2)-(1.4) is valid, if the external bias field  $E_{Bias}$  is substituted by the incident THz field  $E_{THz}(t)$ . For the purposes of analytical solvability and illustrative reasons, it will here be assumed that screening in the detector can be neglected. In other words the detector is assumed to exhibit a linear response on the incident THz field. The current density in the detector antenna can then be described in dependence of the time delay  $\tau$  between incident THz field  $E_{THz}(t)$ , the optical excitation, which defines the electron density in the

detector  $n_{d,CB}(t)$  [equal to Eq. (1.2)], as well as the time dependent carrier mobility  $\mu(t)$  of the detector by a double convolution integral:

$$j(\tau) = e \cdot n_{d,CB}(t) * \mu(t) * E_{THz}(t). \quad (1.6)$$

Here \* denotes the convolution operation. In Fourier space Eq. (1.6) transforms to

$$j(\omega) = e \cdot E_{THz}(\omega) \cdot n_{d,CB}(\omega) \cdot \mu(\omega). \quad (1.7)$$

There are several limitations to this simple model of generation and detection that should be pointed out. Firstly, the assumption of a constant  $\tau_c$  is only valid in the limit of low excitation densities in the CB were the defect density exceeds the electron density and no saturation of defect states occurs. Furthermore, Eq. (1.2) neglects absorption saturation due to Pauli blocking at high excitation densities. Both limitations will be revisited in chapter 4.

For an understanding of the influence of the carrier capture time in the detector material on the frequency response of a PCA detector, it is instructive to consider two simplified limiting cases:

An infinitely short carrier lifetime, i.e. a delta function like carrier density in the CB  $n_{d,CB}(t) = \delta(t)$ .

And an infinitely long carrier lifetime, i.e. a theta function like carrier density in the CB  $n_{d,CB}(t) = \theta(t)$ .

For the first case Eq. (1.7) yields

$$j_{delta}(\omega) = e \cdot E_{THz}(\omega) \cdot \frac{1}{\sqrt{2\pi}} \cdot \mu(\omega), \quad (1.8)$$

where for second case Eq. (1.7) yields

$$j_{theta}(\omega) = e \cdot E_{THz}(\omega) \cdot \left( \frac{-i}{\sqrt{2\pi}\omega} + \delta(\omega) \right) \cdot \mu(\omega). \quad (1.9)$$

From Eq. (1.8) and Eq. (1.9) it is obvious that a detector with a long carrier lifetime exhibits a stronger frequency roll-off towards higher frequencies (proportional to a factor of  $1/\omega$ ) as compared to a short carrier lifetime detector. Since the durations of THz pulses are in the range of 1-2 ps, carrier lifetimes have to be in the sub-ps range to be considered short in this respect. The influence of the carrier lifetime on the detected THz spectrum and other implications will also be reviewed in more detail in chapter 4.

## 1.2 Recombination mechanisms in semiconductors

As illustrated in the previous section, it is beneficial for high bandwidth THz PCAs to employ materials that exhibit very short carrier lifetimes. This is especially important for detector materials because of the strong impact of the carrier lifetime on frequency roll-off. Therefore, this chapter will briefly review the mechanisms that determine the carrier lifetimes in semiconductors, i.e. the timespan between the excitation of an electron-hole pair and its recombination. There are three important processes that contribute to the recombination of electron-hole pairs in semiconductors: Direct radiative recombination, Auger recombination and Shockley-Read-Hall recombination.

Direct radiative recombination is the recombination of an electron-hole pair via the emission of a photon. The lifetime for radiative recombination in InGaAs is typically on the order of 1-10 ns [48] and therefore direct recombination is a negligible mechanism for materials with carrier lifetimes in the picosecond or sub-picosecond range.

Auger recombination is a non-radiative process and results from the electron-electron interaction. The general trait of Auger processes is that one electron (hole) transfers its energy to another electron (hole) via scattering in order to be able to recombine with a hole (electron). The other scattering partner, i.e. the electron (hole), then relaxes back to the minimum of the CB (maximum of the VB) via phonon emission. There are several different types of Auger processes depending on the origin of the recombining electron and hole. The two most important are direct Auger processes, where two free electrons (holes) scatter, and trap assisted Auger processes where a trapped electron (hole), i.e. bound to a defect state (trap) situated within the band gap, scatters with a free electron (hole) in order to recombine either with a trapped hole (electron), bound to another defect state, or with a free hole (electron) [49]. Since all of these processes involve the interaction of three particles, the Auger recombination rates are all proportional to a product of three carrier densities and, for the processes mentioned above, read:

$$R_A(t) = B_n h n^2 + B_p n h^2 + T_n h n n_T + T_p h h_T n + T_{pn} h_T n^2 + T_{np} n_T h^2 \quad (1.10)$$

Here  $n$  and  $h$  are the electron and hole densities in the CB and VB, respectively. The quantities  $n_T$  and  $h_T$  denote the densities of electrons and holes trapped in defect states. The Auger coefficients  $B_i$  and  $T_i$  comprise the quantum mechanical scattering probabilities from an integration over the possible initial and final states. The typical values for  $B_i$  are in the range of  $10^{-28}$ - $10^{-29}$  cm<sup>6</sup>/s [50]. Therefore, the band-band Auger mechanism becomes relevant only for carrier densities in excess of  $10^{19}$  cm<sup>-3</sup> and hence can be neglected for the excitation levels investigated in this work which are on the order of  $10^{18}$  cm<sup>-3</sup>. For Auger recombination with

traps much higher coefficients were deduced from calculations, which are on the order of  $10^{-25} \text{ cm}^6/\text{s}$  [51]. This results in recombination on time scales of 10 ps for carrier and trap densities of  $10^{18} \text{ cm}^{-3}$ . However, the predicted temperature dependence of this process does not coincide with findings from temperature dependent measurements of carrier lifetimes into deep defect states in semiconductors [52] and will therefore also not be considered in this work.

Shockley-Read-Hall recombination is another non-radiative process where an electron (hole) is captured by a defect state within the band gap while energy conservation is satisfied by the emission of one or multiple phonons, depending on the energetic position of the defect state with respect to the band. The combined capture rate can for electrons and holes can be phenomenologically described by [53], [54]:

$$R_{SRH} = N_{T,e} v_{th,e} \sigma_e (1 - f_{T,e}) n + N_{T,h} v_{th,h} \sigma_p (1 - f_{T,h}) p, \quad (1.11)$$

where  $N_{T,e}$  and  $N_{T,h}$  are the densities of electron and hole traps,  $f_{T,e}$  and  $f_{T,h}$  are the fraction of occupied traps,  $v_{th,e}$  and  $v_{th,h}$  is the electron and hole thermal velocity,  $\sigma_e$  and  $\sigma_h$  are their capture cross sections of the respective traps. For typical defect densities of  $N_{T,i}=10^{18} \text{ cm}^{-3}$  and cross sections on the order of  $10^{-14} \text{ cm}^2$  this results in lifetimes of 1 ps and below.

The important physics of the SRH process are contained in the capture cross sections since they incorporate the quantum mechanical probabilities for the phonon emission and are generally dependent on the energy of the carriers, the lattice temperature and the charge state of the trap. For their calculation two different models of phonon emission have been discussed quite controversially [55], [56]. The first is the so called phonon cascade process (PC) the second the multi phonon emission (MPE) process. The former describes the carrier energy relaxation in terms of a cascade of excited bound defect states, where a captured carrier emits a single phonon for each transition from one excited bound state to next lower excited state, until reaching the ground state of bound defect states. The latter describes the energy relaxation in term of an emission of multiple phonons, where the interaction between lattice and electrons is described via an optical deformation potential and calculated in terms of perturbation theory [56]–[59].

Even though calculations of capture cross sections from PC processes yield the right order of magnitude, it has a significant probability only at low temperatures and for shallow defect states [52], [55], [60]. The MPE process has been shown to correctly describe certain deep levels (DX levels) in GaAs and GaP deep levels and can yield high capture cross sections at room temperature [52], [56], [58]. The dominant mechanism of phonon emission during

carrier capture into deep level via SRH recombination is therefore assumed to be due to the MPE process. This will be discussed further in chapter 5.

### 1.3 Low-temperature growth of photoconductive materials

This subchapter provides an overview on the state-of-the-art of growth of semiconductors with short carrier lifetimes. After a short review on the growth of LTG-GaAs, it will lead over to the growth of LTG-In<sub>0.53</sub>Ga<sub>0.47</sub>As suitable for 1550 nm wavelength excitation. Furthermore, it will motivate the main approach followed in this work, namely InGaAs/InAlAs heterostructures.

As explained in the previous chapter, short carrier lifetimes due to SRH recombination can be enhanced by a high density of defect states within the band gap. Alongside the need for short carrier lifetimes, semiconductor materials suitable for THz PCAs need a high dark resistivity, i.e. a low residual carrier concentration. In the case of emitters, this arises from the requirement to apply high bias field strength without device failure caused by high dark currents. In detectors, a low residual carrier concentration reduces the disturbance of the measured THz signal by thermal noise currents, i.e. Johnson-Nyquist noise [61], [62], and therefore helps to increase the dynamic range of the measurement. This fact will be discussed in more detail in chapter 4.

In the case of GaAs with a band gap energy of  $E_B=1.42$  eV for excitation at an 800 nm wavelength, these requirements can be achieved by molecular beam epitaxy (MBE) growth at low substrate temperatures of around 200°C and subsequent annealing. The low substrate temperatures result in a non-stoichiometric growth, more precisely the incorporation of excess arsenic, which leads to the formation of arsenic antisite defects on gallium lattice positions ( $As_{Ga}$ ), also known as the EL2 defect [63], and gallium vacancies defects ( $V_{Ga}$ ) [64]–[66].

The defect densities are strongly dependent on the growth temperature and are typically in the range of  $5 \times 10^{18}$ – $6 \times 10^{20}$  cm<sup>-3</sup> [67]–[69] and  $3 \times 10^{17}$ – $3 \times 10^{18}$  cm<sup>-3</sup> [70], [71] for  $As_{Ga}$  and  $V_{Ga}$  respectively. The energy levels associated with these defect states in GaAs are situated within the band gap and dependent on their charge state, with energy levels of approx. 0.6–0.7 eV below the CB minimum for  $As_{Ga}$  [72]–[74] and 0.19–0.3 eV above the VB maximum for  $V_{Ga}$  [64]. Since the  $As_{Ga}$  defect is a group V element on a group III lattice position, it acts as a double donor. This is partially compensated by the energetically lower  $V_{Ga}$  defect. Hence, a part of the  $As_{Ga}$  defects has single or double positive ionization (for simplicity both will in the following be referred to as  $As_{Ga}^+$ ) while the  $V_{Ga}$  defects are negatively ionized [64], [75], [76]. Furthermore, due to their deep-level nature and high density, the Fermi level is pinned to a mid-gap position and thermal excitation from defect states into the respective bands is

negligible [72]. The ionized  $\text{As}_{\text{Ga}}^+$  defects exhibit a larger capture cross section for electrons in the CB when compared to neutral  $\text{As}_{\text{Ga}}$  (due to their positive charge), and are therefore the main contributor to non-radiative recombination resulting in very short carrier lifetimes in un-annealed LTG-GaAs [76].

However, the high density of arsenic antisite defects enables hopping conductivity, where electrons tunnel between the bound defect states. This accounts for the main contribution to the conductivity of un-annealed LT-GaAs and leads to relatively low resistivity values in the  $\text{k}\Omega\text{cm}$  range [77]. By subsequent annealing, the excess arsenic is redistributed via diffusion, which is promoted by gallium vacancies, resulting in the formation of metallic As precipitates [78], [79]. The precipitate formation strongly increases the resistivity to several  $\text{M}\Omega\text{cm}$ , which is attributed to overlapping Schottky barriers surrounding the precipitates [78], [80]. The electron capture cross section of the precipitates is dependent on their size and the surrounding Schottky barriers. At increasing annealing temperatures the precipitate size is increased and their density is decreased, since the amount of excess arsenic is fixed. Hence, there is an optimum size for the precipitates concerning the SRH recombination rate [cf. Eq. (1.11)] as both capture cross section and trap density, determine the recombination rate. In summary, a careful adjustment of growth temperature as well as annealing temperature and time enables the growth of LTG-GaAs that exhibits a short carrier capture time in the sub-ps range combined with high resistivity [79].

The mechanisms described above for LTG-GaAs tempt to suggest a simple transfer of the methodology to low temperature MBE growth of  $\text{In}_{0.53}\text{Ga}_{0.47}\text{As}$  ( $E_{\text{B}}=0.74\text{ eV}$ ) to obtain suitable photoconductors for 1550 nm excitation. Similar to LTG-GaAs, the low temperature growth of  $\text{In}_{0.53}\text{Ga}_{0.47}\text{As}$  results in the incorporation of excess arsenic of up to 2%, although single crystalline growth was only attainable for an amount of excess arsenic of approx. 0.75% [81]. The energy levels for  $\text{As}_{\text{Ga}}$  defects in LTG- $\text{In}_{1-x}\text{Ga}_x\text{As}$  are found to mostly maintain their energetic position with respect to the VB in LT-GaAs and the energy levels move closer to the CB with rising indium content [82], [83]. For  $\text{In}_{0.53}\text{Ga}_{0.47}$  the defect energy levels are therefore very close to the CB with energies of approx. 91meV below the CB, which corresponds to an activation energy for the un-compensated semiconductor at room temperature of 32 meV [81], [84]. Grandidier et al. measured a band of mid-gap states at energies of around 150 meV below the CB edge via tunneling spectra [85]. They associated the measured energy levels with a combination of the two ionization states of the  $\text{As}_{\text{Ga}}$  defect [86]. One at the above mentioned activation energy of 32 meV and another one at 230 meV below the CB. For the sake of simplicity, the following InGaAs will refer to the  $\text{In}_{0.53}\text{Ga}_{0.47}\text{As}$  composition unless otherwise stated. Due to the proximity of the  $\text{As}_{\text{Ga}}$  related energy levels to the CB, LTG-InGaAs shows a high residual carrier concentration at room temperature in the range of  $1 \times 10^{17} - 1 \times 10^{18}\text{ cm}^{-3}$ , dependent on the excess arsenic concentration and thus growth

temperature [81]. Hence, As-grown LTG-InGaAs exhibits a very low resistivity of 0.01-1  $\Omega\text{cm}$  and is thus unsuitable as photoconductive material [87]. In contrast to LTG-GaAs, precipitation in LTG-InGaAs only takes place at high annealing temperatures of around 600°C [84], [85], [88]. Therefore, arsenic diffusion needs a higher activation energy in InGaAs than in GaAs which suggests a lower density of  $V_{\text{Ga}}$  defects. The assumption of a low  $V_{\text{Ga}}$  density would also explain the high residual carrier concentration, which should be lowered for a high  $V_{\text{Ga}}$  density and its accompanying compensatory behavior, as it is the case in LTG-GaAs. Unfortunately, annealing at temperatures around 600°C cannot be performed in-situ in an MBE chamber since indium and arsenic desorption from the substrate deteriorates the material due to the limited reachable beam-equivalent pressure. Even for ex-situ annealing with high gas pressures, e.g. in a metal oxide vapor phase epitaxy chamber, it is challenging to sustain the arsenic content and crystallinity of the InGaAs layers at such high temperature. Consequently, it is difficult to obtain high resistivity and short carrier lifetimes in LTG-InGaAs in the same way as it is possible for LTG-GaAs. A possible way to increase the resistivity of LTG-InGaAs is p-doping with Beryllium to compensate for the nominal n-doping by the  $\text{As}_{\text{Ga}}$  defects. Hereby the resistivity can be increased to several tens of  $\Omega\text{cm}$  depending on the Be-doping concentration [89][90]. However, the resulting resistivity is still relatively low for application as material for THz PCAs.

Therefore, several other approaches for fast InGaAs-based photoconductors have been tried. Fe-implantation [91], [92], ion irradiation [93], [94] and Fe-doping [95], [96] of InGaAs as well as erbium super-lattices embedded in a InGaAs matrix have been investigated [97], [98]. Although some of these approaches yielded respectable results, none could match the results obtained from LTG-GaAs excited at 800 nm excitation.

Another possible approach is to employ InGaAs/InAlAs heterostructures. The LTG Be-doped versions of these InGaAs/InAlAs heterostructures have been investigated to some extent for application as ultrafast photo detectors and have been shown to exhibit short carrier lifetimes in the sub picosecond range [99]–[102]. The benefit of the LTG-InGaAs/InAlAs heterostructures compared to Bulk LTG-InGaAs is the fact that the LTG-InAlAs layers also exhibit deep trap states that are situated energetically below the  $\text{As}_{\text{Ga}}$  levels of the adjacent InGaAs layers [103]. For sufficiently thin InGaAs layers the traps in the adjacent InAlAs help to further reduce the residual carrier concentration. In combination with Be-doping, LTG-InGaAs/InAlAs heterostructures exhibit resistivity values of several hundreds of  $\Omega\text{cm}$ . The first demonstration of THz emission and detection with LTG Be-doped InGaAs/InAlAs heterostructures was shown by Sartorius et al. [89]. This forms the starting point of the present work with its goal to deepen the understanding of defect incorporation and the resulting carrier dynamics in InGaAs/InAlAs heterostructures in view of building efficient THz PCAs.



## 2. Micro structuring of photoconductive antennas: The mesa structure

This chapter will discuss results on micro-structuring of photoconductive antennas based on LTG and Beryllium doped InGaAs/InAlAs heterostructures. This structuring technique was employed throughout this entire work, for both emitter and detector antennas, and is thus fundamental for further understanding of this work.

The InGaAs/InAlAs heterostructures investigated in this chapter were grown at low temperature, with a substrate temperature of 130°C, and lattice matched on a semi-insulating InP:Fe substrate. The heterostructures consisted of 100 periods of 12 nm thick InGaAs layers followed by 8 nm thick InAlAs layers grown on top of a 777 nm buffer layer of InAlAs. As pointed out in the last chapter the InAlAs layers help to reduce the residual carrier concentration by approx. one order of magnitude. The exact reduction is dependent on the InGaAs and InAlAs layer thicknesses. However, due to the quantum well nature of the InGaAs layers in between the high band gap InAlAs layers and the accompanying shift of the sub-band energies in dependence of the InGaAs layer thickness, there is a lower limit for the InGaAs layer thickness to ensure efficient light absorption at 1550 nm. At 12 nm InGaAs layer thickness there is only a minor shift of the sub band energy from to bulk InGaAs band gap of 0.74 eV to approx. 0.76 eV, while the residual carrier concentration can be reduced by approx. one order of magnitude. Therefore the InGaAs layer thickness of 12 nm presents a good trade-off value. To further reduce the residual carrier concentration all samples were doped with beryllium with a concentration of  $7 \times 10^{17} \text{ cm}^{-3}$ .

The contact metallization of photoconductive antennas is commonly deposited in a planar fashion, i.e. on top of the photoconductive semiconductor material [Fig. 2.1 b)]. This, however, has several disadvantages, some of which are general, some of which apply primarily to InGaAs/InAlAs heterostructures. One general disadvantage is the inherent inhomogeneity of the electrical field of a planar contact as depicted in Fig. 2.1 a), which limits the carrier acceleration within the deeper layers of the heterostructure by the external bias field or the incident THz field for emitter and detector, respectively. Furthermore, there is a vast contribution to the dark current from the non-functional semiconductor material outside of the photoconductive gap region [Fig. 2.1 b)].

The basic principle of the mesa structuring technique is to remove most of the photoconductive material, e.g. the InGaAs/InAlAs layers, from the InP:Fe substrate, leaving it only in the actual photoconductive region that is optically excited. This can be done by dry etching to remove the photoconductive layers and obtain mesa-like structures as depicted

schematically in Fig. 2.1 c) and d) and by scanning electron microscope (SEM) images in Fig. 2.1 e) and f). The dry etch process employed in this work was chemically assisted ion beam etching (CAIBE). In the CAIBE process the dry etching, via the bombardment of the sample with argon ions, is further assisted by highly reactive chlorine gas. The chlorine gas binds to the dangling bonds in the semiconductor material produced by the ion bombardment and thus helps to remove the reactants. By carefully adjusting the chlorine flow, it is possible to equal out the etch rates of the InGaAs and InAlAs layers while also increasing the overall etch rates. The increase of the overall etch rate allows for relatively thin photo resists which allows for an easier resist lift-off and thus smaller realizable structures. The equal etch rates for the two different materials, on the other hand, make it possible to obtain steep and smooth mesa side walls as can be seen in the SEM images of Fig. 2.1 e) and f). After the etch process the contact metallization is deposited on the mesa side walls via sputtering, also visible in Fig. 2.1 e). The standard metallization used throughout this work was a layer metallization with titanium/platinum/gold. The sputtered side contacts significantly improve the homogeneity of the electrical fields within the photoconductive region of the antenna compared to planar-deposited antenna structures. Additionally, since the semi-insulating InP:Fe substrate material has a higher resistivity than the InGaAs/InAlAs layers, it is possible to reduce the dark currents of the antenna by more than one order of magnitude. A more subtle, but very important, additional effect of side contacts, primarily for the case of InGaAs/InAlAs heterostructures, is that each InGaAs layer is contacted individually instead of only the top layer as it would be the case for planar-deposited contact metallization. Thus, the carriers do not need to tunnel through the high band-gap InAlAs barriers while traveling towards the metal contacts. This strongly facilitates current flow in the semiconductor material and thus improves emitter and detector performance.

The improvement in the detectable THz signal amplitude in a TDS system employing mesa structured antennas as opposed to planar antennas is shown in Fig. 2.2. As the figure illustrates, the improvement on the emitter (Tx) side is approx. a factor of two in THz signal amplitude. This is primarily owed to the improvement in bias field homogeneity within the mesa. On the detector (Rx) side, the detected THz signal amplitudes increase by more than one order of magnitude. The big difference in improvement as compared to the emitter is understandable when one considers the relatively small electrical field at the detector induced by the incident THz field compared to the strong DC bias fields at the emitter.

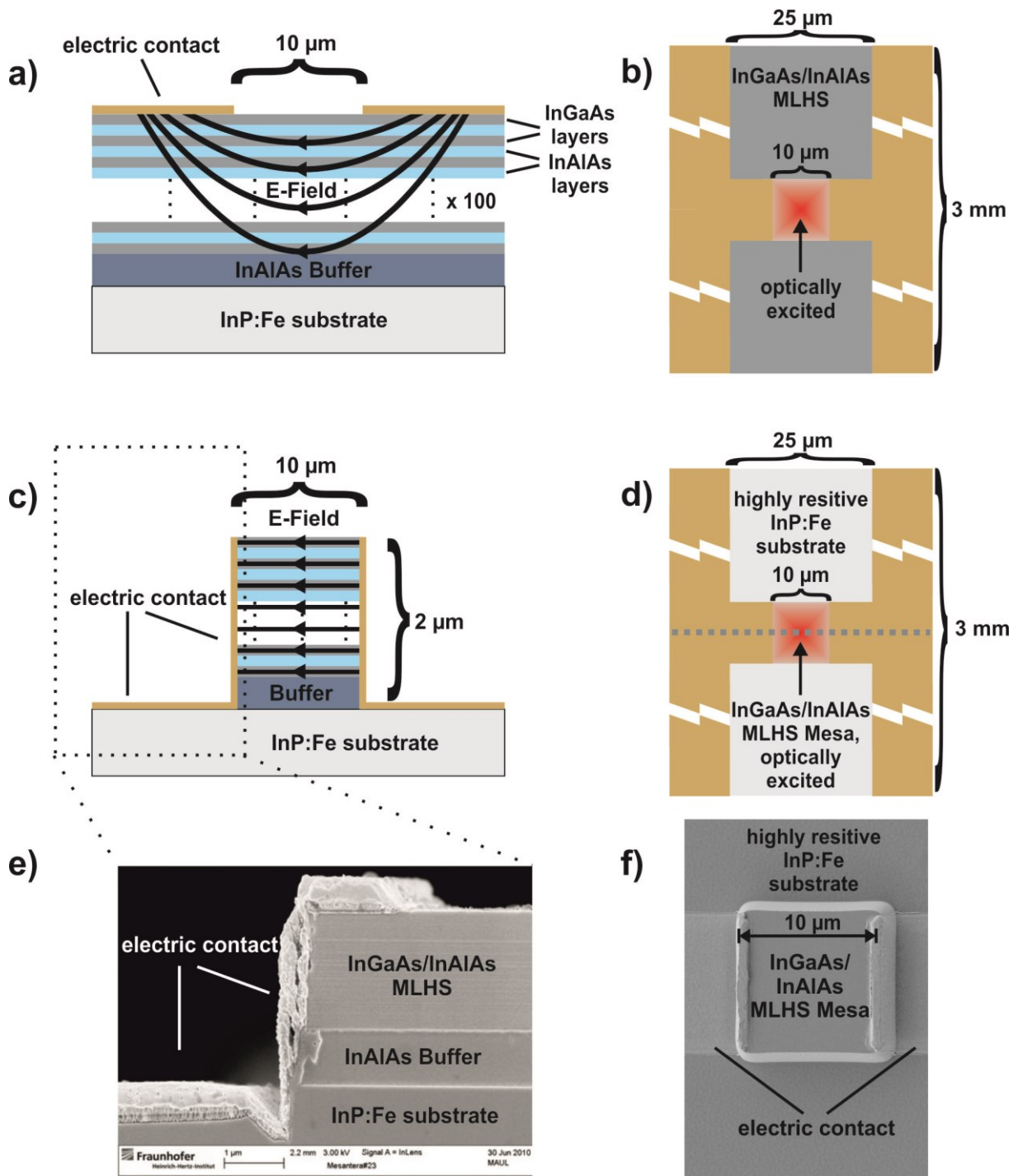


Fig. 2.1 a) and c) show a side view schematic of a planar and a mesa structured InGaAs/InAlAs MLHS, respectively. The black arrows indicate the electrical field in between the gold contacts. b) and d) top view schematic of a planar and a mesa dipole antenna, respectively. e) SEM image of a mesa antenna cleaved across the photoconductive gap as indicated by the grey dotted line in c) and d). f) top view SEM picture of a dipole mesa antenna. a)-d) are adopted and modified from Ref [1].

The overall increase in the detected THz pulse amplitude, when employing mesa antennas instead of planar antennas, was found to be a factor of approx. 27. This increase in amplitude, accompanied by the reduction of the dark conductivity in the detector (cf. chapter 3), yields an increase in the measurable THz bandwidth from 3 THz to 4 THz due to an increased dynamic range.

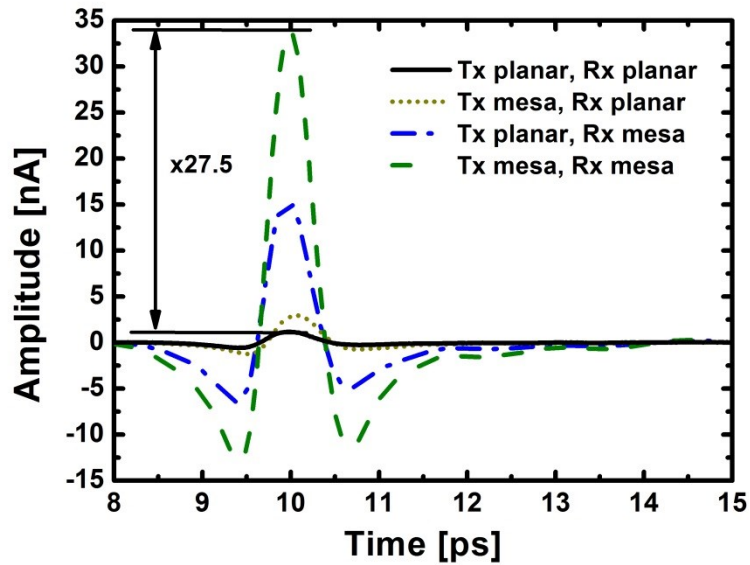


Fig. 2.2 Comparison of THz-TDS pulse traces for planar emitter and detector (P-P), mesa emitter and planar detector (M-P), planar emitter and mesa detector (P-M) and mesa emitter and detector (M-M). The overall increase in pulse amplitude between (P-P) and (M-M) is a factor of 27.5. This figure is adapted and modified from Ref [1].

### 3. High mobility photoconductive THz emitters

As already indicated in section 1.1, the high frequency components of the emitted THz radiation are predominantly defined by the laser pulse width. Therefore, short carrier lifetimes in emitter PCAs are not mandatory for broadband THz emission. A limitation is only given by the repetition rate of the employed laser system, since the PCA must be allowed to relax back to its steady state before the next optical excitation by the next laser pulse. On the other hand, for a given optical excitation and bias field, the electric field amplitude of the emitted THz radiation is determined by the scattering time (cf. Eq. (1.3) and [104]). In the development of semiconductors for the use as emitter PCAs, the emphasis should therefore be put on high carrier mobility, i.e. long carrier scattering times.

This chapter will discuss an approach for PCAs in which the photoconductive region, i.e. where the light absorption and carrier transport takes place, is spatially separated from a trapping/recombination region (SepaRec) which is transparent for 1.55  $\mu\text{m}$  light and contains a high density of defects. In this work, the realization of such a PCA structure is also based on InGaAs/InAlAs heterostructures. The main difference to LTG heterostructures is the abandonment of  $\text{As}_{\text{Ga}}$  incorporation via low temperature growth in the InGaAs layers. Defects for electron and hole capture are generated (almost) exclusively in the InAlAs layers by exploiting a growth characteristic of InAlAs at growth temperatures around 400°C. This growth characteristic arises from the interplay of surface kinetics and thermodynamics on the substrate surface during MBE growth [105]. At temperatures in the range of 300-500°C, this interplay results in an increase of alloy clustering with InAs and AlAs-like regions. The alloy clustering leads to clusters with sizes of up to several nanometers that result in defect states with energies of 0.6-0.7 eV below the CB band edge of InAlAs [105], [106]. The band-gap energy of InAlAs at room temperature is  $E_g=1.47$  eV and hence the defects are situated in a mid-gap position which prevents thermal excitation and leads to a very high resistivity.

Bulk InGaAs grown in the temperature range of 300-500°C exhibits moderate residual carrier concentrations at room temperature with values obtained from Hall measurements of  $N_d-N_a \leq 7 \times 10^{15} \text{ cm}^{-3}$  and a minimum of  $N_d-N_a \leq 7 \times 10^{14} \text{ cm}^{-3}$  at  $T_g=480^\circ\text{C}$  [81]. The defects associated with the residual carrier concentration are  $\text{As}_{\text{Ga}}$  defects as in the case of low temperature growth, however with a much lower density. The room-temperature Hall mobility values are close to  $10^4 \text{ cm}^2/\text{Vs}$  over the complete growth temperature range of 300-500°C. This corresponds to a scattering time in Drude-theory of approx. 250 fs. Furthermore, the InGaAs layers grown in this temperature range show a much sharper absorption edge as compared to LTG InGaAs where the absorption edge is strongly broadened forming an Urbach tail [107].

Similar findings have been made for the absorption edge of LTG GaAs, where the Urbach tail is assumed to be due to the increased density of defect states [108].

The conduction band offset between InAlAs and InGaAs is  $\Delta E_c=0.44$  eV [109], therefore the defect states in the InAlAs layers are still significantly below the CB band edge of adjacent InGaAs layers. Since the wave functions (WF) of the CB electrons in the InGaAs layers penetrate deep enough into the InAlAs barriers, i.e. have a sufficient overlap with the WF of bound defect states, the defects in the InAlAs barrier form effective electron traps. The WF overlap and the number of available traps can be adjusted to a certain degree by varying the barrier thickness. As will be shown later in this chapter, this allows for an additional degree of freedom for tuning the PCA. Fig. 3.1 a) shows a schematic of a heterostructure with 100 periods and Fig. 3.1 b) the band energies and defect levels of the heterostructure. In summary, the approach outlined above makes it possible to grow low defect, high mobility InGaAs layers adjacent to high defect, semi-insulating InAlAs layers at the same growth temperature.

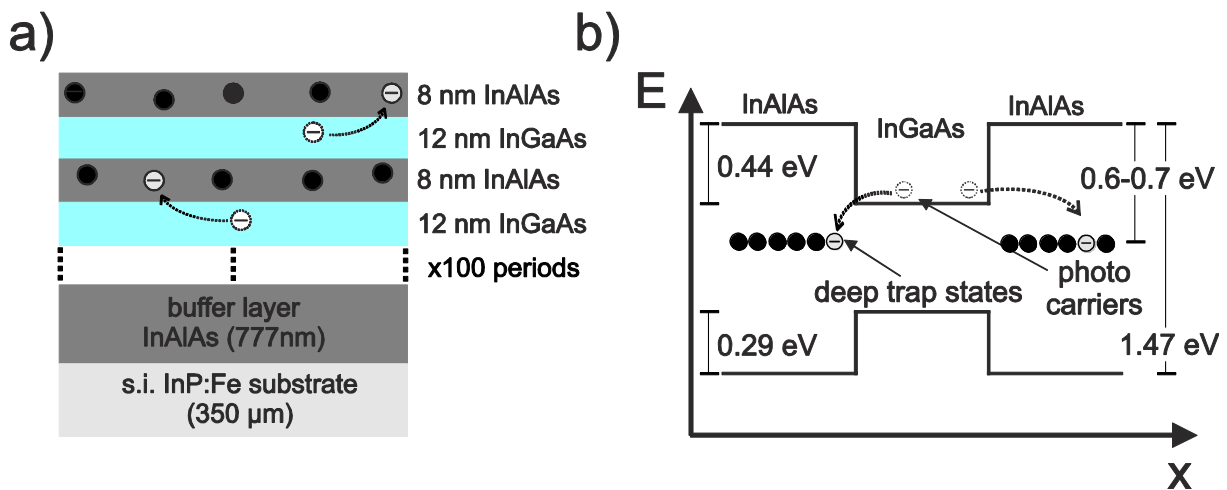


Fig. 3.1a) Schematic drawing of a typical 100-period MLHS with separated trapping/recombination regions, b) band diagram of the heterostructure band energies and the deep trap state positions. This figure is adopted and modified from Ref. [2].

The first proof-of-principle demonstration of such a device was obtained in this work with a 400°C grown, 100 period heterostructure, where each period has a layer thicknesses of 12 nm for InGaAs and 8 nm for InAlAs [2]. While the residual carrier concentrations for undoped MBE-grown InGaAs layers grown at 400°C are low compared to LT-grown undoped InGaAs layers, the values would still be far too high for the high bias field conditions ( $\approx 10$  kV/cm) needed for efficient PCA THz emitters. The resulting residual carriers would lead to high dark currents and thus the device would break down at high bias voltages. However, the presence of the deep defect states in the adjacent InAlAs layers significantly reduces the residual carrier concentration by up to three orders of magnitude, resulting in measured carrier concentrations of  $N_d - N_a \leq 10^{12}$  cm<sup>-3</sup>. The measured Hall mobility values for the heterostructures

were in the range of 1500-3000 cm<sup>2</sup>/Vs. The reduction of the mobility compared to bulk InGaAs is attributed to scattering at defect states in the InAlAs barriers and additional interface scattering at the layer boundaries, which should also be increased by the cluster defects considering their nm-scale size [110], [111]. To investigate the impact of the increased mobility, the sample was structured with a 25 μm strip-line mesa PCA. The PCA was then used as an emitter in a TDS-setup and compared to an LTG Be-doped reference emitter with the same antenna structure and subjected to identical bias field and optical excitation conditions. The measured THz pulse amplitude was higher than the pulse amplitude of the LTG reference by a factor of approximately 6 while having a comparable bandwidth [2].

To gain deeper insight into the influence of the growth temperature on the interplay of the InGaAs and InAlAs layers and the defect incorporation, two sample series with varying growth temperatures were grown. The first sample series (T<sub>g</sub>-Series 1) consisted of six samples grown at substrate temperatures between 325°C and 450°C with 25°C temperature steps. These samples were composed of 30 periods of 12 nm thick InGaAs layers followed by 8 nm thick InAlAs layers on top of an InAlAs buffer layer. The second sample series of four samples (T<sub>g</sub>-Series 2) was composed of the same layer structure as the first series, but consisted of 100 periods and were grown at substrate temperatures between 350°C and 425°C, again in steps of 25°C. To probe the carrier relaxation process, pump-power dependent differential transmission (DT) measurements were performed. An example of the obtained DT signals for T<sub>g</sub>-Series 2 and a LTG Be-doped reference sample are given in Fig. 3.2. The LTG Be-doped sample shows a very rapid and mostly mono-exponential decay due to a very high density of ionized As<sub>Ga</sub><sup>+</sup> defect [cf. chapter 4].

The DT signals of the samples of T<sub>g</sub>-Series 2 show a bi-exponential decay, with a short initial decay on the order of several fs followed by a long decay on the order of several tens of picoseconds. The time constants (τ<sub>1</sub>), associated with the initial short decay, extracted from bi-exponential fits to the DT signals do not correlate with the growth temperature or the THz performance of the PCAs made from the respective samples. This leads to the conclusion that this decay is not due to electron capture into defects in the InAlAs barriers. The origin of this short decay is assumed to be multifaceted: A small part of the signal is due to the coherent interaction of the pump and the probe beam, i.e. an autocorrelation signal, which could not be fully avoided despite the very-thoroughly crossed polarizations of the two beams [112],[113]. Another part of the signal is assumed to be due to thermalization of the carrier population, firstly via carrier-carrier scattering, and secondly with the lattice via longitudinal optical phonon emission and hence the associated absorption recovery in the high energy tail of the laser spectrum. Furthermore, at the given growth temperatures there are still some As<sub>Ga</sub> defects in the InGaAs layers. Since the energy level of the cluster defect states in the InAlAs

layers are lower than the energy level of the  $\text{As}_{\text{Ga}}$  defects, the remaining  $\text{As}_{\text{Ga}}$  defects should be ionized, resulting in fast traps that presumably also contribute to the rapid DT decay.

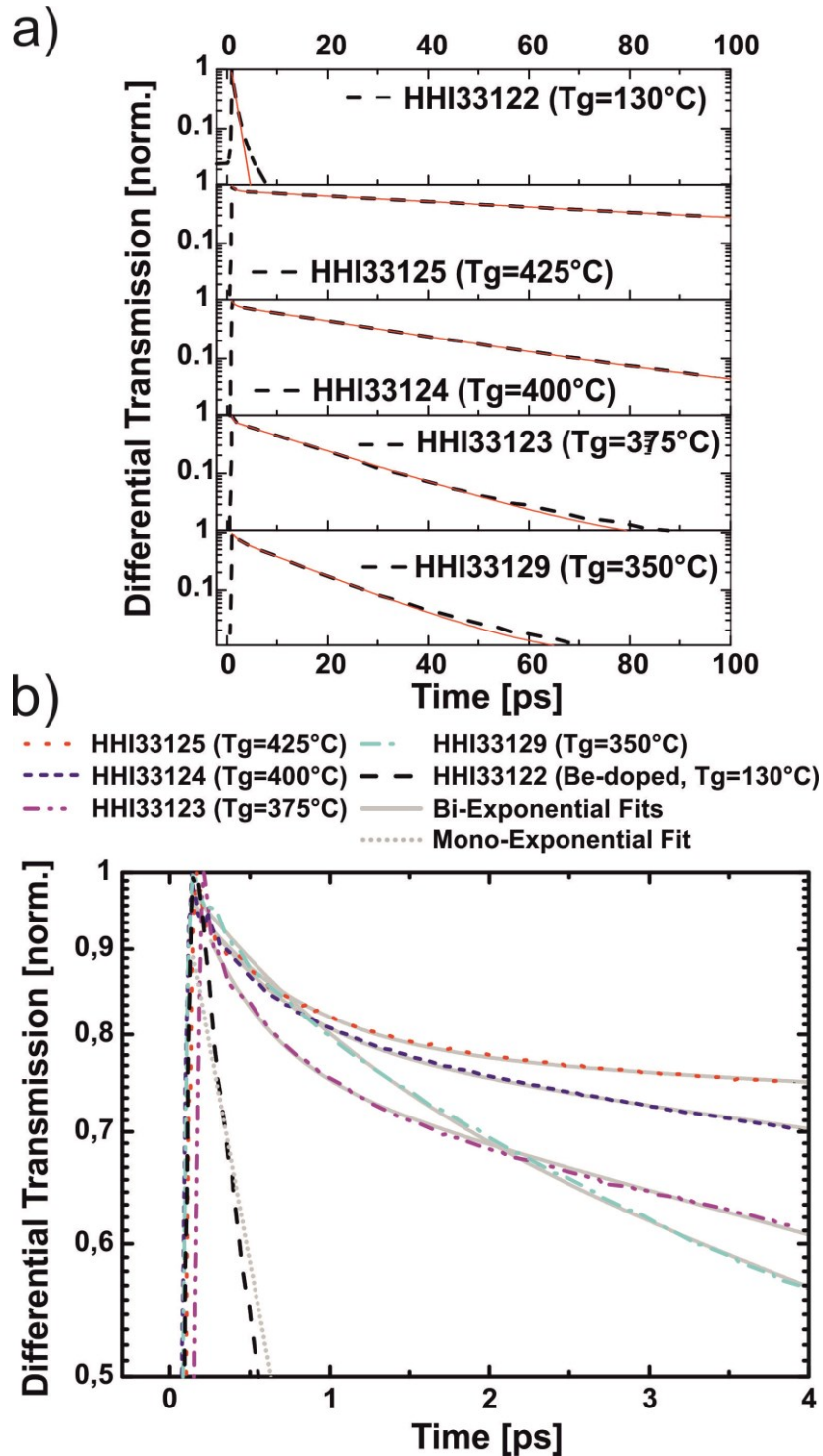


Fig. 3.2 a) DT signals for Tg-Series 2 and a LTG Be-doped reference sample and b) a zoom of the initial short decay in the DT signal. The pump power for all measurements was 16 mW. This figure is adopted and modified from Ref. [4].

In contrast to the time constants  $\tau_1$ , the time constants  $\tau_2$  show a strong dependency on the growth temperature, with a minimum value for samples grown at 350°C and 375°C for  $T_g$ -series 1 and  $T_g$ -series 2, respectively [Fig. 3.2]. This result indicates a maximum in defect incorporation and/or the capture cross section at around 350-375°C. The two curves in Fig. 3.3 are slightly shifted along the x-axis with respect to each other. This shift of the growth temperature presumably arises from uncertainties in the determination of the growth temperature, which is done by linearly extrapolating the temperature of post-growth oxide desorption from the InP substrate surface which takes place in the temperature range of  $T_g=500-520^\circ\text{C}$ . Since the two  $T_g$ -Series were not grown in direct succession, a possible aging of the sample holder might explain the additional offset between the two series. The uncertainty of the growth temperature can be assumed to be on the order of  $\Delta T_g=\pm 15^\circ\text{C}$ . The vertical shift of the two data sets is assumed to be due to the difference in the number of heterostructure periods, i.e. 30 and 100, and hence a difference in the total amount of available traps. Additional photoluminescence (PL) measurements on  $T_g$ -Series 1 further support the assumption of increased defect incorporation in the intermediate growth temperature range [3]. The PL intensities show a distinct minimum for the 375°C-grown sample and a generally similar behavior as for the time constant  $\tau_2$  in dependence of growth temperature; indicating an increase of non-radiative recombination, i.e. SRH recombination, due to defect states in the InAlAs layers.

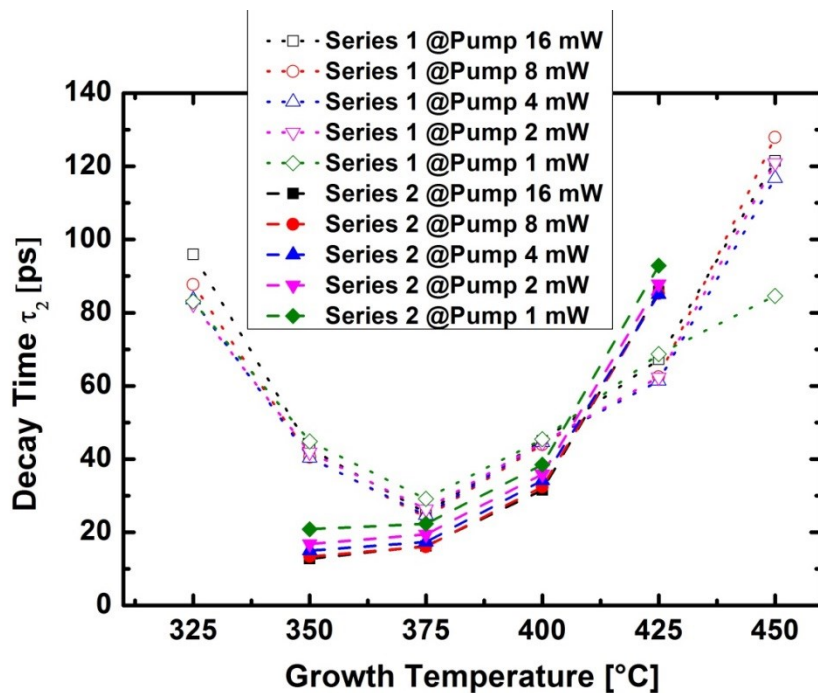


Fig. 3.3 Decay time  $\tau_2$  extracted from bi-exponential fits to the DT signals for  $T_g$ -Series 1 and  $T_g$ -Series 2 for different pump powers. This figure is adopted and modified from Ref. [4].

Furthermore, the DT signals show a weak dependence on the pump power with a slight decrease of the decay time of the absorption at higher pump powers. This decrease is expected to be due to an increased phonon density generated during the thermalization of the electron population with the lattice. For the sake of energy conservation, the carrier capture process generally involves the emission of several phonons with the number of phonons depending on the energy difference between the bound defect state and the electron energy in the CB. In the theoretical description of MPE the probability for the process is increased for higher phonon populations [55], [56], [114]. However, a decrease in the carrier capture time at higher excitation densities is only possible if no trap saturation occurs. Judging from findings for the defect densities in InAlAs obtained via deep-level transient spectroscopy (DLTS), which are found to be on the order of  $10^{16}$ - $10^{17}$   $\text{cm}^{-3}$  [106], and the DT decay times of several tens of picoseconds, the defect densities in the InAlAs layers are most likely low compared to the excitation densities used in the DT measurements. Therefore, the absence of trap saturation suggests that the recombination process of electrons in defect states with holes in the VB is faster or at least on the same order of magnitude as the capture process of electrons in the CB into the defects.

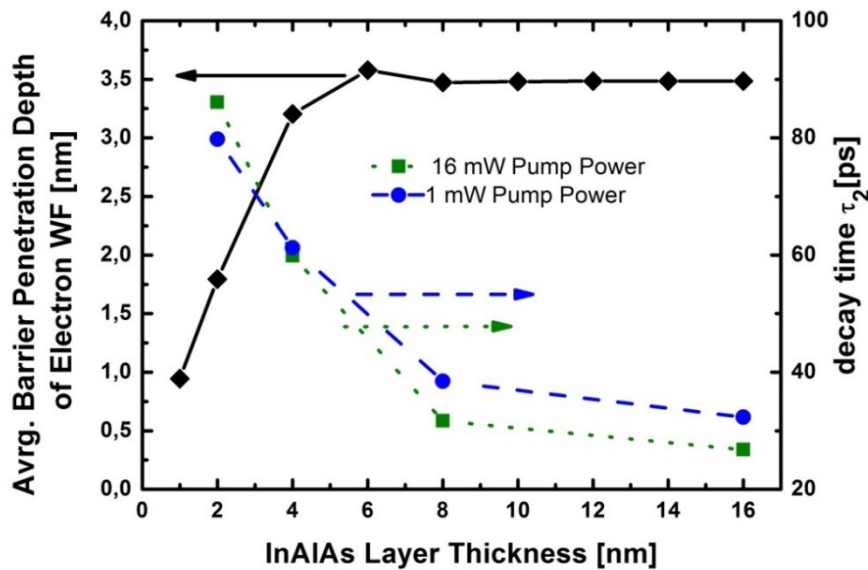


Fig. 3.4 Decay time  $\tau_2$  from bi-exponential fits to the DT signals for 16 mW and 1 mW pump power together with the average penetration depth of the electron WF into the barrier depending on the InAlAs barrier thickness. This figure is adopted and modified from Ref [4].

To put the above conclusions on the capture process to a test, another growth series with varying InAlAs layer thicknesses was grown. The InAlAs layers had thicknesses ( $d_b$ ) of 2 nm, 4 nm, 8 nm and 16 nm at a fixed InGaAs-layer thickness of 12 nm ( $d_b$ -series). All samples comprised of 100 periods and were grown at a substrate temperature of 400°C. The time

constants  $\tau_2$  obtained from bi-exponential fits to the DT data show a decrease of time constants for increasing layer thickness [Fig. 3.4]. This decrease is due to the increased amount of traps with increasing InAlAs volume relative to the fixed InGaAs volume. However, the decrease in decay time does not follow a  $1/x$  behavior, as expected from SRH theory, but rather shows a slightly weaker decrease. This discrepancy can be understood by taking a closer look at the electron WF overlap with the InAlAs barrier. Two examples of probability densities for two electron WFs in the first subband calculated by solving 1D Schrodinger equations of a 30-period heterostructure with 12 nm InGaAs layers for a) 16 nm InAlAs barriers and b) 2 nm InAlAs barriers are shown Fig. 3.5. For the case of the thin barriers, the WFs overlap strongly with the barriers. For a further increase of the barrier thickness the electrons “see” additional trap states within the barriers which should result in an increased capture rate. However, above certain barrier thicknesses the overlap of the calculated electron WFs with the barriers does not increase any further, since the penetration depth is limited by the CB-offset between InAlAs and InGaAs, i.e. the barrier height. Hence, defect states situated deep inside the barriers are not “reachable” for the electrons in the InGaAs layers. This can be seen in Fig. 3.5 a), where the WF probabilities calculated for 16 nm barriers reach a practically zero value in the middle of the barrier.

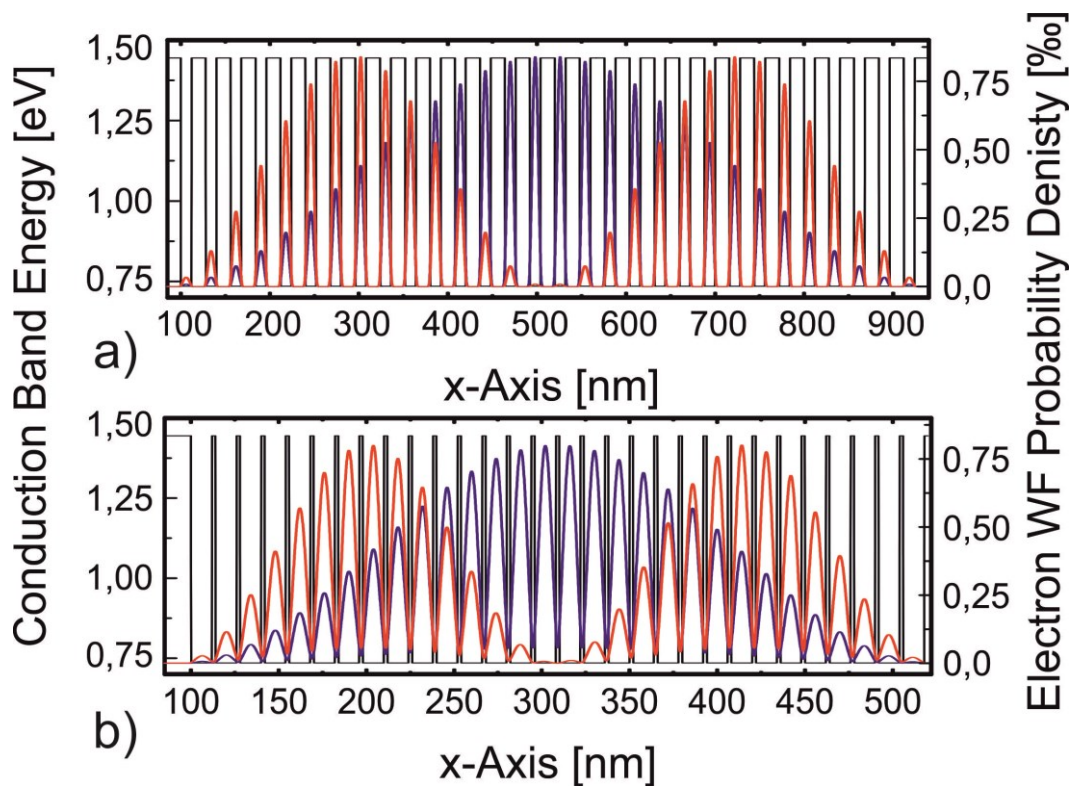


Fig. 3.5 Example of two electron wave functions of the first sub-band together with CB energies calculated for a 30-period heterostructure with 12 nm InGaAs layers for a) 16 nm InAlAs barriers and b) 2 nm InAlAs barriers.

A simple estimate of the penetration depth, here defined as a depth with probability of presence significantly greater than zero ( $\geq 10^{-6}$ ), was calculated by averaging over 30 electron WFs from the first sub-band calculated for 30 period heterostructures with different barrier thicknesses and is also shown in Fig. 3.4. In case of InAlAs layer thicknesses above approx. 7 nm, the trap states in the middle of the barrier have almost no overlap with the electrons, and hence should not contribute to the carrier capture process. It should be noted that for a precise calculation of the capture cross section, the overlap integral of the electron WFs with the localized defect states would have to be solved while taking into account electron-lattice interaction via an optical deformation potential to include multi-phonon emission, however this was beyond the scope of this work.

To investigate the influence of the aforementioned material properties on their applicability as PCA THz emitters, the heterostructures samples of  $T_g$ -series 2 and the  $d_b$ -series were processed with mesa strip-line antennas with 100  $\mu\text{m}$  photoconductive gaps. The PCA emitters were then tested in a THz-TDS setup, as illustrated in Fig. 1.1(a), and compared to a short carrier lifetime, LTG-Be-doped reference PCA. The detector employed for these measurements was a LTG Be-doped 10  $\mu\text{m}$  gap mesa dipole PCA fabricated from the same sample as the reference emitter. The emitters were biased with 10 kV/cm and illuminated with an average optical power of 16 mW. The Fourier THz-TDS spectra obtained from four different samples, instructive of the general behavior of the obtained results, are given in Fig. 3.6. The emitters of  $T_g$ -series 2 and the  $d_b$ -series generally show a THz emission with a central frequency that is slightly shifted to lower frequencies as compared to the LTG Be-doped reference emitter, which is due to the comparatively long capture time [104]. The frequency roll-off in the high frequency range of the normalized spectra is very similar to the LTG reference PCA, because it is governed by the laser pulse duration as predicted in chapter 1.1 and experiments with semi-insulating GaAs conducted by Liu et al. [115]. However, the amplitudes of the signals significantly differ by up to a factor of ten for the sample with the slowest decay time, which shows the strongest THz emission in contrast to the findings of [115].

To determine the emitted THz power, several PCA antennas of each sample of  $T_g$ -series 2 and the  $d_b$ -series were tested with a Golay cell power detector [116]. The applied bias field was again 10 kV/cm and the samples were illuminated with 16 mW of optical power. The results of the measurements for PCAs from samples of  $T_g$ -series 2 in dependence on the measured time constant  $\tau_2$  are shown in Fig. 3.7 a). Again, the emitted THz radiation increases with increasing decay time. A similar behavior was found for antennas made from samples of the  $d_b$ -series [4]. The decay times of all samples, i.e. the time constants of the carrier capture process, are much longer than the time during which the THz emission takes place, which is on the order of 1-2 ps. Therefore, the correlation between a longer decay time and an

increased THz emission cannot be due to the carrier capture process itself. However, since the decay time can be considered to be an adequate measure of the defect density, this correlation is assumed to be due to impurity scattering of electrons at defects in the InAlAs layers. Since, unlike the capture process, impurity scattering does not require the emission of multiple phonons, it has a significantly higher probability. The emitted THz power of the sample with the highest THz emission, i.e. HHI33141, was compared to the LTG reference sample in dependence on the optical excitation. The results are depicted in Fig. 3.7 b).

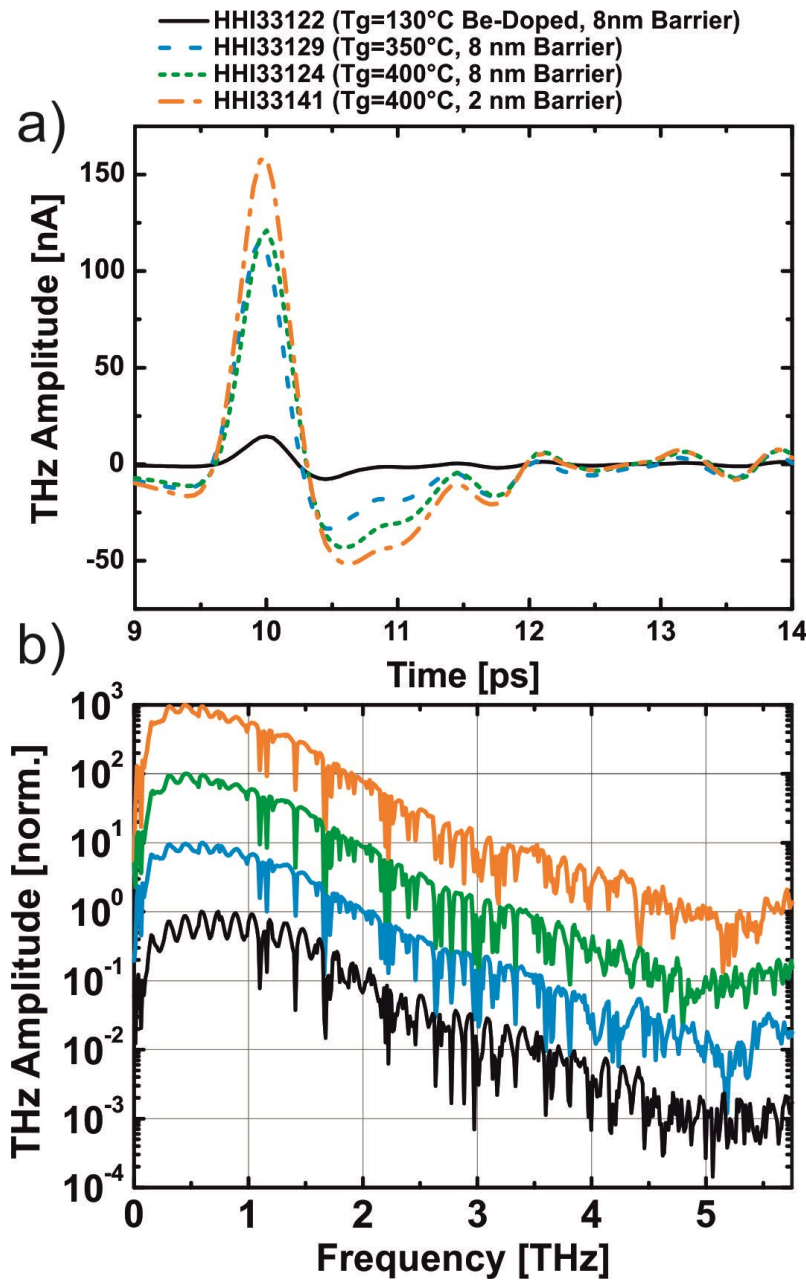


Fig. 3.6 THz-TDS pulse traces and corresponding FFT spectra for three emitters of T<sub>g</sub>-series and d<sub>b</sub>-series as well as the LTG reference emitter with 100 μm strip-line antenna geometry. The bias field was 10 kV/cm and optical power was 16 mW. This figure is adopted and modified from Ref. [4].

As already indicated by the tenfold increase in THz field amplitude in the THz-TDS measurements, the sample HHI33141 shows an emitted THz power which is one hundred times stronger than that of the LTG reference sample. With an applied bias field of 15 kV/cm and 32 mW of optical power, the measured THz power was found to be approx. 64  $\mu$ W, corresponding to an optical-to-THz conversion efficiency of  $2 \times 10^{-3}$ .

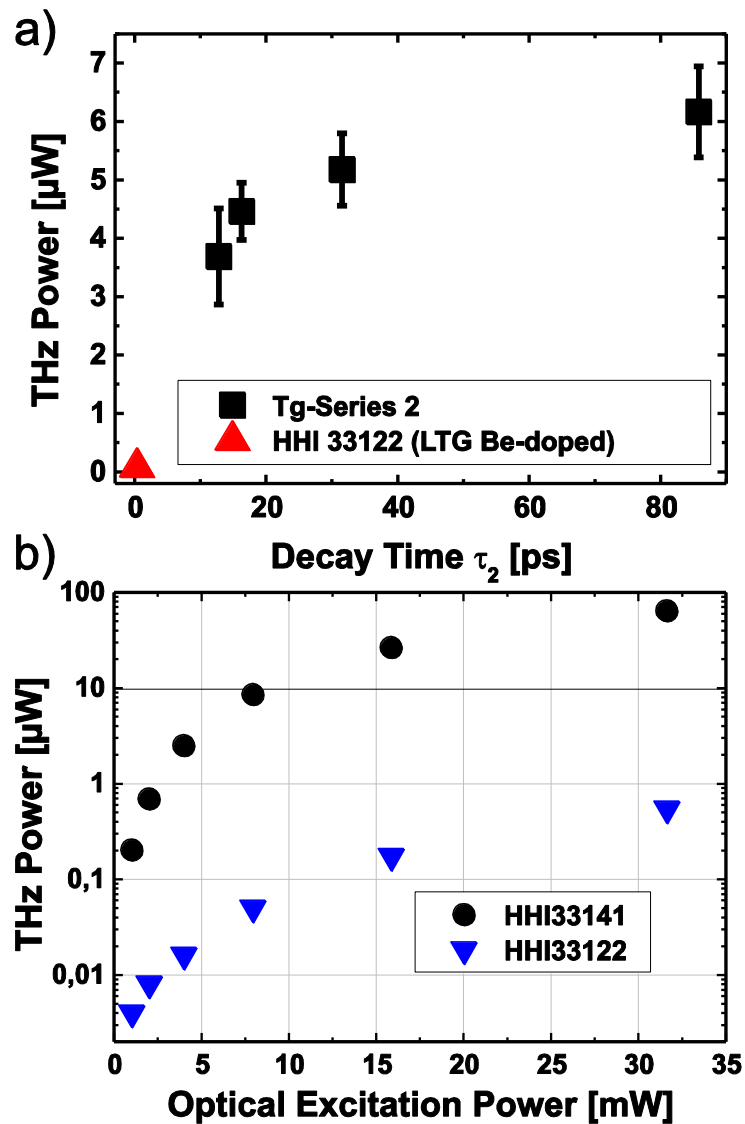


Fig. 3.7 a) THz power for samples of T<sub>g</sub>-series 2 and the LTG reference plotted over the time constant  $\tau_2$  obtained from DT measurements and b) emitted THz power in dependence of the optical excitation power for sample HHI33141 and the LTG reference. This figure was adopted and modified from Ref. [4].

## 4. Short carrier lifetime photoconductive THz detectors

This chapter will discuss the optimization of LTG Be-doped InGaAs/InAlAs heterostructures for THz detectors with high detection bandwidth and high dynamic range. Firstly, the carrier relaxation is described in the form of rate equations and compared to the experimental data from pump power dependent optical pump-probe measurements, i.e. differential transmission (DT), on differently Be-doped samples in a quantitative way. Secondly, the THz detection performance is tested in terms of bandwidth, dynamic range and detector noise. The THz measurements are performed for the same optical excitation densities as in the DT measurements to obtain a quantitative comparison. Thereafter it is shown that, in the case of LTG Be-doped InGaAs/InAlAs heterostructures, the simultaneous demands of high bandwidth and high dynamic range are partially contradictory. However, it is shown that by achieving the proper balance between those two factors, an acceptable trade-off can be found.

As shown in chapter 1.1, the carrier lifetime in the detector has a great influence on the frequency roll-off of the detected signal. Furthermore, the assumption of a mono-exponentially declining carrier density as in Eq. (1.2), i.e. a constant electron capture time  $\tau_c$ , does not take into consideration that for higher CB excitation densities the number of available trap states can be insufficient leading to a saturation of trap states [cf. Eq. (1.11)]. Since the recombination lifetime of trapped electrons with holes can be much longer than the capture time, trap saturation significantly prolongs the electron lifetime in the CB. Therefore, a fundamental prerequisite for the optimization of THz detectors is a detailed knowledge of the underlying carrier relaxation processes and their influence on the THz detection performance.

The central point of the investigation in this chapter is the influence of the beryllium doping concentration on the properties of LTG InGaAs/InAlAs heterostructures. As described in Chap. 1.3, the energy levels of  $As_{Ga}$  defects are approximately 91-150 meV below the CB minimum, which leads to a vast amount of thermally excited electrons in the CB at room temperature due to thermal excitation. To lower the Fermi level, and therefore obtain a higher resistivity, it is mandatory to counter-dope the heterostructures with an acceptor dopant. The samples were therefore doped with beryllium, which is a group II element and thus acts as an acceptor in the III-V semiconductors. Grandidier et al. [85] found a competition between Be and  $As_{Ga}$  since both are incorporated at group III lattice positions. The density of  $As_{Ga}$  defects in undoped LTG-InGaAs grown at substrate temperatures of 220°C was found to be approx.  $3 \times 10^{19} \text{ cm}^{-3}$  [85]. In this work all LTG-InGaAs/InAlAs heterostructure samples were grown at a substrate temperature of 130°C, which was found to result in even higher  $As_{Ga}$  defect densities. Furthermore, all samples were found to remain n-type, even for doping

concentrations as high as  $1.2 \times 10^{19} \text{ cm}^{-3}$ . This leads to the conclusion that Be-doping of LTG-InGaAs/InAlAs heterostructures results in the (partial) ionization of  $\text{As}_{\text{Ga}}$  defects and a pinning of the Fermi level to a mid-gap position. More precisely, in the following it will be assumed that the density of Be-dopants equals the density of  $\text{As}_{\text{Ga}}^+$  defects.

Since fast electron capture in InGaAs occurs predominately into ionized  $\text{As}_{\text{Ga}}^+$  defects, due to their larger capture cross-section as compared to neutral  $\text{As}_{\text{Ga}}$ , the Be-doping furthermore results in a decrease of the carrier lifetime. To investigate the electron capture mechanisms into the  $\text{As}_{\text{Ga}}^+$  defects and their subsequent recombination with holes, DT measurements in dependence on the optical excitation power were performed. The investigated sample series comprised four samples with different Be-doping concentrations and hence different densities of fast  $\text{As}_{\text{Ga}}^+$  defects. All four samples consisted of 100 periods of 12 nm InGaAs followed by 8 nm of InAlAs on top of a 777 nm InAlAs buffer layer. The samples were all grown lattice matched to a semi-insulating InP:Fe substrate at a substrate temperature of  $130^\circ\text{C}$  in an elementary source MBE. The Be-doping concentrations of the four samples were chosen to be  $3 \times 10^{17} \text{ cm}^{-3}$ ,  $9 \times 10^{17} \text{ cm}^{-3}$ ,  $2 \times 10^{18} \text{ cm}^{-3}$  and  $4 \times 10^{18} \text{ cm}^{-3}$ . Furthermore, all samples were in-situ annealed at  $500^\circ\text{C}$  for 60 min. After growth, the samples were micro-structured with mesa-type dipole antennas comprising a  $10 \mu\text{m}$  by  $10 \mu\text{m}$  footprint, equal to the structure depicted in Fig. 2.1 e), to ensure a precisely defined excitation area for DT measurements and to obtain performant PCAs for THz-TDS measurements. The excitation source for all DT measurements was an Er-doped fiber laser with a repetition rate of 100 MHz. The optical spot size was chosen to be  $12 \mu\text{m}$ , thus fully illuminating the mesa-structures.

To describe the measurements, with the time-dependent carrier density in the CB  $n(t)$  and the saturation carrier density in the CB  $N_0$ , the DT signal is given by:

$$\frac{\Delta T}{T_0} = \frac{T(t) - T_0}{T_0} = \exp\left(\alpha L \frac{n(t)}{N_0}\right) - 1 \quad (4.1)$$

Where  $T(t)$  is the time-dependent transmission and  $T_0 = \exp(-\alpha L)$  is the static linear transmission with absorption coefficient  $\alpha$  and sample thickness  $L$ . The time-dependent carrier density  $n(t)$  is modelled by a set of four coupled-rate equations:

$$\frac{dn}{dt} = G(t, n) - \frac{n}{\tau_e} \left(1 - \frac{n_T}{N_{\text{As}}^+}\right) \quad (4.2)$$

$$\frac{dn_T}{dt} = \frac{n}{\tau_e} \left(1 - \frac{n_T}{N_{\text{As}}^+}\right) - B_R(N_{\text{As}} - N_{\text{As}}^+ + n_T)n_{\text{Be}} \quad (4.3)$$

$$\frac{dn_{\text{Be}}}{dt} = \frac{h}{\tau_h} \left(1 - \frac{n_{\text{Be}}}{N_{\text{As}}^+}\right) - B_R(N_{\text{As}} - N_{\text{As}}^+ + n_T)n_{\text{Be}} \quad (4.4)$$

$$\frac{dh}{dt} = G(t, n) - \frac{h}{\tau_e} \left(1 - \frac{n_{Be}}{N_{As}^+}\right) \quad (4.5)$$

Here Eq. (4.2) and Eq. (4.3) describe the population of electrons in the CB and  $As_{Ga}$  defects, respectively. Eq. (4.4) describes the hole population in Be acceptors and Eq. (4.5) the hole population in the VB. The density of  $As_{Ga}$  and  $As_{Ga}^+$  defects are given by  $N_{As}$  and  $N_{As}^+$ , respectively. Since it is assumed that each Be acceptor ionizes one  $As_{Ga}$  defect, the density of positively ionized Be acceptors in Eq. (4.4) and Eq. (4.5) were set equal to the density of  $As_{Ga}^+$  defects  $N_{As}^+$ .

The significant finding of this model is that holes are captured by ionized Be acceptors and recombination occurs between localized electrons and holes in their respective trap states. The validity of this assumption as well as that of the whole model is elaborated in great detail in Ref. [5] and will here be discussed merely in a qualitative way. The recombination rate of electrons with holes in this model is proportional to the density of unionized  $As_{Ga}$  ( $N_{As} - N_{As}^+ + n_T$ ), the density of occupied (unionized) Be acceptors ( $n_{Be}$ ) and a factor comprising the wave function (WF) overlap of the two bound trap states ( $B_R$ ). The recombination process thus involves two localized states and has a reduced probability as compared to the capture process of free electrons with a bound defect state. This is in accordance with the measurement results, where the recombination lifetime is found on the order of several tens to hundreds of picoseconds as will be shown later.

The terms  $(1 - n_T/N_{As}^+)$  and  $(1 - n_{Be}/N_{As}^+)$  describe electron trap ( $As_{Ga}^+$ ) and hole trap (Be) filling, respectively. The electron capture time  $\tau_e$  can be written according to Eq. (1.11) as:

$$\tau_e = (N_{As}^+ v_{th} \sigma_e^{As^+})^{-1} \quad (4.6)$$

With the electron thermal velocity  $v_{th}$  ( $\approx 5.5 \times 10^7$  cm/s for  $T=300$  K) and the electron capture cross section for ionized  $As_{Ga}^+$  defects  $\sigma_e^{As^+}$ . An equal expression can be formulated for the hole capture time  $\tau_h$ .

For low pump powers of approx. 0.2 mW, corresponding to a pulse energy of 2 pJ, the excited carrier density in the CB ( $n \leq 10^{17} \text{ cm}^{-3}$ ) is well below the amount of available  $As_{Ga}^+$  defects at all doping levels. Hence trap saturation can be neglected, i.e.  $(1 - n_T/N_{As}^+ \approx 1)$ , and Eq. (4.2) decouples from the other three equations. The solution of  $n(t)$  is then given by a function which is mono-exponentially decreasing with  $\tau_e$  after the excitation. Furthermore Eq. (4.1) can be expanded for small exponents since  $n(t) \ll N_0$ , which yields:

$$\Delta T \cong \alpha L \frac{n(t)}{N_0} \propto \exp(-t/\tau_e) \quad (4.7)$$

This relation can be seen clearly in the DT signal and the respective decay times extracted from mono-exponential fits in Fig. 4.1 a) and its inset. The capture cross-section of  $\text{As}_{\text{Ga}}^+$  can then be calculated from the decay times at different Be-doping concentrations according to Eq. (4.6) which gives a value of  $\sigma_e^{\text{As}^+} \approx 2 \times 10^{-14} \text{ cm}^2$ . This is comparable to the values obtained for  $\text{As}_{\text{Ga}}^+$  defects in GaAs [76] and is reasonable within the theory of MPE processes of electron capture on charged defects.

At increased pump powers, the samples with lower Be-doping concentrations are successively driven into CB electron density regimes, where trap filling in the relaxation process is no longer negligible. These regimes are especially interesting since the excitation densities are on the same order of magnitude as the usual excitation levels used for PCAs in THz-TDS systems. There are two distinct types of trap filling:

The first type is partial trap filling, meaning that a significant number of traps are filled during the decay, but the initial CB density does not exceed the number of available traps, i.e.  $0 < n_T/N_{\text{As}}^+ < 1$ . In this case the decay time is prolonged by a factor of  $(1 - n_T(t)/N_{\text{As}}^+)$ . Since time constants for electron-hole recombination are on the order of several tens of picoseconds even for high doping concentrations, the second term in Eq. (4.3) can be ignored and Eq. (4.3) decouples from Eq. (4.4). The relaxation of the electron density in the CB can then be solved analytically, which yields:

$$n(t) \approx n_{ex} \exp\left(-\left(\frac{n_{ex}}{N_{\text{As}}^+}\right) \frac{t}{\tau_e}\right). \quad (4.8)$$

The second type of trap filling is the regime of complete trap saturation which occurs when the initial electron density in the CB exceeds the  $\text{As}_{\text{Ga}}^+$  density. In this case the trap states are rapidly filled and the decay of the CB density is governed by the electron-hole recombination time. As shown in Ref. [5] the time dependence of the electron density in the CB is the given by:

$$n^{\text{sat}}(t) = n_0^{\text{sat}} - B_R N_{\text{As}}^+ N_{\text{As}} t, \quad 4.9$$

where  $n_0^{\text{sat}}$  denotes the remaining electron density in the CB when complete trap saturation occurs.

Both trap filling regimes can nicely be observed in the logarithmic plots of DT signals in Fig. 4.1(b) for 2 mW ( $\equiv 20$  pJ) and in Fig. 4.1(c) for 16 mW ( $\equiv 160$  pJ) excitation. In Fig. 4.1(b) the sample with  $3 \times 10^{17} \text{ cm}^{-3}$  Be-doping shows complete trap saturation after an initial short

decay, whereas the sample with  $9 \times 10^{17} \text{ cm}^{-3}$  doping only shows partial trap filling and hence a slightly prolonged decay time. For 16 mW this sample is also driven into saturation and the onset of partial trap filling is visible for the  $2 \times 10^{18} \text{ cm}^{-3}$  doped sample.

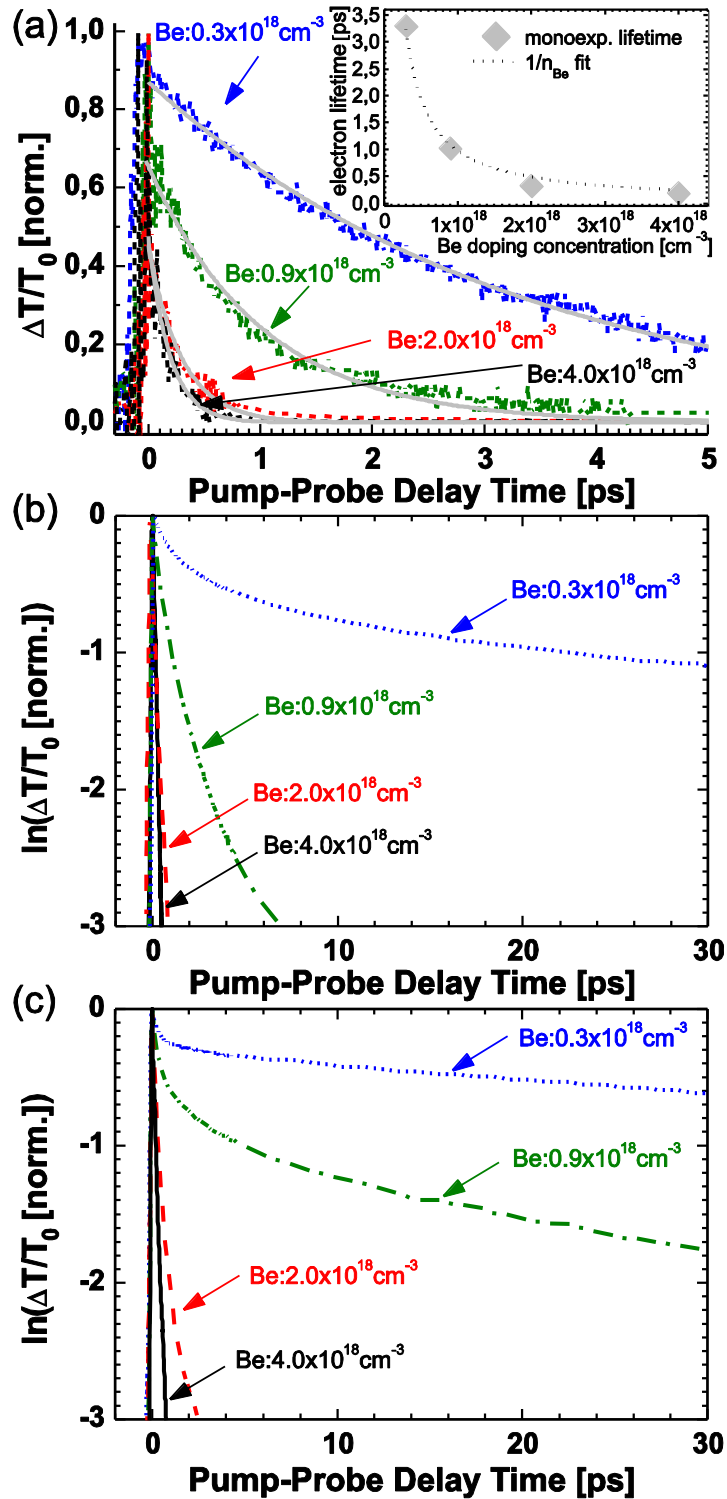


Fig. 4.1 a) DT signal at 0.2 mW pump power for different Be-doping levels and the time constants extracted from mono-exponential fits (inset). Logarithmic plots of the DT signal for different Be-doping levels at b) 2 mW pump power and c) 16 mW pump power.

The interesting question, in view of the applicability of these heterostructures as THz PCA detectors, is how the carrier lifetime and the saturation behavior influences their THz performance as THz detectors. Aside from validating the model predictions of chapter 1.1, concerning the detector bandwidth and signal amplitudes, another performance-determining factor which has to be reviewed is the noise current in the detector. Noise potentially limits the detectable bandwidth and dynamic range of the detector assuming the emitter noise is not dominating.

Therefore, all mesa dipole PCAs were tested as THz detectors under the exact same optical excitation conditions as in the DT measurements to obtain the highest possible comparability. The emitter for the experiments was a 25  $\mu\text{m}$  strip-line mesa antenna made from the  $4 \times 10^{18} \text{ cm}^{-3}$  doped heterostructure operated with a 50 V bias and 25 mW of optical excitation power. The measurements were performed with a high speed THz-TDS system with a mechanical shaker to introduce the time delay between the optical pulse at the emitter and the detector. The position of mechanical delay is detected with a precision of 1.3 fs by an optical sensor. The delay position signal is recorded together with the detector signal by a 50 kS/s field-programmable gate array (FPGA) with a 24 bit analog/digital converter. Additionally, the system features measurement rates of up to 25 pulse traces per second. The high measurement rate significantly reduces time position errors arising from expansion and contraction of the optical elements in the setup due to thermal fluctuations over the course of one single trace measurement. All-together, this allows to minimize errors in the amplitude measurement due to an error of the corresponding time position [7]. To achieve a higher dynamic range the average of several single traces is taken. This is in contrast to the lock-in detection scheme, usually used in THz-TDS, where the signal at each time-step is recorded with several tens or hundreds of milliseconds integration time and where thermal drift can cause strong fluctuations over the course of the measurement. Of course, in order to use this fast measurement scheme the THz signals are required to be high enough to render lock-in detection expendable. However, if this requirement is fulfilled the measurement scheme allows for measurements where the dynamic range is not limited by measurement errors of the system but the THz PCAs themselves [7].

As illustrated before, the Be-doping concentration strongly influences the carrier capture and recombination processes in the heterostructures. Unfortunately, an increased Be-doping concentration also decreases carrier mobility. As can be seen in Fig. 4.2, the measured Hall mobility is decreased in dependence of Be-doping concentration. This decrease qualitatively follows the decrease of the unsaturated decay time and hence the density of ionized defects [cf. inset in Fig. 4.1(a)]. The reduction in mobility is thus attributed to an increase of scattering on ionized  $\text{As}_{\text{Ga}}$  defects and ionized Be-dopants. The THz amplitudes detected for an excitation power of 0.25 mW at the detector, i.e. without trap saturation, are also shown in Fig. 4.2. The detector signal amplitude is decreased proportionally to the decrease in mobility

in accordance with the considerations of chapter 1.1. This behavior is generally followed by all samples at higher excitation powers except for the  $0.3 \times 10^{18} \text{ cm}^{-3}$  doped detector, which first shows an onset of saturation at 4 mW and then a decrease of the signal amplitude at optical powers in excess of 8 mW [6]. This saturation behavior is assumed to be due to the influence of the free carrier screening polarization.

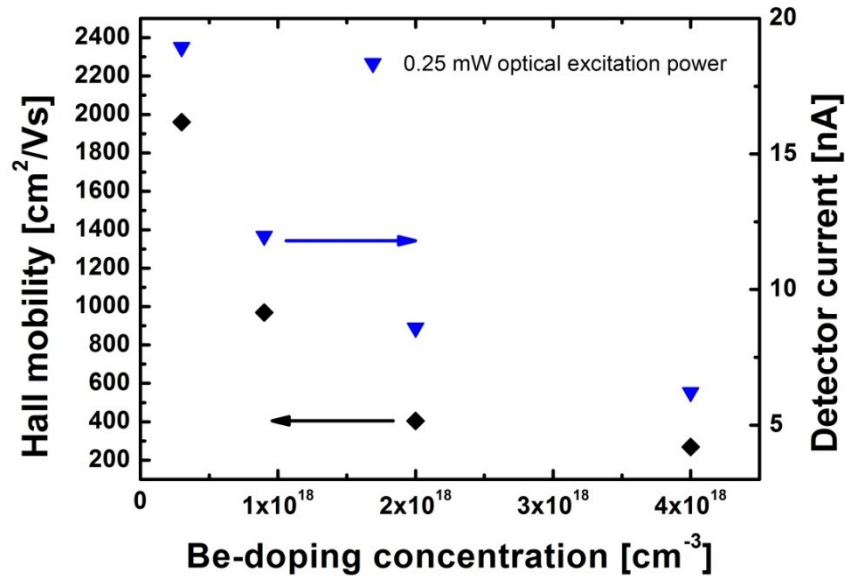


Fig. 4.2 Measured hall mobility and THz-TDS detector current at an optical excitation of 0.25 mW in dependence on the Be-doping concentration for all four samples. This figure was adopted and modified from Ref. [6].

This can also be seen in the Fourier spectra obtained from the THz-TDS measurements. The spectra for 0.25 mW, 2 mW and 16 mW excitation power of all detector samples are shown in Fig. 4.3. The spectra are obtained from the Fourier transformation of an average over 1000 pulse traces each with a measurement time of 60 ms, i.e. a total measurement time of 60 s. The frequency roll-off of the spectra obtained at a 0.25 mW excitation generally shows a steeper frequency roll-off for samples with a longer unsaturated carrier life time, i.e. lower Be-doping concentration, which is in accordance with the considerations concerning detector lifetime of chapter 1.1. At higher excitation powers, the increased roll-off becomes more prominent for the two samples with low doping concentrations as they are driven into the regime of trap saturation and thus exhibit a drastically increased electron lifetime. The aforementioned saturation of the signal amplitude in the time domain for higher optical excitation of the  $0.3 \times 10^{18} \text{ cm}^{-3}$  doped sample, transfers in the frequency domain to saturation of the spectral amplitudes above 1 THz. The highly doped samples, on the other hand, do not show a change in frequency roll-off behavior, in accordance with their constantly short carrier lifetime for all excitation powers obtained from the DT measurements.

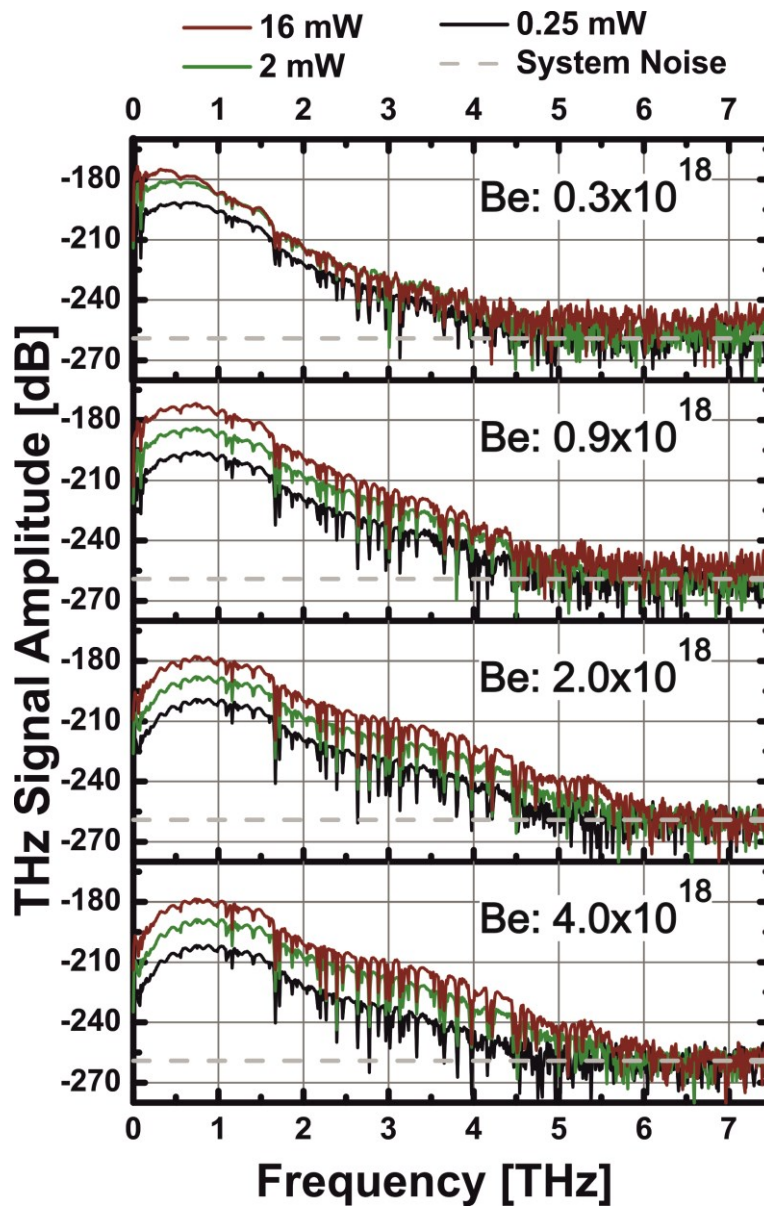


Fig. 4.3 Fourier spectra obtained from THz-TDS measurements at excitation powers at the detector PCAs of 0.25 mW, 2 mW and 16 mW for the four different doping concentrations. The system noise measured with an open detection circuit is shown as a dashed line. This figure is adopted and modified from Ref. [6].

Another important feature, which is visible in the case of the two samples with lower Be-doping, is the increased noise floor for higher excitation powers, i.e. the signals for frequencies above 6.5 THz. The noise floors of the highly doped samples, on the other hand, remain constant at increased excitation powers, appearing to be dominated by other noise contributions. Therefore the noise of the detection electronics was measured with an open circuit, i.e. without a connected detector, and is shown as a dashed line in Fig. 4.3. As can be seen Fig. 4.3, the noise level of the detection system has the same magnitude as the noise

floor of the two highly doped samples. Hence, in for these two samples the determination of their noise floor is not possible.

For low emitter noise, which is the case for all emitters investigated in this work, the detector noise determines the dynamic range and thus also the detectable bandwidth. Furthermore, the information that can be extracted from spectroscopic data has been shown to be mainly limited by the noise of the measurement [117], [118]. It is therefore important to investigate potential noise contributions and their effect on the operation conditions of PCA detectors.

There are three types of noise that can have a potential contribution: thermal Nyquist noise, shot noise (SH) and generation-recombination (GR) noise. In previous investigations Nyquist noise was found to give the dominant contribution to the detector noise current [119], [120]. GR and SH noise on the other hand were found to be negligible because both noise contributions scale with the square root of the detector current that is induced by the THz field. Since detector currents are usually in the lower nA range, the noise GR and SH noise contributions are small. The Nyquist noise however is only dependent on the resistivity of the material and its temperature. The Nyquist noise current is given by:

$$I_{Ny} = \sqrt{4 \cdot K_B \cdot T \cdot \Delta f \cdot R^{-1}}, \quad (4.10)$$

where  $K_b$ ,  $T$  and  $\Delta f$  are the Boltzmann factor, temperature and the measurement bandwidth, respectively.  $R$  denotes the detector resistance. Generally the resistance has to be taken as a function of the frequency and has to be integrated over the measurement bandwidth frequency range to determine the noise current value. However, since the measurement bandwidth for the above measurements is approx. 16 Hz, the resistance can be safely approximated by its DC value.

To further determine the Nyquist noise of the detector, the root mean square (rms) noise current in the detector was measured for different optical excitation powers without an incident THz field. Furthermore, the noise currents were calculated according to Eq. (4.10) from the average, i.e. time integrated, detector resistance. The detector resistance was therefore calculated by solving the rate equation model (4.2)-(4.5). The results are both illustrated in Fig. 4.4. There is a good qualitative agreement of the simulated noise currents with the measured noise current in the case of the two samples with low doping. However, the absolute noise current values differ by a factor of approx. 2. This difference is assumed to be due to the fact that the rate equation model does not include thermal re-excitation of carriers from trap states which can have a significant contribution during the relaxation process. The general behavior of the calculation and the measurement indicates that the origin of the noise current is indeed Nyquist noise. Even though there seems to be a minor increase of the

measured noise current in the two samples with higher doping, the measured values are again on the level of the system noise and the results are hence inconclusive. The predictions from the calculation indicate that, at least for the  $4 \times 10^{18} \text{ cm}^{-3}$  doped sample, the noise level should be defined by the system noise and not the PCA itself. Therefore, detection electronics with lower noise figures could potentially further increase the dynamic range in case of this detector PCA. To see how the interplay of signal amplitude, frequency roll-off and noise in dependence of Be-doping concentration and excitation power influences the dynamic range and detectable bandwidth of the detector signals, these two quanta were extracted from the detected THz spectra.

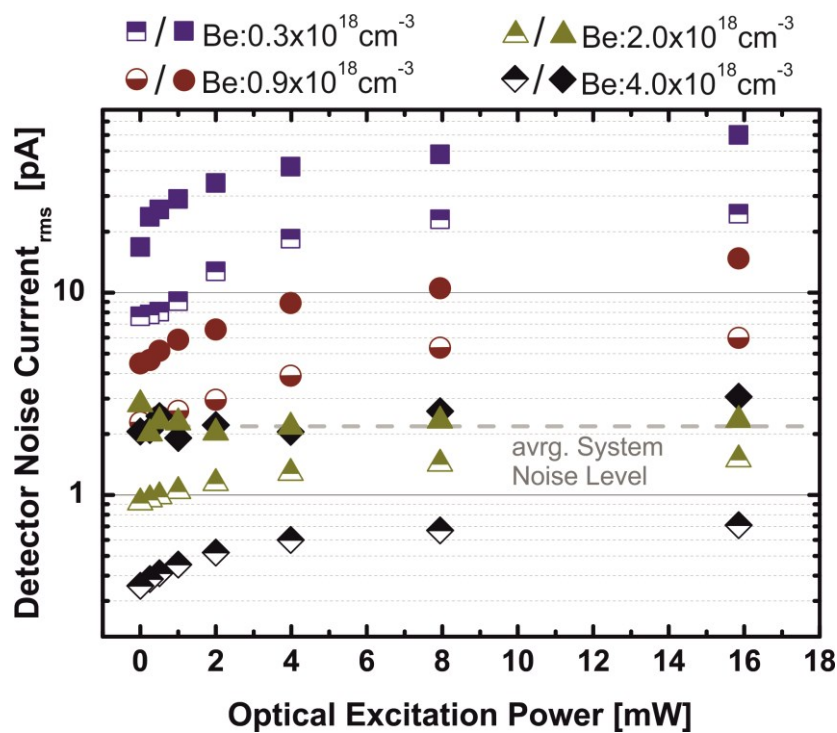


Fig. 4.4 Measured (full symbols) and calculated (half symbols) rms noise currents in the detector. The rms noise current of the detection system measured without a connected detector is shown as a dashed line. This figure was adopted and modified from Ref. [6].

The noise floor was therefore defined as the average spectral amplitude in the frequency range between 6.5 THz and 10 THz, where it is safe to assume that no THz signal is present. The detectable bandwidth was defined to be the highest frequency with an amplitude 6 dB above the noise floor. The accordingly obtained values are given in Fig. 4.5 a) and b). The two low doping detectors exhibit a saturation behavior and then a decrease in dynamic range as the optical excitation was increased [Fig. 4.5 a)]. The reason for this is that the Nyquist noise current increases stronger at higher optical excitation than the detector signal does. The strong increase of the Nyquist noise current is due to the long carrier lifetimes of those PCAs at high excitation powers which results in a low average resistance. In combination with the increased

roll-off behavior, also due to the prolonged carrier lifetime, the detectable bandwidth decreases for high excitation powers. Interestingly, the  $2.0 \times 10^{18} \text{ cm}^{-3}$  doped detector exhibits a higher dynamic range and bandwidth than the  $4.0 \times 10^{18} \text{ cm}^{-3}$  doped detector. This indicates a trade-off between short carrier lifetime and long carrier scattering time, i.e. signal amplitudes, which are both strongly influenced by the Be-doping concentration, as elaborated before. This insight provides the means for precisely targeted doping levels of the detector materials.

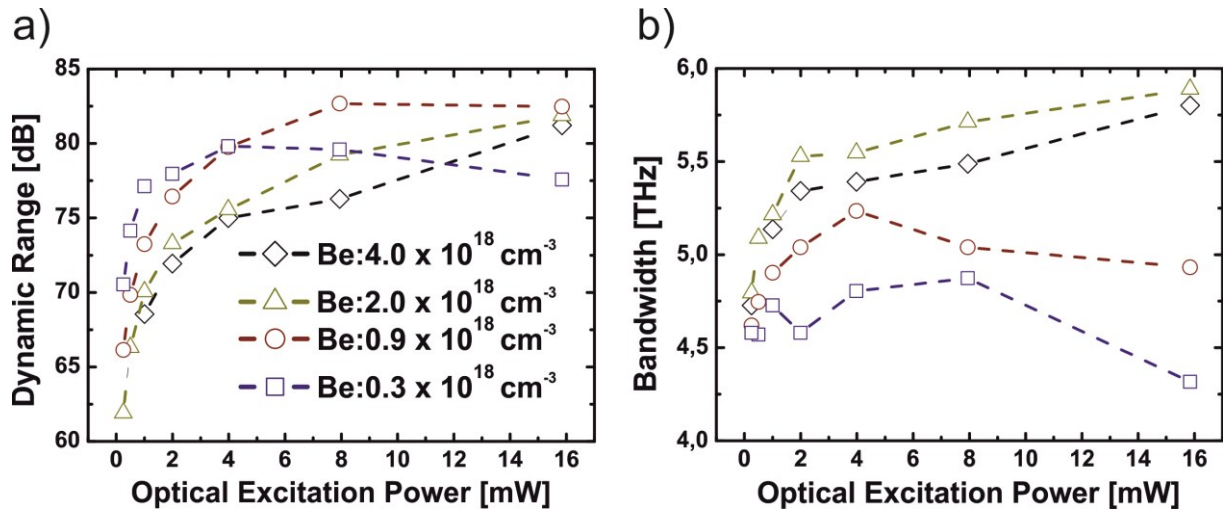


Fig. 4.5 a) Dynamic range and b) detectable bandwidth extracted from THz spectra for different excitation powers at the detector and for four different Be-doping concentrations. This figure was adopted and modified from Ref. [6].

In a further experiment, a high mobility emitter as described in chapter 3 was used in order to overcome the system noise limitation. The emitter was a  $100 \mu\text{m}$  strip-line antenna excited with 25 mW of optical power and with an applied bias of 120 V. For this configuration another noise contribution appeared to be dominant over the Nyquist noise. The noise current increased proportional to the square root of detector current induced by the THz field, and hence SH and GR noise are possible candidates for this noise current. However since GR noise is very low in short lifetime materials (due to the very low photoconductive gain), the noise current is attributed to shot noise. Even though the noise current is increased by the shot noise contribution, the dynamic range is still increased because shot noise scales only with the square root of the detector current. Therefore, with the combination of the short carrier lifetime detectors and the high mobility emitters of chapter 3, it is possible to obtain THz spectra with a detectable bandwidth of 6 THz and 90 dB dynamic range for a measurement time of 10 min. For a single trace measurement, i.e. 60 ms measurement time, the dynamic range is still 60 dB and the detectable bandwidth is in excess of 4 THz. Both measurements are illustrated in Fig. 4.6. This is a huge improvement compared to the un-optimized planar-planar detectors in chapter 2, where only 2.5 THz bandwidth was obtainable and only by the use of lock-in detection and a measurement time in excess of 30 min.

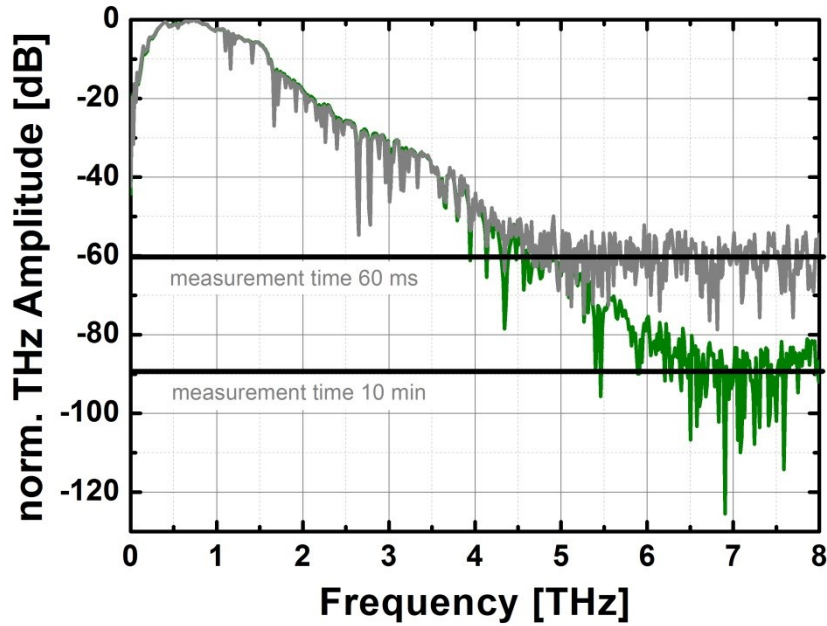


Fig. 4.6 THz spectra for two different measurement durations obtained from a  $4.0 \times 10^{18} \text{ cm}^{-3}$  Be-doped detector with 16 mW optical excitation and a high mobility emitter excited at 25 mW and with 12 kV/cm of applied bias field. This figure is adopted and modified from Ref. [6].

#### 4.1 All-fiber electronically controlled optical sampling THz-TDS system

With these strongly improved THz emitters and detectors, it is possible to obtain THz signals with high bandwidth and high dynamic range for significantly reduced measurement times. To further reduce the measurement time, a system approach was investigated where the time delay between the emitter and detector pulses is achieved by a fast electro-optical modulation technique instead of a slow mechanical delay stage [cf. Fig. 1.1]. The time delay between the optical excitation pulses of the emitter and detector is here achieved by the use of two lasers, one of which can be tuned in its repetition rate with a piezo crystal in the laser cavity. First, the repetition rate of the laser containing the piezo is locked to the repetition rate  $f$  of the other laser by the use of a proportional-integral-derivative controller. Then, the repetition rate of the first laser is slightly changed with a periodical modulation. This leads to a time dependent phase difference  $\Delta\Phi(t)$  between the pulse trains of the two lasers and which is equivalent to a time delay that is given by  $\tau(t) = \Delta\Phi(t) / 2\pi f$  [121], [122]. This principle is known as electronically controlled optical sampling (ECOPS) and has been previously demonstrated for titanium-sapphire based free-space THz-TDS system operating at 800 nm wavelength with LTG-GaAs detectors and emitters [122]. In the present work, the first demonstration of a completely fiber-coupled ECOPS system operating at 1560 nm with measurement rates of up to 8 kHz, i.e. 8000 pulse traces per second, was performed [8].

Fig. 4.7 a) shows two examples of single THz pulse traces obtained at measurement rates of 2 kHz and 8 kHz (inset). For 2 kHz measurement rate the complete scan range of the time delay is 180 ps, while for the 8 kHz measurement rate the scan range is reduced to 20 ps due to mechanical limitation of the piezo crystal. The spectrum in Fig. 4.7 b) is a Fourier transformation of a pulse trace obtained from averaging over 1000 single pulse traces measured at 2 kHz. In this case, the spectral bandwidth of the system reaches values of up to 2 THz with a dynamic range of 76 dB. The inset of Fig. 4.7 b) shows the dependence of the dynamic range on the number of averages which follows a typical logarithmic behavior, as indicated by the linear fit curve in the logarithmic plot. For a single measurement at 2 kHz measurement rate, i.e. 500  $\mu$ s measurement time, the system still reaches 47 dB dynamic range.

The increased roll-off and lower dynamic range of the THz spectrum in Fig. 4.7 b), as compared to the spectrum in Fig. 4.6, measured with only 60 ms measurement time has several potential influences: One influence is the difference in the measurement windows, which are 180 ps and 67 ps for Fig. 4.7 b) and Fig. 4.6, respectively. This gives a measurement time per ps of delay of 2.77 ms and 0.9 ms for Fig. 4.7 b) and Fig. 4.6, respectively. Thus, the measurement times per point of the traces of both spectra are almost comparable and can not explain the difference. The second influence is that the laser pulse widths of the two ECOPS lasers were approx. 140 fs. This is due to fact that the pre-compensation of the fiber dispersion, which was done with a dispersion compensating fiber, was not fully optimized to match the length of the fiber delivery. This could explain the increased roll-off behavior obtained in the ECOPS system. The last influence is the timing jitter between the two ECOPS lasers, which is on the order of 50 fs. This time position error broadens the THz pulse width of an averaged trace, which also transfers in the Fourier domain to increased roll-off and hence reduced bandwidth.

While the fiber length adjustment can easily be done more precisely in future systems to obtain shorter laser pulses, the improvement of the timing jitter is a slightly more difficult task, involving a more stable design of the piezo holder to minimize eigen-oscillations as well as a more sophisticated control algorithm, e.g. a frequency lock to higher harmonics of the piezo oscillation.

Nevertheless, the results shown in Fig. 4.7 represent the fastest fiber-coupled THz measurement system demonstrated so far and open up a plurality of new possible applications for THz spectroscopy, where high measurement speeds with simultaneous low system costs are the defining factors for the applicability of THz-TDS systems.

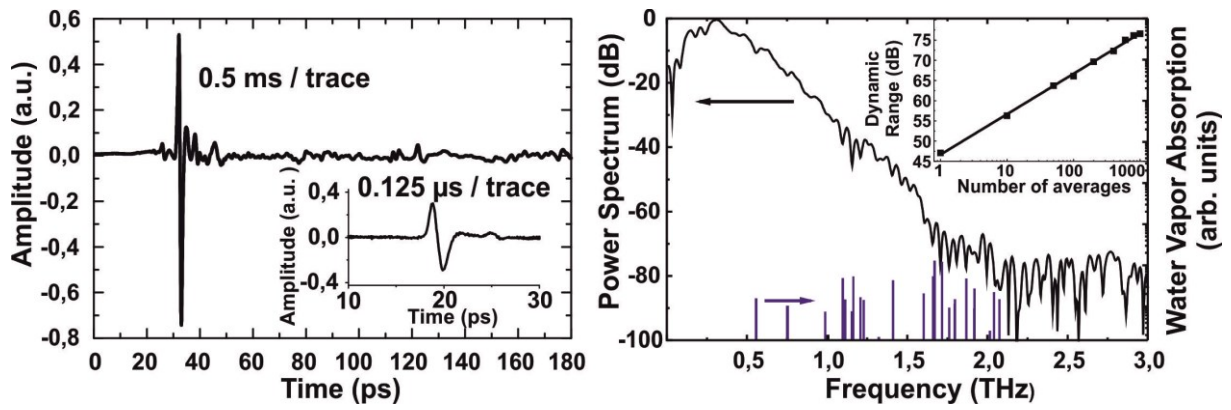


Fig. 4.7 a) Single pulse traces obtained from ECOPS measurement rates of 2 kHz and 8 kHz (inset). b) Fourier spectrum obtained from averaging over pulse 1000 traces measured at 2 kHz. The dependence of the dynamic range on the number of averages at 2 kHz is shown in the inset. This figure was adopted and modified from Ref. [8].

## 5. Photoconductors for 1030 nm pulsed laser excitation

In this chapter the results on the investigation and optimization of photoconductive semiconductor structures for excitation with ytterbium-doped femtosecond fiber lasers, with a center wavelength of 1030 nm, will be reviewed. From an application point of view, the change of the center wavelength from 1550 nm to 1030 nm has the disadvantage that cost efficient off-the-shelf optical components from telecom applications are not available at a wavelength of 1030 nm. However, the big advantage of femtosecond ytterbium fiber lasers, over their erbium-fiber counterparts, is the higher achievable average output power. While erbium fiber usually have output powers in the range of a few hundred mW, ytterbium femtosecond lasers offer up to 4.5 W average power with pulse durations below 100 fs [11]. The high output powers open up the possibility of efficiently exciting emitter structures which feature large photoconductive areas, e.g. with gap sizes of several hundred micrometers, as well as multi-channel detectors, where several detector antennas are excited simultaneously, all pumped with a single laser source. This offers the opportunity for building THz imaging and tomography systems with improved measurement speeds, as will be shown later in this chapter.

The band gap energies of the previously discussed InGaAs/InAlAs PCAs were designed to offer sufficient light absorption at 1550 nm, with band gap energies of approx. 0.76 eV in case of the usual 12 nm of InGaAs layer thickness used in this work. Therefore, the PCAs can also be excited at a center wavelength of 1030 nm, i.e. photon energies around 1.2 eV. Considering that the joint density of states (JDOS), i.e. the number of available states for an optical transition in dependence of the photon energy, is higher for higher photon energies, the absorption of 1030 nm light is increased as compared to 1550 nm. On the other hand, the carriers are excited into band states up high in the CB with excess energies of approx. 440 meV.

To investigate how the dynamics of the hot carriers change the THz generation and detection characteristics an emitter and a detector, both manufactured from a LTG Be-doped InGaAs/InAlAs sample with 100 periods of 12 nm InGaAs and 8 nm InAlAs, were excited at 1030 nm wavelength and tested in a DT setup and a THz-TDS setup. The results were then compared to results obtained for 1550 nm excitation. To obtain comparable excitation conditions the incident photon density was kept equal for both wavelength with a value of  $1.65 \times 10^{14} \text{ cm}^{-2}$ , i.e. 5 mW at 1550 nm and 3.32 mW at 1030 nm for a spot size of 10  $\mu\text{m}$  at 100 MHz laser repetition rate [9]. The signal amplitudes obtained from TDS measurements at 1030 nm are significantly increased by more than one order of magnitude as compared to the 1550 nm excitation. This can be mostly attributed to the increased absorption for 1030 nm

wavelength. The spectra however show a strongly increased frequency roll-off behavior indicating a prolonged carrier lifetime for hot electrons. This was further confirmed by DT measurements at 1030 nm pump and 1030 nm probe where the carrier lifetime was extended at low excitation from 230 fs to 2.7 ps [9].

To further investigate the influence of the carrier excess energy on the carrier lifetime and capture process, another set of four samples was grown. The first sample in the series was a standard heterostructure sample which served as a reference and consisted of 100 periods of 12 nm InGaAs and 8 nm InAlAs and with a Be-doping concentration of  $4 \times 10^{18} \text{ cm}^{-3}$ . To examine the assumption, that the excess energy reduces carrier capture probability, the three other samples had intentionally shifted band gap energies and hence a lower amount of carrier excess energy at an excitation wavelength of 1060 nm.

There are two possible ways to obtain samples with higher band gap energies while maintaining the lattice match to the InP substrate. The first one is to reduce the InGaAs layer thicknesses in the LTG heterostructures in order to shift the sub-band energies in the InGaAs layers towards higher energies. The other one is to employ a quaternary composition with additional aluminum content, i.e. LTG InAlGaAs, which also shifts the band gap towards higher energies in dependence of the aluminum content. An overview of the growth parameter and the measured Hall data of all four samples are given in Table 1.

The first approach was achieved with a LTG Be-doped heterostructure sample with InGaAs and InAlAs layer thicknesses of 3 nm and 4 nm, respectively, and with 400 periods to keep the total InGaAs thickness equal to the reference sample, i.e. 1.2  $\mu\text{m}$ . The 3 nm layer thickness results in a calculated shift of the first sub-band absorption to approx. 0.94 eV, i.e. 1300 nm wavelength. The choice of the InGaAs layer thickness is a trade-off between a sufficient shift of the band gap energy and the maintenance of an acceptable carrier mobility, which is strongly decreased for thinner layers because of the increasing contribution from surface roughness scattering at the layer boundaries [cf. Table 1]. The sample was additionally Be-doped, for the reasons explained in the previous chapter, with a concentration of  $4 \times 10^{18} \text{ cm}^{-3}$ .

For band gap shifted PCAs based on a quaternary composition, two different samples were grown both comprising a 1.2  $\mu\text{m}$  bulk layer of  $\text{In}_{0.52}\text{Al}_{0.28}\text{Ga}_{0.20}\text{As}$ . One of the samples was un-doped and the other was doped with  $4 \times 10^{18} \text{ cm}^{-3}$  of Beryllium to further increase the amount of ionized  $\text{As}_{\text{Ga}}$  defects. The chosen composition of  $\text{In}_{0.52}\text{Al}_{0.28}\text{Ga}_{0.20}\text{As}$  results in a calculated band gap energy of 1.1 eV, i.e. approx. 1120 nm wavelength. As elaborated in chapter 1.3, the energy levels of the  $\text{As}_{\text{Ga}}$  defects in  $\text{In}_x\text{Ga}_{1-x}\text{As}$  maintain their energetic position, to a good approximation, with respect to the VB. If this behavior is assumed to be

maintained in case of a quaternary alloy, the energy levels of the  $As_{Ga}$  defects in  $In_{0.52}Al_{0.28}Ga_{0.20}As$  should be situated at approx. 0.5 eV below the CB edge. The low amount of thermally excited carriers at room temperature as determined by Hall measurements for both quaternary samples supports this assumption [cf. Table 1].

Sample	Structure	Periods	Growth Temperature [°C]	Be-Doping [ $cm^{-3}$ ]	Resistivity [ $\Omega cm$ ]	Mobility [ $cm^2/Vs$ ]	Residual Carrier conc. [ $cm^{-3}$ ]
1	12 nm InGaAs/ 8 nm InAlAs	100	130	$4 \times 10^{18}$	850	308	$2.39 \times 10^{13}$
2	3 nm InGaAs/ 4 nm InAlAs	400	130	$4 \times 10^{18}$	7285	127	$6.72 \times 10^{12}$
3	1.2 $\mu m$ $In_{0.52}Al_{0.28}Ga_{0.20}As$	bulk	130	-	8238	1130	$6.7 \times 10^{11}$
4	1.2 $\mu m$ $In_{0.52}Al_{0.28}Ga_{0.20}As$	bulk	130	$4 \times 10^{18}$	29050	331	$6.5 \times 10^{11}$

Table 1 Growth parameters and Hall data of the growth series. This table was adopted and modified from Ref. [10].

To investigate the ultra-fast carrier relaxation process, all samples were measured with transient white-light pump-probe (TWPP) spectroscopy. In case of TWPP spectroscopy the probe is a white-light super-continuum generated by the self-phase modulation of a femtosecond pulse in a sapphire crystal. The pump is generated by a tunable optical parametric amplifier (OPA), which enables to tune the pump wavelength over a wide range. Both, the sapphire crystal and the OPA were driven by a Ti:Sapphire laser with a 1 kHz regenerative amplifier. The transmitted white-light probe was recorded in a grating spectrometer to resolve the transmission spectrally. Thus, the experiment measures the differential transmission in dependence of energy and time. Hence, it is possible to obtain a detailed picture of the relaxation process of the (hot) carriers. Additionally, linear absorption spectra were recorded to determine the band gap energies and compare them to the calculated values.

The linear absorption spectra are shown in Fig. 5.1 a)-Fig. 5.4 a) for samples 1 to 4, respectively. The linear absorption spectra all show typical features of an LTG semiconductor with strongly broadened Urbach-like absorption edges due to disorder [107] and thus only faintly visible sub-bands features in case of the two heterostructures, i.e. samples 1 and 2. All measured band edge energies agree well with the previously calculated values. As pointed out before, the absorption in the short wavelength range around 1060 nm for sample 1 is increased due to the higher JDOS as compared to the near band edge absorption around

1550 nm, i.e. approx. by a factor 5. Sample 2 also shows a very high absorption in at 1060 nm which is again due to the increased JDOS for elevated energies. The Be-doped quaternary sample, i.e. sample 4, shows additional broadening in the band tail as compared to the un-doped quaternary sample 3, which can be attributed to additional tail states induced by the Be-doping.

The normalized TWPP spectra of the four samples are shown in Fig. 5.1 b) and c), Fig. 5.2 b) and c), Fig. 5.3 b) and Fig. 5.4 b). Both heterostructure samples were excited at two different pump wavelengths of 1250 nm and 1060 nm. The quaternary samples were excited only at 1060 nm due to their higher band gap. The pump power for all measurements was 15  $\mu$ W with a spot size of 260  $\mu$ m, which results in photon densities of  $1.5 \times 10^{14} \text{ cm}^{-2}$  and  $1.77 \times 10^{14} \text{ cm}^{-2}$  for 1060 nm and 1250 nm wavelength, respectively. This corresponds to induced carrier densities in the range of  $n_e \geq 1 \times 10^{18} \text{ cm}^{-3}$  for the 1060 nm excitation of samples 3 and 4 as well as the 1250 nm excitation of samples 1 and 2. Though, due to the elevated absorption in the cases of the 1060 nm excitation of samples 1 and 2, the carrier densities here reach values of up to  $n_e \geq 4 \times 10^{18} \text{ cm}^{-3}$  for the upper layers of the heterostructure samples. Since the densities of ionized  $\text{As}_{\text{Ga}}$  defects can be assumed to be on the same order of magnitude, partial trap filling cannot be completely ruled out. However, it can be assumed that no strong trap saturation occurs [cf. chapter 4]. The vertical axes in the TWPP spectra indicate the time delay between pump and probe pulses, while the horizontal axes show the spectral components of the white light probe pulse. The color map values indicate the normalized differential transmission signal. Here, a positive color map value corresponds to increased transmission induced by the pump and a negative color map value corresponds to pump induced absorption. Since the DOS for the electrons in the CB is smaller than the DOS of the holes in the VB, the TWPP signals are dominated by the electron population. Therefore, the discussion can be mostly limited to the dynamics of the electron population in the CB. After the excitation by the pump pulse the TWPP signals of all samples show an initial fast thermalization of the electrons with each other via electron- electron (e-e) scattering on a time scale of 50-100 fs, as it can be expected for the high electron densities of  $n_e \geq 10^{18} \text{ cm}^{-3}$  present in these measurements. The subsequent energy relaxation of the electron population after this initial e-e thermalization strongly depends on the sample and the excitation wavelength and will in the following be discussed for each sample individually.

The TWPP spectrum for the 1060 nm excitation of sample 1 is shown in Fig. 5.1 b). After the initial e-e scattering the majority of the electron population relaxes down to the band edge via longitudinal-optical (LO) phonon emission on a time scale of approx. 1.6 ps. The relaxed electron population in the vicinity of the band edge results in a strong increase of the TWPP signal, due to the lower DOS in this energy range and the resultant Pauli blocking. The near band edge population subsequently decays on a time scale of 1.8-2 ps due to non-radiative

captured into defect states. To further investigate the impact of the electron excess energy on the electron lifetime, sample 1 was excited at a longer pump wavelength of 1250 nm, i.e. photon energies of around 0.97 eV. The obtained TWPP spectrum is shown in Fig. 5.1 c). The overall TWPP signal is weaker than for the 1060 nm excitation, which is due to the lower absorption of the pump wavelength and hence lower induced carrier density. As in the case of the 1060 nm excitation, at least a part of the electron population relaxes towards the band edge before being captured by defect states. However, a part of the electrons appear to be captured before reaching the band edge.

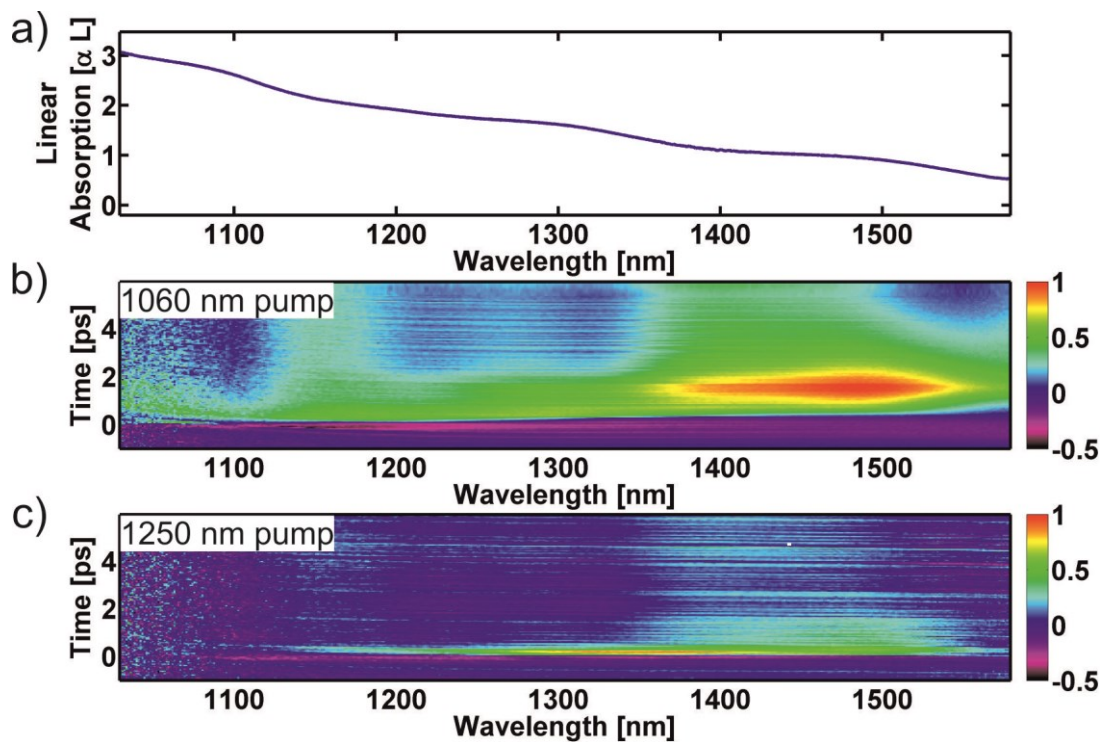


Fig. 5.1 a) Linear absorption spectrum of a sample 1 and TWPP spectra for a pump wavelength of b) 1060 nm and c) 1250 nm. The pump power for the TWPP measurement was  $15 \mu\text{W}$  for both wavelengths. This figure was adopted and modified from Ref. [10].

In case of sample 2 excited at a pump wavelength of 1060 nm [Fig. 5.2 b)], i.e. a significant amount of excess energy, a similar behavior is observed. The electron population is relaxed towards the band edge via LO-phonon emission on a time scale of approx. 300 fs and is subsequently captured into defect states. At 1250 nm excitation [Fig. 5.2 c)], i.e. at the band edge, the initial electron population forms a cold Fermi distribution due to the lack of excess energy, which is subsequently broadened due to the redistribution of electrons via e-e scattering and also electron-phonon (e-ph) scattering on a time scale of 300 fs. This redistribution of the electrons into other CB states results in a reduction of the Pauli blocking and hence in a partial decay of the transmission signal. This decay is superimposed by the

decay component caused by the non-radiative capture process into defect states, which takes place on a time scale of approx. 1.3 ps.

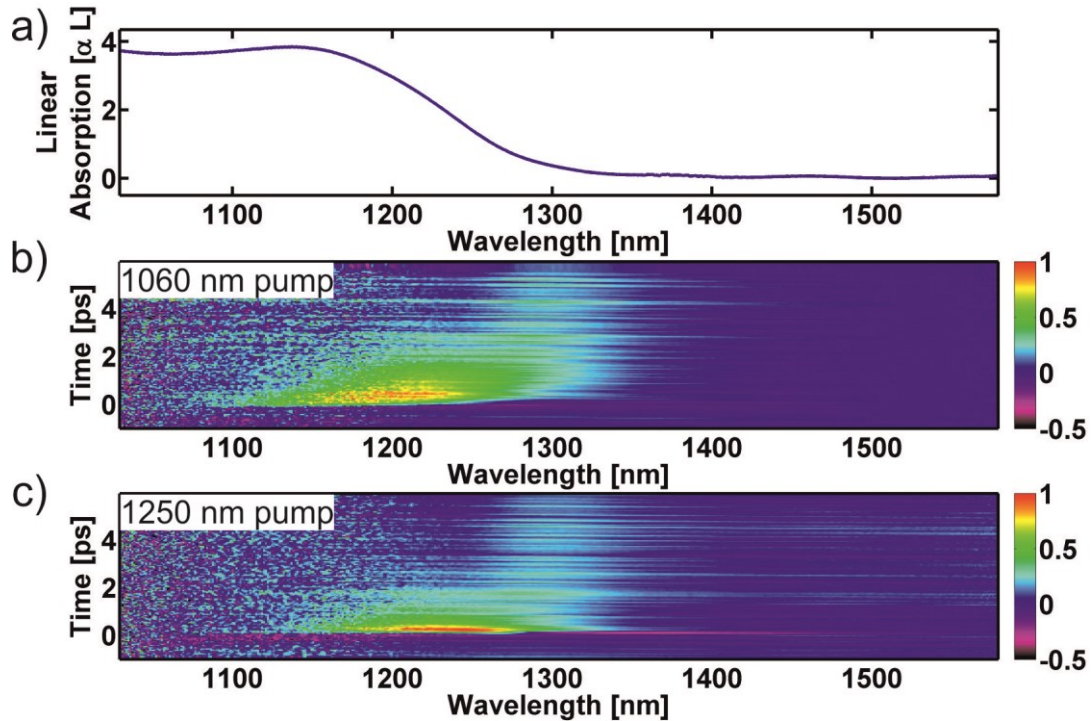


Fig. 5.2 a) Linear absorption spectrum of a sample 2 and TWPP spectra for a pump wavelength of b) 1060 nm and c) 1250 nm. The pump power for the TWPP measurements was  $15 \mu\text{W}$  for both wavelengths. This figure was adopted and modified from Ref. [10].

For sample 3 [Fig. 5.3 b)], there is an initial short decay of the signal on a time scale of 300 fs, followed by a longer decay component on a time scale of 3 ps. The initial short signal decay can again be attributed to a redistribution of the electrons via e-e and e-ph scattering. The second decay component of the TWPP signal is due to electron capture into  $\text{As}_{\text{Ga}}$  defects. The rather long decay time of 3 ps in this sample can be explained by the fact that the  $\text{As}_{\text{Ga}}$  defects are mostly neutral due to the lack of Be-doping [cf. chapter 4]. However, the decay time is still much shorter than the one observed for un-doped or moderately doped InGaAs/InAlAs heterostructures [5].

In the case of sample 4 excited at 1060 nm [Fig. 5.4 b)] the electron population is again redistributed via e-e and e-ph scattering on a time scale of approx. 300 fs. However, the TWPP signal of this sample is much broader as compared to sample 3. This can be attributed to the increased amount of band tail states caused by the additional Be-doping. The subsequent decay due to non-radiative carrier capture into defect states in this sample is found to have a time constant of approx. 1.3 ps.

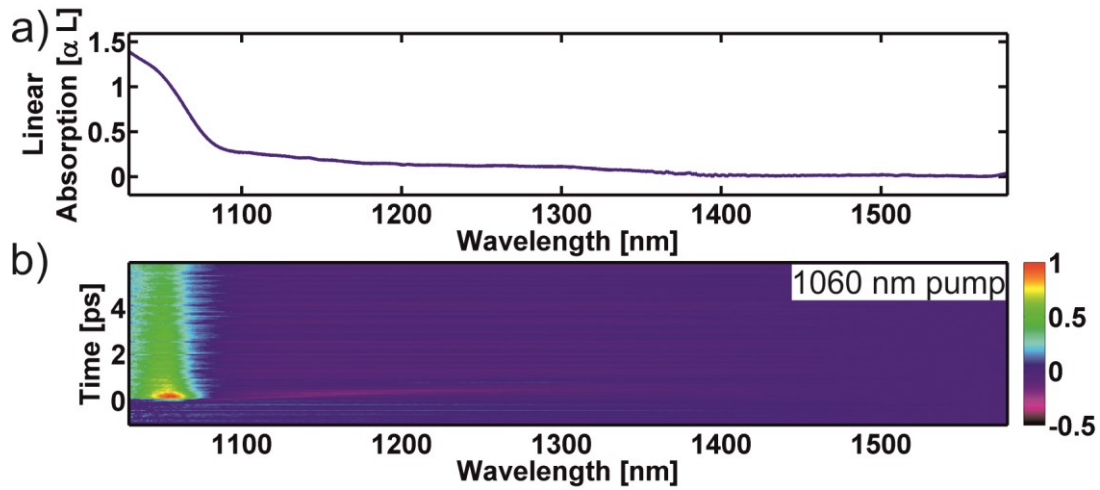


Fig. 5.3 a) Linear absorption spectrum of sample 3 and b) TWPP spectra for a pump wavelength of 1060 nm at a pump power of 15  $\mu$ W. This figure was adopted and modified from Ref. [10].

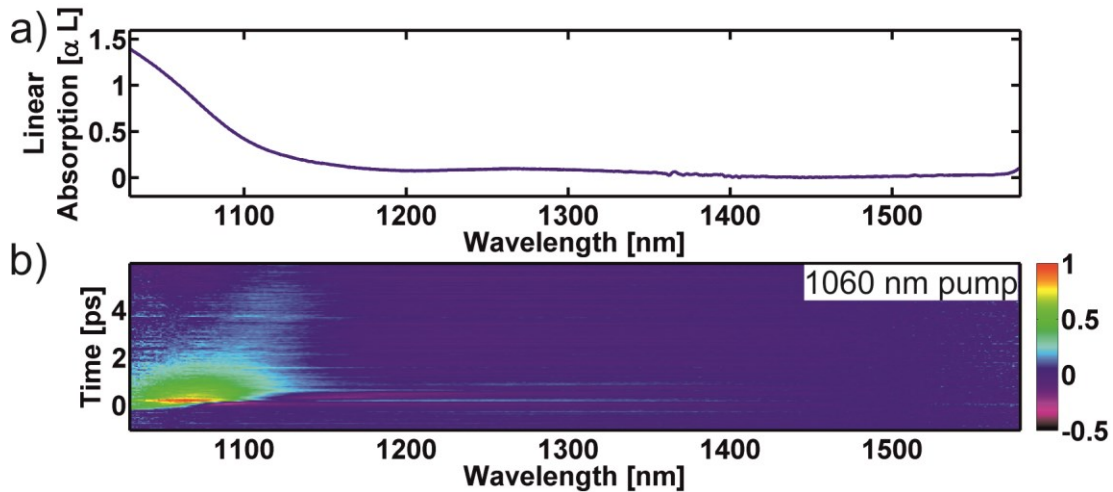


Fig. 5.4 a) Linear absorption spectrum of sample 4 and b) TWPP spectra for a pump wavelength of 1060 nm at a pump power of 15  $\mu$ W. This figure was adopted and modified from Ref. [10].

A general trait of all measurements in which the photon energy is significantly above the band gap energy of the samples, is that the energy relaxation of the electrons is dominated by LO-phonon emission rather than by non-radiative capture into defect states via multi phonon emission. The highly Be-doped samples of chapter 4 excited at 1550 nm wavelength exhibited electron capture times of  $<200$  fs. The initial LO-phonon emission time, i.e. for small phonon occupation numbers  $N_{Ph} \ll 1$ , is on the order of 300 fs. Hence for a near band gap excitation the electron capture probability is of the same magnitude as the LO-phonon emission probability. For higher photon energies and hence electron excess energies both processes become much more difficult and will therefore be discussed merely qualitatively.

At high excess energies each electron hole-pair produces a number  $n_{ph,LO} = E_c / E_{ph,LO}$  of LO-phonons, with  $E_c$  being the excess carrier energy and  $E_{ph,LO}$  the LO-phonon energy. The lifetime of LO-phonons at room temperature in GaAs has been found to be approx. 4 ps [123]. Assuming a similar lifetime for the present samples, the energy relaxation of the hot electron population via-LO-phonon emission produces a non-thermal phonon distribution with a large phonon occupation number  $N_{ph} \gg 1$  for small  $k$ -vector LO-phonons [124]. This increased phonon occupation number in turn increases the probability of phonon absorption by electrons. This effect should lead to an inhibition of the electron energy relaxation via LO-phonon emission, i.e. the formation of a phonon bottleneck. However, such a behavior is not visible in the TWPP measurements. A possible explanation can be offered by  $k$ -vector and energy conservation constrains combined with the non-thermal characteristics of the phonon distribution. The quadratic energy dispersion relation for the CB electrons forbids electrons which have already relaxed to states lower in the CB from re-absorbing a previously emitted phonon with a smaller  $k$ -vector [125].

The energy dependence of the capture cross section can be described within the framework of non-radiative multi phonon emission (MPE) [126]. The dependence of the electron capture cross section on the electron energy  $E$  is then dependent on the depth  $E_D > 0$  and the charge state of the defect. Furthermore, it is dependent on the lattice relaxation energy  $A$ , which describes the energy difference between the initial and final state of the lattice in the MPE process [126]. The qualitative energy dependence of the capture process can then be categorized in terms of the electron-lattice coupling strength  $C_{e-l} = A/(E + E_D)$ . For weak  $\ln(C_{e-l}) < 0$  or intermediate  $\ln(C_{e-l}) = 0$  electron-lattice coupling and the case of an attractive defect potentials, as it is the case for positively ionized  $As_{Ga}$  defects, the electron capture cross section is a monotonically declining function of the electron energy  $E$ . However, in the case of a strong electron-lattice coupling  $\ln(C_{e-l}) > 0$  there is a distinct maximum of the capture cross section for a given electron energy  $E > 0$  dependent on  $C_{e-l}$ . Since in all measurements the electrons appear to relax to the band edge before being captured, it can be assumed that the electron lattice coupling  $C_{e-l}$  of  $As_{Ga}$  defects in InGaAs or InAlGaAs is in the weak or intermediate regime.

To examine how the electron relaxation deduced from the TWPP measurements, influences the characteristics of THz PCA detectors, all samples were processed with dipole mesa-antennas with a 10  $\mu m$  photoconductive gap and evaluated in a THz TDS system excited by a pulsed ytterbium doped fiber laser at 1060 nm wavelength and a repetition rate of 20 MHz. The THz emitter used for these measurements was a large area emitter with a 400  $\mu m$  strip-line antenna manufactured from sample 2 which was biased at 200 V. The pulse traces and spectra obtained from the measurements are shown in Fig. 5.5. As expected from the

discussion in chapters 1 and 4, the prolonged photoconductivity of the sample 1 under 1060 nm excitation results in a stronger frequency roll-off behavior with a maximum detectable bandwidth of only 3 THz. The THz-signals of the three band-gap shifted samples show an improved frequency roll-off behavior due to the shorter electron lifetime. However, the PCA detectors made from the two quaternary samples exhibit a stronger frequency roll-off and noise level as compared to sample 2. This could be indicative of a prolonged photoconductivity due to long-lived carriers which are not visible in the TWPP measurements. This matter could be resolved in future optical-pump THz-Probe measurements.

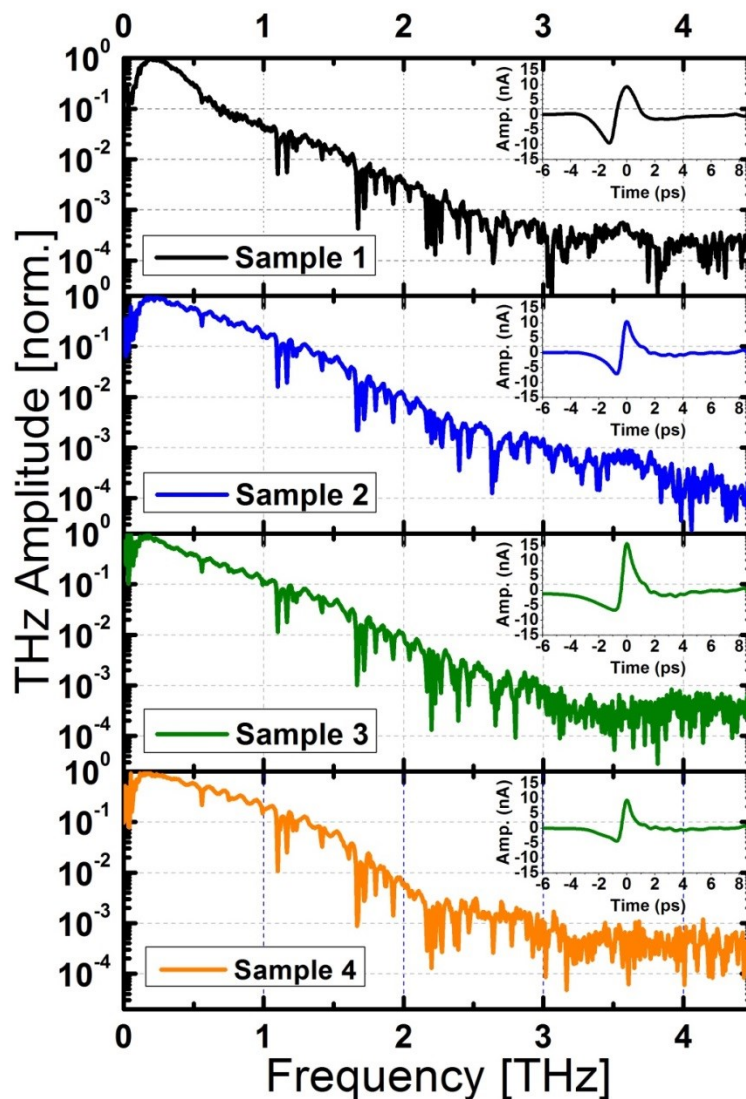


Fig. 5.5 THz-TDS spectra and their corresponding pulse traces (insets) of all four samples excited at 1060 nm. The lock-in integration time was chosen to be 300 ms per measurement point. This figure was adopted and modified from Ref. [10].

In summary, the insights obtained from the measurements discussed in this chapter concerning carrier hot carrier relaxation and its impact on PCA behavior, form a fundamental basis for further investigations and development of photoconductive materials based on InGaAs/InP for 1060 nm excitation.

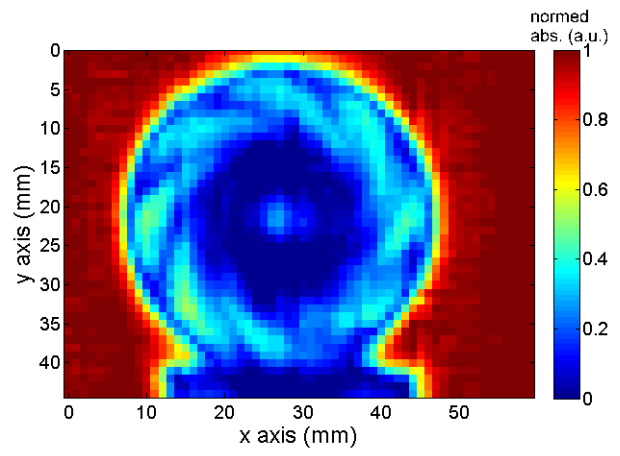
## **5.1 Ytterbium fiber-laser based multichannel THz-TDS system**

This subchapter will briefly discuss the results of the development of a THz-TDS tomography system based on a large area emitter and a multi-channel detector array, both driven by a pulsed high power ytterbium-doped fiber laser source. The laser source consisted of a commercial fiber oscillator with an average output power of 100 mW and an Yb-doped rod-type fiber amplifier with a length of 80 cm and a mode field diameter of 50  $\mu\text{m}$  pumped at 976 nm. The resulting average output power was 4.5 W at a repetition rate of 20 MHz. The photoconductor material for the emitter was a high mobility InGaAs/InAlAs heterostructure sample as described in chapter 3 and featured a 400  $\mu\text{m}$  gap strip-line antenna geometry biased with 125 V. The detector array was manufactured from a LTG Be-doped InGaAs/InAlAs heterostructure, similar to sample 1 of this chapter, and consisted of a line-array of 15 discrete 7.5  $\mu\text{m}$  dipole detector antennas with a spacing of 1 mm in between the channels. The detector array was optically excited with a line focus while the THz signal was focused onto the photoconductive gap by a cylindrical silicon lens. The exact THz-TDS setup geometry and the THz optics used are described in Ref. [11]. The detector signals were then recorded by a mutli-channel lock-in amplifier. An example of a sample and a THz image of that sample measured with this system are shown in Fig. 5.6. As can be seen, the optically hidden parts in the outer ring of the structure are clearly visible in the THz image. The lateral resolution of the system is approx. 1 mm in each direction, which is on the order of the wavelength (in air) of the maximal frequency component of the THz spectrum of around 300 GHz. Considering that the cylindrical lens in the THz path only focuses the THz beam in in one spatial direction and hence limits the overall signal strength at the detector as compared to a hyper-hemispherical silicon lens, this result is already quite remarkable for a proof-of-principle demonstration. By using a multi-channel array the measurement time can be reduced approx. by a factor equal to the number of channels as compared to a single pixel measurement, i.e. by a factor of 15 in this system.

In future systems, arrays with 64 or 128 channels are feasible. In combination with fast time delays, e.g. electro-optically controlled sampling [cf. chapter 4.1], this principle can yield very fast THz imaging or tomography systems with measurement times of seconds rather than minutes.



**a)**



**b)**

Fig. 5.6 a) Plastic pump wheel sample b) THz image of the sample in a) constructed from the maximum of the transmitted THz amplitudes. This figure was adopted and modified from Ref. [11].

## 6. Conclusion and Outlook

The present work investigated the physics of terahertz (THz) generation and detection in photoconductive antennas (PCA) based on the InGaAs/InP material system, aimed for an excitation with erbium-doped or ytterbium-doped pulsed fiber laser sources. Over the course of this work the potential of micro-structuring as well as several semiconductor growth approaches and optimization strategies were discussed, always in close review of the underlying ultra-fast carrier dynamics in the semiconductor material. Furthermore, different approaches for fast and efficient THz time domain spectroscopy (THz-TDS) systems were investigated. This final chapter will give a brief summary and conclusion as well as an outlook on possible future research in the field.

In chapter 2 a micro-structuring approach for PCAs was investigated on the basis of low temperature grown (LTG) InGaAs/InAlAs heterostructures. It was shown that mesa-shaped photoconductive regions, with the contact metallization sputtered to the mesa side walls, yield an increase of the emitted THz pulse amplitudes by a factor of 2.5 when compared to PCA emitters featuring a simple planar contact metallization. This was attributed to the improved homogeneity of the electrical fields within the photoconductive region and in-plane field vectors with respect to the InGaAs layers. For similarly structured PCA detectors, these two effects were found to have an even greater impact with a sensitivity increase of more than one order of magnitude was achievable as compared to a planar metallization.

Chapter 3 discussed the growth of high mobility PCAs based on an approach featuring spatially separated trapping and photoconductive regions. This approach was realized via MBE growth of InGaAs/InAlAs heterostructures at intermediate growth temperatures of around 400°C, where defects are introduced merely in the InAlAs barriers in the form of deep alloy clustering defects. The InGaAs layers were found to grow mostly defect free in this temperature range, which resulted in high carrier mobility and a reduced residual carrier concentration. The ultra-fast carrier dynamics in these structures were determined by optical pump-probe measurements, which revealed that the carrier lifetimes can be efficiently tuned via the growth temperature as well as the InAlAs barrier thicknesses. The THz-TDS measurements of PCAs emitters manufactured from these samples indicated that a strong carrier lifetime reduction, i.e. high defect density, is not favorable for high THz emission powers. This result was attributed to electron scattering at defect sites which prevents efficient THz generation. However, a certain defect density in the InAlAs barriers and barrier thicknesses were found to be mandatory for a sufficiently high reduction of the residual carrier in the InGaAs layers and hence high dark resistivity of the PCAs. For optimal growth conditions, the resulting photoconductor characteristics lead to an enhancement by two orders

of magnitude of the emitted THz power as compared to LTG Be-doped InGaAs/InAlAs heterostructures.

In chapter 4 the ultra-fast carrier dynamics in beryllium doped LTG InGaAs/InAlAs heterostructures were investigated by means of optical pump-probe and THz-TDS measurements in dependence of the Be-doping concentration. The carrier capture and recombination dynamics were therefore described by a set of coupled rate equations for the carrier densities in conduction and valence band, as well as the involved defect states and then compared to experimental results. A central finding of the pump-probe measurements is, that electrons are predominately captured by ionized arsenic antisite ( $\text{As}_{\text{Ga}}$ ) defects while Be-dopants are responsible for hole capturing. The subsequent recombination of electrons with holes is found to take place between localized states at  $\text{As}_{\text{Ga}}$  and Be-dopant sites, respectively. The amount of ionized  $\text{As}_{\text{Ga}}$  defects is strongly dependent on the Be-doping concentration. As a consequence, the carrier capture and recombination time can be greatly influenced, and thus adjusted, via Be-doping. For doping concentrations of  $4 \times 10^{18} \text{ cm}^{-3}$  an ultra-fast electron capture time of below 200 fs was achieved. Furthermore, chapter 4 reviewed the influence of the carrier capture time, possible defect state saturation at higher optical excitation densities and carrier-impurity scattering on the THz detection characteristics of THz PCAs detectors manufactured from the samples. The frequency characteristics of the detected THz signals were found to be strongly influenced by the carrier capture time in accordance with the theoretical predictions elaborated in the introductory part of this work in chapter 1. Furthermore, it was shown that the carrier capture time strongly influences the Nyquist noise currents of the PCAs detectors, due to the changes of the average conductivity. Nyquist noise was found to have a major contribution to the detector noise currents. Additionally, detector shot noise was found to become a relevant noise source at high incident THz field strengths. Via the combination of the results and developments of chapters 2-4, namely mesa-structuring, ultra-fast Be-doped PCA detectors and high mobility PCA emitters, it was possible to obtain THz-TDS signals with detector amplitudes that were increased by a factor of 1000 as compared to the state of the art, featuring a spectral bandwidth in excess of 6 THz with 90 dB dynamic range. This improvement allowed for TDS measurements that originally demanded a measurement time of several tens of minutes to be performed within 60 ms. The last part of chapter 4 reviewed the research on THz-TDS measurement systems based on the principle of electronically controlled optical sampling. By employing this technique it was possible to demonstrate a fast all-fiber coupled THz-TDS system with measurement rates of up to 8 kHz.

In chapter 5, photoconductive materials and PCAs for an excitation with ytterbium doped fiber pulse lasers with a central wavelength of 1060 nm were discussed. Therefore, Be-doped LTG InGaAs/InAlAs heterostructures with different InGaAs layer thicknesses, and hence sub-

band energies, as well as bulk LTG InAlGaAs samples with band gap energies of approx. 1.1 eV were investigated. Transient white light pump-probe measurements were performed to investigate the carrier energy relaxation and capture processes in dependence of the excitation wavelength and hence the excess energy of the carriers. As a general result, the energy relaxation of hot electrons in LTG InGaAs/InAlAs and LTG InAlGaAs is dominated by longitudinal optical phonon emission and not electron capture into  $\text{As}_{\text{Ga}}$  defects via non-radiative multi-phonon emission. Consequently, the transient photoconductivity of these samples is prolonged for photon energies significantly above the band gap. This finding was further verified by the frequency characteristics of PCAs detectors in THz-TDS measurements at an excitation wavelength of 1060 nm. The last part of chapter 5, briefly discussed the development of a multi-channel THz-TDS system for the purpose of THz tomography based on a high power ytterbium fiber laser and a 15-channel PCA detector array.

In summary, the investigations performed in this work concerning the growth of photoconductive materials and pump-probe measurements performed on these materials granted further insight into possible methods of controlled defect incorporation and the basic physical processes of non-radiative carrier capture and recombination in defect states. Furthermore, in connection with THz-TDS measurements the influence of the defect related ultra-fast carrier dynamics on the physics of photoconductive THz generation and detection in these materials was investigated. Based on the improved PCAs, it demonstrated methods to build cost-efficient, compact and fast fiber laser based THz-TDS systems. These developments now enable for a much more widespread application of THz-TDS systems, not just in laboratories but also for industrial applications.

Concerning the perspective on future work in the field of PCA development there are several options for further research. These include the investigation of defect incorporation in InGaAs by means of doping with transition metals, e.g. Rhodium or Ruthenium, which are known to introduce defect states in a mid-gap position [127]. Additionally, the approach of separated capture/recombination and photoconductive regions can potentially be extended from a merely spatial separation to a quantum mechanical separation by using different probabilities of presence of electrons in different sub-bands. For future THz-TDS systems further research and development of systems with electronically controlled time delay, such as the one presented in chapter 4, seems to be the most promising route to take.

## 7. Publications

Since the present thesis is written in a cumulative way, the authors publications discussed in this work are summarized in this chapter. Therefore the publications are order according to the chapters they were discussed in, together with a statement of the individual contributions of the author to the respective publications.

### Micro structuring of photoconductive antennas: The mesa structure

- [1] H. Roehle, R. J. B. Dietz, H. J. Hensel, J. Böttcher, H. Künzel, D. Stanze, M. Schell, and B. Sartorius, “Next generation 1.5 micrometer terahertz antennas: mesa-structuring of InGaAs/InAlAs photoconductive layers.,” *Opt. Express*, vol. 18, no. 3, pp. 2296–301, Feb. 2010.
- Most of the experimental work and data evaluation
  - Most of the writing of the publication

### High mobility photoconductive THz emitters

- [2] R. J. B. Dietz, M. Gerhard, D. Stanze, M. Koch, B. Sartorius, and M. Schell, “THz generation at 1.55  $\mu\text{m}$  excitation : six-fold increase in THz conversion efficiency by separated photoconductive and trapping regions,” *Opt. Express*, vol. 19, no. 27, pp. 122–126, 2011.
- Most of the experimental work and data evaluation
  - Most of the writing of the publication
- [3] T. Jung, R. Dietz, A. Chernikov, F. Kuik, B. Sartorius, M. Schell, M. Koch, and S. Chatterjee, “Photoluminescence study of (GaIn)As/(AlIn)As-based THz antenna materials for 1.55  $\mu\text{m}$  excitation,” *J. Lumin.*, vol. 138, pp. 179–181, Jun. 2013.
- Sample design and preparation
  - Part of the measurements together with T. Jung
  - Discussion and evaluation of the data together with T. Jung and S. Chatterjee
- [4] R. J. B. Dietz, B. Globisch, M. Gerhard, A. Velauthapillai, D. Stanze, H. Roehle, M. Koch, T. Göbel, and M. Schell, “64  $\mu\text{W}$  pulsed terahertz emission from growth optimized InGaAs/InAlAs heterostructures with separated photoconductive and trapping regions,” *Appl. Phys. Lett.*, vol. 103, no. 6, p. 061103, 2013.

- Design of the sample series, design of the lithography masks
- Construction of the differential transmission setup
- Most of the measurements together with B. Globisch
- Most of the data evaluation, simulation and writing of the publication

**Short carrier lifetime detectors based on LT-grown Beryllium doped InGaAs/InAlAs heterostructures**

- [5] B. Globisch\*, R. J. B. Dietz\*, D. Stanze, T. Göbel, and M. Schell, “Carrier dynamics in Beryllium doped low-temperature-grown InGaAs/InAlAs,” *Appl. Phys. Lett.*, vol. 104, no. 17, p. 172103, 2014.

- Design of the sample series
  - Construction of the differential transmission setup
  - Discussion of the data and derivation of the rate equation model together with B. Globisch
  - Part of the writing of the publication
- \*Both authors contributed equally

- [6] R. J. B. Dietz\*, B. Globisch\*, H. Roehle, D. Stanze, T. Göbel, and M. Schell, “Influence and adjustment of carrier lifetimes in InGaAs/InAlAs photoconductive pulsed terahertz detectors : 6 THz bandwidth and 90dB dynamic range,” *Opt. Express*, vol. 22, no. 16, pp. 615–623, 2014.

- Design of the sample series and the lithography masks
  - Most of the measurements
  - Discussion and data evaluation together with B. Globisch
  - Most of the writing of the publication
- \*Both authors contributed equally

- [7] N. Vieweg, F. Rettich, A. Deninger, H. Roehle, R. Dietz, T. Göbel, and M. Schell, “Terahertz-time domain spectrometer with 90 dB peak dynamic range,” *J. Infrared, Millimeter, Terahertz Waves*, vol. 35, no. 10, pp. 823-832, 2014.

- Preparation of the emitter and detector modules
- Part of the writing of the publication

- [8] R. J. B. Dietz\*, N. Vieweg\*, T. Puppe\*, A. Zach, B. Globisch, T. Göbel, P. Leisching, and M. Schell, “All fiber coupled THz-TDS system with kHz measurement rate based on electronically controlled optical sampling,” *Opt. Lett.*, vol. 39, no. 22, pp. 6482–6485, 2014.
- Design of the THz PCAs, lithography mask design and construction of the PCA modules
  - Most of the measurements together with N. Vieweg and T. Puppe
  - Most of the writing of the publication
- \*Authors contributed equally

### **Photoconductors for 1030 nm pulsed laser excitation**

- [9] R. J. B. Dietz, R. Wilk, B. Globisch, H. Roehle, D. Stanze, S. Ullrich, S. Schumann, N. Born, M. Koch, B. Sartorius, and M. Schell, “Low Temperature Grown Be-doped InGaAs/InAlAs Photoconductive Antennas Excited at 1030 nm,” *J. Infrared, Millimeter, Terahertz Waves*, vol. 34, no. 3–4, pp. 231–237, 2013.
- Design of the sample series and the lithography masks
  - Construction of the differential transmission setup
  - All of the measurements together with R. Wilk, S. Schumann and N. Born
  - All of the writing of the publication
- [10] R. J. B. Dietz, A. Brahm, A. Wilms, A. Vellauthapillai, C. Lammers, B. Globisch, M. Koch, G. Notni, A. Tünnermann, T. Göbel and M. Schell, “Low temperature grown photoconductive antennas for pulsed 1060 nm excitation: Influence of excess energy on the electron relaxation,” *J. Infrared, Millimeter, Terahertz Waves*, vol. 36, no. 1, pp. 60-71, 2015.
- Design of the sample series and the lithography masks
  - Preparation of the samples
  - Part of the measurements
  - All of the data evaluation and writing of the publication
- [11] A. Brahm, A. Wilms, R. J. B. Dietz, T. Göbel, M. Schell, G. Notni, and A. Tünnermann, “Multichannel terahertz time-domain spectroscopy system at 1030 nm excitation wavelength,” *Opt. Express*, vol. 22, no. 11, p. 12982, May 2014.
- Design of the wafer and the lithography masks
  - Part of the writing of the publication

## I. BIBLIOGRAPHY

- [1] H. Roehle, R. J. B. Dietz, H. J. Hensel, J. Böttcher, H. Künzel, D. Stanze, M. Schell, and B. Sartorius, “Next generation 1.5  $\mu\text{m}$  terahertz antennas: mesa-structuring of InGaAs/InAlAs photoconductive layers,” *Opt. Express*, vol. 18, no. 3, pp. 2296–2301, Feb. 2010.
- [2] R. J. B. Dietz, M. Gerhard, D. Stanze, M. Koch, B. Sartorius, and M. Schell, “THz generation at 1.55  $\mu\text{m}$  excitation : six-fold increase in THz conversion efficiency by separated photoconductive and trapping regions,” *Opt. Express*, vol. 19, no. 27, pp. 122–126, 2011.
- [3] T. Jung, R. Dietz, A. Chernikov, F. Kuik, B. Sartorius, M. Schell, M. Koch, and S. Chatterjee, “Photoluminescence study of (GaIn)As/(AlIn)As-based THz antenna materials for 1.55  $\mu\text{m}$  excitation,” *J. Lumin.*, vol. 138, pp. 179–181, Jun. 2013.
- [4] R. J. B. Dietz, B. Globisch, M. Gerhard, A. Velauthapillai, D. Stanze, H. Roehle, M. Koch, T. Göbel, and M. Schell, “64  $\mu\text{W}$  pulsed terahertz emission from growth optimized InGaAs/InAlAs heterostructures with separated photoconductive and trapping regions,” *Appl. Phys. Lett.*, vol. 103, no. 6, p. 061103, 2013.
- [5] B. Globisch, R. J. B. Dietz, D. Stanze, T. Göbel, and M. Schell, “Carrier dynamics in Beryllium doped low-temperature-grown InGaAs/InAlAs,” *Appl. Phys. Lett.*, vol. 104, no. 17, p. 172103, Apr. 2014.
- [6] R. J. B. Dietz, B. Globisch, H. Roehle, D. Stanze, T. Göbel, and M. Schell, “Influence and adjustment of carrier lifetimes in InGaAs/InAlAs photoconductive pulsed terahertz detectors : 6 THz bandwidth and 90dB dynamic range,” *Opt. Express*, vol. 22, no. 16, pp. 615–623, 2014.
- [7] N. Vieweg, F. Rettich, A. Deninger, H. Roehle, R. Dietz, T. Göbel, and M. Schell, “Terahertz-time domain spectrometer with 90 dB peak dynamic range,” *J. Infrared, Millimeter, Terahertz Waves*, vol. 35, no. 10, pp. 823–832, Jul. 2014.
- [8] R. J. B. Dietz, N. Vieweg, T. Puppe, A. Zach, B. Globisch, T. Göbel, P. Leisching, and M. Schell, “All fiber coupled THz-TDS system with kHz measurement rate based on electronically controlled optical sampling,” *Opt. Lett.*, vol. 39, no. 22, pp. 6482–6485, 2014.
- [9] R. J. B. Dietz, R. Wilk, B. Globisch, H. Roehle, D. Stanze, S. Ullrich, S. Schumann, N. Born, M. Koch, B. Sartorius, and M. Schell, “Low Temperature Grown Be-doped InGaAs/InAlAs Photoconductive Antennas Excited at 1030 nm,” *J. Infrared, Millimeter, Terahertz Waves*, vol. 34, no. 3–4, pp. 231–237, Mar. 2013.
- [10] R. Dietz, A. Brahm, A. Velauthapillai, A. Wilms, C. Lammers, B. Globisch, M. Koch, G. Notni, and M. Schell, “Low temperature grown photoconductive antennas for pulsed 1060 nm excitation : Influence of excess energy on the electron relaxation,” *J. Infrared, Millimeter, Terahertz Waves*, vol. 36, no. 1, pp. 60–71, 2015.
- [11] A. Brahm, A. Wilms, R. J. B. Dietz, T. Göbel, M. Schell, G. Notni, and A. Tünnermann, “Multichannel terahertz time-domain spectroscopy system at 1030 nm excitation wavelength,” *Opt. Express*, vol. 22, no. 11, p. 12982, May 2014.
- [12] B. S. Williams, “Terahertz quantum-cascade lasers,” *Nat. Photonics*, vol. 1, no. 9, pp. 517–525, Sep. 2007.

- [13] D. H. Auston, K. P. Cheung, and P. R. Smith, "Picosecond photoconducting Hertzian dipoles," *Appl. Phys. Lett.*, vol. 45, no. 3, p. 284, 1984.
- [14] C. Fattinger and D. Grischkowsky, "Terahertz beams," *Appl. Phys. Lett.*, vol. 54, no. 6, p. 490, 1989.
- [15] M. van Exter, C. Fattinger, and D. Grischkowsky, "Terahertz time-domain spectroscopy of water vapor," *Opt. Lett.*, vol. 14, no. 20, p. 1128, 1989.
- [16] R. H. M. Groeneveld and D. Grischkowsky, "Picosecond time-resolved far-infrared experiments on carriers and excitons in GaAs-AlGaAs multiple quantum wells," *J. Opt. Soc. Am. B*, vol. 11, no. 12, p. 2502, Dec. 1994.
- [17] R. Kaindl, M. Carnahan, D. Hägele, R. Lövenich, and D. S. Chemla, "Ultrafast terahertz probes of transient conducting and insulating phases in an electron-hole gas," *Nature*, vol. 423, p. 734, 2003.
- [18] B. E. Cole, J. B. Williams, B. T. King, M. S. Sherwin, and C. R. Stanley, "Coherent manipulation of semiconductor quantum bits with terahertz radiation," *Nature*, vol. 410, no. 6824, pp. 60–3, Mar. 2001.
- [19] M. Kubouchi, K. Yoshioka, R. Shimano, A. Mysyrowicz, and M. Kuwata-Gonokami, "Study of Orthoexciton-to-Paraexciton Conversion in Cu<sub>2</sub>O by Excitonic Lyman Spectroscopy," *Phys. Rev. Lett.*, vol. 94, no. 1, p. 016403, 2005.
- [20] S. Leinß, T. Kampfrath, K. v. Volkman, M. Wolf, J. Steiner, M. Kira, S. Koch, A. Leitenstorfer, and R. Huber, "Terahertz Coherent Control of Optically Dark Paraexcitons in Cu<sub>2</sub>O," *Phys. Rev. Lett.*, vol. 101, no. 24, p. 246401, Dec. 2008.
- [21] A. Bonvalet, J. Nagle, V. Berger, A. Migus, J.-L. Martin, and M. Joffre, "Femtosecond infrared emission resulting from coherent charge oscillations in quantum wells," *Phys. Rev. Lett.*, vol. 76, no. 23, pp. 4392–4395, 1996.
- [22] D. Golde, M. Wagner, D. Stehr, H. Schneider, M. Helm, A. M. Andrews, T. Roch, G. Strasser, M. Kira, and S. W. Koch, "Fano Signatures in the Intersubband Terahertz Response of Optically Excited Semiconductor Quantum Wells," *Phys. Rev. Lett.*, vol. 102, no. 12, p. 127403, 2009.
- [23] T. M. Korter and D. F. Plusquellic, "Continuous-wave terahertz spectroscopy of biotin: vibrational anharmonicity in the far-infrared," *Chem. Phys. Lett.*, vol. 385, no. 1–2, pp. 45–51, Feb. 2004.
- [24] D. G. Allis, a. M. Fedor, T. M. Korter, J. E. Bjarnason, and E. R. Brown, "Assignment of the lowest-lying THz absorption signatures in biotin and lactose monohydrate by solid-state density functional theory," *Chem. Phys. Lett.*, vol. 440, no. 4–6, pp. 203–209, Jun. 2007.
- [25] D. G. Allis, P. M. Hakey, and T. M. Korter, "The solid-state terahertz spectrum of MDMA (Ecstasy) – A unique test for molecular modeling assignments," *Chem. Phys. Lett.*, vol. 463, no. 4–6, pp. 353–356, Oct. 2008.

- [26] H. Zhang, K. Siegrist, D. F. Plusquellic, and S. K. Gregurick, "Terahertz spectra and normal mode analysis of the crystalline VA class dipeptide nanotubes.," *J. Am. Chem. Soc.*, vol. 130, no. 52, pp. 17846–57, Dec. 2008.
- [27] M. Hishida and K. Tanaka, "Long-Range Hydration Effect of Lipid Membrane Studied by Terahertz Time-Domain Spectroscopy," *Phys. Rev. Lett.*, vol. 106, no. 15, p. 158102, Apr. 2011.
- [28] Y. He, P. Ku, J. Knab, J. Chen, and a. Markelz, "Protein Dynamical Transition Does Not Require Protein Structure," *Phys. Rev. Lett.*, vol. 101, no. 17, p. 178103, Oct. 2008.
- [29] R. M. Woodward, V. P. Wallace, R. J. Pye, B. E. Cole, D. D. Arnone, E. H. Linfield, and M. Pepper, "Terahertz pulse imaging of ex vivo basal cell carcinoma.," *J. Invest. Dermatol.*, vol. 120, no. 1, pp. 72–8, Jan. 2003.
- [30] P. C. Ashworth, E. Pickwell-MacPherson, E. Provenzano, S. E. Pinder, A. D. Purushotham, M. Pepper, and V. P. Wallace, "Terahertz pulsed spectroscopy of freshly excised human breast cancer.," *Opt. Express*, vol. 17, no. 15, pp. 12444–54, Jul. 2009.
- [31] S. Sy, S. Huang, Y.-X. J. Wang, J. Yu, A. T. Ahuja, Y.-T. Zhang, and E. Pickwell-MacPherson, "Terahertz spectroscopy of liver cirrhosis: investigating the origin of contrast," *Phys. Med. Biol.*, vol. 55, no. 24, pp. 7587–96, Dec. 2010.
- [32] C.-C. Chen, D.-J. Lee, T. Pollock, and J. F. Whitaker, "Pulsed-terahertz reflectometry for health monitoring of ceramic thermal barrier coatings," *Opt. Express*, vol. 18, no. 4, pp. 3477–86, Feb. 2010.
- [33] W. L. Chan, J. Deibel, and D. M. Mittleman, "Imaging with terahertz radiation," *Reports Prog. Phys.*, vol. 70, no. 8, pp. 1325–1379, Aug. 2007.
- [34] C. Jansen, S. Wietzke, O. Peters, M. Scheller, N. Vieweg, M. Salhi, N. Krumbholz, C. Jördens, T. Hochrein, and M. Koch, "Terahertz imaging: applications and perspectives," *Appl. Opt.*, vol. 49, no. 19, pp. E48–57, Jul. 2010.
- [35] F. W. Smith, H. Q. Le, V. Diadiuk, M. A. Hollis, A. R. Calawa, S. Gupta, M. Frankel, D. R. Dykaar, G. A. Mourou, and T. Y. Hsiang, "Picosecond GaAs-based photoconductive optoelectronic detectors," *Appl. Phys. Lett.*, vol. 54, no. 10, p. 890, 1989.
- [36] A. C. Warren, N. Katzenellenbogen, D. Grischkowsky, J. M. Woodall, M. R. Melloch, and N. Otsuka, "Subpicosecond, freely propagating electromagnetic pulse generation and detection using GaAs:As epilayers," *Appl. Phys. Lett.*, vol. 58, p. 1512, 1991.
- [37] L. Xu, X.-C. Zhang, and D. H. Auston, "Terahertz beam generation by femtosecond optical pulses in electro-optic materials," *Appl. Phys. Lett.*, vol. 61, no. 15, p. 1784, 1992.
- [38] Q. Wu and X.-C. Zhang, "Free-space electro-optic sampling of terahertz beams," *Appl. Phys. Lett.*, vol. 67, no. 24, p. 3523, 1995.
- [39] P. Jepsen, C. Winnewisser, M. Schall, V. Schyja, S. R. Keiding, and H. Helm, "Detection of THz pulses by phase retardation in lithium tantalate," *Phys. Rev. E*, vol. 53, no. 4, pp. 3052–3054, 1996.

- [40] D. J. Cook and R. M. Hochstrasser, "Intense terahertz pulses by four-wave rectification in air," *Opt. Lett.*, vol. 25, no. 16, pp. 1210–2, Aug. 2000.
- [41] M. Kress, T. Löffler, S. Eden, M. Thomson, and H. G. Roskos, "Terahertz-pulse generation by photoionization of air with laser pulses composed of both fundamental and second-harmonic waves," *Opt. Lett.*, vol. 29, no. 10, pp. 1120–2, May 2004.
- [42] E. R. Brown, F. W. Smith, and K. A. McIntosh, "Coherent millimeter-wave generation by heterodyne conversion in low-temperature-grown GaAs photoconductors," *J. Appl. Phys.*, vol. 73, no. 3, p. 1480, 1993.
- [43] H. Ito, F. Nakajima, T. Furuta, K. Yoshino, Y. Hirota, and T. Ishibashi, "Photonic terahertz-wave generation using antenna-integrated uni-travelling-carrier photodiode," *Electron. Lett.*, vol. 39, no. 25, 2003.
- [44] A. Stöhr, A. Malcoci, A. Sauerwald, I. C. Mayorga, R. Güsten, and D. S. Jäger, "Ultra-Wide-Band Traveling-Wave Photodetectors for Photonic Local Oscillators," *J. Light. Technol.*, vol. 21, no. 12, p. 3062–, 2003.
- [45] P. U. Jepsen, R. H. Jacobsen, and S. R. Keiding, "Generation and detection of terahertz pulses from biased semiconductor antennas," *J. Opt. Soc. Am. B*, vol. 13, no. 11, p. 2424, 1996.
- [46] C. Kittel and P. McEuen, *Introduction to solid state physics*, vol. 10, no. 6. 1976, p. 43.
- [47] J. Jackson, *Classical electrodynamics*, 3. Edition. John Wiley & Sons, 1998.
- [48] C. Henry, R. Logan, F. Merritt, and C. Bethea, "Radiative and nonradiative lifetimes in n-type and p-type 1.6  $\mu\text{m}$  InGaAs," *Electron. Lett.*, vol. 20, no. 9, 1984.
- [49] P. Landsberg and D. Robbins, "The first 70 semiconductor Auger processes," *Solid. State. Electron.*, vol. 21, pp. 1289–1294, 1978.
- [50] B. Sermage, D. Chemla, D. Sivco, and A. Y. Cho, "Comparison of Auger recombination in GaInAs-AlInAs multiple quantum well structure and in bulk GaInAs," *Quantum Electron. IEEE J.*, vol. 22, no. 6, pp. 774–780, 1986.
- [51] A. Haug, "Auger Recombination with Traps," *Phys. status solidi*, vol. 97, p. 481, 1980.
- [52] C. Henry and D. Lang, "Nonradiative capture and recombination by multiphonon emission in GaAs and GaP," *Phys. Rev. B*, vol. 15, no. 2, pp. 989–1016, Jan. 1977.
- [53] W. Shockley and W. Read Jr., "Statistics of the recombinations of holes and electrons," *Phys. Rev.*, vol. 87, no. 46, pp. 835–842, 1952.
- [54] R. Hall, "Electron-hole recombination in germanium," *Phys. Rev.*, p. 6, 1952.
- [55] A. Haug, "Strahlungslose Rekombination in Halbleitern (Theorie)," *Festkörperprobleme 12*, pp. 411–447, 1972.
- [56] D. V. Lang and C. H. Henry, "Nonradiative Recombination at Deep Levels in GaAs and GaP by Lattice-Relaxation Multiphonon Emission," *Phys. Rev. Lett.*, vol. 35, no. 22, pp. 1525–1528, Jun. 1975.

- [57] K. Huang and A. Rhys, "Theory of light absorption and non-radiative transitions in F-centres," *Proc. R. Soc. Lond. A*, vol. 204, no. 1078, pp. 406–423, 1950.
- [58] H. Goto, Y. Adachi, and T. Ikoma, "Cross section of multiphonon-emission carrier capture at deep centers in compound semiconductors," *Phys. Rev. B*, vol. 22, no. 2, pp. 782–796, 1980.
- [59] Y. Q. Kang, J. H. Zheng, H. S. Tan, and S. C. Ng, "Charge-state effects of deep centres in semiconductors on non-radiative capture of carriers by multiphonon processes," *Appl. Phys. A Mater. Sci. Process.*, vol. 63, no. 1, pp. 37–43, Jul. 1996.
- [60] H. I. Ralph and F. D. Hughes, "Capture cross section of trapping centres in polar semiconductors," *Solid State Commun.*, vol. 9, no. 17, pp. 1477–1480, Sep. 1971.
- [61] H. Nyquist, "Thermal agitation of electric charge in conductors," *Phys. Rev.*, vol. 32, pp. 110–113, 1928.
- [62] J. Johnson, "Thermal agitation of electricity in conductors," *Phys. Rev.*, vol. 32, pp. 97–109, 1928.
- [63] D. Look, D. Walters, M. Manasreh, J. Sizelove, C. Stutz, and K. Evans, "Anomalous Hall-effect results in low-temperature molecular-beam-epitaxial GaAs: Hopping in a dense EL2-like band," *Phys. Rev. B. Condens. Matter*, vol. 42, no. 6, pp. 3578–3581, Aug. 1990.
- [64] S. Zhang and J. Northrup, "Chemical potential dependence of defect formation energies in GaAs: Application to Ga self-diffusion," *Phys. Rev. Lett.*, vol. 67, no. 17, pp. 2339–2342, 1991.
- [65] R. Jansen and O. Sankey, "Theory of relative native-and impurity-defect abundances in compound semiconductors and the factors that influence them," *Phys. Rev. B*, vol. 39, no. 5, pp. 3192–3206, 1989.
- [66] G. Baraff and M. Schlüter, "Binding and formation energies of native defect pairs in GaAs," *Phys. Rev. B*, vol. 33, no. 10, pp. 7346–7348, 1986.
- [67] M. Kaminska, Z. Liliental-Weber, E. R. Weber, T. George, J. B. Kortright, F. W. Smith, B.-Y. Tsauro, and a. R. Calawa, "Structural properties of As-rich GaAs grown by molecular beam epitaxy at low temperatures," *Appl. Phys. Lett.*, vol. 54, no. 19, p. 1881, 1989.
- [68] K. M. Yu, M. Kaminska, and Z. Liliental-Weber, "Characterization of GaAs layers grown by low temperature molecular beam epitaxy using ion beam techniques," *J. Appl. Phys.*, vol. 72, no. 7, p. 2850, 1992.
- [69] R. Feenstra, J. Woodall, and G. Pettit, "Observation of bulk defects by scanning tunneling microscopy and spectroscopy: Arsenic antisite defects in GaAs," *Phys. Rev. Lett.*, vol. 71, no. 8, 1993.
- [70] J. Störmer, W. Triftshäuser, N. Hozhabri, and K. Alavi, "Vacancy-type defects in molecular beam epitaxy low temperature grown GaAs, a positron beam lifetime study," *Appl. Phys. Lett.*, vol. 69, no. 13, p. 1867, 1996.
- [71] D. J. Keeble, M. T. Umlor, P. Asoka-Kumar, K. G. Lynn, and P. W. Cooke, "Annealing of low-temperature GaAs studied using a variable energy positron beam," *Appl. Phys. Lett.*, vol. 63, no. 1, p. 87, 1993.

- [72] H. Shen, F. C. Rong, R. Lux, J. Pamulapati, M. Taysing-Lara, M. Dutta, E. H. Poindexter, L. Calderon, and Y. Lu, "Fermi level pinning in low-temperature molecular beam epitaxial GaAs," *Appl. Phys. Lett.*, vol. 61, no. 13, p. 1585, 1992.
- [73] Y. H. Chen, Z. Yang, Z. G. Wang, and R. G. Li, "Temperature dependence of the Fermi level in low-temperature-grown GaAs," *Appl. Phys. Lett.*, vol. 72, no. 15, p. 1866, 1998.
- [74] D. C. Look, Z.-Q. Fang, H. Yamamoto, J. R. Sizelove, M. G. Mier, and C. E. Stutz, "Deep traps in molecular-beam-epitaxial GaAs grown at low temperatures," *J. Appl. Phys.*, vol. 76, no. 2, p. 1029, 1994.
- [75] M. Luysberg, H. Sohn, a. Prasad, P. Specht, Z. Liliental-Weber, E. R. Weber, J. Gebauer, and R. Krause-Rehberg, "Effects of the growth temperature and As/Ga flux ratio on the incorporation of excess As into low temperature grown GaAs," *J. Appl. Phys.*, vol. 83, no. 1, p. 561, 1998.
- [76] a. J. Lochtefeld, M. R. Melloch, J. C. P. Chang, and E. S. Harmon, "The role of point defects and arsenic precipitates in carrier trapping and recombination in low-temperature grown GaAs," *Appl. Phys. Lett.*, vol. 69, no. 10, p. 1465, 1996.
- [77] J. K. Luo, H. Thomas, D. V. Morgan, and D. Westwood, "Transport properties of GaAs layers grown by molecular beam epitaxy at low temperature and the effects of annealing," *J. Appl. Phys.*, vol. 79, no. 7, p. 3622, 1996.
- [78] A. C. Warren, J. M. Woodall, J. L. Freeouf, D. Grischkowsky, D. T. McInturff, M. R. Melloch, and N. Otsuka, "Arsenic precipitates and the semi-insulating properties of GaAs buffer layers grown by low-temperature molecular beam epitaxy," *Appl. Phys. Lett.*, vol. 57, no. 13, p. 1331, 1990.
- [79] I. Gregory, C. Tey, a. Cullis, M. Evans, H. Beere, and I. Farrer, "Two-trap model for carrier lifetime and resistivity behavior in partially annealed GaAs grown at low temperature," *Phys. Rev. B*, vol. 73, no. 19, p. 195201, May 2006.
- [80] A. Warren, J. Woodall, P. Kirchner, and X. Yin, "Role of excess As in low-temperature-grown GaAs," *Phys. Rev. B*, 1992.
- [81] H. Künzel, J. Böttcher, R. Gibis, and G. Urmann, "Material properties of Ga<sub>0.47</sub>In<sub>0.53</sub>As grown on InP by low-temperature molecular beam epitaxy," *Appl. Phys. Lett.*, vol. 61, no. 11, p. 1347, 1992.
- [82] A. Irvine and D. Palmer, "First observation of the EL2 lattice defect in indium gallium arsenide grown by molecular-beam epitaxy," *Phys. Rev. Lett.*, vol. 68, no. 14, pp. 2168–2171, 1992.
- [83] A. Mircea, A. Mitonneau, J. Hallais, and M. Jaros, "Study of the main electron trap in Ga<sub>1-x</sub>In<sub>x</sub>As alloys," *Phys. Rev. B*, vol. 16, no. 8, pp. 3665–3675, Oct. 1977.
- [84] K. Biermann, "Untersuchungen an auf InP basierenden Halbleitern mit sub-ps Responsezeiten," Humboldt-Universität zu Berlin, 2007.
- [85] B. Grandidier, H. Chen, R. M. Feenstra, D. T. McInturff, P. W. Juodawlkis, and S. E. Ralph, "Scanning tunneling microscopy and spectroscopy of arsenic antisites in low temperature grown InGaAs," *Appl. Phys. Lett.*, vol. 74, no. 10, p. 1439, 1999.

- [86] E. Seebauer and M. Kratzer, *Charged Semiconductor Defects: Structure, Thermodynamics and Diffusion*. Springer Science & Business Media, 2008.
- [87] S. Gupta, J. Whitaker, and G. Mourou, "Ultrafast carrier dynamics in III-V semiconductors grown by molecular-beam epitaxy at very low substrate temperatures," *Quantum Electron. IEEE J.*, vol. 28, no. October, 1992.
- [88] J. P. Ibbetson, J. S. Speck, a. C. Gossard, and U. K. Mishra, "Observation of arsenic precipitates in GaInAs grown at low temperature on InP," *Appl. Phys. Lett.*, vol. 62, no. 18, p. 2209, 1993.
- [89] B. Sartorius, H. Roehle, H. Künzel, J. Böttcher, M. Schlak, D. Stanze, H. Venghaus, and M. Schell, "All-fiber terahertz time-domain spectrometer operating at 1.5  $\mu\text{m}$  telecom wavelengths," *Opt. Express*, vol. 16, no. 13, pp. 9565–9570, 2008.
- [90] A. Takazato, M. Kamakura, T. Matsui, J. Kitagawa, and Y. Kadoya, "Detection of terahertz waves using low-temperature-grown InGaAs with 1.56  $\mu\text{m}$  pulse excitation," *Appl. Phys. Lett.*, vol. 90, no. 10, p. 101119, 2007.
- [91] M. Suzuki and M. Tonouchi, "Fe-implanted InGaAs photoconductive terahertz detectors triggered by 1.56  $\mu\text{m}$  femtosecond optical pulses," *Appl. Phys. Lett.*, vol. 86, no. 16, p. 163504, 2005.
- [92] M. Suzuki and M. Tonouchi, "Fe-implanted InGaAs terahertz emitters for 1.56  $\mu\text{m}$  wavelength excitation," *Appl. Phys. Lett.*, vol. 86, no. 5, p. 051104, 2005.
- [93] J. C. Delagnes, P. Mounaix, H. Němec, L. Fekete, F. Kadlec, P. Kužel, M. Martin, and J. Mangeney, "High photocarrier mobility in ultrafast ion-irradiated In<sub>0.53</sub>Ga<sub>0.47</sub>As for terahertz applications," *J. Phys. D: Appl. Phys.*, vol. 42, no. 19, p. 195103, Oct. 2009.
- [94] N. Chimot, J. Mangeney, L. Joulaud, P. Crozat, H. Bernas, K. Blary, and J. F. Lampin, "Terahertz radiation from heavy-ion-irradiated In<sub>0.53</sub>Ga<sub>0.47</sub>As photoconductive antenna excited at 1.55  $\mu\text{m}$ ," *Appl. Phys. Lett.*, vol. 87, no. 19, p. 193510, 2005.
- [95] O. Hatem, J. Cunningham, E. H. Linfield, C. D. Wood, a. G. Davies, P. J. Cannard, M. J. Robertson, and D. G. Moodie, "Terahertz-frequency photoconductive detectors fabricated from metal-organic chemical vapor deposition-grown Fe-doped InGaAs," *Appl. Phys. Lett.*, vol. 98, no. 12, p. 121107, 2011.
- [96] C. D. Wood, O. Hatem, J. E. Cunningham, E. H. Linfield, a. G. Davies, P. J. Cannard, M. J. Robertson, and D. G. Moodie, "Terahertz emission from metal-organic chemical vapor deposition grown Fe:InGaAs using 830 nm to 1.55  $\mu\text{m}$  excitation," *Appl. Phys. Lett.*, vol. 96, no. 19, p. 194104, 2010.
- [97] A. Schwagmann, Z.-Y. Zhao, F. Ospald, H. Lu, D. C. Driscoll, M. P. Hanson, a. C. Gossard, and J. H. Smet, "Terahertz emission characteristics of ErAs:InGaAs-based photoconductive antennas excited at 1.55  $\mu\text{m}$ ," *Appl. Phys. Lett.*, vol. 96, no. 14, p. 141108, 2010.
- [98] F. Ospald, D. Maryenko, K. von Klitzing, D. C. Driscoll, M. P. Hanson, H. Lu, a. C. Gossard, and J. H. Smet, "1.55  $\mu\text{m}$  ultrafast photoconductive switches based on ErAs:InGaAs," *Appl. Phys. Lett.*, vol. 92, no. 13, p. 131117, 2008.

- [99] R. Takahashi and Y. Kawamura, "Ultrafast 1.55  $\mu\text{m}$  photoresponses in low-temperature-grown InGaAs/InAlAs quantum wells," *Appl. Phys. Lett.*, vol. 65, no. 14, pp. 1790–1792, 1994.
- [100] Y. Chen, S. S. Prabhu, S. E. Ralph, and D. T. McInturff, "Trapping and recombination dynamics of low-temperature-grown InGaAs/InAlAs multiple quantum wells," *Appl. Phys. Lett.*, vol. 72, no. 4, p. 439, 1998.
- [101] K. Biermann, D. Nickel, K. Reimann, M. Woerner, T. Elsaesser, and H. Künzel, "Ultrafast optical nonlinearity of low-temperature-grown GaInAs/AlInAs quantum wells at wavelengths around 1.55  $\mu\text{m}$ ," *Appl. Phys. Lett.*, vol. 80, no. 11, p. 1936, 2002.
- [102] H. Kuenzel and K. Biermann, "Low-temperature-grown 1.55  $\mu\text{m}$  GaInAs/AlInAs quantum wells for optical switching: MBE growth and optical response," *Indium Phosphide Relat. Mater. Conf. 2002. IPRM. 14th*, pp. 343–346, 2002.
- [103] W.-U. Oh, J.-E. Oh, S.-R. Ryoo, S.-H. Paek, C.-K. Chung, and T.-W. Kang, "Growth temperature and annealing effects on deep traps of In<sub>0.52</sub>Al<sub>0.48</sub>As grown by molecular beam epitaxy," *J. Appl. Phys.*, vol. 74, no. 11, p. 7016, 1993.
- [104] L. Duvillearet, F. Garet, J.-F. Roux, and J.-L. Coutaz, "Analytical modeling and optimization of terahertz time-domain spectroscopy experiments, using photoswitches as antennas," *IEEE J. Sel. Top. Quantum Electron.*, vol. 7, no. 4, pp. 615–623, 2001.
- [105] J. E. Oh, P. K. Bhattacharya, Y. C. Chen, O. Aina, and M. Mattingly, "The Dependence of the Electrical and Optical Properties of Molecular Beam Epitaxial In<sub>0.52</sub>Al<sub>0.48</sub>As on Growth Parameters : Interplay of Surface Kinetics and Thermodynamics," *J. Electron. Mater.*, vol. 19, no. 5, pp. 435–441, 1990.
- [106] H. Hoenow, H.-G. Bach, J. Bottcher, F. Gueissaz, H. Künzel, F. Scheffer, and C. Schramm, "Deep levels analysis of Si doped MBE grown AlInAs layers," in *Indium Phosphide and Related Materials, 1992., Fourth International Conference on*, 1992, pp. 136–139.
- [107] F. Urbach, "The long-wavelength edge of photographic sensitivity and of the electronic absorption of solids," *Phys. Rev.*, vol. 92, p. 1324, 1953.
- [108] X. Zhou and H. Van Driel, "Femtosecond carrier kinetics in low-temperature-grown GaAs," *Appl. Phys. Lett.*, vol. 61, no. 25, pp. 3020–3022, 1992.
- [109] J. S. Weiner, D. S. Chemla, D. A. B. Miller, T. H. Wood, D. Sivco, and A. Y. Cho, "Room-temperature excitons in 1.6  $\mu\text{m}$  band gap GaInAs/AlInAs quantum wells," *Appl. Phys. Lett.*, vol. 46, no. 7, p. 619, 1985.
- [110] H. Sakaki, T. Noda, K. Hirakawa, M. Tanaka, and T. Matsusue, "Interface roughness scattering in GaAs/AlAs quantum wells," *Appl. Phys. Lett.*, vol. 51, no. 23, p. 1934, 1987.
- [111] R. Gottinger, A. Gold, G. Abstreiter, G. Weimann, and W. Schlapp, "Interface roughness scattering and electron mobilities in thin GaAs quantum wells," *Europhys. Lett.*, vol. 6, no. 2, pp. 183–188, 1988.
- [112] Z. Vardeny and J. Tauc, "Picosecond coherence coupling in the pump and probe technique," *Opt. Commun.*, vol. 39, no. 6, pp. 396–400, Nov. 1981.

- [113] A. Othonos, "Probing ultrafast carrier and phonon dynamics in semiconductors," *J. Appl. Phys.*, vol. 83, no. 4, p. 1789, 1998.
- [114] J. Zheng, H. Tan, and S. Ng, "Theory of non-radiative capture of carriers by multiphonon processes for deep centres in semiconductors," *J. Phys. Condens. Matter*, vol. 6, pp. 1695–1706, 1994.
- [115] T.-A. Liu, M. Tani, and C.-L. Pan, "THz radiation emission properties of multienergy arsenic-ion-implanted GaAs and semi-insulating GaAs based photoconductive antennas," *J. Appl. Phys.*, vol. 93, no. 5, p. 2996, 2003.
- [116] M. J. E. Golay, "Theoretical Consideration in Heat and Infra-Red Detection, with Particular Reference to the Pneumatic Detector," *Rev. Sci. Instrum.*, vol. 18, no. 5, p. 347, 1947.
- [117] P. U. Jepsen and B. M. Fischer, "Dynamic range in terahertz time-domain transmission and reflection spectroscopy," *Opt. Lett.*, vol. 30, no. 1, pp. 29–31, Jan. 2005.
- [118] L. Duvillaret, F. Garet, and J.-L. Coutaz, "Influence of noise on the characterization of materials by terahertz time-domain spectroscopy," *J. Opt. Soc. Am. B*, vol. 17, no. 3, p. 452, 2000.
- [119] M. van Exter and D. R. Grischkowsky, "Characterization of an optoelectronic terahertz beam system," *IEEE Trans. Microw. Theory Tech.*, vol. 38, no. 11, pp. 1684–1691, 1990.
- [120] E. Castro-Camus, L. Fu, J. Lloyd-Hughes, H. H. Tan, C. Jagadish, and M. B. Johnston, "Photoconductive response correction for detectors of terahertz radiation," *J. Appl. Phys.*, vol. 104, no. 5, p. 053113, 2008.
- [121] F. Tauser, C. Rausch, J. H. Posthumus, and F. Lison, "Electronically controlled optical sampling using 100 MHz repetition rate fiber lasers," in *SPIE Proc. SPIE 6881, Commercial and Biomedical Applications of Ultrafast Lasers VIII*, 2008, vol. 688100.
- [122] Y. Kim and D.-S. Yee, "High-speed terahertz time-domain spectroscopy based on electronically controlled optical sampling," *Opt. Lett.*, vol. 35, no. 22, pp. 3715–7, Nov. 2010.
- [123] J. Kash, J. Tsang, and J. Hvam, "Subpicosecond time-resolved Raman spectroscopy of LO phonons in GaAs," *Phys. Rev. Lett.*, vol. 54, no. 19, pp. 2151–2154, 1985.
- [124] S. E. Esipov and Y. B. Levinson, "The temperature and energy distribution of photoexcited hot electrons," *Adv. Phys.*, vol. 36, no. 3, pp. 331–383, Jan. 1987.
- [125] W. Pötz and P. Kocevār, *Hot Carriers in Semiconductor Nanostructures*. Elsevier, 1992, pp. 87–120.
- [126] R. Pässler, "Nonradiative multiphonon capture of thermal and hot carriers by deep traps in semiconductors for the alternative regimes of small and large lattice relaxation," *Czechoslov. J. Phys.*, vol. 34, pp. 377–401, 1984.
- [127] B. Srocka, H. Scheffler, and D. Bimberg, "Rhodium- and iridium-related deep levels in In<sub>0.53</sub>Ga<sub>0.47</sub>As," *Appl. Phys. Lett.*, vol. 64, no. 20, p. 2679, 1994.

## **II. APPENDIX**



**Paper I:**

**Optics Express, vol. 18, no. 3, pp. 2296–2301, 2010**



# Next generation 1.5 $\mu\text{m}$ terahertz antennas: mesa-structuring of InGaAs/InAlAs photoconductive layers

H. Roehle, R.J.B. Dietz, H.J. Hensel, J. Böttcher, H. Künzel, D. Stanze, M. Schell,  
and B. Sartorius

*Fraunhofer Institute for Telecommunications, Heinrich-Hertz-Institut,  
Einsteinufer 37, 10587 Berlin, Germany*

*\*Corresponding author: [roehle@hhi.fraunhofer.de](mailto:roehle@hhi.fraunhofer.de)*

**Abstract:** Mesa-structuring of InGaAs/InAlAs photoconductive layers is performed employing a chemical assisted ion beam etching (CAIBE) process. Terahertz photoconductive antennas for 1.5  $\mu\text{m}$  operation are fabricated and evaluated in a time domain spectrometer. Order-of-magnitude improvements versus planar antennas are demonstrated in terms of emitter power, dark current and receiver sensitivity.

©2010 Optical Society of America

**OCIS codes:** (300.6495) Spectroscopy, terahertz; (260.5150) Photoconductivity.

---

## References and links

1. M. Suzuki and M. Tonouchi, "Fe-implanted InGaAs photoconductive terahertz detectors triggered by 1.56  $\mu\text{m}$  femtosecond optical pulses," *Appl. Phys. Lett.* **86**, 163504 (2005)
2. N. Chimot, J. Mangeney, L. Joulaud, P. Crozat, H. Bernas, K. Blary, and J. F. Lampin, "Terahertz radiation from heavy-ion-irradiated In<sub>0.53</sub>Ga<sub>0.47</sub>As photoconductive antenna excited at 1.55  $\mu\text{m}$ ," *Appl. Phys. Lett.* **87**, 193510 (2005)
3. B. Sartorius, H. Roehle, H. Künzel, J. Böttcher, M. Schlak, D. Stanze, H. Venghaus, and M. Schell, "All-fiber terahertz time-domain spectrometer operating at 1.5  $\mu\text{m}$  telecom wavelengths," *Opt. Express* **16**, 9565-9570 (2008)
4. E.R. Brown, "A photoconductive model for superior GaAs THz photomixers," *Appl. Phys. Lett.* **75**, 769 (1999)
5. Duvillaret, L.; Garet, F.; Roux, J.-F.; Coutaz, J.-L., "Analytical modeling and optimization of terahertz time-domain spectroscopy experiments, using photoswitches as antennas," *Selected Topics in Quantum Electronics, IEEE Journal of*, **7**, no.4, pp.615-623, Jul/Aug 2001

## 1. Introduction

Terahertz systems operated at 1.5  $\mu\text{m}$  wavelength can benefit from the large variety of lasers and fiber components developed and matured originally for telecom applications. Thus compact, flexible and cost effective THz sensor systems can be assembled. For a long time, the photoconductive antennas (PCAs) for 1.5  $\mu\text{m}$  had been the bottleneck. Low temperature (LT) growth of InGaAs on InP using molecular beam epitaxy (MBE) then gave the needed ultrafast response - similar to the case of LT GaAs. Unfortunately, in contrast to LT GaAs, LT InGaAs exhibits a high dark conductivity, so far preventing its use for PCAs. Hence alternative techniques like Fe-implantation [1] or ion-irradiation [2] of InGaAs have been tried - with limited success up to now. Recently a structure has been developed where thin (12 nm) InGaAs photoconductive layers are embedded between InAlAs trapping layers [3]. In this approach, the resistivity had been increased by several orders of magnitude. One hundred periods of LT InGaAs/InAlAs were grown in order to also achieve sufficient photo efficiency. THz antennas for 1.5  $\mu\text{m}$  were fabricated, and good performance of a fiber coupled 1.5  $\mu\text{m}$  time domain (TD) system was demonstrated [3]. In this paper we present developments on the next generation of 1.5  $\mu\text{m}$  PCAs, especially by applying a kind of mesa-structuring of the

photoconductive layers. The concept and its technological realization are described in parts 2 and 3. Electrical characteristics and THz output powers are subject of parts 4 and 5, respectively. Finally, in part 6 the improvements achieved in TD systems are evaluated.

## 2. Concept for improved PCA's by mesa structuring

A general disadvantage of photoconductive antennas with on-top metal contacts results from the decreasing in-plane electrical field component (Fig. 1) in the depth of the photoconductor [4]. In our multi-layer structure (100 periods InGaAs/InAlAs), unfortunately, this problem is enhanced due to the many interfaces at the intermediate InAlAs layers with higher bandgap. The interaction of photocarriers with the electric field is reduced, and in the receiver the carrier flow is hindered by the multi-layer design.

One possibility to solve this problem is to apply mesa-type structures with electrical side contacts (Fig. 1c). Here, the electrical field is directly applied even to deeper layers, and the current in the receiver does not need to traverse heterostructure barriers. The mesa structuring offers a second advantage: The photoconductive material can be removed, wherever it contributes to the dark current but not to the photo current (Fig. 1b). This because the photo-excited spot and thus the width of the photo-current region are in the 10  $\mu\text{m}$  range. The dark current, however, flows between the full length (3 mm) of the antenna strip lines. Therefore, the area outside the optical excitation spot contributes about 300 times more to the dark current than the optically excited area itself. Since the semi-insulating (s.i.) InP substrate has a much higher resistivity than the photoconductive layers, the overall dark current can be significantly reduced by removing photoconductive material outside of the optically excited area or by structuring an isolating trench between electric contacts and those parts of the layer that do not contribute to photo-conductivity, as indicated in figure 1d and as visible in the SEM picture in figure 2b.

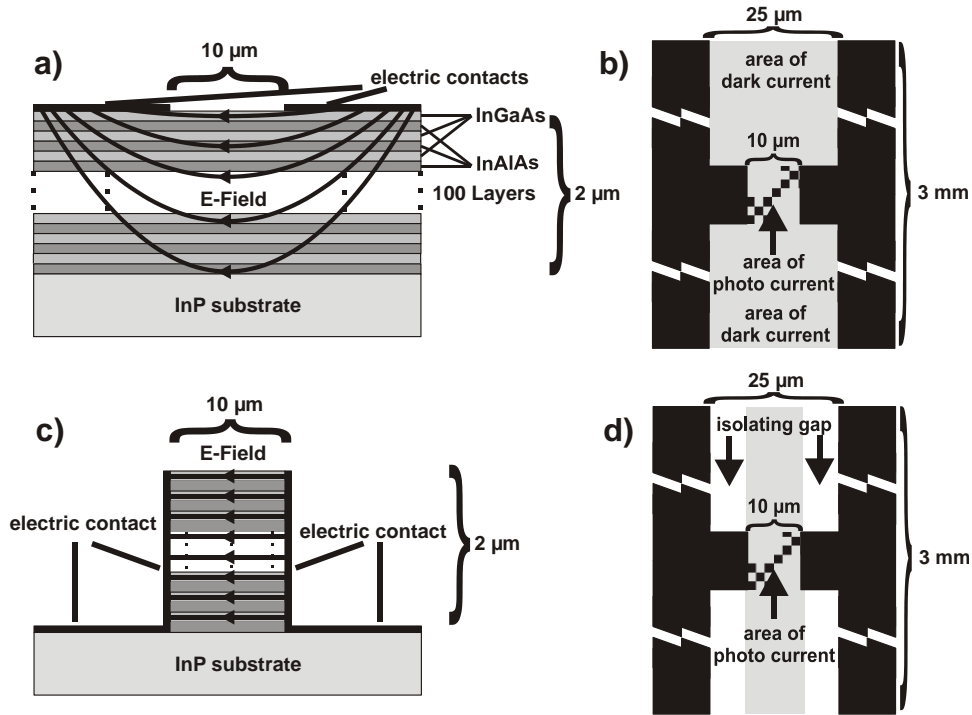


Fig. 1. Planar (a, b) versus mesa (c, d) structured antennas. Side view (a, c) and top view (b, d)

### 3. Mesa etching technique

The challenge in the mesa etching process is caused by the different materials in the multi-layer structure, the overall thickness, and the need for flat vertical walls for good electrical contact features. Key challenge is the extremely low etching rate of InAlAs. Wet chemical etching leads to strong undercuts of the InGaAs and thus has to be excluded. Even in an ion beam etching (IBE) process, the InAlAs withstands the  $\text{Ar}^+$  beam better than the photo mask, which consequently is removed before the process is ended. In addition, the etched flanks are rough and surface degradations come up during processing. So we employed a chemically assisted ( $\text{Cl}_2$ ) ion beam etching process (CAIBE). The material is exposed to the  $\text{Ar}^+$  beam and additionally to a stream of highly reactive  $\text{Cl}_2$  gas. The etching of InAlAs is significantly accelerated, and by properly adjusting substrate temperature, the  $\text{Ar}^+$  beam energy and intensity, and the flow rate of the  $\text{Cl}_2$  gas stream, the etch rates for InGaAs and InAlAs can be balanced. After optimization, steep flanks with good surface quality have been achieved applying this process.

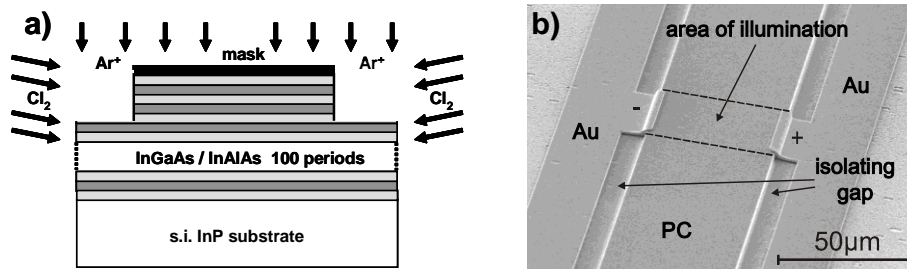


Fig. 2. (a) Scheme of the CAIBE Process, (b) SEM picture of a mesa-structured stripline antenna

The last step concerns the integration of the THz antennas with electric side contacts to the mesa structured photoconductor. Au is sputter-deposited and structured as shown in the SEM picture (Fig. 2b) for a strip line antenna. The metal side contact at the area of illumination can clearly be seen. In all other regions, isolating trenches separate metal and photoconductor, which go down to the s.i. InP substrate, and thus serve to minimize the dark current.

### 4. Electrical characteristics: mesa versus planar structures

First, the improvements of the photoconductive characteristics under CW illumination at  $1.5 \mu\text{m}$  are investigated using dipole antennas with  $10 \mu\text{m}$  gap and  $25 \mu\text{m}$  strip line distance. For the previous planar structure (Fig. 3a) the photo current is only slightly increased relative to the (high) dark current. In figure 3b the improvements due to the mesa structure become clearly visible. The photo current at  $10 \text{ mW}$  optical power is now by a 5 times higher than the (low) dark current. The dark current is successfully reduced by removing the parasitic contributions from outside the excited photoconductive gap. This effect is studied in more detail in figure 3c comparing dark currents in planar and mesa structures. We measure a reduction of the dark current by a factor of 23. Although this is a notable reduction, just from geometry we would expect a significantly higher factor: The width ratio of excited spot to antenna strip lines is  $10/3000$ , resulting in a factor 300. The width of the dipole gap is  $10 \mu\text{m}$  while there are  $25 \mu\text{m}$  between the antenna striplines, reducing the calculated geometrical improvement factor to 120. The measured improvement factor, however, is only 23. The origin of this discrepancy can be understood by looking at the photo currents as follows:

The effective photo currents - the differences between current with and without illumination - are depicted in figure 3d for planar and mesa structures. One can notice an increase of the photo current by a factor 5 for the mesa structured device. Excitation power and externally applied voltage are the same in both cases. Thus we attribute the improvement to the side contacts. The in-depth electrical field is higher for the mesa structures, and currents from the

deeper layers go directly to the contacts, without crossing intermediate barriers of the heterostructure. This, however, also holds for the dark current through the mesa structure. Thus one can expect an increase similar to that for the photo current by a factor of 5. This explains the discrepancy observed for the dark current reduction discussed above.

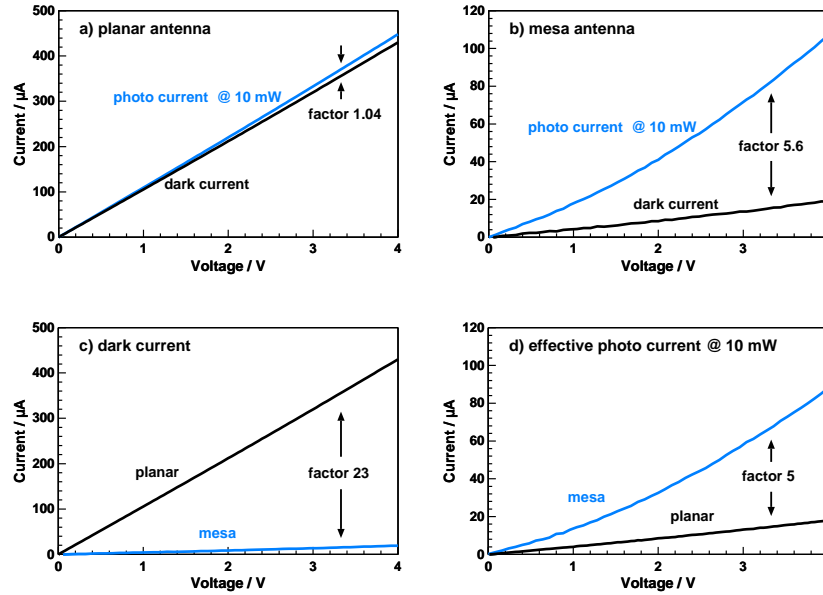


Fig. 3. Comparison of planar versus mesa antennas (dipole  $25/10 \mu\text{m}$ ): dark and photo current: (a) planar antenna (b) mesa antenna planar and mesa structure: (c) dark current (d) photo current at 10 mW minus dark current

In summary: Photo current, as well as dark current, in the photoconductive gap is increased by a factor 5 thanks to the side contacts of the mesa. Parasitic dark currents outside the gap are reduced by a factor 120 (dipole  $25/10 \mu\text{m}$ , antenna length  $3000 \mu\text{m}$ ) thanks to removing the material contributing only to dark currents. The measured overall dark current is reduced by a factor 23 due to the coexistence of both effects.

## 5. Improving the THz output power

Next the improvement in THz output power with the mesa structure is studied. A factory calibrated Golay cell allows for absolute measurements of the averaged output power. The emitters are strip line antennas with a gap of  $25 \mu\text{m}$ . The antennas are excited by 100 fs pulses at a center wavelength of  $1.55 \mu\text{m}$  from a fiber ring laser (Menlo Systems) with a repetition rate of 100 MHz. The antennas of planar and mesa type are packaged into fiber coupled housings developed at HHI. An  $\text{N}_2$  purged THz path with 2 inch parabolic mirrors focuses the emission onto the Golay cell. Optical excitation power and emitter bias voltage are varied within the measurements. Our results are summarized in figure 4. The THz output power at 40 mW mean optical excitation shows a quadratic behavior with increasing bias voltage, as expected within the scope of basic models [5]. The averaged THz power at 14 V and 40 mW is  $0.33 \mu\text{W}$ , corresponding to a THz peak power of about 4.7 mW if a THz pulse width of 0.7 ps is assumed. With a bias of 25 V and 16 mW optical excitation power we measured an average THz output of  $1.24 \mu\text{W}$  (17.7 mW peak) from the mesa antenna. In general, the increase in THz output power due to the mesa structuring is about a factor of 5 to 6.5, depending slightly on the optical excitation power and bias voltage.

The impact of the optical excitation power on THz emission (at 14 V bias voltage) is shown in figure 4b. Here the expected super-linear characteristics appear only at low excitation powers. A linear range follows, and for the mesa antenna even a sub-linear increase can be observed

above 20 mW. We attribute this to saturation and/or screening effects, but further investigations are necessary to understand and to avoid these limitations. For the present devices an excitation power of 20 mW appears reasonable. In conclusion, mesa compared to planar antennas deliver five times higher THz output power at similar operating parameters.

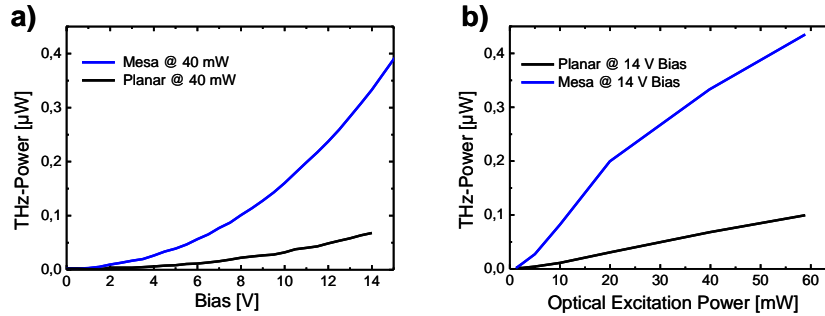


Fig. 4. THz output power measured with a Golay cell in dependence (a) on bias voltage, at 40 mW optical power, and (b) on optical power, at 14 V bias voltage

## 6. Performance of mesa antennas in a time domain system

The evaluation of the novel mesa-type PCAs is concluded by measurements in the time domain system shown in figure 5. Strip line ( $25\ \mu\text{m}$ ) emitters and dipole ( $10\ \mu\text{m}$ ) receivers are packaged into fiber coupled modules. The average excitation power is 20 mW for emitter and receiver respectively. The emitter bias voltage is 10 V, modulated at 5 kHz. The THz emission is focused by off-axis parabolic mirrors onto the detector, and the THz path is purged with dry nitrogen to avoid water vapor absorption (Fig. 5). The planar antennas are step by step replaced by the new mesa devices, first only on the emitter site, then only on the receiver site, and in the end at both sites. The difference between the minimum and the maximum values within one pulse of the received signal is taken as a measure for the performance of the respective configuration. The value obtained in the system with conventional planar antennas serves as a reference.

First, the emitter is changed from planar type to mesa type. The amplitude is increased by a factor 2.5 (Fig. 6). In order to compare this with the Golay cell results, where the THz power is measured, the pulse trace current values are squared and integrated. The improvement found here for the mesa in this example is a factor of 5.8 in power, which is in good agreement with the factor of 6.4 measured using the Golay cell for the underlying parameter values of 10 V and 20 mW. Next, we investigate planar emitters and mesa receivers (Fig. 6b). The amplitude is increased by a factor 11 - 12 compared to planar receivers. The mesa side contacts allow for an increased coupling of the THz field and a significantly improved charge transfer in the depth of the photoconductive layers since they allow current flow without traversing barriers and borders. As result, the improvements of mesa structures on the receiver are higher than on the emitter side.

Finally, we use mesa structures both for the emitter and the receiver. The measured improvement in amplitude is a factor of 27.5, corresponding to the product of the values for only emitter (x 2.5) or only receiver (x 11). The significant higher received signal allows the use of electronic preamplifiers with lower gain and thus higher bandwidth. So improved signal/noise ratio, higher speed of measurements and investigation of weaker signals are made possible by the novel antennas. In addition to the higher amplitude, we also observe that the THz pulse width is reduced by about 100 fs compared to the planar structure. Consequently, the Fourier spectrum (Fig. 6d) now extends beyond 4 THz, compared to 3 THz for the non-mesa antennas (not shown). Unfortunately, the relative noise floor of the FFT spectrum does not decrease proportionally with the increasing signal strength due to limitations in the absolute precision of the delay timebase.

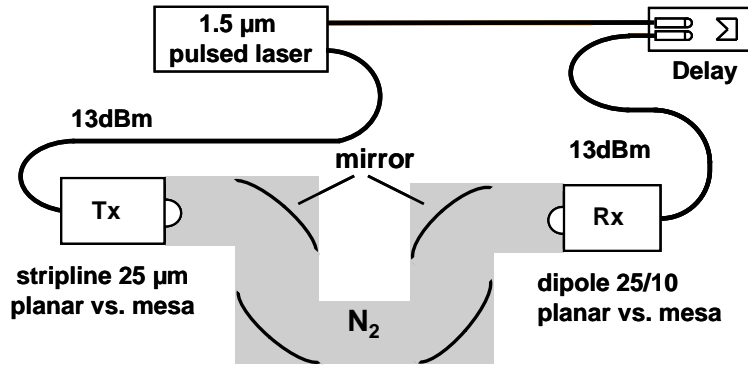


Fig. 5. Scheme of the THz Time Domain System

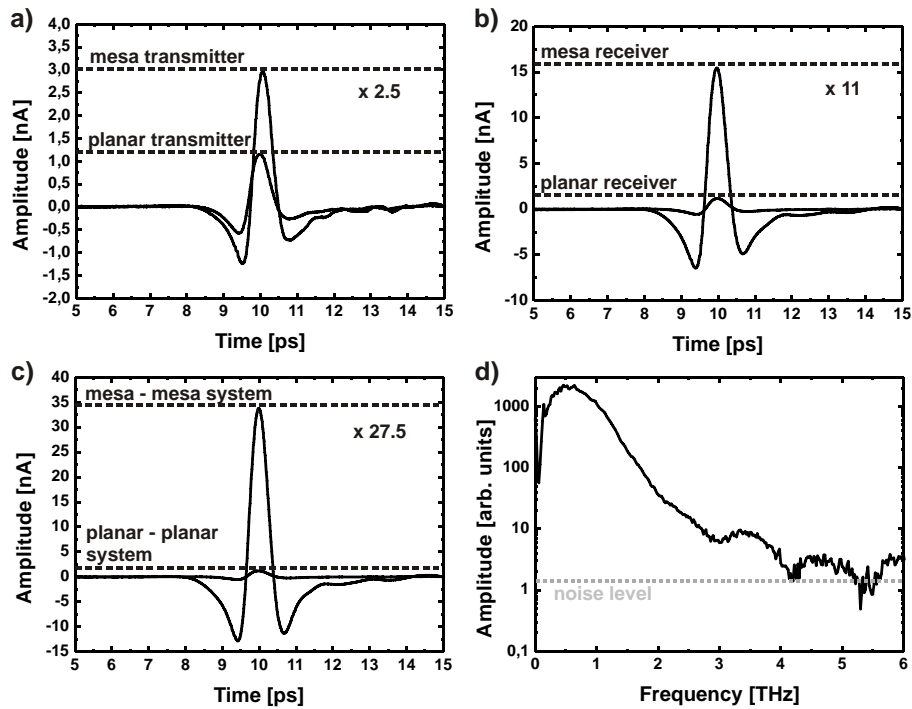


Fig. 6. Detected TD signal traces applying mesa antennas versus planar antennas: (a) mesa emitter, (b) mesa receiver, (c) mesa system, (d) FFT spectrum of mesa system

### Summary and outlook

InGaAs/InAlAs photoconductive antennas for 1.5 μm operation have been improved by mesa-etching of the conductive layers. Electrical side contacts to the multi-layer structure are applied, and layers are removed in regions contributing only to parasitic dark currents.

Consequently, photo currents are increased by a factor 5 and parasitic dark currents are suppressed. The emitted THz power is increased by more than a factor 5 compared to conventional planar antennas, the receiver sensitivity is improved by a factor of 11. All in all, the complete mesa systems outperform the previous planar systems by a factor 27.5 in detected amplitude. The noise limit of the Fourier spectrum has been extended beyond 4 THz. Summarized, the new generation of THz antennas with mesa-structured photoconductive layers represents a considerable advancement for 1.5 μm THz TD systems.

**Paper II:**

**Optics Express, vol. 19, no. 27, pp. 122–126, 2011**



# THz generation at 1.55 $\mu\text{m}$ excitation: six-fold increase in THz conversion efficiency by separated photoconductive and trapping regions

Roman J.B. Dietz,<sup>1,\*</sup> Marina Gerhard,<sup>1</sup> Dennis Stanze,<sup>1</sup> Martin Koch,<sup>2</sup>  
Bernd Sartorius<sup>1</sup> and Martin Schell<sup>1</sup>

<sup>1</sup>Fraunhofer Institute for Telecommunications, Heinrich-Hertz-Institute, Einsteinufer 37, 10587 Berlin, Germany

<sup>2</sup>Department of Physics, Philipps-Universität Marburg, Renthof 5, 35032 Marburg, Germany

[Roman.Dietz@hhi.fraunhofer.de](mailto:Roman.Dietz@hhi.fraunhofer.de)

**Abstract:** We present first results on photoconductive THz emitters for 1.55  $\mu\text{m}$  excitation. The emitters are based on MBE grown  $\text{In}_{0.53}\text{Ga}_{0.47}\text{As}/\text{In}_{0.52}\text{Al}_{0.48}\text{As}$  multilayer heterostructures (MLHS) with high carrier mobility. The high mobility is achieved by spatial separation of photoconductive and trapping regions. Photoconductive antennas made of these MLHS are evaluated as THz emitters in a THz time domain spectrometer (THz TDS). The high carrier mobility and effective absorption significantly increases the optical-to-THz conversion efficiency with THz bandwidth in excess of 3 THz.

©2010 Optical Society of America

**OCIS codes:** (260.5150) Physical optics: Photoconductivity, (300.6495) Spectroscopy: Spectroscopy, terahertz

---

## References and links

1. P. Jepsen, D. G. Cooke, M. Koch, "Terahertz spectroscopy and imaging – Modern techniques and applications," *Laser & Photonics Review* 5, 124 (2011), <http://onlinelibrary.wiley.com/doi/10.1002/lpor.201000011/abstract>
2. M. B. Ketchen, et al., "Generation of sub-picosecond electrical pulses on coplanar transmission lines," *Appl. Phys. Lett.*, vol. **48**, 751–753, (1986). <http://link.aip.org/link/doi/10.1063/1.96709>
3. P. R. Smith, D. H. Auston, M. C. Nuss, "Subpicosecond photoconducting dipole antennas," *Quantum Electronics, IEEE Journal of*, vol. **24**, no. 2, 255–260, (1988). <http://dx.doi.org/10.1109/3.121>
4. A. C. Warren, N. Katzenellenbogen, D. Grischkowsky, J. M. Woodall, M. R. Melloch, N. Otsuka, "Subpicosecond, freely propagating electromagnetic pulse generation and detection using GaAs:As epilayers," *Appl. Phys. Lett.* **58**, 1512–1514, (1991) <http://link.aip.org/link/doi/10.1063/1.105162>
5. H. M. Heiliger, M. Vosseburger, H. G. Roskos, H. Kurz, R. Hey, K. Ploog, "Application of liftoff low-temperature-grown GaAs on transparent substrates for THz signal generation," *Appl. Phys. Lett.* 69, 2903 (1996) <http://link.aip.org/link/doi/10.1063/1.117357>
6. S. Matsuura, M. Tani, K. Sakai, "Generation of coherent terahertz radiation by photomixing in dipole photoconductive antennas," *Appl. Phys. Lett.* 70, 559 (1996). <http://link.aip.org/link/doi/10.1063/1.118337>
7. M. Tani, S. Matsuura, K. Sakai, S. Nakashima, "Emission characteristics of photoconductive antennas based on low-temperature-grown GaAs and semi-insulating GaAs," *Appl. Opt.* **36**, 7853–7859 (1997) <http://www.opticsinfobase.org/abstract.cfm?URI=ao-36-30-7853>
8. K. Ezdi et al., "A hybrid time-domain model for pulsed terahertz dipole antennas," *J. Europ. Opt. Soc. Rap. Public.* 09001 Vol 4 (2009) [http://www.jeos.org/index.php/jeos\\_rp/article/view/09001](http://www.jeos.org/index.php/jeos_rp/article/view/09001)
9. N. Vieweg, M. Mikulics, M. Scheller, K. Ezdi, R. Wilk, H. W. Hübers, M. Koch, "Impact of the contact metallization on the performance of photoconductive THz antennas," *Opt. Express* **16**, 19695–19705 (2008) <http://www.opticsinfobase.org/abstract.cfm?URI=oe-16-24-19695>
10. K. A. McIntosh et al., "Investigation of ultrashort photocarrier relaxation times in low-temperature-grown GaAs," *Appl. Phys. Lett.* 70, 354 (1997), <http://link.aip.org/link/doi/10.1063/1.118412>
11. M. Griebel et al., "Tunable subpicosecond optoelectronic transduction in superlattices of self-assembled ErAs nanoislands," *Nature Materials* 2, 122–126 (2003), doi:10.1038/nmat819
12. C. Kadow, A. W. Jackson, A. C. Gossard, S. Matsuura, G. A. Blake, "Self-assembled ErAs islands in GaAs for optical-heterodyne THz generation," *Appl. Phys. Lett.* 76, 3510 (2000). <http://link.aip.org/link/doi/10.1063/1.126690>

13. J. Sigmund et al., "Structure investigation of LTG-GaAsSb as a new material for photoconductive THz antennas," *Appl. Phys. Lett.* **87**, 252103 (2005), <http://link.aip.org/link/doi/10.1063/1.2149977>
14. K. Bertulis et al., "GaBiAs: A material for optoelectronic terahertz devices," *Appl. Phys. Lett.* **88**, 201112 (2006), <http://link.aip.org/link/doi/10.1063/1.2205180>
15. M. Suzuki, M. Tonouchi, "Fe-implanted InGaAs terahertz emitters for 1.56  $\mu\text{m}$  wavelength excitation," *Appl. Phys. Lett.* **86**, 051104 (2005). <http://link.aip.org/link/doi/10.1063/1.1861495>
16. M. Suzuki, M. Tonouchi, "Fe-implanted InGaAs photoconductive terahertz detectors triggered by 1.56  $\mu\text{m}$  femtosecond optical pulses," *Appl. Phys. Lett.* **86**, 163504 (2005). <http://link.aip.org/link/doi/10.1063/1.1901817>
17. R. Wilk et al., "THz Time-Domain Spectrometer Based on LT-InGaAs Photoconductive Antennas Exited by a 1.55  $\mu\text{m}$  Fibre Laser," *Conference on Lasers and Electro-Optics, 2007*, vol., no., pp.1-2, 6-11 May 2007 <http://ieeexplore.ieee.org/stamp/stamp.jsp?tp=&arnumber=4452856&isnumber=4452320>
18. B. Sartorius et al., "All-fiber terahertz time-domain spectrometer operating at 1.5  $\mu\text{m}$  telecom wavelengths," *Opt. Express* **16**, 9565-9570 (2008) <http://www.opticsinfobase.org/abstract.cfm?URI=oe-16-13-9565>
19. A. Schwagmann et al., "Terahertz emission characteristics of ErAs:InGaAs-based photoconductive antennas excited at 1.55 $\mu\text{m}$ ," *Appl. Phys. Lett.* **96**, 41108 (2010) <http://link.aip.org/link/doi/10.1063/1.3374401>
20. C. D. Wood et al., "Terahertz emission from metal-organic chemical vapor deposition grown Fe:InGaAs using 830 nm to 1.55 $\mu\text{m}$  excitation," *Appl. Phys. Lett.* **96**, 194104 (2010) <http://link.aip.org/link/doi/10.1063/1.3427191>
21. O. Hatem et al., "Terahertz-frequency photoconductive detectors fabricated from metal-organic chemical vapor deposition-grown Fe-doped InGaAs," *Appl. Phys. Lett.* **98**, 121107 (2011) <http://link.aip.org/link/doi/10.1063/1.3571289>
22. J. Oh, P. Bhattacharya, Y. Chen, O. Aina, M. Mattingly, "The dependence of the electrical and optical properties of molecular beam epitaxial  $\text{In}_{0.52}\text{Al}_{0.48}\text{As}$  on growth parameters: Interplay of surface kinetics and thermodynamics," *Journal of Electronic Materials* Vol.19, No.5, pp. 435-441 (1990) <http://www.springerlink.com/content/010544084t85h872/>
23. H. Hoenow et al., "Deep level Analysis of Si Doped MBE Grown AlInAs Layers," 4th International Conference on Indium Phosphide and Related Materials, pp. 136-139, (1992) <http://ieeexplore.ieee.org/stamp/stamp.jsp?arnumber=00235658>
24. J. S. Weiner et al., "Room temperature excitons in 1.6 $\mu\text{m}$  band-gap GaInAs/AlInAs quantum wells," *Appl. Phys. Lett.* **46**, 619 (1985) <http://link.aip.org/link/doi/10.1063/1.95504>
25. H. Kuenzel et al., "Material properties of Ga<sub>0.47</sub>In<sub>0.53</sub>As grown on InP by low-temperature molecular beam epitaxy," *Appl. Phys. Lett.* **61**, 1347 (1992) <http://link.aip.org/link/doi/10.1063/1.107587>
26. H. Roehle et al., "Next generation 1.5  $\mu\text{m}$  terahertz antennas: mesa-structuring of InGaAs/InAlAs photoconductive layers," *Optics Express* Vol. 18, Iss. 3, pp. 2296–2301 (2010) <http://www.opticsinfobase.org/oe/abstract.cfm?URI=oe-18-3-2296>
27. P. Uhd Jepsen, R. H. Jacobsen, and S. R. Keiding, "Generation and detection of terahertz pulses from biased semiconductor antennas," *J. Opt. Soc. Am. B* **13**, 2424-2436 (1996) <http://www.opticsinfobase.org/abstract.cfm?URI=josab-13-11-2424>

## 1. Introduction

Terahertz time domain spectroscopy (TDS) is by far the method of most importance within the rapidly developing and prosperous field of terahertz technology [1]. This method is based on the optical or optoelectronic generation and detection of short THz pulses by non-linear crystals or semiconductor based photoconductive antennas (PCA). In the latter case it is crucial to employ a material that exhibits very short carrier lifetimes in order to obtain broadband THz spectra.

The first generation of THz radiation from PCAs was achieved with radiation damaged silicon-on-sapphire [2,3]. Later experiments employed low temperature (LT) molecular beam epitaxy (MBE) grown GaAs, which rapidly became the state of the art material [4-6]. For all material systems the THz pulses were excited by titanium sapphire femtosecond lasers at wavelengths around 800 nm.

In the last 20 years there have been numerous approaches to increase the performance of photoconductive antennas, e.g. investigating antenna structure [7,8], metallization [9] and carrier lifetime [10] or by utilizing new material systems, such as GaAs:ErAs [11,12], LT GaAsSb [13] and GaAsBi [14]. The first attempt of PCAs based on InGaAs, for excitation

with cost-effective fibre lasers at wavelengths around 1.55  $\mu\text{m}$ , was made by Suzuki and Tonouchi [15,16]. Recently, it was shown that LT MBE grown Beryllium doped InGaAs/InAlAs heterostructures are suitable for broadband THz emitters and detectors [17]. Subsequently, a completely fibre coupled THz TDS system based on these antennas was introduced [18]. Since then other groups also demonstrated THz emission and detection in InGaAs based materials [19-21].

Despite these great efforts there is still vast potential for improvement of InGaAs based PCAs. As mentioned above, short carrier lifetimes are a key feature for broadband THz PCAs. These short carrier lifetimes are generally realized by inducing defect states into the respective semiconductor material. These defect states can be realized by strong doping [20,21], ion implantation [15,16], growth conditions, e.g. LT growth [17], or the growth of special recombination centers [19]. Additional important characteristics for efficient THz emitters are efficient absorption, a sufficiently high carrier mobility and high dark resistivity, i.e. low residual carrier concentrations.

However, it is difficult to fulfill all of the above requirements, since high defect material typically shows a strongly reduced carrier mobility due to elastic and inelastic (i.e. trapping) scattering of carriers at defect sites. Furthermore, in case of InGaAs the defects states are energetically situated relatively close to the conduction band. This shifts the Fermi level closer to the conduction band edge which results in low dark resistivity at room temperature.

The Fermi level can be lowered by counter doping with an acceptor-type dopant. However, counter doping further reduces carrier mobility. In addition, light absorption is also reduced in high defect materials.

In this work we present a new approach to circumvent some of these obstacles. The basic idea is to spatially separate the photoconductive region, i.e. where light absorption and carrier transport take place, from regions that exhibit high defect densities and that are transparent for 1.55  $\mu\text{m}$  excitation, thus solely acting as trapping and recombination regions.

## 2.Principle and Growth

A device meeting the above mentioned requirements can be realized by MBE growth of InGaAs/InAlAs multi-layer heterostructures (MLHS) (as depicted in Fig 1a) when utilizing a special characteristic of MBE growth of InAlAs. Within a substrate temperature range between  $T_s = 300 - 500$   $^{\circ}\text{C}$  the growth of InAlAs shows strong alloy clustering effects with InAs-like and AlAs-like regions featuring cluster sizes of several nanometers, with a maximum cluster density for  $T_s \approx 400$   $^{\circ}\text{C}$  [22]. The activation energies of these cluster defects have been measured to be in the region of  $E_A = 0.6-0.7$  eV [22,23] which results in the InAlAs to be semi-insulating.

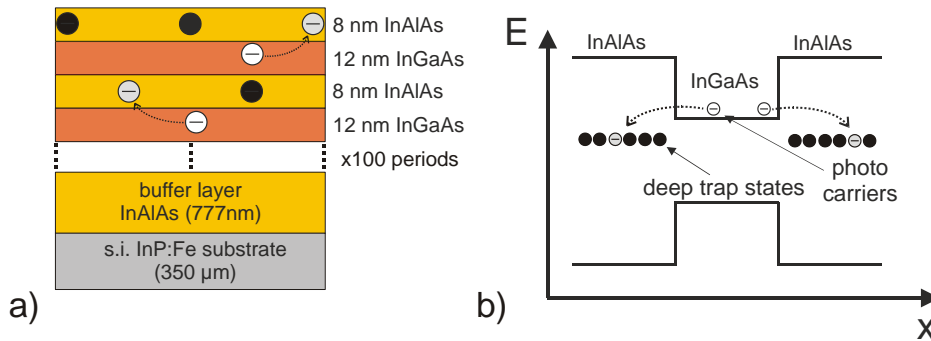


Fig 1. a) Schematic of InGaAs/InAlAs heterostructure, with 100 periods of a 12 nm InGaAs layer followed by a 8 nm InAlAs layer with cluster-induced defects acting as electron traps. b) Schematic of the respective band-diagram in real space with deep cluster-induced defect states.

For the growth of a MLHS at this temperature and considering the conduction band offset between InAlAs ( $E_g=1.47$  eV at 300 K) and InGaAs ( $E_g=0.74$  eV at 300 K) of approximately  $\Delta E_c = 0.44$  eV [24], this results in defect states within the InAlAs layers that are energetically situated significantly below the conduction band of adjacent InGaAs layers, as depicted schematically in Fig 1. b).

If the InAlAs layers are sufficiently thin, i.e. the the electron wave function of an optically excited electron in the conduction band of an InGaAs layer has a sufficiently large overlap with the cluster defect states in the adjacent InAlAs layer, these defects can act as effective traps for those electrons.

In addition, the MBE growth of InGaAs at substrate temperatures around 400 - 500 °C shows a minimum for the residual carrier concentration, with  $N_A-N_D < 3 \cdot 10^{-15}$  cm<sup>-3</sup> and Hall mobility values for bulk material of  $\mu_{H,InGaAs} = 10000$  cm<sup>2</sup>/Vs [25]. Hence, the growth of a InGaAs/InAlAs MLHS should lead to short carrier lifetimes while maintaining effective absorption, high dark resistivity and high carrier mobility in the photoconductive layer.

The InGaAs/InAlAs MLHS investigated in this work were grown by elemental source molecular beam epitaxy on semi insulating InP:Fe substrates at an approximate substrate temperature of 400 °C. First a 777 nm InAlAs buffer layer was grown followed by 100 periods of 12 nm InGaAs layers and 8 nm InAlAs layers.

We measured Hall mobility values for the MLHS grown at  $T_s = 400$  °C of  $\mu_{H,400-MLHS} = 1500-3000$  cm<sup>2</sup>/Vs. The decrease in Hall mobility compared to the bulk InGaAs value is due to the fact that trapping of carriers into defect states in the InAlAs layers also contributes to the scattering time which is probed by hall mobility measurements. Nevertheless the mobility of the MLHS grown at 400°C is still almost one magnitude higher than that of LT-grown ( $T_s=130$ °C) Be-doped MLHS with Hall mobility values of  $\mu_{H,LT-MLHS} < 500$  cm<sup>2</sup>/Vs.

### 3. THz TDS Measurements

In order to evaluate the 400 °C grown material as a THz emitter, the samples were processed as mesa-type antennas as described in [26] with a stripline type antenna geometry and a stripline separation of 25 μm. A similarly structured conventional LT grown Be-doped InGaAs/InAlAs MLHS served as a reference emitter in all measurements.

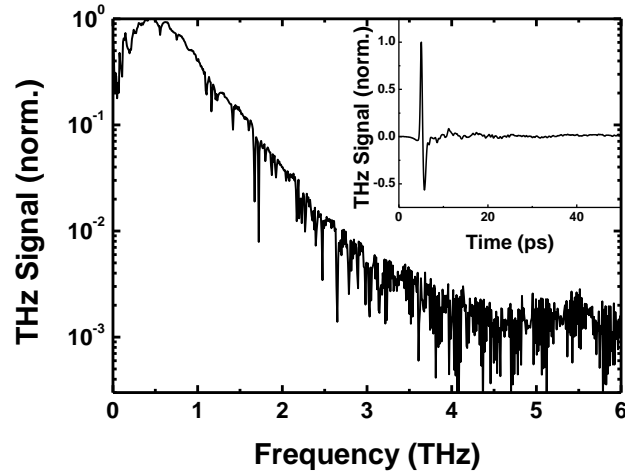


Fig 2. THz pulse trace and corresponding FFT spectrum for a conventional LT-grown Be-doped MLHS THz emitter grown at  $T_s = 130$  °C (this is serves as a reference).

For detection we used a photoconductive receiver also based on LT-grown Be-doped InGaAs/InAlAs MLHS processed with a 10  $\mu\text{m}$  gap dipole mesa-type antenna. The THz TDS setup consisted of a pre-compensated pulsed Er-doped fibre laser with a repetition rate of 100 MHz and pulses with approximately 80 fs FWHM pulse width. A mechanical delay stage was used to introduce a delay between pump and probe pulse. The laser was focused onto the emitter and detector with a spot size of approximately 10  $\mu\text{m}$ . The THz beam path consisted of hyper-hemispherical silicon lenses attached to the backside of each antenna and two off-axis parabolic mirrors in between to focus the THz emission onto the detector. Figure 2 shows Fourier spectrum of the signal from the LT-reference antenna with the corresponding THz pulse trace in the inset. Figure 3 shows the FFT spectrum and THz pulse obtained from the new emitter material. In both cases a bias field of 2 kV/cm and an optical excitation of 10 mW at emitter and 20 mW at the detector were applied. As can be seen the spectral bandwidth of the new design is comparable to the one obtained with the LT grown reference, both extending well beyond 3 THz. The high bandwidth obtained with the new device suggests that the device exhibits relatively fast carrier trapping times, thus supporting the assumption of an effective trapping mechanism within the device.

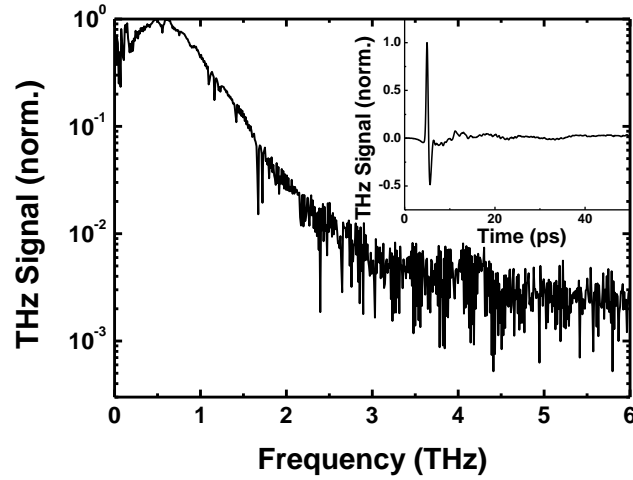


Fig 3. THz pulse trace and corresponding FFT Spectrum for a MLHS grown at  $T_s = 400^\circ\text{C}$ , with separated trapping and photoconductive regions

#### 4. Dependence on bias field and optical-to-THz conversion efficiency

To further evaluate the new material, we measured the peak-to-peak amplitude of the THz pulse obtained by TDS measurements in dependence of the applied bias field as well as in dependence on the optical power incident on the emitter antenna. Again an LT grown Be-doped MLHS antenna served as a reference.

The THz amplitude over applied bias field is shown in Fig.4. As can be seen the new MLHS grown at  $400^\circ\text{C}$  shows a much stronger THz emission than the LT reference. We attribute this to the improved carrier mobility in the new material. This can be understood within the framework of the classical Maxwell and Drude-model [27], where the emitted THz field is directly proportional to the derivative of the time-varying photocurrent which in turn is proportional to the mobility. In Figure 5 the THz amplitude is shown in dependence of the optical excitation power at the emitter for a constant bias field of 2 kV/cm. The new material shows a significantly higher light sensitivity compared to the LT reference, which we attribute

to a shaper absorption band edge and the higher mobility in the 400 °C grown material compared to the LT-grown material.

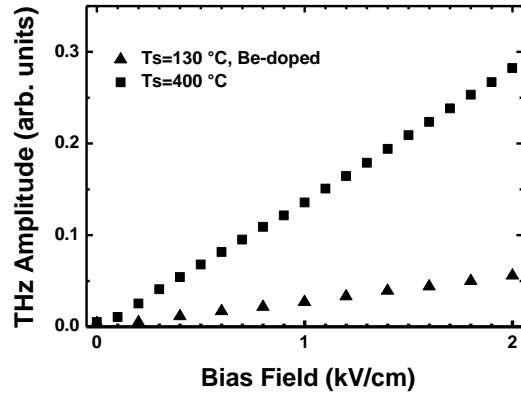


Fig 4. Emitted THz-pulse amplitude detected by a PCA receiver in a THz TDS setup, as a function of applied bias field at the emitter for a MLHS grown at  $T_s = 400$  °C (squares) and a MLHS grown at  $T_s = 130$  °C, Be-doped (triangles). The applied optical power was 10 mW for both emitter and receiver.

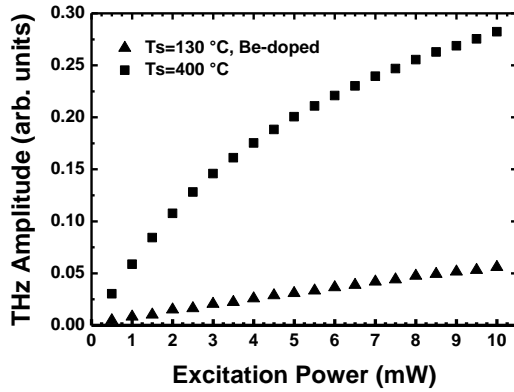


Fig 5. Emitted THz-pulse amplitude detected by a PCA receiver in a THz TDS setup, as a function of optical excitation power at the emitter for a MLHS grown at  $T_s = 400$  °C (squares) and a MLHS grown at  $T_s = 130$  °C, Be-doped (triangles). The applied emitter bias field was 2 kV/cm.

## 5. Conclusion and Outlook

We presented a new concept and the first realization of InGaAs based THz emitters that combine fast trapping times with high mobility and efficient absorption. The new emitters are capable of broadband THz emission while raising the optical-to-THz conversion efficiency by almost one order of magnitude. Future designs comprising optimized growth conditions and trapping layer thicknesses will potentially further improve the performance of these pulsed THz emitters.

Acknowledgement: We thank Deutsche Forschungsgemeinschaft for funding this work under grant KO 1520/5-1 and SA/784/4-1

**Paper III:**

**Journal of Luminescence, vol. 138, pp. 179–181, 2013**



# Photoluminescence study of (GaIn)As/(AlIn)As-based THz antenna materials for 1.55 $\mu\text{m}$ excitation

T. Jung<sup>a,\*</sup>, R. Dietz<sup>b</sup>, A. Chernikov<sup>a</sup>, F. Kuik<sup>a</sup>, B. Sartorius<sup>b</sup>, M. Schell<sup>b</sup>, M. Koch<sup>a</sup>, S. Chatterjee<sup>a</sup>

<sup>a</sup>*Faculty of Physics, Philipps-Universität Marburg, Renthof 5, D-35032 Marburg, Germany*

<sup>b</sup>*Fraunhofer Institute for Telecommunications, Heinrich Hertz Institute, Einsteinufer 37, D-10587 Berlin, Germany*

---

## Abstract

The influence of localization and disorder in (GaIn)As/(AlIn)As heterostructures with spatially separated photoconductive and recombination regions designed as material for THz antennas for telecom applications at 1.55  $\mu\text{m}$  is investigated by photoluminescence spectroscopy. The emission is studied as a function of lattice temperature for a series of samples with different growth temperatures. Strain-induced disorder is identified as the main contribution to carrier localization. In addition, inhomogeneous broadening as well as PL intensity are strongly influenced by the impurity density in the barrier material. The optimal configuration as THz antenna material is achieved at a growth temperature of 375  $^{\circ}\text{C}$ .

---

**Keywords:** III-IV semiconductors, photoluminescence, disorder, THz-emitters

## 1. Introduction

Terahertz (THz) time-domain spectroscopy (TDS) is the method of paramount importance and potential within the rapidly developing field of THz technology [1–3]. This technique is based on the optoelectronic generation and detection of short THz pulses either in non-linear crystals or in semiconductor-based photoconductive antennas. In particular, the latter scheme is widely used. For these applications, it is essential that the antenna material combines an ultra-short carrier lifetime in the range of a few hundreds of femtoseconds and high carrier mobility; see [4, 5] for more details. Originally, photoconductive antennas were made from radiation-damaged silicon-on-sapphire [6, 7]. Later, low-temperature (LT) GaAs became the standard material [8–10]. Both material systems are typically excited with laser pulses in the 800 nm range provided by Ti:sapphire lasers.

Many attempts have been made over the last 15 years to optimize photoconductive emitters and receivers regarding, e.g., the antenna structure [10, 11], metallization [12], and carrier lifetime [13]. Additionally, new material systems have been explored including LT-Ga(AsSb) [14], Ga(AsBi) [15], and GaAs with ErAs islands [16, 17], only to name a few. Much effort was directed towards the development of antennas for excitation at the so-called "telecom wavelength" around 1550 nm using more cost-efficient fibre

lasers. In 2005 ion-implanted InGaAs was demonstrated as antenna material for this frequency window [18–21]. Later, LT molecular beam epitaxy (MBE) grown Be-doped (GaIn)As/(AlIn)As quantum wells on InP substrate were introduced [22]. An all-fibre coupled THz spectrometer without any free-space paths was demonstrated using antennas fabricated from these materials [23, 24]. However, further doping of LT grown antenna materials typically reduces carrier mobility due to scattering effects. To avoid this, a most recent approach intends the spatial separation of the antennas photoconductive regions from regions with high defect densities, thus ensuring short carrier lifetimes while maintaining high carrier mobility. This separation can be achieved under certain growth conditions. A first experimental demonstration that this scheme works well for terahertz emission was recently reported by Dietz et al. for a structure grown at 400  $^{\circ}\text{C}$  [25].

In this paper, we present a comprehensive characterization of the photoluminescence (PL) properties of a series of such (GaIn)As/(AlIn)As heterostructures grown at substrate temperatures between 325  $^{\circ}\text{C}$  and 450  $^{\circ}\text{C}$ . The photoluminescence data are correlated with X-ray diffraction (XRD) measurements. In particular, we investigate localization and disorder effects in the (GaIn)As layers and how they are influenced by different growth conditions. We aim to identify the optimal combination between fast non-radiative capture and minimal localization effects.

## 2. Samples and Experiment

We study a series of samples grown onto (100)-oriented InP:Fe substrates using MBE at substrate temperatures of 325, 350, 375, 400, 425, and 450  $^{\circ}\text{C}$ . The initial substrate temperature was set to 500  $^{\circ}\text{C}$  which was then ramped to the desired final growth temperature. Next, a  $\sim 0.8 \mu\text{m}$

---

\*Corresponding author. Tel: +49 6421 2824427, fax: +49 6421 2827036

Email address: [tilmann.jung@physik.uni-marburg.de](mailto:tilmann.jung@physik.uni-marburg.de) (T. Jung)

(GaIn)As buffer layer was grown on top of the substrate. The active structural element was repeated 30 times, consisting of 12 nm (GaIn)As quantum wells with 8 nm (AlIn)As barriers. Finally, a 10 nm (GaIn)As cap layer concluded the growth of the structure.

For the PL measurements, a Ti:sapphire laser emitting 100 fs pulses at 80 MHz centered at 800 nm is used as a pump. We focus the laser to obtain an excitation photon fluence at the sample surface of  $2 \cdot 10^{14}$  photons  $\text{cm}^{-2}$  per pulse, corresponding to the typical excitation conditions for THz antenna applications. The samples are mounted in a He-flow cryostat, enabling measurements from 4 K to room temperature. The PL is collected in reflection geometry and is imaged into an optical spectrum analyzer using 0.3 NA collection optics.

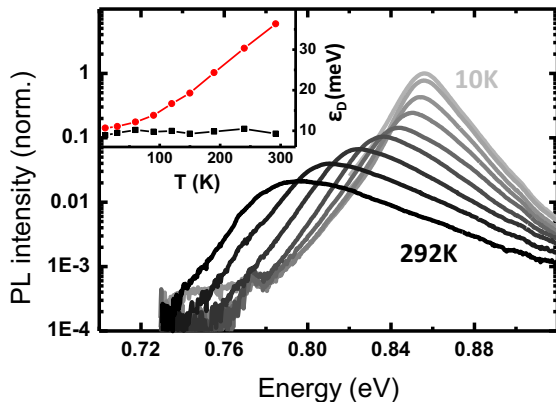


Figure 1: Exemplary PL spectra for the sample grown at 375 °C taken for lattice temperatures from 10 K to room temperature shown from top (grey) to bottom (black). The PL maximum shifts to lower energies with increasing lattice temperature while the peak broadens significantly; no clear s-shape is observed. The inset shows the exponential fit parameters for the lower (black squares) and the higher energy flank (red dots).

To characterize the samples we acquire PL spectra at lattice temperatures of 10, 30, 60, 90, 120, 150, 190, 240 and 292 K (room temperature). A typical data set is shown in Fig. 1 for the sample grown at 375 °C. The peak emission continuously shifts towards lower energies and the lines broaden as the lattice temperature increases. The non-Lorentzian shape of the low energy flank indicates inhomogeneous broadening. To quantify the lineshape of the PL, we now fit the high- and low-energy flanks of the emission with exponential functions  $I_{PL} \sim \exp\{-E/\varepsilon_D\}$ . This function corresponds to the typical density of the band-tail states in a disordered system [26, 27] and is well suited for the description of Boltzmann-shaped high-energy flanks. The fit parameters  $\varepsilon_D$  are now plotted versus lattice temperature for both flanks as shown in the inset of Fig. 1. As expected, the  $\varepsilon_D$  value for the high-energy flank roughly corresponds to  $k_B T$  and thus increases with lattice temperature. However, a constant  $\varepsilon_D$  value of about 10 meV is found for the low-energy flank,

determined by the inhomogeneous broadening associated with disorder. Similar observations are made for the samples grown at temperatures of 325, 350, and 400 °C.

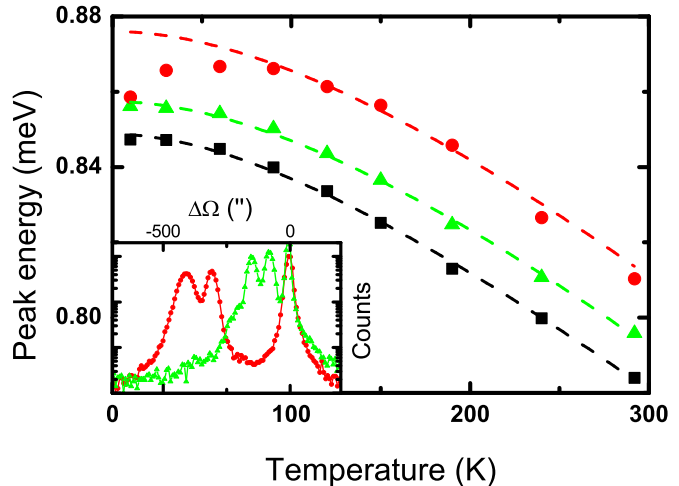


Figure 2: Peak energy over lattice temperature for three different samples. Growth temperatures at 325 °C (black squares), 375 °C (green triangles) and 425 °C (red dots). The dashed lines represent Varshni-like behavior. The inset shows the XRD measurements of the 375 °C and the 425 °C samples in their respective color.

The influence of localization is typically studied by analysing the temperature dependence of the PL maxima [26, 28]. We plot the maxima of the low-power emission spectra versus lattice temperature for the samples grown at 325, 375, and 425 °C in Fig. 2. The data are fit with the standard Varshni model for the temperature dependent band-gap shift, the results are shown as dashed lines. Little to no deviations from Varshni-behavior are found for low and medium growth temperatures up to 400 °C while at high growth temperatures of 425 °C and above, we find clear signatures of the so-called s-shape. The latter is typically observed in disordered systems as a hallmark of carrier hopping between localized states [29, 30]. The s-shape further allows the determination of the characteristic localization scale [28]. Here, the localization energy is estimated to  $\varepsilon_0 \approx 6 \text{ meV} (+ - 1) \text{ meV}$ , roughly corresponding to the value extracted from the low-energy flank.

### 3. Results and discussion

The physical origin of this increased localization is found in XRD measurements shown in the inset of Fig. 2. Here, the angular dependence of the XRD intensity is plotted for the samples grown at 375 °C and 425 °C on a logarithmic scale. The peak indicating the substrate is set to an angle of 0 mrad in both cases while the other two peaks are assigned to the (GaIn)As and the (AlIn)As layers. The 425 °C sample yields a significantly higher deviation of the deposited material stack from the substrate, indicating a differing lattice constant, i.e., higher strain. The localization effects in the heterostructures grown at temperatures

of 425 °C and above are therefore correlated to the lattice mismatch and are thus strain-induced. However, even in this case the deduced disorder parameter is rather small when compared to other material systems [26, 30, 31].

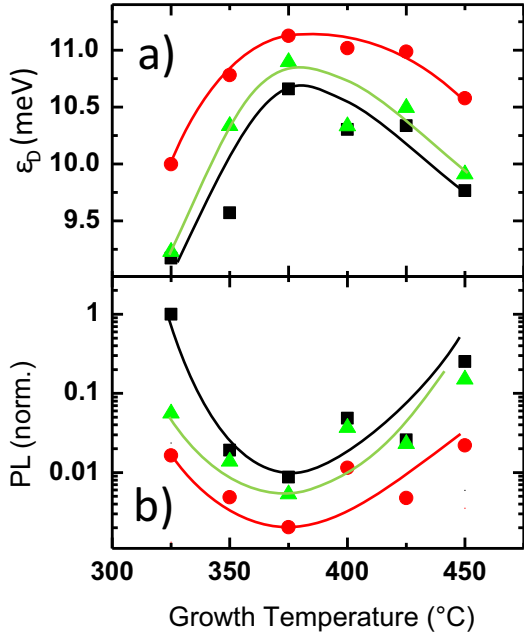


Figure 3: a) Comparison of the exponential factors fitted to the lower energy part of the PL spectra in dependence of the growth temperature. The data represents measurements obtained at 10 K (black squares), 150 K (green triangles) and 292 K (red dots). A significant broadening is observed for the 375 °C sample. b) Normalized PL intensity vs. growth temperature plotted semi-logarithmically showing a significant dip for 375 °C growth temperature. The lines are guides to the eye in both a) and b).

So far, we have dealt with the quantification of localization for each sample and thus growth temperature individually. Now we compare the samples with respect to inhomogeneous broadening and PL intensity to identify the optimal growth conditions for THz antennas. For this purpose, we fit the lower energy part of the measured PL spectra with an exponential curve to quantify the broadening, as done in Fig. 1. The obtained exponential fit parameters are plotted versus growth temperature in Fig. 3a for measurements at lattice temperatures of 10, 150, and 292 K. The broadening increases only slightly with increasing lattice temperature. However, a much more significant increase is found at the intermediate growth temperature of 375 °C. This increased broadening indicates a second, independent mechanism, which influences carrier dynamics, besides strain.

For further analysis we compare the integrated PL intensities as a figure-of-merit for the relative quantum efficiency of the materials. Fast carrier capture is one of the desired material properties for a receiver and typically manifests itself in a low PL emission strength. The PL

intensities are plotted as a function of growth temperature for different lattice temperatures in Fig. 3b. A strong drop in emission intensity at 375 °C is found. Note, that while normalized data is shown, the relative intensities for the different growth temperatures are comparable and the emission at room temperature is quenched by roughly one to two orders of magnitude compared to the 10 K data. Both the PL intensity drop and the increase of the exponential fit factors indicate a significant influence of the growth temperature on the carrier dynamics. Former studies suggest a temperature dependent arsenic cluster formation in the (AlIn)As barrier material, maximizing the effect in the corresponding temperature region [32]. The local internal strain induces the formation of deep level impurities reaching a maximum density at a growth temperature of 375 °C. This leads to non-radiative carrier recombination, as well as to very fast carrier entrapping in the barrier, explaining both increase of the PL linewidth and dramatic intensity decrease.

#### 4. Conclusions

In conclusion, we have investigated a series of (GaIn)As/(AlIn)As QW samples for THz antenna applications at the telecom wavelength of 1.55  $\mu\text{m}$ . Most samples show no disorder-related signatures of carrier hopping between localized states. Only when the growth temperature of the material is increased beyond 425 °C, weak influence of localization with a characteristic energy scale around 6 meV is observed in the PL. Supported by XRD measurements, the origin of this localization is attributed to strain. In addition, optimal growth temperatures with respect to non-radiative recombination are identified to be 375 °C. The corresponding short carrier-lifetimes yield promising perspectives for the desired THz-applications [25].

This work was supported by the Deutsche Forschungsgemeinschaft under grant KO 1520/5-1 and SA/784/4-1.

#### References

- [1] P. H. Siegel, *IEEE T. Microw. Theory.* **50**, 910 (2002).
- [2] M. Tonouchi, *Nat. Photonics* **1**, 97 (2007).
- [3] P. U. Jepsen, D. G. Cooke, and M. Koch, *Laser Photonics Rev.* **5**, 124 (2011).
- [4] P. U. Jepsen, R. H. Jacobsen, and S. R. Keiding, *J. Opt. Soc. Am. B* **13**, 2424 (1996).
- [5] Z. S. Piao, M. Tani, and K. Sakai, *Jpn. J. Appl. Phys.* **1** **39**, 96 (2000).
- [6] M. B. Ketchen, D. R. Grischkowsky, C. C. Chi, I. N. Duling, N. J. Halas, J. M. Halbout, J. A. Kash, and G. P. Li, *Appl. Phys. Lett.* **48**, 751 (1986).
- [7] P. R. Smith, D. H. Auston, and M. C. Nuss, *IEEE J. Quantum Elect.* **24**, 255 (1988).
- [8] H. M. Heiliger, M. Vossebürger, H. G. Roskos, H. Kurz, R. Hey, and K. Ploog, *Appl. Optics* **69**, 2903 (1996).
- [9] S. Matsuura, M. Tani, and K. Sakai, *Appl. Phys. Lett.* **70**, 559 (1996).
- [10] M. Tani, S. Matsuura, K. Sakai, and S. Nakashima, *Appl. Optics* **36**, 7853 (1997).

- [11] K. Ezdi, B. Heinen, C. Jördens, N. Vieweg, N. Krumbholz, R. Wilk, M. Mikulics, and M. Koch, *J. Eur. Opt. Soc-Rapid* **4**, 09001 (2009).
- [12] N. Vieweg, M. Mikulics, M. Scheller, K. Ezdi, R. Wilk, H. W. Hübers, and M. Koch, *Opt. Express* **16**, 19695 (2008).
- [13] K. A. McIntosh, K. B. Nichols, S. Verghese, and E. R. Brown, *Appl. Phys. Lett.* **70**, 354 (1997).
- [14] J. Sigmund, C. Sydlo, H. L. Hartnagel, N. Benker, H. Fuess, F. Rutz, T. Kleine-Ostmann, and M. Koch, *Appl. Phys. Lett.* **87**, 252103 (2005).
- [15] K. Bertulis, A. Krotkus, G. Aleksejenko, V. Pačebutas, R. Adomavičius, G. Molis, and S. Marcinkevičius, *Appl. Phys. Lett.* **88**, 201112 (2006).
- [16] C. Kadow, A. W. Jackson, A. C. Gossard, S. Matsuura, and G. A. Blake, *Appl. Phys. Lett.* **76**, 3510 (2000).
- [17] M. Griebel, J. H. Smet, D. C. Driscoll, J. Kuhl, C. A. Diez, N. Freytag, C. Kadow, A. C. Gossard, and K. Von Klitzing, *Nat. Mater.* **2**, 122 (2003).
- [18] M. Suzuki, and M. Tonouchi, *Appl. Phys. Lett.* **86**, 051104 (2005).
- [19] M. Suzuki, and M. Tonouchi, *Appl. Phys. Lett.* **86**, 163504 (2005).
- [20] N. Chimot, J. Mangeney, L. Joulaud, P. Crozat, H. Bernas, K. Blary, and J. F. Lampin, *Appl. Phys. Lett.* **87**, 193510 (2005).
- [21] N. J. Mangeney, *J. Infrared Millim. Te.* 10.1007/s10762-011-9848-8 (2011).
- [22] R. Wilk, M. Mikulics, K. Biermann, H. Künzel, I. Z. Kozma, R. Holzwarth, B. Sartorius, M. Mei, and M. Koch, THz Time-Domain Spectrometer Based on LT-InGaAs Photoconductive Antennas Exited by a 1.55  $\mu$ m Fibre Laser, in *Conference on Lasers and Electro-Optics 2007 Technical Digest (Optical Society of America, Washington, DC)* (2007).
- [23] N. Krumbholz, C. Jansen, M. Scheller, T. Müller-Wirts, S. Lübbecke, R. Holzwarth, R. Scheunemann, R. Wilk, B. Sartorius, H. Roehle, D. Stanze, J. Beckmann, L. S. von Chrzanowski, U. Ewert, and M. Koch, *Proc. SPIE Int. Soc. Opt. Eng.*, 748504 (2009).
- [24] B. Sartorius, H. Roehle, H. Künzel, J. Bottcher, M. Schlak, D. Stanze, H. Venghaus, and M. Schell, *Opt. Express* **16**, 9565 (2008).
- [25] R. J. B. Dietz, M. Gerhard, D. Stanze, M. Koch, B. Sartorius, and M. Schell, *Opt. Express* **19**, 25911 (2011).
- [26] O. Rubel, M. Galluppi, S. D. Baranovskii, K. Volz, L. Geelhaar, H. Riechert, P. Thomas, and W. Stolz, *J. Appl. Phys.* **98**, 063518 (2005).
- [27] T. Niebling, O. Rubel, W. Heimbrodtt, W. Stolz, S. D. Baranovskii, P. J. Klar, and J. F. Geisz, *J. Phys.-Condens. Mat.* **29**, 015217 (2008).
- [28] S. D. Baranovskii, R. Eichmann, and P. Thomas, *Phys. Rev. B* **58**, 19 (1998).
- [29] P. G. Eliseev, P. Perlin, J. Lee, and M. Osinski, *Appl. Phys. Lett.* **71**, 569 (1997).
- [30] S. Imhof, A. Thränhardt, A. Chernikov, M. Koch, N. Köster, K. Kolata, S. Chatterjee, S. W. Koch, X. F. Lu, S. R. Johnson, D. A. Beaton, T. Tiedje, and O. Rubel, *Appl. Phys. Lett.* **96**, 131115 (2010).
- [31] A. Chernikov, S. Horst, M. Koch, K. Volz, S. Chatterjee, S. W. Koch, T. A. Wassner, B. Laumer, and M. Eickhoff, *Appl. Phys. Lett.* **130**, 2256 (2010).
- [32] A. Hase, H. Künzel, D. R. T. Zahn, and W. Richter, *J. Appl. Phys.* **76**, 2459 (1994).

**Paper IV:**

**Applied Physics Letters, vol. 103, no. 6, p. 061103, 2013**



# 64 $\mu$ W pulsed THz emission from growth optimized InGaAs/InAlAs heterostructures with separated photoconductive and trapping regions

Roman J. B. Dietz,<sup>1,a)</sup> Björn Globisch,<sup>1</sup> Marina Gerhard,<sup>2</sup> Ajanthkrishna Velauthapillai,<sup>2</sup> Dennis Stanze,<sup>1</sup> Helmut Roehle,<sup>1</sup> Martin Koch,<sup>2</sup> Thorsten Göbel<sup>1</sup> and Martin Schell<sup>1</sup>

<sup>1</sup>Fraunhofer Institute for Telecommunications, Heinrich-Hertz-Institute, Einsteinufer 37, 10587 Berlin, Germany

<sup>2</sup>Department of Physics, Philipps-Universität Marburg, Renthof 5, 35032 Marburg, Germany

**Abstract:** We present results on optimized growth temperatures and layer structure design of high mobility photoconductive THz emitters based on molecular beam epitaxy (MBE) grown In<sub>0.53</sub>Ga<sub>0.47</sub>As/In<sub>0.52</sub>Al<sub>0.48</sub>As multilayer heterostructures (MLHS). The photoconductive antennas (PCA) made of these MLHS are evaluated as THz emitters in a THz time domain spectrometer and with a Golay cell. We measured a THz bandwidth in excess of 4 THz and average THz powers of up to 64  $\mu$ W corresponding to an optical power-to-THz power conversion efficiency of up to  $2 \times 10^{-3}$ .

Terahertz time domain spectroscopy (THz TDS) is among the most promising methods for industrial and scientific applications within the rapidly developing and promising field of terahertz technology.<sup>1</sup> In order to find widespread applications, THz TDS systems have to be compact, stable and cost effective. Therefore, various attempts have been made to exploit readily available Er-doped femtosecond fiber lasers at 1550 nm wavelength, of-the-shelf telecom components as well as efforts to design suitable InGaAs based PCAs.<sup>2,3,4,5,6</sup> However, great potential remains for further improvement of InGaAs based PCAs concerning their efficiency and output power. It has recently been shown that InAlAs/InGaAs MLHS grown by MBE at substrate temperatures of approx. 400 °C exhibit a high optical-to-THz conversion efficiency and broadband THz emission.<sup>7</sup> In this growth temperature range InGaAs shows a minimum of defect incorporation with a residual carrier concentration on the order of  $n = 10^{16} \text{ cm}^{-3}$ .<sup>8</sup> On the contrary, InAlAs exhibits increased defect incorporation in this temperature range, associated with alloy clustering due to the interplay of surface kinetics and thermodynamics during the MBE growth process.<sup>9</sup> By exploiting above characteristics it is possible to obtain InAlAs/InGaAs MLHS with low defect density and high mobility InGaAs layers adjacent to high defect InAlAs layers for carrier trapping at the same growth temperature.

For further understanding and optimization of these MLHS for THz generation we investigated the influence of growth temperature and InAlAs layer thickness on the defect incorporation, carrier relaxation dynamics and THz emission characteristics.

Therefore, we performed differential transmission (DT) measurements, THz time domain spectroscopy (TDS) and determined the emitted THz power with a Golay cell. To investigate the influence of the MBE growth temperature two sample series were grown. The first one with substrate temperatures ranging from  $T_g = 325 \text{ °C}$  to  $T_g = 450 \text{ °C}$  in steps of 25 °C with 30 periods of 12 nm InGaAs and 8 nm InAlAs ( $T_g$ -series 1), and the second series ( $T_g$ -Series 2) with temperatures ranging from  $T_g = 350 \text{ °C}$  to  $T_g = 425 \text{ °C}$  in 25 °C steps grown with 100 periods and the same layer thicknesses as in  $T_g$ -Series 1.

In order to probe the carrier relaxation dynamics we performed DT measurements using an Er-doped femtosecond fiber laser with 100 MHz repetition rate and a center wavelength of 1560 nm as excitation source. The pump and probe beam were focused on the sample with a spot size of approx. 15  $\mu\text{m}$  diameter. Their polarizations were kept orthogonal to avoid interference effects between pump and probe beam. The probe power was kept constant at 0.1 mW while the pump power was varied between 1 mW and 16 mW in order to investigate possible trap saturation effects. Fig. 1(a) shows an example of the measured DT signals for a pump power of 16 mW for  $T_g$ -Series 2 as well as the DT measurement of a low temperature (LT) grown ( $T_g = 130 \text{ °C}$ ) and Beryllium doped MLHS sample. This sample will serve as a reference, since LT-grown Be-doped MLHS are known to exhibit very fast carrier trapping and have been demonstrated to be suitable materials for THz PCAs.<sup>6</sup> The LT-grown Be-doped MLHS sample shows a fast mono-exponential decay with a decay time of approx. 550 fs for 1 mW (not shown) and approx.  $\tau_1 = 770 \text{ fs}$  at 16 mW of pump power. This fast decay in the DT signal is governed by electron trapping out of the conduction band (CB) into As<sub>Ga</sub>-anti-site defect related trap states inside the InGaAs layers.<sup>10,11</sup>

<sup>a)</sup> Electronic mail: [Roman.Dietz@hhi.fraunhofer.de](mailto:Roman.Dietz@hhi.fraunhofer.de).  
Tel.: +493031002522

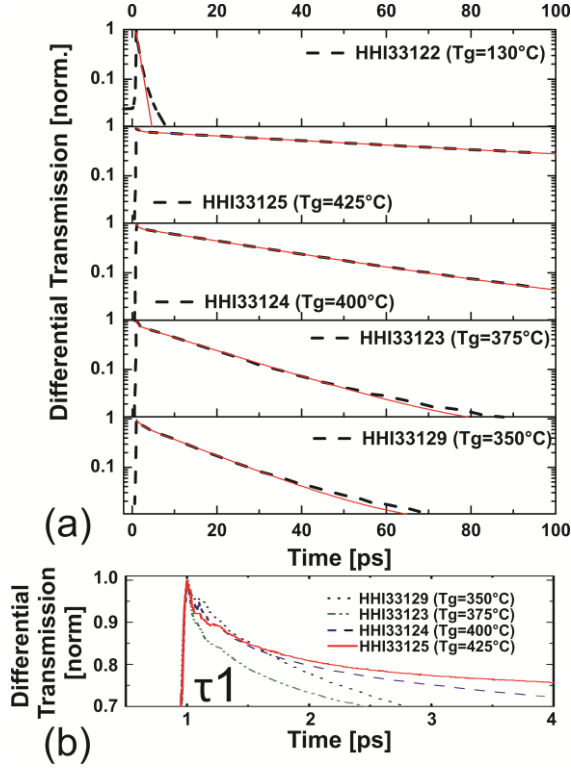


FIG. 1. Example of differential transmission signals measured with 16 mW pump power and at 0.1 mW probe power for samples of  $T_g$ -series 2 and a LT-grown Be-Doped MLHS as reference sample. (b) Example of the short decay component  $\tau_1$  for samples of  $T_g$ -series 2. The thin red solid lines in (a) indicate the fit functions, mono-exponential for the LT-grown reference and bi-exponential for all other samples.

The slight increase of the decay time for increased pump powers, which also leads to a deviation from a purely mono-exponential decay, is assumed to be due to partial trap state filling. Trap state filling occurs because of the relatively slow recombination of electrons within trap states with holes in the valence band (VB), for which the time constant is assumed to be on the order of several tens of picoseconds. The samples of  $T_g$ -Series 1 and 2 on the other hand show two distinct decay components: A relatively small component with a very fast decay time ( $\tau_1$ ) on the order of a few hundred femtoseconds (example in Fig. 1(b)) and a dominating decay component with a relatively slow decay time ( $\tau_2$ ) of several tens of picoseconds. The origin of the short time constant  $\tau_1$  is manifold: Part of the signal is due to the coherent interaction of pump and probe beam that is present despite the thoroughly crossed polarization. Furthermore, some of the absorption recovery is due to the redistribution of the carrier population in the CB via carrier-carrier scattering and phonon emission. Another part is assumed to originate from fast carrier trapping into a small amount of  $As_{Ga}$ -related defects in the InGaAs layers that exist even for these elevated growth temperatures. This contribution becomes slightly more dominant for samples grown at  $T_g \leq 375^\circ\text{C}$ . However, there is no strong correlation of this combined short decay  $\tau_1$

with growth temperature or THz dynamics of the samples. The second time constant  $\tau_2$  is associated with electron trapping into defect states within the InAlAs layer and shows a strong dependence on growth temperature (Fig. 2). Furthermore we see a strong correlation between THz dynamics and  $\tau_2$ , as will be shown later on. As visible in Fig. 2 there is a minimum of  $\tau_2$  for samples grown at  $T_g = 375^\circ\text{C}$  and  $T_g = 350^\circ\text{C}$ , for series 1 and 2, respectively. This indicates the expected maximum of defect incorporation in the InAlAs layers at these growth temperatures. The two growth series seem to be shifted in temperature with respect to each other. This is supposed to originate from a systematic error in the calibration of  $T_g$  that is constant over each growth series. The temperature calibration was performed via the observation of oxide desorption from the InP substrate on the RHEED signal at  $T_g \approx 500^\circ\text{C}$ . We assume an uncertainty of up to  $\Delta T_g = \pm 15^\circ\text{C}$  in this calibration, especially for growth series that were not grown in direct succession as it is the case for  $T_g$ -series 1 and 2. The vertical shift, i.e. the on average faster decay times for samples from  $T_g$ -Series 2, is attributed to the increased number of periods, i.e. 100 versus 30, thus offering a higher total amount of traps.

The fastest decay time with  $\tau_2 = 12.78 \pm 0.04$  ps for sample HHI33129 is still at least one order of magnitude higher than for LT-grown samples. This indicates that the capture cross section and/or the density of the trap states in the InAlAs layers is still small compared to arsenic anti-site related trap states obtained via LT-growth of InGaAs. We see a minor influence of the pump power on the slow decay component  $\tau_2$  tending towards faster relaxation for higher pump powers and for samples with high defect densities, i.e.  $T_g = 350\text{--}400^\circ\text{C}$ . Higher electron excitation densities result, after thermalization with the lattice, in a higher phonon density that in turn increases the carrier trapping probability into defect states within the InAlAs layers.

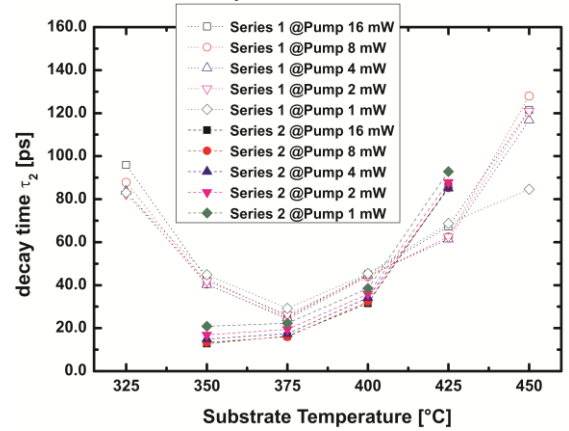


FIG. 2. Fit results for slow decay time constant  $\tau_2$  extracted from bi-exponential fits on DT measurements for  $T_g$ -series 1 (empty symbols) and  $T_g$ -series 2 (filled symbols) at various pump powers.

For a detailed analysis of the carrier capture into trap states associated with defects in the InAlAs barrier, we investigated the influence of the barrier thickness ( $d_B$ ) on carrier relaxation dynamics. Therefore, samples with 2 nm, 4 nm, 8 nm, 16 nm of InAlAs layer thickness were grown while keeping the InGaAs thickness fixed at 12 nm ( $d_B$ -Series). All samples consisted of 100 periods and were grown at substrate temperature of approx.  $T_g = 400^\circ\text{C}$ .

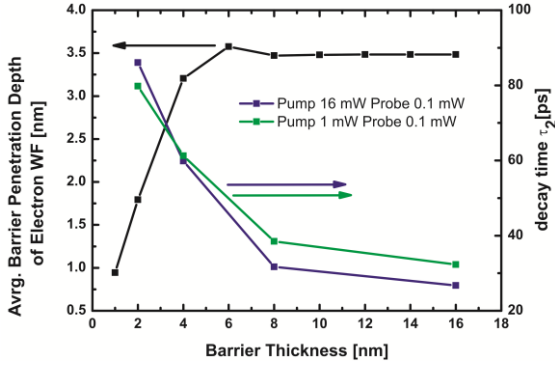


FIG. 3. Fit results for decay time constant  $\tau_2$  from bi-exponential fit on differential transmission signals for samples with different barrier thicknesses (right) and the calculated average penetration depth of the electron wave-function in to the barrier as a function of barrier thickness (left). The lines are guidelines for the eyes.

Additionally, we calculated the electron wave functions (WF) solving one dimensional (1D) Schroedinger equation for a 30 period MLHS. The WF was used to calculate an averaged penetration depth of the WF into the barrier, by summing over all positions within the barrier with non-zero WF values and averaging over all 30 (in 1D) degenerate energy eigenvalues of the first sub-band. Considering a homogeneous trap density within the barrier, this quantity gives a measure of how many defect states are “reachable” by an electron. The results from the DT measurements on the samples and the results from the above mentioned calculation are shown in Fig. 3. As can be seen from the measurements, an increased barrier thickness leads to a faster decay. This is due to the higher absolute number of available and/or reachable trap states in the InAlAs barrier assuming that the trap state density is independent of the barrier thickness and solely dependent on  $T_g$ . The slightly reduced slope of the curve for 1 mW pump supports this assumption if possible trap saturation at higher carrier densities is taken into account.

In order to investigate the THz emission the samples were structured with mesa-type strip-line antennas with gap sizes of  $100\ \mu\text{m}$  and employed as emitters in a THz-TDS setup.<sup>6</sup> The applied receiver was a mesa-type dipole antenna with a gap size of  $10\ \mu\text{m}$  and a contact line separation of  $25\ \mu\text{m}$  made from the LT Be-doped reference sample HHI33122 shown in Fig. 1(a). For the sake of brevity we only show pulse traces and spectra for four of the

samples. The sample parameters and the measured  $\tau_2$  are given in Table I. As visible in Fig. 4(b) the THz-TDS spectrum of the fast LT-sample shows a slight shift of the spectral maximum towards higher frequencies compared to the other samples. However, no significant difference in overall bandwidth or dynamic range is evident. This strongly suggests that the bandwidth of the generated THz radiation is mainly governed by the rising edge of the carrier density, i.e. the exiting laser pulse duration, and not trapping or recombination dynamics. This is in agreement with studies conducted on Si:GaAs by Liu et al.<sup>12</sup>

Sample	$T_g$ [ $^\circ\text{C}$ ]	Be-doping [ $\text{cm}^{-3}$ ]	$d_B$ [nm]	decay time [ps]
33122	130	$3 \times 10^{18}$	8	$0.77 \pm 0.07$ ( $\tau_1$ )
33129	350	no doping	8	$12.78 \pm 0.04$ ( $\tau_2$ )
33124	400	no doping	8	$31.53 \pm 0.04$ ( $\tau_2$ )
33141	400	no doping	2	$86.0 \pm 0.2$ ( $\tau_2$ )

Table I. List of samples measured in THz-TDS Setup with respective growth and DT parameters.

Furthermore, the samples with slower decay time show strongly increased THz emission amplitudes under equal excitation conditions as visible from the THz pulse traces in Fig. 4(a).

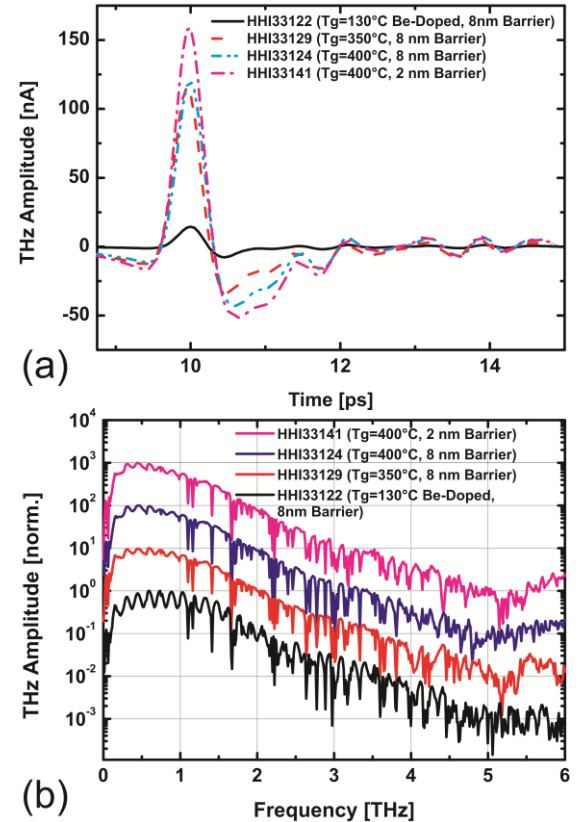


FIG. 4. Pulse traces (a) and corresponding Fourier spectra (b) obtained for  $100\ \mu\text{m}$  strip-line antennas made of samples listed in Table I. The receiver was a  $10\ \mu\text{m}$  dipole antenna made from sample HHI33122. Emitter bias was  $10\ \text{kV/cm}$  and  $16\ \text{mW}$  optical power for both, emitter and receiver. The spectra are shifted vertically for clarity.

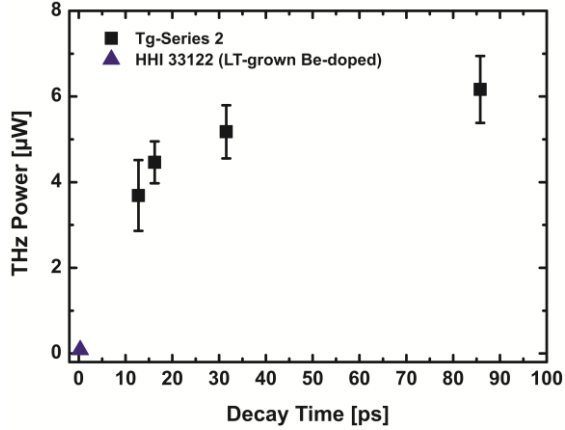


FIG. 5. Measured average THz power obtained from samples of  $T_g$ -Series 2 and the LT-grown Be-doped sample in dependence on the decay time obtained from DT measurements. The bias field strength was 10 kV/cm and 16 mW of optical power were used for all measurements.

In order to quantify the emitted THz power, the coherent receiver, i.e. the dipole antenna, was substituted with a Golay cell. For each sample of  $T_g$ -Series 2 and the  $d_B$ -Series several 100  $\mu\text{m}$  strip-line antennas were tested in this setup to eliminate adjustment errors and possible fluctuations of antenna quality. We observe a clear increase of the average emitted THz power for samples with increasing decay time  $\tau_2$  for both sample series as shown in Figure 5 and 6.

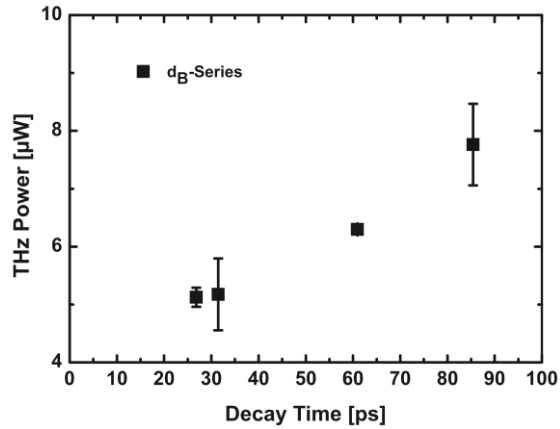


FIG. 6. Measured average THz power obtained from samples of the  $d_B$ -Series in dependence on the decay time obtained from DT measurements. The bias field strength was 10 kV/cm and 16 mW of optical power were used for all measurements.

Considering that the measured decay time of all samples (except HHI33122) is long compared to the time scale on which the THz radiation is produced, i.e.  $< 2$  ps, this result is counterintuitive. However, this correlation does not necessarily mean that the underlying physical process is carrier capture. The decay time  $\tau_2$  can be considered an adequate measure of the trap state density in the InAlAs layers. Considering this, the decrease in THz emission can be explained in terms of an elastic scattering process of electrons that is trap density related and hence limiting the carrier mobility. There are two possible mechanisms for this scattering process. One is scattering due to

surface roughness at the interfaces between InAlAs and InGaAs layers that is increased for increased clustering in the InAlAs layers. However, in case of the  $d_B$ -series this explanation would only be valid if surface roughness is strongly dependent on the InAlAs layer thickness which we assume is not the case. More plausible is elastic scattering directly at the defects within the InAlAs barrier. Other than a capture process, an elastic scattering process does not require the emission of phonons for the sake of energy conservation. An elastic scattering process is thus assumed to have a much higher probability than a capture process at the same defect state.

We like to point out, that complete removal of the InAlAs layers, i.e. bulk InGaAs, increases dark conductivity by several orders of magnitude due to the relatively high residual carrier concentration of InGaAs of  $n \approx 10^{16} \text{ cm}^{-3}$  and thus would render the application of sufficiently strong bias fields impossible. This is also the case for growth temperatures of  $T_g \geq 450^\circ\text{C}$  where the reduced density in the InAlAs barriers does not suffice to obtain an overall semi-insulating sample.

The maximum applicable field strength for 100  $\mu\text{m}$  strip-line antennas reached up to 15 kV/cm. The dependence of the THz power on the optical excitation power emitted by antennas from samples HHI33122 and 33141 are given in Fig. 7. At 32 mW optical excitation we measured an average THz output power for the antenna from HHI33141 of 64  $\mu\text{W}$  corresponding to an optical power-to-THz power conversion efficiency of  $2 \times 10^{-3}$ .

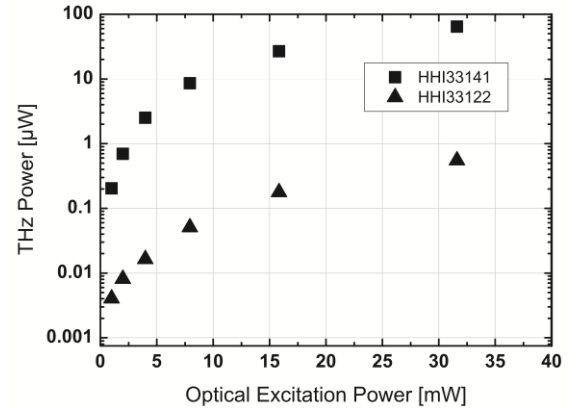


FIG. 7. Emitted THz power of a 100  $\mu\text{m}$  strip-line antenna from sample HHI33141 and HHI33122 in dependence on the optical excitation power at a bias field of 15 kV/cm.

In conclusion we have shown that the carrier relaxation shows a (local) minimum at a growth temperature of around  $T_g = 350\text{-}375^\circ\text{C}$ . Additionally the carrier relaxation time decreases when the barrier thickness is decreased. However, the emitted THz bandwidth has been shown to be mostly independent on the carrier relaxation time in the semiconductor and is hence governed by the excitation laser pulse width. Furthermore, the THz emission efficiency is reduced for increasing trap densities, which is associated with trap related

elastic carrier scattering. For optimal growth parameters of the semiconductor material we measured 64  $\mu\text{W}$  of emitted average THz power for 32 mW of optical excitation. This corresponds to an achieved optical-to-THz conversion efficiency of  $2 \times 10^{-3}$  which is two orders of magnitude higher than values accessible with LT-grown Be-doped InGaAs/InAlAs MLHS and the highest value for InGaAs based emitters reported so far. This work was funded by the German Research Foundation (DFG).

<sup>1</sup> P.U. Jepsen, D.G. Cooke, and M. Koch, *Laser & Photonics Reviews* **5**, 124 (2011).

<sup>2</sup> M. Suzuki and M. Tonouchi, *Applied Physics Letters* **86**, 051104 (2005).

<sup>3</sup> B. Sartorius, H. Roehle, H. Künzel, J. Böttcher, M. Schlak, D. Stanze, H. Venghaus, and M. Schell, *Optics Express* **16**, 9565 (2008).

<sup>4</sup> A. Schwagmann, Z.-Y. Zhao, F. Ospald, H. Lu, D.C. Driscoll, M.P. Hanson, a. C. Gossard, and J.H. Smet, *Applied Physics Letters* **96**, 141108 (2010).

<sup>5</sup> C.D. Wood, O. Hatem, J.E. Cunningham, E.H. Linfield, a. G. Davies, P.J. Cannard, M.J. Robertson, and D.G. Moodie, *Applied Physics Letters* **96**, 194104 (2010).

<sup>6</sup> H. Roehle, R.J.B. Dietz, H.J. Hensel, J. Böttcher, H. Künzel, D. Stanze, M. Schell, and B. Sartorius, *Optics Express* **18**, 2296 (2010).

<sup>7</sup> R.J.B. Dietz, M. Gerhard, D. Stanze, M. Koch, B. Sartorius, and M. Schell, *Optics Express* **19**, 122 (2011).

<sup>8</sup> H. Künzel, J. Böttcher, R. Gibis, and G. Urmann, *Applied Physics Letters* **61**, 1347 (1992).

<sup>9</sup> J.E. Oh, P.K. Bhattacharya, and Y.C. Chen, *Journal of Electronic Materials* **19**, (1990).

<sup>10</sup> K. Biermann, D. Nickel, K. Reimann, M. Woerner, T. Elsaesser, and H. Künzel, *Applied Physics Letters* **80**, 1936 (2002).

<sup>11</sup> B. Grandidier, H. Chen, R.M. Feenstra, D.T. McInturff, P.W. Juodawlkis, and S.E. Ralph, *Applied Physics Letters* **74**, 1439 (1999).

<sup>12</sup> T.-A. Liu, M. Tani, and C.-L. Pan, *Journal of Applied Physics* **93**, 2996 (2003).



**Paper V:**

**Applied Physics Letters, vol. 104, no. 17, p. 172103, 2014**



# 64 $\mu$ W pulsed THz emission from growth optimized InGaAs/InAlAs heterostructures with separated photoconductive and trapping regions

Roman J. B. Dietz,<sup>1,a)</sup> Björn Globisch,<sup>1</sup> Marina Gerhard,<sup>2</sup> Ajanthkrishna Velauthapillai,<sup>2</sup> Dennis Stanze,<sup>1</sup> Helmut Roehle,<sup>1</sup> Martin Koch,<sup>2</sup> Thorsten Göbel<sup>1</sup> and Martin Schell<sup>1</sup>

<sup>1</sup>Fraunhofer Institute for Telecommunications, Heinrich-Hertz-Institute, Einsteinufer 37, 10587 Berlin, Germany

<sup>2</sup>Department of Physics, Philipps-Universität Marburg, Renthof 5, 35032 Marburg, Germany

**Abstract:** We present results on optimized growth temperatures and layer structure design of high mobility photoconductive THz emitters based on molecular beam epitaxy (MBE) grown In<sub>0.53</sub>Ga<sub>0.47</sub>As/In<sub>0.52</sub>Al<sub>0.48</sub>As multilayer heterostructures (MLHS). The photoconductive antennas (PCA) made of these MLHS are evaluated as THz emitters in a THz time domain spectrometer and with a Golay cell. We measured a THz bandwidth in excess of 4 THz and average THz powers of up to 64  $\mu$ W corresponding to an optical power-to-THz power conversion efficiency of up to  $2 \times 10^{-3}$ .

Terahertz time domain spectroscopy (THz TDS) is among the most promising methods for industrial and scientific applications within the rapidly developing and promising field of terahertz technology.<sup>1</sup> In order to find widespread applications, THz TDS systems have to be compact, stable and cost effective. Therefore, various attempts have been made to exploit readily available Er-doped femtosecond fiber lasers at 1550 nm wavelength, of-the-shelf telecom components as well as efforts to design suitable InGaAs based PCAs.<sup>2,3,4,5,6</sup> However, great potential remains for further improvement of InGaAs based PCAs concerning their efficiency and output power. It has recently been shown that InAlAs/InGaAs MLHS grown by MBE at substrate temperatures of approx. 400 °C exhibit a high optical-to-THz conversion efficiency and broadband THz emission.<sup>7</sup> In this growth temperature range InGaAs shows a minimum of defect incorporation with a residual carrier concentration on the order of  $n = 10^{16} \text{ cm}^{-3}$ .<sup>8</sup> On the contrary, InAlAs exhibits increased defect incorporation in this temperature range, associated with alloy clustering due to the interplay of surface kinetics and thermodynamics during the MBE growth process.<sup>9</sup> By exploiting above characteristics it is possible to obtain InAlAs/InGaAs MLHS with low defect density and high mobility InGaAs layers adjacent to high defect InAlAs layers for carrier trapping at the same growth temperature.

For further understanding and optimization of these MLHS for THz generation we investigated the influence of growth temperature and InAlAs layer thickness on the defect incorporation, carrier relaxation dynamics and THz emission characteristics.

Therefore, we performed differential transmission (DT) measurements, THz time domain spectroscopy (TDS) and determined the emitted THz power with a Golay cell. To investigate the influence of the MBE growth temperature two sample series were grown. The first one with substrate temperatures ranging from  $T_g = 325 \text{ °C}$  to  $T_g = 450 \text{ °C}$  in steps of 25 °C with 30 periods of 12 nm InGaAs and 8 nm InAlAs ( $T_g$ -series 1), and the second series ( $T_g$ -Series 2) with temperatures ranging from  $T_g = 350 \text{ °C}$  to  $T_g = 425 \text{ °C}$  in 25 °C steps grown with 100 periods and the same layer thicknesses as in  $T_g$ -Series 1.

In order to probe the carrier relaxation dynamics we performed DT measurements using an Er-doped femtosecond fiber laser with 100 MHz repetition rate and a center wavelength of 1560 nm as excitation source. The pump and probe beam were focused on the sample with a spot size of approx. 15  $\mu\text{m}$  diameter. Their polarizations were kept orthogonal to avoid interference effects between pump and probe beam. The probe power was kept constant at 0.1 mW while the pump power was varied between 1 mW and 16 mW in order to investigate possible trap saturation effects. Fig. 1(a) shows an example of the measured DT signals for a pump power of 16 mW for  $T_g$ -Series 2 as well as the DT measurement of a low temperature (LT) grown ( $T_g = 130 \text{ °C}$ ) and Beryllium doped MLHS sample. This sample will serve as a reference, since LT-grown Be-doped MLHS are known to exhibit very fast carrier trapping and have been demonstrated to be suitable materials for THz PCAs.<sup>6</sup> The LT-grown Be-doped MLHS sample shows a fast mono-exponential decay with a decay time of approx. 550 fs for 1 mW (not shown) and approx.  $\tau_1 = 770 \text{ fs}$  at 16 mW of pump power. This fast decay in the DT signal is governed by electron trapping out of the conduction band (CB) into As<sub>Ga</sub>-anti-site defect related trap states inside the InGaAs layers.<sup>10,11</sup>

<sup>a)</sup> Electronic mail: [Roman.Dietz@hhi.fraunhofer.de](mailto:Roman.Dietz@hhi.fraunhofer.de).  
Tel.: +493031002522

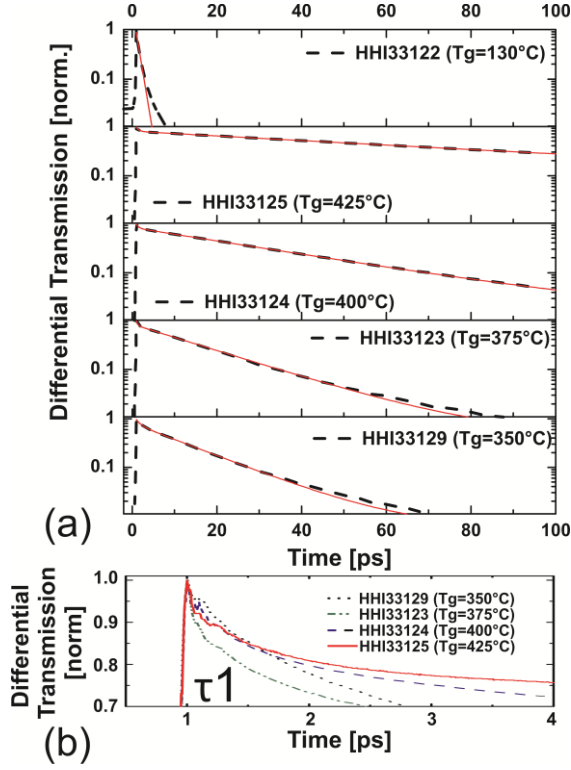


FIG. 1. Example of differential transmission signals measured with 16 mW pump power and at 0.1 mW probe power for samples of  $T_g$ -series 2 and a LT-grown Be-Doped MLHS as reference sample. (b) Example of the short decay component  $\tau_1$  for samples of  $T_g$ -series 2. The thin red solid lines in (a) indicate the fit functions, mono-exponential for the LT-grown reference and bi-exponential for all other samples.

The slight increase of the decay time for increased pump powers, which also leads to a deviation from a purely mono-exponential decay, is assumed to be due to partial trap state filling. Trap state filling occurs because of the relatively slow recombination of electrons within trap states with holes in the valence band (VB), for which the time constant is assumed to be on the order of several tens of picoseconds. The samples of  $T_g$ -Series 1 and 2 on the other hand show two distinct decay components: A relatively small component with a very fast decay time ( $\tau_1$ ) on the order of a few hundred femtoseconds (example in Fig. 1(b)) and a dominating decay component with a relatively slow decay time ( $\tau_2$ ) of several tens of picoseconds. The origin of the short time constant  $\tau_1$  is manifold: Part of the signal is due to the coherent interaction of pump and probe beam that is present despite the thoroughly crossed polarization. Furthermore, some of the absorption recovery is due to the redistribution of the carrier population in the CB via carrier-carrier scattering and phonon emission. Another part is assumed to originate from fast carrier trapping into a small amount of  $As_{Ga}$ -related defects in the InGaAs layers that exist even for these elevated growth temperatures. This contribution becomes slightly more dominant for samples grown at  $T_g \leq 375^\circ\text{C}$ . However, there is no strong correlation of this combined short decay  $\tau_1$

with growth temperature or THz dynamics of the samples. The second time constant  $\tau_2$  is associated with electron trapping into defect states within the InAlAs layer and shows a strong dependence on growth temperature (Fig. 2). Furthermore we see a strong correlation between THz dynamics and  $\tau_2$ , as will be shown later on. As visible in Fig. 2 there is a minimum of  $\tau_2$  for samples grown at  $T_g = 375^\circ\text{C}$  and  $T_g = 350^\circ\text{C}$ , for series 1 and 2, respectively. This indicates the expected maximum of defect incorporation in the InAlAs layers at these growth temperatures. The two growth series seem to be shifted in temperature with respect to each other. This is supposed to originate from a systematic error in the calibration of  $T_g$  that is constant over each growth series. The temperature calibration was performed via the observation of oxide desorption from the InP substrate on the RHEED signal at  $T_g \approx 500^\circ\text{C}$ . We assume an uncertainty of up to  $\Delta T_g = \pm 15^\circ\text{C}$  in this calibration, especially for growth series that were not grown in direct succession as it is the case for  $T_g$ -series 1 and 2. The vertical shift, i.e. the on average faster decay times for samples from  $T_g$ -Series 2, is attributed to the increased number of periods, i.e. 100 versus 30, thus offering a higher total amount of traps.

The fastest decay time with  $\tau_2 = 12.78 \pm 0.04$  ps for sample HHI33129 is still at least one order of magnitude higher than for LT-grown samples. This indicates that the capture cross section and/or the density of the trap states in the InAlAs layers is still small compared to arsenic anti-site related trap states obtained via LT-growth of InGaAs. We see a minor influence of the pump power on the slow decay component  $\tau_2$  tending towards faster relaxation for higher pump powers and for samples with high defect densities, i.e.  $T_g = 350\text{--}400^\circ\text{C}$ . Higher electron excitation densities result, after thermalization with the lattice, in a higher phonon density that in turn increases the carrier trapping probability into defect states within the InAlAs layers.

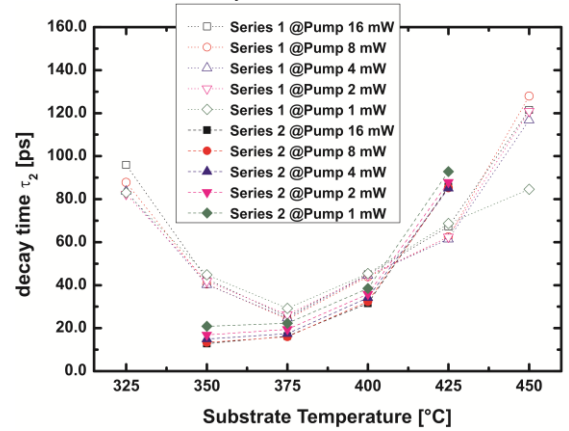


FIG. 2. Fit results for slow decay time constant  $\tau_2$  extracted from bi-exponential fits on DT measurements for  $T_g$ -series 1 (empty symbols) and  $T_g$ -series 2 (filled symbols) at various pump powers.

For a detailed analysis of the carrier capture into trap states associated with defects in the InAlAs barrier, we investigated the influence of the barrier thickness ( $d_B$ ) on carrier relaxation dynamics. Therefore, samples with 2 nm, 4 nm, 8 nm, 16 nm of InAlAs layer thickness were grown while keeping the InGaAs thickness fixed at 12 nm ( $d_B$ -Series). All samples consisted of 100 periods and were grown at substrate temperature of approx.  $T_g = 400^\circ\text{C}$ .

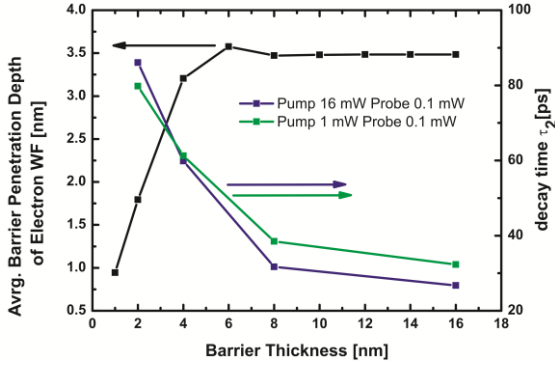


FIG. 3. Fit results for decay time constant  $\tau_2$  from bi-exponential fit on differential transmission signals for samples with different barrier thicknesses (right) and the calculated average penetration depth of the electron wave-function in to the barrier as a function of barrier thickness (left). The lines are guidelines for the eyes.

Additionally, we calculated the electron wave functions (WF) solving one dimensional (1D) Schroedinger equation for a 30 period MLHS. The WF was used to calculate an averaged penetration depth of the WF into the barrier, by summing over all positions within the barrier with non-zero WF values and averaging over all 30 (in 1D) degenerate energy eigenvalues of the first sub-band. Considering a homogeneous trap density within the barrier, this quantity gives a measure of how many defect states are “reachable” by an electron. The results from the DT measurements on the samples and the results from the above mentioned calculation are shown in Fig. 3. As can be seen from the measurements, an increased barrier thickness leads to a faster decay. This is due to the higher absolute number of available and/or reachable trap states in the InAlAs barrier assuming that the trap state density is independent of the barrier thickness and solely dependent on  $T_g$ . The slightly reduced slope of the curve for 1 mW pump supports this assumption if possible trap saturation at higher carrier densities is taken into account.

In order to investigate the THz emission the samples were structured with mesa-type strip-line antennas with gap sizes of  $100\ \mu\text{m}$  and employed as emitters in a THz-TDS setup.<sup>6</sup> The applied receiver was a mesa-type dipole antenna with a gap size of  $10\ \mu\text{m}$  and a contact line separation of  $25\ \mu\text{m}$  made from the LT Be-doped reference sample HHI33122 shown in Fig. 1(a). For the sake of brevity we only show pulse traces and spectra for four of the

samples. The sample parameters and the measured  $\tau_2$  are given in Table I. As visible in Fig. 4(b) the THz-TDS spectrum of the fast LT-sample shows a slight shift of the spectral maximum towards higher frequencies compared to the other samples. However, no significant difference in overall bandwidth or dynamic range is evident. This strongly suggests that the bandwidth of the generated THz radiation is mainly governed by the rising edge of the carrier density, i.e. the exiting laser pulse duration, and not trapping or recombination dynamics. This is in agreement with studies conducted on Si:GaAs by Liu et al.<sup>12</sup>

Sample	$T_g$ [ $^\circ\text{C}$ ]	Be-doping [ $\text{cm}^{-3}$ ]	$d_B$ [nm]	decay time [ps]
33122	130	$3 \times 10^{18}$	8	$0.77 \pm 0.07$ ( $\tau_1$ )
33129	350	no doping	8	$12.78 \pm 0.04$ ( $\tau_2$ )
33124	400	no doping	8	$31.53 \pm 0.04$ ( $\tau_2$ )
33141	400	no doping	2	$86.0 \pm 0.2$ ( $\tau_2$ )

Table I. List of samples measured in THz-TDS Setup with respective growth and DT parameters.

Furthermore, the samples with slower decay time show strongly increased THz emission amplitudes under equal excitation conditions as visible from the THz pulse traces in Fig. 4(a).

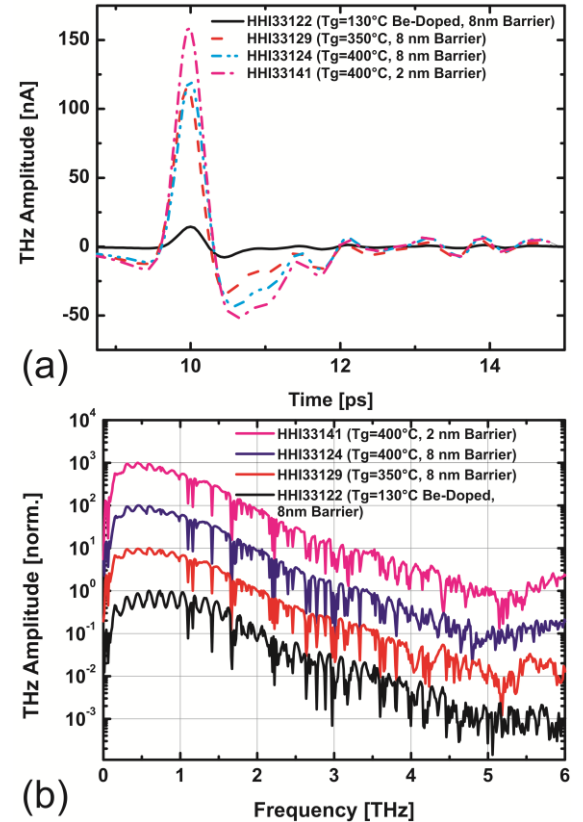


FIG. 4. Pulse traces (a) and corresponding Fourier spectra (b) obtained for  $100\ \mu\text{m}$  strip-line antennas made of samples listed in Table I. The receiver was a  $10\ \mu\text{m}$  dipole antenna made from sample HHI33122. Emitter bias was  $10\ \text{kV/cm}$  and  $16\ \text{mW}$  optical power for both, emitter and receiver. The spectra are shifted vertically for clarity.

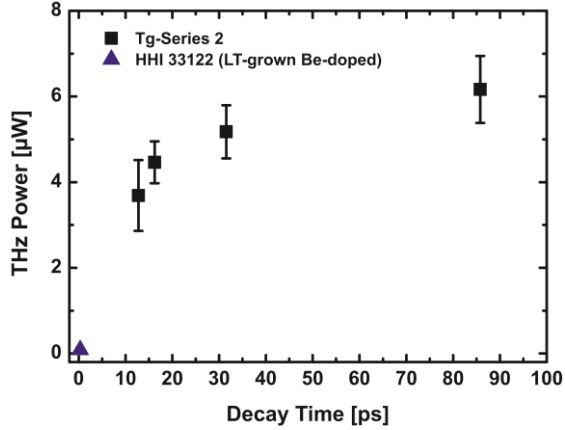


FIG. 5. Measured average THz power obtained from samples of  $T_g$ -Series 2 and the LT-grown Be-doped sample in dependence on the decay time obtained from DT measurements. The bias field strength was 10 kV/cm and 16 mW of optical power were used for all measurements.

In order to quantify the emitted THz power, the coherent receiver, i.e. the dipole antenna, was substituted with a Golay cell. For each sample of  $T_g$ -Series 2 and the  $d_B$ -Series several 100  $\mu\text{m}$  strip-line antennas were tested in this setup to eliminate adjustment errors and possible fluctuations of antenna quality. We observe a clear increase of the average emitted THz power for samples with increasing decay time  $\tau_2$  for both sample series as shown in Figure 5 and 6.

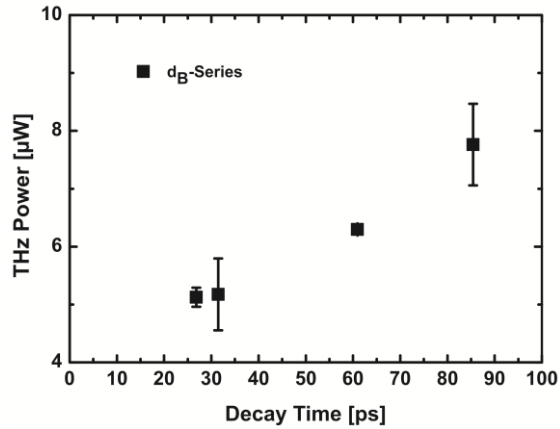


FIG. 6. Measured average THz power obtained from samples of the  $d_B$ -Series in dependence on the decay time obtained from DT measurements. The bias field strength was 10 kV/cm and 16 mW of optical power were used for all measurements.

Considering that the measured decay time of all samples (except HHI33122) is long compared to the time scale on which the THz radiation is produced, i.e.  $< 2$  ps, this result is counterintuitive. However, this correlation does not necessarily mean that the underlying physical process is carrier capture. The decay time  $\tau_2$  can be considered an adequate measure of the trap state density in the InAlAs layers. Considering this, the decrease in THz emission can be explained in terms of an elastic scattering process of electrons that is trap density related and hence limiting the carrier mobility. There are two possible mechanisms for this scattering process. One is scattering due to

surface roughness at the interfaces between InAlAs and InGaAs layers that is increased for increased clustering in the InAlAs layers. However, in case of the  $d_B$ -series this explanation would only be valid if surface roughness is strongly dependent on the InAlAs layer thickness which we assume is not the case. More plausible is elastic scattering directly at the defects within the InAlAs barrier. Other than a capture process, an elastic scattering process does not require the emission of phonons for the sake of energy conservation. An elastic scattering process is thus assumed to have a much higher probability than a capture process at the same defect state.

We like to point out, that complete removal of the InAlAs layers, i.e. bulk InGaAs, increases dark conductivity by several orders of magnitude due to the relatively high residual carrier concentration of InGaAs of  $n \approx 10^{16} \text{ cm}^{-3}$  and thus would render the application of sufficiently strong bias fields impossible. This is also the case for growth temperatures of  $T_g \geq 450^\circ\text{C}$  where the reduced density in the InAlAs barriers does not suffice to obtain an overall semi-insulating sample.

The maximum applicable field strength for 100  $\mu\text{m}$  strip-line antennas reached up to 15 kV/cm. The dependence of the THz power on the optical excitation power emitted by antennas from samples HHI33122 and 33141 are given in Fig. 7. At 32 mW optical excitation we measured an average THz output power for the antenna from HHI33141 of 64  $\mu\text{W}$  corresponding to an optical power-to-THz power conversion efficiency of  $2 \times 10^{-3}$ .

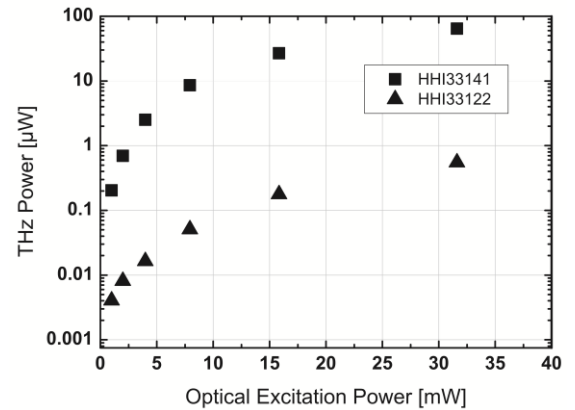


FIG. 7. Emitted THz power of a 100  $\mu\text{m}$  strip-line antenna from sample HHI33141 and HHI33122 in dependence on the optical excitation power at a bias field of 15 kV/cm.

In conclusion we have shown that the carrier relaxation shows a (local) minimum at a growth temperature of around  $T_g = 350\text{-}375^\circ\text{C}$ . Additionally the carrier relaxation time decreases when the barrier thickness is decreased. However, the emitted THz bandwidth has been shown to be mostly independent on the carrier relaxation time in the semiconductor and is hence governed by the excitation laser pulse width. Furthermore, the THz emission efficiency is reduced for increasing trap densities, which is associated with trap related

elastic carrier scattering. For optimal growth parameters of the semiconductor material we measured 64  $\mu\text{W}$  of emitted average THz power for 32 mW of optical excitation. This corresponds to an achieved optical-to-THz conversion efficiency of  $2 \times 10^{-3}$  which is two orders of magnitude higher than values accessible with LT-grown Be-doped InGaAs/InAlAs MLHS and the highest value for InGaAs based emitters reported so far. This work was funded by the German Research Foundation (DFG).

<sup>1</sup> P.U. Jepsen, D.G. Cooke, and M. Koch, *Laser & Photonics Reviews* **5**, 124 (2011).

<sup>2</sup> M. Suzuki and M. Tonouchi, *Applied Physics Letters* **86**, 051104 (2005).

<sup>3</sup> B. Sartorius, H. Roehle, H. Künzel, J. Böttcher, M. Schlak, D. Stanze, H. Venghaus, and M. Schell, *Optics Express* **16**, 9565 (2008).

<sup>4</sup> A. Schwagmann, Z.-Y. Zhao, F. Ospald, H. Lu, D.C. Driscoll, M.P. Hanson, a. C. Gossard, and J.H. Smet, *Applied Physics Letters* **96**, 141108 (2010).

<sup>5</sup> C.D. Wood, O. Hatem, J.E. Cunningham, E.H. Linfield, a. G. Davies, P.J. Cannard, M.J. Robertson, and D.G. Moodie, *Applied Physics Letters* **96**, 194104 (2010).

<sup>6</sup> H. Roehle, R.J.B. Dietz, H.J. Hensel, J. Böttcher, H. Künzel, D. Stanze, M. Schell, and B. Sartorius, *Optics Express* **18**, 2296 (2010).

<sup>7</sup> R.J.B. Dietz, M. Gerhard, D. Stanze, M. Koch, B. Sartorius, and M. Schell, *Optics Express* **19**, 122 (2011).

<sup>8</sup> H. Künzel, J. Böttcher, R. Gibis, and G. Urmann, *Applied Physics Letters* **61**, 1347 (1992).

<sup>9</sup> J.E. Oh, P.K. Bhattacharya, and Y.C. Chen, *Journal of Electronic Materials* **19**, (1990).

<sup>10</sup> K. Biermann, D. Nickel, K. Reimann, M. Woerner, T. Elsaesser, and H. Künzel, *Applied Physics Letters* **80**, 1936 (2002).

<sup>11</sup> B. Grandidier, H. Chen, R.M. Feenstra, D.T. McInturff, P.W. Juodawlkis, and S.E. Ralph, *Applied Physics Letters* **74**, 1439 (1999).

<sup>12</sup> T.-A. Liu, M. Tani, and C.-L. Pan, *Journal of Applied Physics* **93**, 2996 (2003).

## APL Supplementary Material

### Carrier dynamics in Beryllium doped low-temperature-grown InGaAs/InAlAs

B. Globisch, R. J. B. Dietz, D. Stanze, T. Göbel, M. Schell

*Fraunhofer Institute for Telecommunications, Heinrich Hertz Institute, Einsteinufer 37, 10587 Berlin, Germany*

This supplementary material contains the derivation of the analytical equations for the carrier population in the CB in the cases of trap saturation and partial trap filling, i.e. the derivation of Eq. (6) and Eq. (7) of the main article are described.

First, we account for carrier conservation in Eqs. (3). Electrons in the CB and electrons trapped by ionized arsenic antisites equal holes in the VB and trapped holes in ionized Be dopants. Hence, the following equation holds for all times  $t$ :

$$n(t) + n_T(t) = n_{Be}(t) + h(t) \quad (\text{A1})$$

Additionally, we introduce dimensionless variables in order to simplify the subsequent analysis:

$$N = n / N_{As}^+; \quad N_T = n_T / N_{As}^+; \quad N_{Be} = n_{Be} / N_{As}^+; \quad t' = t / \tau_e \quad (\text{A2})$$

Here, carrier densities are normalized to the number of ionized antisites  $N_{As}^+$  and time is measured in units of the electron trapping time  $\tau_e$ . Inserting Eq. (A1) and Eq. (A2) into Eqs. (3) of the main article yields:

$$\frac{dN}{dt'} = \tilde{G}(t', N) - N(1 - N_T) \quad (\text{A3a})$$

$$\frac{dN_T}{dt'} = N(1 - N_T) - \tilde{B}_R \left( \frac{N_{As}}{N_{As}^+} - 1 + N_T \right) N_{Be} \quad (\text{A3b})$$

$$\frac{dN_{Be}}{dt'} = \frac{\tau_e}{\tau_h} (N + N_T - N_{Be}) - \tilde{B}_R \left( \frac{N_{As}}{N_{As}^+} - 1 + N_T \right) N_{Be}. \quad (\text{A3c})$$

Here,  $\tilde{G}(t', N)$  and  $\tilde{B}_R = B_R \tau_c N_{As}^+$  denote the normalized generation rate and the normalized recombination rate. The dynamic equation for the valence band holes has been eliminated with Eq. (A1). Subsequently, Eqs. (A3a)-(A3c) are expanded under trap saturation conditions and partial trap filling, respectively.

#### Trap saturation

The condition of complete electron trap saturation means that the each arsenic antisite defect is occupied by an electron from the CB. Saturation occurs when the density of excited electrons outnumbers the density of trapping states. After the initial trap filling process  $N_T$  is clamped to its maximum value  $N_T \approx 1$  since electron trapping is much faster than electron recombination. Taking this situation as the starting point of the dynamic development each recombined electron is directly replaced by another free electron from the CB (detailed balance). Hence, the two terms on the RHS of Eq. (A3b) are equal as long as the saturation condition holds true. The same assumption holds true for holes captured by negatively charged Be dopants in Eq. (A3c). In order to simplify the terms in Eqs. (A3) we consider small deviations from this temporary equilibrium and write:

$$N_T(t') \approx 1 - \varepsilon u(t'), \quad (\text{A4a})$$

$$N_{Be}(t') \approx 1 - \varepsilon v(t'). \quad (\text{A4b})$$

Here,  $\varepsilon$  is a small parameter and  $u(t')$ ,  $v(t')$  denote the time dependent deviations from the saturation condition. Inserting Eq. (A4a) and Eq. (A4b) into Eqs. (A3) and neglecting terms in  $\varepsilon^2$  yields:

$$\frac{dN}{dt'} = \tilde{G}(t', N) - \varepsilon N u, \quad (\text{A5a})$$

$$\varepsilon \frac{du}{dt'} = \varepsilon N u - \varepsilon \tilde{B}_R \left( \frac{N_{As}}{N_{As}^+} v - u \right) - \tilde{B}_R \frac{N_{As}}{N_{As}^+}, \quad (\text{A5b})$$

$$\varepsilon \frac{dv}{dt'} = \frac{\tau_e}{\tau_h} \varepsilon N v - \varepsilon \tilde{B}_R \left( \frac{N_{As}}{N_{As}^+} v - u \right) - \tilde{B}_R \frac{N_{As}}{N_{As}^+}. \quad (\text{A5c})$$

Now, Eq. (A5b) and Eq. (A5c) can be solved by the detailed balance relation mentioned above:

$$0 = \varepsilon N u - \varepsilon \tilde{B}_R \left( \frac{N_{As}}{N_{As}^+} v - u \right) - \tilde{B}_R \frac{N_{As}}{N_{As}^+}, \quad (\text{A6a})$$

$$0 = \frac{\tau_e}{\tau_h} \varepsilon N v - \varepsilon \tilde{B}_R \left( \frac{N_{As}}{N_{As}^+} v - u \right) - \tilde{B}_R \frac{N_{As}}{N_{As}^+}. \quad (\text{A6b})$$

Solving for  $u$  and  $v$  and inserting the results in Eq. (A5a) leads to the expression:

$$\frac{dN}{dt'} = -N \frac{\tilde{B}_R \frac{N_{As}}{N_{As}^+} \frac{\tau_e}{\tau_h}}{N \frac{\tau_e}{\tau_h} + \tilde{B}_R \left( \frac{N_{As}}{N_{As}^+} - 1 \right)}. \quad (\text{A7})$$

In order to simplify Eq. (A7) we solve Eq. (A3b) for  $N_T = N_{Be} = 1$ . In this case one neglects the refilling of traps with conduction band electrons and simply accounts for carrier recombination.

$$N_T^{sat}(t') = 1 - \tilde{B}_R \frac{N_{As}}{N_{As}^+} t'. \quad (\text{A8})$$

Eq. (A8) describes a linear decay of the trapping centers with  $\tilde{B}_R N_{As} / N_{As}^+$ . Since carrier capture is assumed to be much faster than carrier recombination the condition:

$$\tilde{B}_R \frac{N_{As}}{N_{As}^+} \ll 1 \quad (\text{A9})$$

holds true. Using this relation in Eq. (A7) we obtain:

$$\frac{dN}{dt'} \approx -\tilde{B}_R \frac{N_{As}}{N_{As}^+}. \quad (\text{A10})$$

Hence, the dynamics of the population in CB is completely determined by the recombination process. Solving Eq. (A10) and transforming back to real quantities leads to:

$$n^{sat}(t) = n_0^{sat} - \tilde{B}_R N_{As} N_{As}^+ t, \quad (\text{A11})$$

Here,  $n_0^{sat}$  is the conduction band population when trap saturation occurs. The discussion of Eq. (A11) is done in the main article.

### Partial trap filling

For partial trap filling the number density of electrons excited to the CB is still small compared to the total number of trapping centers. Nevertheless, it is assumed to be high enough to decrease the probability for carrier trapping due to partial trap filling. Since carrier recombination is much slower than carrier capture we neglect the second term on the RHS of Eq. (A3b). For simplicity, we account for the generation term in Eq. (A3a) by an appropriate initial condition. Hence, the dynamic equations reduce to:

$$\frac{dN}{dt'} = -N(1 - N_T); \quad N(t=0) = N_{ex}, \quad (\text{A12})$$

$$\frac{dN_T}{dt'} = N(1 - N_T); \quad N_T(t=0) = 0. \quad (\text{A13})$$

These above equations can be solved analytically and the result for the conduction band population reads:

$$N(t') = \frac{(N_{ex} - 1)}{1 - 1/N_{ex} \exp\{-(N_{ex} - 1)t'\}}, \quad (\text{A14})$$

Note that  $N$  is normalized to  $N_{As}^+$ . Hence the term  $N_{ex} - 1$  describes the difference between excited electrons in CB and the number of available trapping centers  $N_{As}^+$ . Next, we analyze Eq. (A14) with respect to partial trap filling, i.e.  $-1 < N_{ex} - 1 < 0$ .

$$N(t') = \frac{(1 - N_{ex})}{1/N_{ex} \exp\{(1 - N_{ex})t'\} - 1} \approx N_{ex}(1 - N_{ex}) \exp\{-(1 - N_{ex})t'\}, \quad (\text{A15})$$

with  $1/N_{ex} > 1$ ,  $\exp\{(1 - N_{ex})t'\} > 1$  for all  $t' > 0$ . Since the number of excited carriers has assumed to be smaller than  $N_{As}^+$  the quadratic term in  $N_{ex}$  can be neglected. Transforming back to real quantities yields Eq. (7) of the main article:

$$n(t) \approx n_{ex} \exp\left\{-\left(1 - \frac{n_{ex}}{N_{As}^+}\right) \frac{t}{\tau_e}\right\}, \quad (\text{A16})$$

with  $n_{ex} = N_{ex} N_{As}^+$ .

**Paper VI:**

**Optics Express, vol. 22, no. 16, pp. 615–623, 2014**



# Influence and adjustment of carrier lifetimes in InGaAs/InAlAs photoconductive pulsed terahertz detectors: 6 THz bandwidth and 90dB dynamic range

Roman J.B. Dietz,<sup>1,2,\*</sup> Björn Globisch,<sup>1,2</sup> Helmut Roehle,<sup>1</sup> Dennis Stanze,<sup>1</sup> Thorsten Göbel,<sup>1</sup> and Martin Schell<sup>1</sup>

<sup>1</sup>Fraunhofer Institute for Telecommunications, Heinrich-Hertz-Institute, Einsteinufer 37, 10587 Berlin, Germany

<sup>2</sup>Authors contributed equally

\*[Roman.Dietz@hhi.fraunhofer.de](mailto:Roman.Dietz@hhi.fraunhofer.de)

**Abstract:** We investigate the influence of Beryllium (Be) doping on the performance of photoconductive THz detectors based on molecular beam epitaxy (MBE) of low temperature (LT) grown In<sub>0.53</sub>Ga<sub>0.47</sub>As/In<sub>0.52</sub>Al<sub>0.48</sub>As multilayer heterostructures (MLHS). We show how the optical excitation power affects carrier lifetime, detector signal, dynamic range and bandwidth in THz time domain spectroscopy (TDS) in dependence on Be-doping concentration. For optimal doping we measured a THz bandwidth in excess of 6 THz and a dynamic range of up to 90 dB.

©2014 Optical Society of America

**OCIS codes:** (040.2235) Far infrared or terahertz; (260.5150) Physical optics: Photoconductivity; (300.6495) Spectroscopy: Spectroscopy, terahertz; (320.7130) Ultrafast processes in condensed matter, including semiconductors.

---

## References and links

1. H. Roehle, R. Dietz, B. Sartorius, and M. Schell, "Fiber-coupled terahertz TDS combining high speed operation with superior dynamic range," 37th Int. Conf. Infrared, Millimeter, Terahertz Waves, 1-2 (2012).
2. P. Jepsen, D. G. Cooke, M. Koch, "Terahertz spectroscopy and imaging – Modern techniques and applications," *Laser Photonics Rev.* **5**, 124 (2011). <http://onlinelibrary.wiley.com/doi/10.1002/lpor.201000011/abstract>.
3. M. Suzuki, M. Tonouchi, "Fe-implanted InGaAs terahertz emitters for 1.56  $\mu\text{m}$  wavelength excitation," *Appl. Phys. Lett.* **86** (5), 051104 (2005). <http://link.aip.org/link/doi/10.1063/1.1861495>.
4. B. Sartorius, H. Roehle, H. Künzel, J. Böttcher, M. Schlak, D. Stanze, H. Venghaus, and M. Schell, "All-fiber terahertz time-domain spectrometer operating at 1.5  $\mu\text{m}$  telecom wavelengths," *Opt. Express* **16** (13), 9565-9570 (2008) <http://www.opticsinfobase.org/abstract.cfm?URI=oe-16-13-9565>.
5. A. Schwagmann, Z.-Y. Zhao, F. Ospald, H. Lu, D. C. Driscoll, M. P. Hanson, A. C. Gossard, and J. H. Smet, "Terahertz emission characteristics of ErAs:InGaAs-based photoconductive antennas excited at 1.55  $\mu\text{m}$ ," *Appl. Phys. Lett.* **96** (14), 41108 (2010) <http://link.aip.org/link/doi/10.1063/1.3374401>.
6. C. D. Wood, O. Hatem, J. E. Cunningham, E. H. Linfield, A. G. Davies, P. J. Cannard, M. J. Robertson, and D. G. Moodie, "Terahertz emission from metal-organic chemical vapor deposition grown Fe:InGaAs using 830 nm to 1.55  $\mu\text{m}$  excitation," *Appl. Phys. Lett.* **96** (19), 194104 (2010).
7. H. Roehle, R. J. B. Dietz, H. J. Hensel, J. Böttcher, H. Künzel, D. Stanze, M. Schell, and B. Sartorius, "Next generation 1.5  $\mu\text{m}$  terahertz antennas: mesa-structuring of InGaAs/InAlAs photoconductive layers," *Opt. Express* **18** (3), 2296-2301 (2010) <http://www.opticsinfobase.org/oe/abstract.cfm?URI=oe-18-3-2296>.
8. R.J.B. Dietz, M. Gerhard, D. Stanze, M. Koch, B. Sartorius, and M. Schell, "THz generation at 1.55  $\mu\text{m}$  excitation: six-fold increase in THz conversion efficiency by separated photoconductive and trapping regions," *Opt. Express* **19** (27), 122-126 (2011).

9. R.J.B. Dietz, B. Globisch, M. Gerhard, A. Velauthapillai, D. Stanze, H. Roehle, M. Koch, T. Göbel, and M. Schell, "64  $\mu$ W pulsed THz emission from growth optimized InGaAs/InAlAs heterostructures with separated photoconductive and trapping regions," *Appl. Phys. Lett.* **103** (6), 061103 (2013).
10. P. Uhd Jepsen, R. H. Jacobsen, and S. R. Keiding, "Generation and detection of terahertz pulses from biased semiconductor antennas," *J. Opt. Soc. Am. B* **13** (11), 2424-2436 (1996)  
<http://www.opticsinfobase.org/abstract.cfm?URI=josab-13-11-2424>.
11. L. Duvallaret, F. Garet, J. F. Roux, and J.-L. Coutaz, "Influence of noise on the characterization of materials by terahertz time-domain spectroscopy," *IEEE J. Quantum Electron.*, **7** (4), 615-623 (2001).
12. E. Castro-Camus, M. B. Johnston, J. Lloyd-Hughes, "Simulation of fluence-dependent photocurrent in terahertz photoconductive receivers," *Semicond. Sci. Technol.* **27** (11), 115011 (2012).
13. B. Globisch, R.J.B. Dietz, D. Stanze, R. Roehle, T. Göbel, and M. Schell, "Carrier dynamics in Beryllium doped low-temperature-grown InGaAs/InAlAs," *Appl. Phys. Lett.* **104** (17), 172103 (2014).
14. B. Grandidier, Huajie Chen, R. M. Feenstra, D. T. McInturff, P. W. Juodawlkis, and S.E. Ralph, "Scanning tunneling microscopy and spectroscopy of arsenic antisites in low temperature grown InGaAs," *Appl. Phys. Lett.* **74** (10), 1439 (1999).
15. L. Duvallaret, F. Garet, and J. Coutaz, "Influence of noise on the characterization of materials by terahertz time-domain spectroscopy," *J. Opt. Soc. Am. B* **17** (3), 452-461 (2000).
16. P. Jepsen, B. Fischer, "Dynamic range in terahertz time-domain transmission and reflectionspectroscopy," *Opt. Lett.* **30** (1), 29-31 (2005).
17. M. Van Exter, D. Grischkowsky, "Characterization of an optoelectronic terahertz beam system," *IEEE Trans. Microw. Theory Techn.*, **38** (11), 1684-1691 (1990).
18. E. Castro-Camus, L. Fu, J. Lloyd-Hughes, H. H. Tan, C. Jagadish, and M. B. Johnston, "Photoconductive response correction for detectors of terahertz radiation," *J. Appl. Phys.*, **104** (5), 053113 (2008).

## 1. Introduction

Over the past decade, terahertz time domain spectroscopy (THz TDS) has matured from pure scientific research and expensive laboratory sized setups to industrial applications and compact, portable THz-TDS systems [1]. Therefore, many future applications for terahertz technology have come into close reach [2]. A great portion of this development originates from the utilization of readily available Er-doped femtosecond fiber lasers at 1550 nm wavelength, of-the-shelf telecom components, and the design of suitable photoconductive antennas (PCAs) [3-7]. More recently, progress has been made concerning photoconductive THz emitters based on InGaAs/InAlAs multi-layer heterostructures (MLHS) [8]. Here, MBE growth at substrate temperatures of approx. 375-400 °C together with an adjusted heterostructure design led to good optical-to-THz conversion efficiencies with output powers up to 64  $\mu$ W [9]. However, the results of principal physical models of THz generation and detection predict that material development for emitters and receivers has to be done separately, since the main requirements are different [10-12]. The goal of this paper is the careful investigation of how the interplay of carrier lifetime and carrier mobility in PCA detectors influences THz bandwidth, dynamic range and detector noise. Therefore, we investigated four different samples of low temperature (LT) grown Beryllium (Be)-doped InGaAs/InAlAs MLHS with different nominal Be-doping concentrations of  $0.3 \times 10^{18} \text{ cm}^{-3}$ ,  $0.9 \times 10^{18} \text{ cm}^{-3}$ ,  $2.0 \times 10^{18} \text{ cm}^{-3}$  and  $4.0 \times 10^{18} \text{ cm}^{-3}$  (cf. Table 1). To obtain a detailed picture of the carrier trapping, carrier recombination and trap saturation dynamics, the samples were probed via differential transmission (DT) measurements at different pump pulse powers. A detailed presentation of the results on the DT measurements performed with these samples and their theoretical interpretation has been published in [13]. After giving a brief overview on these DT results for illustration, this paper focuses on the influence of carrier dynamics and carrier lifetime on PCA detector performance in a THz-TDS system made from the exact same samples.

## 2. Influence of Beryllium Doping on the Carrier Lifetime

The dominating mechanism of electron relaxation from the conduction band (CB) in LT-grown Be-doped InGaAs/InAlAs MLHS is phonon-assisted electron capture into arsenic anti-

site defects ( $\text{As}_{\text{Ga}}$ ) and subsequent recombination with a hole. More precisely, electron capture is dominated by the part of the arsenic antisite defects that has been positively ionized ( $\text{As}_{\text{Ga}}^+$ ) due to doping with Be-acceptors and hence lowering the Fermi level. Since, to a good approximation, every Be-dopant ionizes one  $\text{As}_{\text{Ga}}$  defect, the density of fast traps is equal to the Be-doping concentration [13, 14]. The time constants for the electron capture process are typically on the order of a few hundred femtoseconds (fs) to picoseconds (ps) depending on the  $\text{As}_{\text{Ga}}^+$  density. The time constant for the recombination process of electrons captured in  $\text{As}_{\text{Ga}}$  defects with holes is on the order of a few tens of ps to hundreds of ps. As pointed out in [13], there is strong evidence that the recombination occurs with holes captured by Be-dopants rather than with free holes in the valence band (VB) and hence is also dependent on the Be-doping concentration. However, even for high doping concentrations the recombination time remains on the order of several tens of picoseconds. The excitation source for all DT and THz-TDS measurements was a mode-locked fiber ring laser with a center wavelength of 1550 nm, a pulse width of approx. 90 fs and 100 MHz repetition rate. The excitation spot size was approx. 12  $\mu\text{m}$  for both DT and THz TDS measurements in order to obtain similar excitation conditions for a quantitative comparison between both measurements. Additionally, all the samples were structured with mesa-type dipole antennas with a 10  $\mu\text{m}$   $\times$  10  $\mu\text{m}$  photoconductive gap. Hence, the optically excited photoconductive region was precisely defined for both measurement methods.

The results obtained from DT measurements at 1550 nm pump and probe wavelength are given in Fig. 1(a), Fig. 1(b) and Fig. 1(c) for a low (0.25 mW), intermediate (2 mW) and a high pump power (16 mW), respectively. These excitation powers correspond to carrier densities in the CB directly after fs-excitation of approx.  $1 \times 10^{17} \text{ cm}^{-3}$ ,  $6.5 \times 10^{17} \text{ cm}^{-3}$  and  $1.28 \times 10^{18} \text{ cm}^{-3}$ , respectively. For the calculation of these carrier densities, the absorption saturation due to the limited density of states in the CB over the photon energies covered by the excitation laser pulse was taken into account.

For 0.25 mW pump power none of the samples shows significant trap filling as the induced carrier density in the CB is at least a factor of three smaller than the  $\text{As}_{\text{Ga}}^+$  density of every sample. Thus the absorption relaxation, i.e. the DT signal, can be fitted by assuming a mono exponentially declining carrier density within the CB. The respective fit results for the electron lifetime from the DT data are given in Table 1, the corresponding capture cross section according to Shockley-Read-Hall theory for the  $\text{As}_{\text{Ga}}^+$  defects was determined to  $\sigma_e^{\text{As}^+} \approx 2 \times 10^{-14} \text{ cm}^2$  [13].

Sample	$T_g$ [°C]	Be-doping [cm <sup>-3</sup> ]	Unsaturated capture time [ps]	Scattering time from Hall mobility data [fs]
MLHS 1	130	$0.3 \times 10^{18}$	3.29	50.15
MLHS 2	130	$0.9 \times 10^{18}$	1.03	24.76
MLHS 3	130	$2 \times 10^{18}$	0.32	10.36
MLHS 4	130	$4 \times 10^{18}$	0.19	6.882

Table 1. List of samples used as detectors in THz-TDS Setup with respective growth and DT parameters.

For the intermediate pump power of 2 mW MLHS 1 already shows a very slow absorption recovery. This is because the induced carrier density in the CB is on the same order as the available  $\text{As}_{\text{Ga}}^+$  trap density, i.e.  $\approx 0.3 \times 10^{18} \text{ cm}^{-3}$ . Hence, the DT signal is dominated by the recombination time of electrons in  $\text{As}_{\text{Ga}}$  defects with holes captured by Be-dopants, since this process forms a bottleneck for the carrier relaxation. MLHS 2 shows a slightly increased absorption recovery time which is caused by partial filling of the available  $\text{As}_{\text{Ga}}^+$  traps.

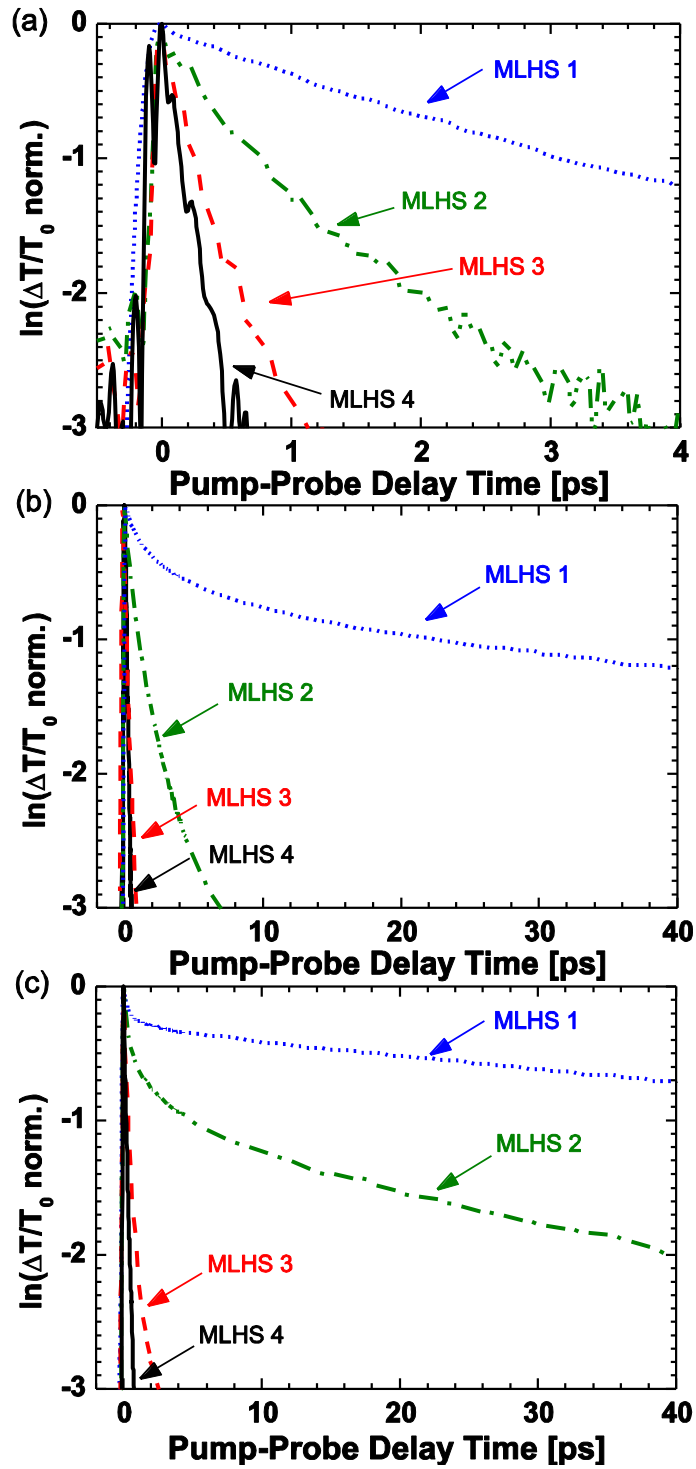


Fig 1. Plot of the logarithmic DT signals measured for (a) 0.25 mW, (b) 2 mW and (c) 16 mW pump power for all four different doping levels. At 0.25 mW all signals decay mono-exponentially. At 2 mW, there is an onset of trap saturation for MLHS 2 and 1, respectively. For 16 mW, both MLHS 1 and 2 show strong trap saturation, while MLHS 3 and 4 only show minor partial trap filling.

MLHS 3 and 4 show no significant increase of absorption recovery time due to the high amount of  $\text{As}_{\text{Ga}}^+$  that still exceeds the density of electrons in CB at this excitation power. For 16 mW pump power [Fig. 1(c)], the samples MLHS 1 and 2 both show strong  $\text{As}_{\text{Ga}}^+$  trap saturation and thus very long relaxation times in the DT signal, again governed by the electron-hole recombination time. The DT signal of MLHS 3 shows a slight deviation from a mono-exponential decay and an increased carrier lifetime due to partial trap filling. MLHS 4 still shows almost no change in the DT signal since the density of  $\text{As}_{\text{Ga}}^+$  traps, i.e.  $n_t \approx 4 \times 10^{18} \text{ cm}^{-3}$ , is still significantly higher than the excited carrier density in the CB of  $n_e \approx 1.28 \times 10^{18} \text{ cm}^{-3}$ .

### 3. Influence of the Optical Power on the detected THz Signal and Bandwidth

For further investigation of the influence of the Be-doping concentration and the resulting carrier dynamics on the THz detection properties, we performed THz-TDS measurements in dependence of the optical power at the detector. The photoconductive THz emitter used for the measurements in this chapter was a strip-line mesa-antenna with 25  $\mu\text{m}$  gap made from the  $4.0 \times 10^{18} \text{ cm}^{-3}$  Be-doped sample MLHS 4. For all measurements the applied bias was 50 V at an optical excitation power of 25 mW. For an efficient out-coupling of the THz radiation, the emitter and the respective detectors were attached to hyper-hemispherical HRFZ silicon substrate lenses. Furthermore, two off-axis parabolic mirrors for THz collimation and focusing were used.

The peak-to-peak signals obtained from THz-TDS measurements for the case of low excitation power (0.25 mW) are given in Fig. 2. In this low carrier density regime, the potential influence of THz field screening by free carriers in the CB and VB can be safely neglected leaving only two main influences to the current signal. One is the carrier scattering time (cf. Table 1) which limits carrier velocity and hence the detector current. The other influence is the carrier capture time which limits the integrated detector current, i.e. the value of the convolution integral in TDS detection Eq. (1). The scattering time extracted from Hall mobility data and the unsaturated carrier capture time from DT measurements at 0.25 mW are also shown in Fig. 2. It should be noted that the carrier capture time enters the carrier scattering time via Matthiessens rule since carrier capture is inelastic scattering.

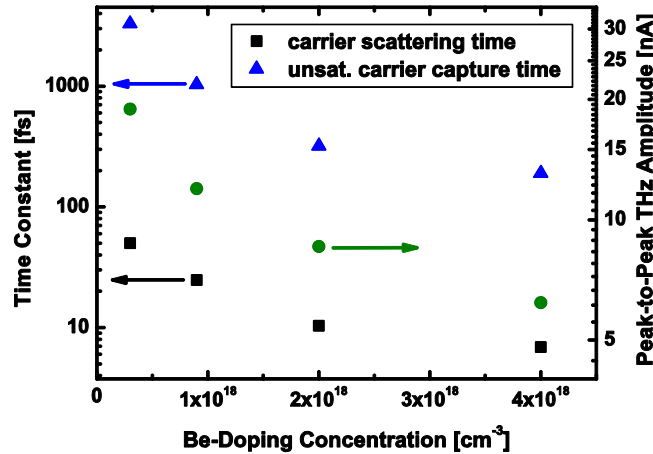


Fig. 2. Measured scattering time constants (black squares), unsaturated capture time constants (blue triangles) for DT measurements and THz peak-to-peak detector current (green circles) from THz-TDS measurements at an optical excitation of 0.25 mW.

However, because scattering mechanisms such as phonon scattering and more importantly elastic ionized impurity scattering due to the Be-doping are dominant in our case, the contribution of carrier capture to the carrier scattering time can be safely neglected.

For an understanding of the influence of carrier capture time on the frequency behavior of a PCA detector, it is instructive to consider two simplified limiting cases:

1. An infinitely *short* carrier lifetime, i.e. a Dirac delta function like carrier density in the CB:  $n(t) = \delta(t)$ .
2. An infinitely *long* carrier lifetime, i.e. a theta function like carrier density in the CB:  $n(t) = \theta(t)$ .

The TDS current of the detector for a linear response with respect to the electric field, i.e. neglecting influences such as THz field screening by charged carriers, can be described by the convolution:

$$j(\tau) = \sigma(t) * E_{THz}(t) = e \cdot n(t) * \mu(t) * E_{THz}(t), \quad (1)$$

which in Fourier space is given by

$$j(\omega) = e \cdot n(\omega) \cdot \mu(\omega) \cdot E_{THz}(\omega). \quad (2)$$

Here  $\sigma$  is the conductivity,  $E_{THz}$  is the incident THz field,  $n$  is the carrier density,  $\mu$  is the mobility,  $*$  denotes the convolution operation and  $e$  is the elementary charge.

For the first case Eq. (2) yields

$$j_{delta}(\omega) = e \cdot \frac{1}{\sqrt{2\pi}} \cdot \mu(\omega) \cdot E_{THz}(\omega), \quad (3)$$

where for second case Eq. (2) yields

$$j_{theta}(\omega) = e \cdot \left( \frac{i}{\sqrt{2\pi\omega}} + \delta(\omega) \right) \cdot \mu(\omega) \cdot E_{THz}(\omega). \quad (4)$$

From Eq. (3) and Eq. (4) it is obvious that for a slow, integrating detector one would expect a nonzero DC component in the signal and a faster roll-off towards higher frequencies as compared to a Dirac-like sampling detector. To investigate the effects of partial trap filling and trap saturation on the THz detector performance in terms of dynamic range and bandwidth we performed THz-TDS measurements in dependence of the optical excitation at the receiver. The obtained THz-TDS spectra for 0.25 mW, 2 mW and 16 mW excitation power are given in Fig. 3. The measurement time for each trace was approx. 1 minute (average over 1000 pulse traces measured at 16 Hz).

In case of the 0.25 mW, i.e. without trap saturation, MLHS 1 shows the highest THz peak-to-peak amplitude (cf. Fig. 2). When compared with the other samples it is obvious that the amplitude increase is mostly due to an increase of lower frequency components, i.e.  $< 2$  THz. At higher frequencies, e.g. 2-4 THz, the detected amplitudes are smaller as compared to the other MLHS. We attribute this to the slow trapping time (cf. Table 1). A closer investigation of the results in Fig. 2 reveals that, in general, longer carrier lifetimes in the detector shift the center frequency towards lower frequencies and enhance the frequency roll-off, as expected from Eq. (3) and Eq. (4). Furthermore, it agrees with predictions from more sophisticated Monte Carlo calculations in [12].

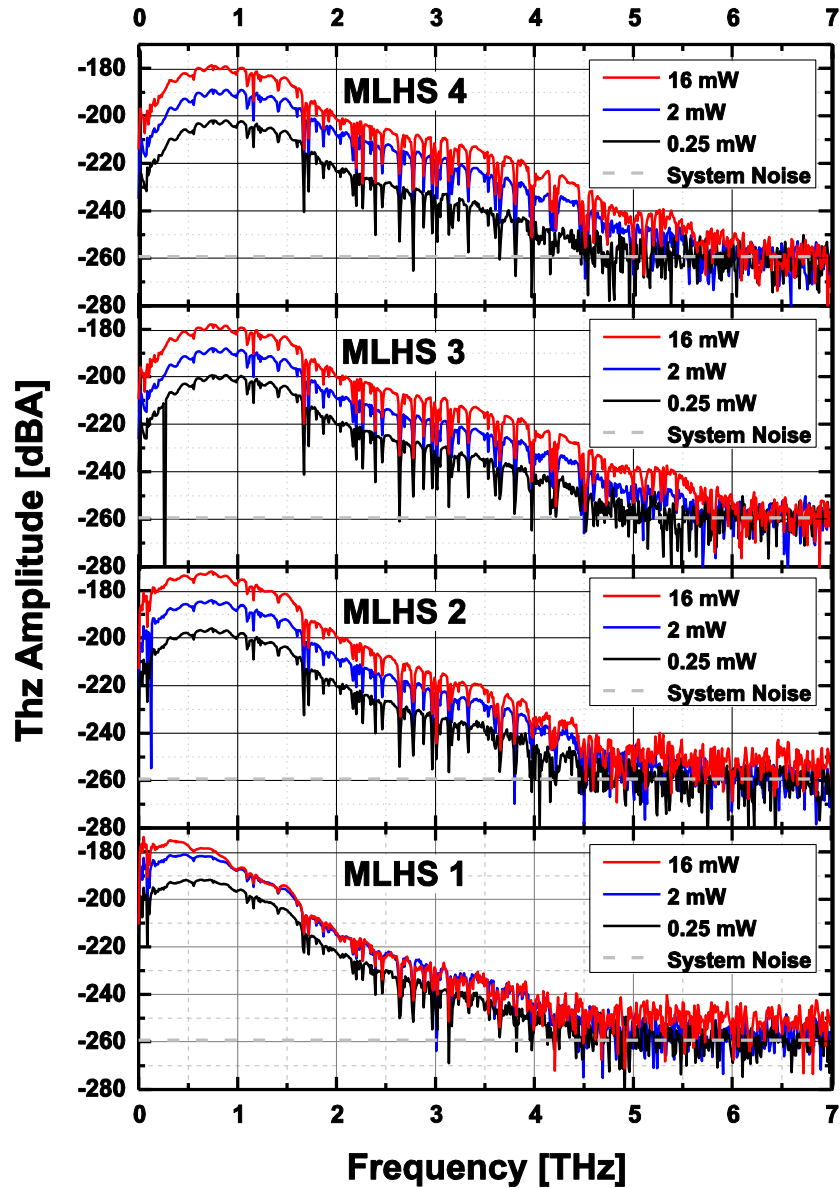


Fig. 3 THz-TDS spectra obtained from detectors made from the different MLHS samples for 0.25 mW, 2 mW and 16 mW of optical excitation power at the detector. The grey striped line indicates the noise of the detection electronics without a connected antenna.

The  $2.0 \times 10^{18} \text{ cm}^{-3}$  doped MLHS 3 shows the highest signal in the frequency range of 2-4 THz at this low excitation power, indicating a trade-off between fast trapping and high mobility. The dynamic range for all detectors under this excitation condition was limited by the noise of the detection system itself and not the respective MLHS. The system noise amplitude measured with an open circuit, i.e. without an antenna, is depicted as a grey line in Fig. 3. For medium optical excitation power of 2 mW, the frequency roll-off for MLHS 2-4 remains almost equal to the roll-off at 0.25 mW. For MLHS 1, a minor shift of the center frequency towards lower frequencies and a slightly steeper roll-off is visible. Considering the prolonged carrier lifetime of MLHS 1 at this excitation condition (cf. Fig. 1(b)) the change of the

frequency roll-off is weaker than what would be expected from Eq. (4). The relative increase of the THz signal amplitude as compared to the other samples is small indicating the onset of a saturation behavior, as will be discussed later in more detail.

At 16 mW MLHS 1 shows a further red shift of the center frequency as expected for this long carrier lifetime and hence a mostly integrating antenna behavior. The peak in the frequency components around 5-30 GHz originates from resonances in the contact metallization. The damping of these resonances is reduced for long carrier lifetimes. MLHS 2 also shows a steeper frequency roll-off due to the prolonged carrier lifetime at 16 mW. However the effect is not as pronounced as for the MLHS 1. MLHS 3-4 show almost no difference in the roll-off behavior and MLHS 3 shows only a slight shift of the center frequency and thus a superior bandwidth. These results indicate that the benefit of a short carrier capture time outweighs the lower detector signals due to the simultaneous increase of the carrier scattering time for higher Be doping concentrations. Furthermore, in case of MLHS 1 we observed a strong saturation and even reduction of the detector peak-to-peak pulse amplitude for higher excitation powers which can be seen in Fig. 4. We assume that the decrease is due to screening of the incident THz field by free and trapped carriers which in case for MLHS 1 gets relevant due to the long carrier capture and recombination lifetimes. In this case the detector response is not linear in the electric field since the carrier acceleration becomes dependent on the CB carrier density and Eq. (1) loses its validity. A model describing carrier screening effects in the semiconductor response of a PCA has been proposed by Jepsen et al. [10].

The peak-to-peak amplitudes of MLHS 2 to 4 do not show such a saturation behavior even at higher optical excitation powers suggesting a linear response. The slight sub-linear behavior of the peak-to-peak amplitude with respect to the optical power is assumed to be due to absorption saturation. The amplitudes of MLHS 2-4 are therefore determined by the carrier scattering time and the carrier capture lifetime which enters via the convolution integral [Eq. (1)] as explained before.

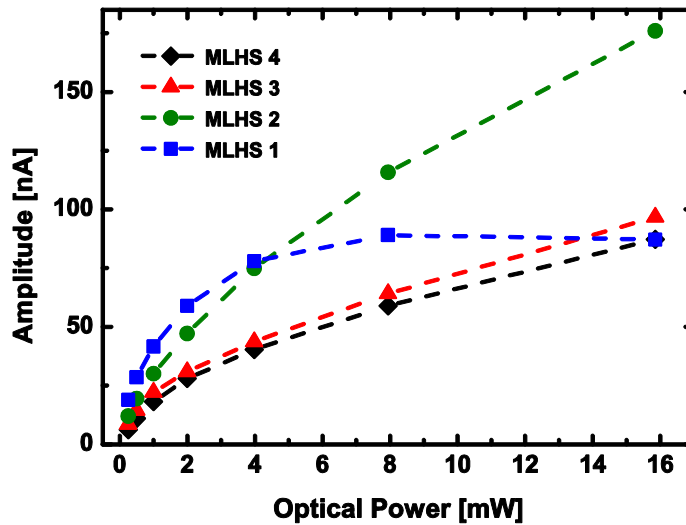


Fig. 4. Peak-to-peak amplitude of the detected THz-TDS pulse in dependence of the optical excitation power at the detectors made from MLHS 1-4. The striped lines are guidelines for the eyes.

#### 4. Noise and Bandwidth

Another important characteristic of THz detectors is the electronic detector noise which potentially limits the dynamic range and thus the detectable bandwidth. Duvillaret et al. [15] and Jepsen et al. [16] have analyzed how noise limits the extractable data in THz-TDS spectroscopy. Even though, the authors of [15] show that emitter noise dominates the noise in TDS measurements they find that detector noise contributions are not negligible. Grischkowsky and Van Exter [17] as well as Castro-Camus et al. [18] have shown that the major detector noise contribution arises from thermal Nyquist noise. Shot noise and generation-recombination (GR) noise are found to have only minor influence as they scale with the square root of the THz field induced detector current which is generally relatively small. The Nyquist noise current is given by:

$$I_N = \sqrt{4 \cdot K_B \cdot T \cdot \Delta f \cdot R^{-1}} \quad (5)$$

where  $K_B$ ,  $T$  and  $\Delta f$  are Boltzmann constant, absolute temperature and measurement bandwidth, respectively.  $R$  is the detector resistance. Since the measurement of the signal in TDS detection is essentially a DC or very low frequency current measurement, the time average resistance of the detector is sufficient for analysis.

We measured the average root-mean-square (rms) noise current in the detector, without an incident THz field, in dependence of the optical power at the detector. Additionally, we calculated the Nyquist noise currents from PCA resistances by numerically solving the carrier density equations given in [13]. Both results are given in Fig. 5. For MLHS 1 and 2 there is a strong increase ( $\sim$ factor 7) in the measured and calculated Nyquist noise current for higher excitation powers, which is due to the long carrier lifetimes in the saturation regimes and hence a low average resistivity. For MLHS 1 and 2 the general behavior of the Nyquist noise as a function of optical excitation power, is covered quite well by the simulation results. However, the absolute values differ by a factor of approx. 2. Here, it should be noted that thermal re-excitation of carriers from trap states into to the CB and the VB was not included in the calculation. After the optical excitation and until electrons and holes in trap states have recombined, only Quasi Fermi levels are defined.

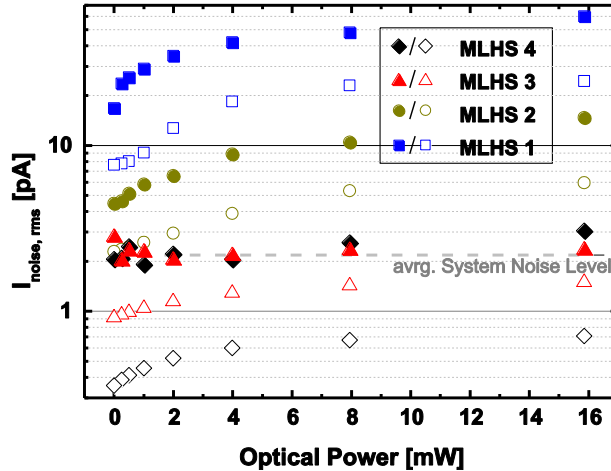


Fig. 5 Measured (full symbols) root mean square noise current and calculated Nyquist noise current (open symbols) shown in dependence of the optical excitation power for four different detectors made from MLHS 1-4. The grey striped line indicates the system noise measured with an open circuit.

During this time the probability for thermal re-excitation is increased, leading to a further reduction of the samples resistance. This effect could explain the discrepancy between measurement and simulation.

For MLHS 3 and 4 the measured noise currents seem to show a minor increase ( $\sim$  factor 1.5). However, since the measured noise currents are very close to the average system noise level (measured with an open circuit) the result is inconclusive. The prediction of the simulation for MLHS 3 is within the margin of the factor 2 discrepancy. The simulation of MLHS 4, however, is significantly lower than the measured one, suggesting that the system noise could be the limiting factor in this case.

To further examine the influence of the Be-doping level, we extracted the dynamic range and measurable bandwidth from all measured TDS spectra at different detector excitation powers for each of the MLHS samples. The noise floor for the dynamic range calculation was defined as the average value of the spectral amplitude between 6.5 and 10 THz. The detectable bandwidth was defined as the highest frequency component with an amplitude 6 dB above the noise floor in the respective THz power spectrum. The obtained results are given in Figs. 6(a) and 6(b). For MLHS 1, the dynamic range decreases for excitation powers in excess of 4 mW due to the amplitude saturation and the increase in Nyquist noise. In conjunction with the strong frequency roll-off, the detectable bandwidth is significantly limited at high excitation powers. Similarly, MLHS 2 shows a saturation behavior of the dynamic range for the highest excitation power due to an increased noise level (cf. Fig. 5) and a decrease of the detectable bandwidth for higher excitation. Both MLHS 3 and 4 show no saturation in the dynamic range or bandwidth as expected from their short carrier lifetime for all excitation levels. Interestingly, the highest measurable bandwidth is not obtained for MLHS 4 which features the shortest carrier lifetime. Instead, the slightly higher carrier lifetime and scattering time of MLHS 3 leads to an increase of the detected THz current. Since the noise level is defined by the system noise for these samples, the THz bandwidth increases for higher detector currents as long as the carrier lifetime is short enough. Considering the noise calculations shown in Fig. 5, MLHS 4 could potentially exceed the dynamic range of MLHS 3 if the system noise could be further reduced.

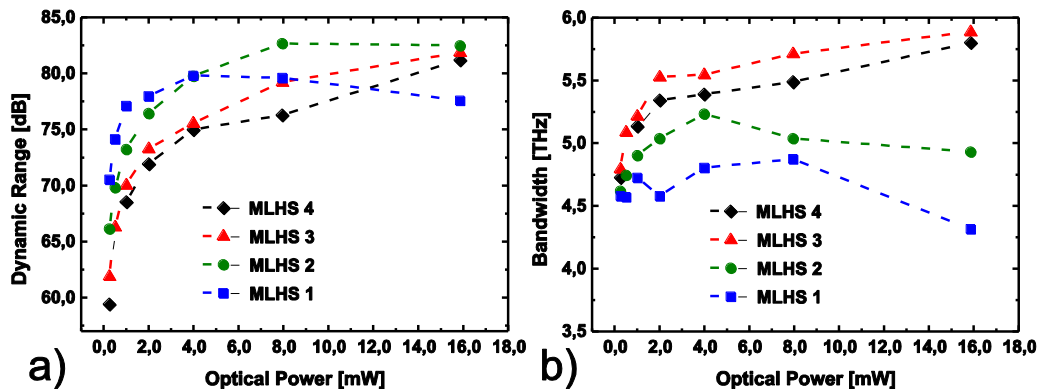


Fig. 6. (a) Dynamic range and (b) detectable bandwidth of the THz-TDS signal in dependence of the optical excitation power for four different detectors made from MLHS 1-4. The striped lines are guidelines for the eyes.

In an attempt to overcome the system noise limitation and increase the dynamic range, we employed a 100  $\mu$ m strip-line emitter fabricated from a high mobility MLHS which has a significantly higher THz output than LT-grown Be-doped MLHS [8, 9]. The bias of the emitter was 100 V and the optical excitation was set to 25 mW. As detector we employed MLHS 4, which features the fastest trapping time. The average noise floor in the spectra was

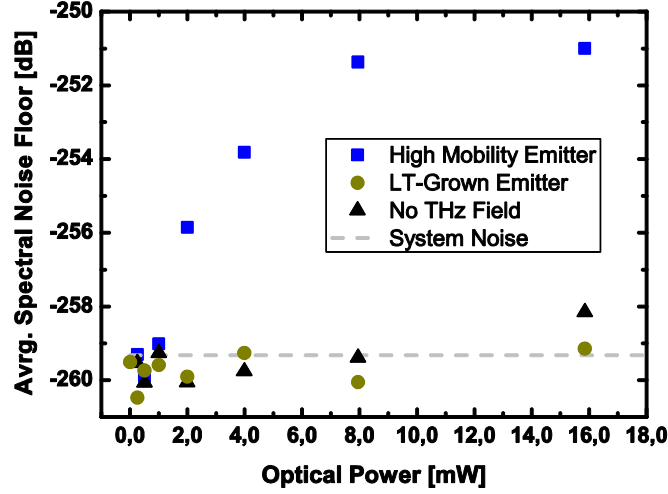


Fig. 7. Average noise floor in THz-TDS spectra taken between 6.5 THz and 10THz in dependence of the optical excitation power at the detector made from MLHS 4 and for a high mobility MLHS emitter at 100 V bias (blue squares), a LT-grown emitter made from MLHS 4 at 50 V bias (green circles) and without an incident THz field (black triangles).

extracted for different excitation powers at the detector for the high mobility emitter, the LT-grown emitter and without a THz field present, which is shown in Fig. 7. In accordance with our previous results the noise of the LT grown emitter is on the order of the system level. However, there is an increase of the noise floor for higher excitation levels if a THz field is present in case of the high mobility emitter. The square root like behavior strongly suggests that the increase is due to shot noise from the detector current which in turn, to a good approximation, is directly proportional to the optical excitation power at the detector and is given by:

$$I_N = \sqrt{2 \cdot e \cdot I_{THz}} \propto \sqrt{2 \cdot e \cdot P_{opt,det}} \quad (6)$$

Here  $I_{THz}$  is the THz-field induced detector current,  $P_{opt,det}$  is the optical power at the detector and  $e$  is the elementary charge. Since for the high mobility emitter the detector currents have much higher values (approx. 285 nA for 16 mW excitation at the detector) the shoot noise contribution appears to become significant. However, since the shoot noise scales with the square root of the detector current were as the signal scales linear with the detector current the dynamic range is further increased as compared to the previous emitter.

Finally we increased the emitter bias to 120 V and averaged over ten thousand trace taken at 16 Hz (approx. 10 min) resulting in a measureable bandwidth of over 6 THz and approx. 90 dB dynamic range as can be seen in Fig. 8. For this emitter and detector combination the spectrum of a single pulse trace with a measurement time of 62.5 ms still shows a dynamic range in excess of 65 dB and a bandwidth >4.5 THz (not shown).

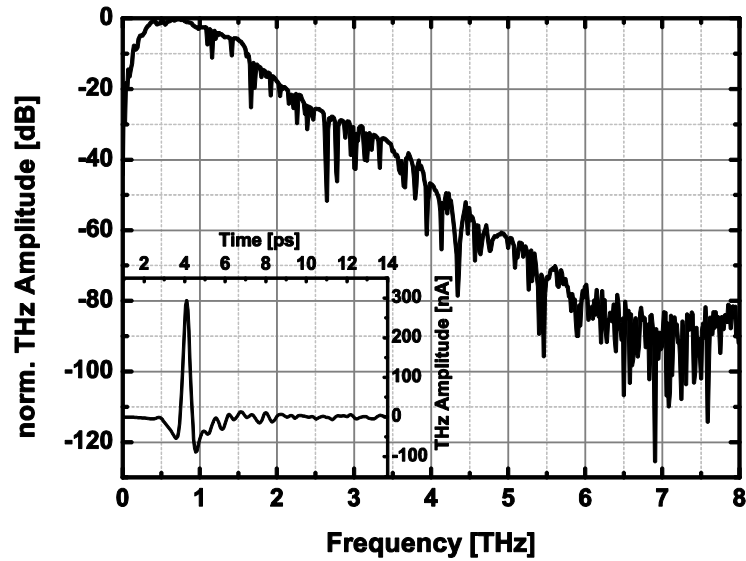


Fig. 8. FFT spectrum obtained for a high mobility MLHS emitter at 120 V bias and 25 mW optical excitation and a detector made from MLHS 4 at 16 mW optical excitation. The spectrum is obtained by averaging ten thousand pulse traces at 16 Hz measurement rate (approx. 10 min). The corresponding THz Pulse trace is shown in the inset.

## 5. Conclusion and Outlook

We have shown that knowledge of the influence of Beryllium doping on carrier dynamics in LT-grown InGaAs/InAlAs MLHS is crucial for the design of THz-TDS detectors made from this material. We have found that trap saturation, i.e. long carrier lifetime, limits the detector dynamic range and bandwidth because of increased frequency roll-off and Nyquist noise. Furthermore, we have shown that in case of detectors with short carrier lifetimes and sufficiently strong THz fields the shot noise in the detector becomes a relevant noise source. Finally, it was demonstrated that for fast LT-grown InGaAs/InAlAs detectors, i.e. with appropriate Be doping concentration, together with highly efficient THz emitters it is possible to obtain PCA based THz-TDS measurement systems at 1550 nm excitation with 90 dB dynamic range and more than 6 THz bandwidth.

**Paper VII:**

**J. Infrared, Millimeter, Terahertz Waves, vol. 35, no. 10,  
pp. 823-832, 2014**



# Terahertz-time domain spectrometer with 90 dB peak dynamic range

N. Vieweg<sup>1\*</sup>, F. Rettich<sup>1</sup>, A. Deninger<sup>1</sup>, H. Roehle<sup>2</sup>, R. Dietz<sup>2</sup>, T. Göbel<sup>2</sup>, M. Schell<sup>2</sup>

<sup>1</sup>*TOPTICA Photonics AG, Lochhamer Schlag 19, 82166 München, Germany*

<sup>2</sup>*Fraunhofer Institute for Telecommunications, Heinrich Hertz Institute, Einsteinufer 37, 10587 Berlin, Germany*

Tel.: 0049 89 85837 147

Fax: 0049 89 85837 200

\*corresponding author: [nico.vieweg@toptica.com](mailto:nico.vieweg@toptica.com)

Abstract:

Many time-domain terahertz applications require systems with high bandwidth, high signal-to-noise ratio and fast measurement speed. In this paper we present a terahertz time-domain spectrometer based on 1550 nm fiber laser technology and InGaAs photoconductive switches. The delay stage offers both a high scanning speed of up to 60 traces / s and a flexible adjustment of the measurement range from 15 ps – 200 ps. Owing to a precise reconstruction of the time axis, the system achieves a high dynamic range: a single pulse trace of 50 ps is acquired in only 44 ms, and transformed into a spectrum with a peak dynamic range of 60 dB. With 1000 averages, the dynamic range increases to 90 dB and the measurement time still remains well below one minute. We demonstrate the suitability of the system for spectroscopic measurements and terahertz imaging.

Keywords: terahertz time domain spectroscopy, femtosecond fiber laser, InGaAs photoconductive switches, terahertz imaging

## Introduction

Terahertz waves feature unique properties: like microwaves, terahertz radiation passes through a plethora of non-conducting materials, including paper, cardboard, plastics, wood, ceramics and glass-fiber composites [1]. In contrast to microwaves, terahertz waves have a smaller wavelength and thus offer sub-millimeter spatial resolution. Whilst many different techniques coexist today, terahertz generation and detection with photoconductive switches has found particularly widespread use [2], [3]. Terahertz time-domain spectroscopy (THz TDS) [4] has become an established method for phase and amplitude-sensitive measurements with high time resolution and outstanding bandwidth. Recent applications of THz-TDS range from fundamental research [5], [6], medical diagnostics [7], security applications [8] to non destructive testing [9]–[12].

THz-TDS instrumentation has come a long way from free-space setups and bulky laboratory equipment to much more compact and inexpensive alternatives. In the past, terahertz pulses were mainly generated with GaAs photoconductive switches, which required laser excitation below 870 nm and often involved complex Ti:Sapphire lasers. With the advent of 1.5  $\mu\text{m}$  fiber lasers and recent InGaAs/InAlAs-based terahertz emitters [13], a trend towards telecom-based technology has become evident. Terahertz spectrometers operating at 1.5  $\mu\text{m}$

take full advantage of mature and cost-efficient telecom components and are thus well suited for real-world applications [14]. These advances notwithstanding, state-of-the-art THz-TDS systems usually achieve the targeted signal-to-noise (SNR) ratios via time-consuming signal averaging methods, which is no hurdle if the quality of the signal is more important than the measurement speed. However, there is still no system on the market that combines fast measurement speed with a top-level SNR performance and high bandwidth. Applications that call for such a system include studies of dynamic processes in biomolecules [15], measurements under rapidly changing environmental conditions, e.g. varying temperatures or magnetic fields [16], and inline process control of plastic materials [17].

In this paper we present a compact fiber-coupled THz-TDS system based on 1.5  $\mu\text{m}$  fiber laser technology and InGaAs/InAlAs photoconductive switches. Due to a precise reconstruction of the time axis, the system drastically reduces the effect of jitter noise and achieves a high dynamic range in conjunction with broad bandwidth and fast measurement speed.

The performance of our system and its key components – femtosecond laser, terahertz antennas and delay stage – are described in the next section of this paper. Special emphasis will then be given to jitter noise and the reconstruction of the time axis. We conclude with application examples in the fields of spectroscopy and imaging.

## **Terahertz time domain spectrometer**

### **System design and performance**

A photograph and a schematic representation of the spectrometer are shown in Figure 1 (a) and (b), respectively. The system comprises a 1.5  $\mu\text{m}$  femtosecond fiber laser with dispersion compensation. A 50 / 50 fiber splitter divides the output beam into an emitter and a detector branch. Both optical paths feature highly precise, fiber-coupled mechanical delay stages: the emitter path includes a fast, scanning delay and the receiver path a slow, long-travel delay. Laser, fiber splitter, delay stages, driver electronics, power supply as well as a microcomputer for system control and data acquisition are all housed in one 19" box (48 x 40 x 20 cm). The system is equipped with an Ethernet data interface to allow flexible control e.g. via LabView software.

The optical pulses in both arms are guided to fiber-coupled, InGaAs-based photoconductive switches, which serve as terahertz emitter and detector. The fiber-pigtailed design permits a flexible arrangement in either transmission or reflection geometry. The emitter converts the laser light into a terahertz pulse [18]. More precisely, the laser pulse excites charge carriers in the emitter antenna, which are accelerated by an externally applied bias field. The resulting current transient gives rise to an electromagnetic pulse - the terahertz pulse that is radiated into free space. The detection process is similar to the generation process. The laser pulse optically gates the detector antenna, while the generated charge carriers are accelerated by the electric field of the incident terahertz pulse. The resulting photocurrent is directly proportional to the terahertz electric field. A characteristic of any THz-TDS system is that the width of the generated terahertz pulse ( $\sim 1$  ps) is much longer than the width

of the probing laser pulse ( $\sim 80$  fs). Thus, only a fraction of the terahertz pulse is sampled each time the laser pulse hits the detector antenna. To retrieve the full pulse shape, the terahertz pulse is scanned by varying the time delay between the two optical paths.

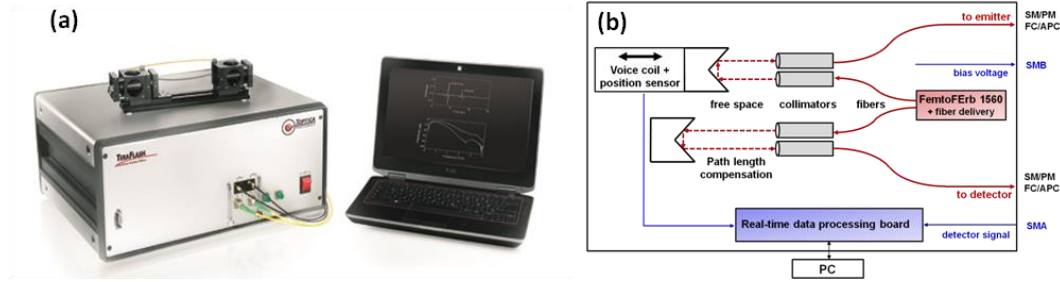


Figure 1: (a) Photograph of the terahertz time-domain system and (b) schematic representation. Blue lines denote electric connections, red lines the optical paths.

Figure 2 (a) shows the amplitude spectrum achieved with our system. The terahertz spectrum contains frequency components from 50 GHz to about 4.5 THz with a signal peak at approx. 480 GHz. The inset in Figure 2 (b) presents a typical time-domain signal measured with the system. A single trace of 50 ps can be acquired in only 44 ms. Via the control software, the scan range can be flexibly changed between 15 ps and 200 ps. The width of the terahertz pulse, i.e. the time difference between the maximum and minimum amplitude, amounts to 650 fs.

Figure 2 (b) shows the dependence of the peak dynamic range (PDR) on the number of averaged time traces. For a single measurement (acquisition time 44 ms), the PDR is 60 dB. This value increases with the number of averages: for 100 averages and a total acquisition time of only 4.4 s, a PDR of 82 dB is obtained. The PDR increases to 90 dB for 1000 averages. The dependence of the peak dynamic range on the number of averages  $N_{ave}$  and, consequently, the total measurement time  $t_{meas}$  is given by

$$PDR(dB) \propto 20 \log(\sqrt{N_{ave}}) \propto 20 \log(\sqrt{t_{meas}}). \quad (\text{Eq.1})$$

The PDR of 90 dB presents, to the best of our knowledge, a record for commercial TD-THz systems.

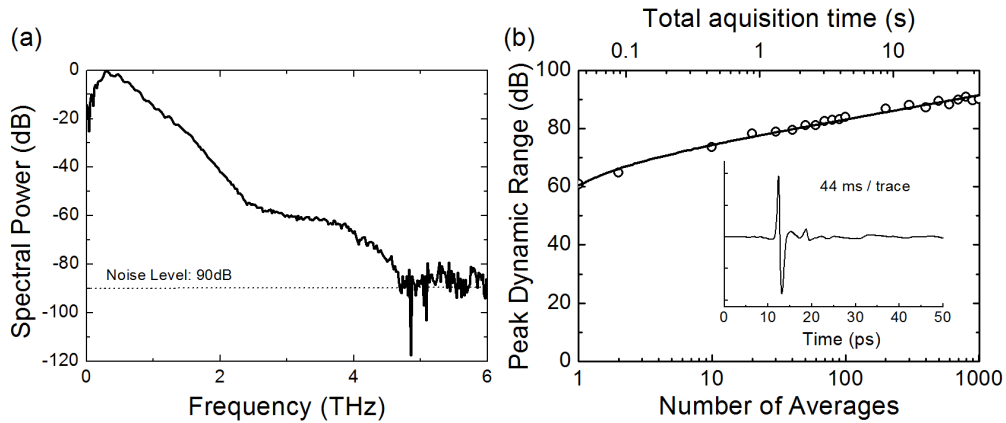


Figure 2: (a) Amplitude spectrum with a bandwidth that exceeds 4.5 THz. (b) Peak dynamic range at 480 GHz (black squares, right axis) and total acquisition time (red circles, left axis) versus the number of averaged time traces. The solid line depicts a fit of Eq. 1. A single trace of 50 ps is measured in 44 ms (inset).

### Femtosecond laser

The spectrometer uses a robust all-fiber-based femtosecond laser system (Toptica FemtoFERb 1560 with fiber delivery FD5-PM). The laser radiation is centered at 1560 nm, the repetition rate is 100 MHz and the pulse width is typically 80 fs. The laser provides approx. 60 mW power at the polarization-maintaining fiber output. Pump diode, active fiber and driver electronics are integrated in one box (21 x 12 x 7.5 cm), which only requires a 12 V external power supply. Both the emitter and the receiver branch employ single-mode, polarization-maintaining fibers of approx. 5 m length. To account for dispersion effects in the fiber delivery, the laser includes dispersion-compensating fibers (DCF) which are spliced into the fiber-optic beam path.

### Delay stages

#### Long-travel delay line

A long-travel delay line introduces a constant timing offset and thus compensates any changes of the terahertz path and/or fiber length. It comprises a motor-driven corner-cube mirror with a 4-fold optical path, and produces a delay of up to 3000 ps. The value of the time delay is measured with a resolution of 1.3 fs.

#### Fast and highly precise delay

A second, fast and equally precise delay provides the time variation required for sampling the terahertz pulse with high accuracy. It consists of a voice-coil driven corner-cube mirror combined with a digital, high-precision position sensor. The sensor records 50000 time stamps per second, with a resolution of 1.3 fs. These time stamps are synchronized with the readout of the signal values from the terahertz receiver. Data acquisition is accomplished both during the forward and the backward movement of the mirror, which minimizes the “dead time” of the system. The acquisition time of one pulse trace varies with the chosen delay range, since the swing speed of the voice coil is maintained constant. Consequently, a long travel distance requires more time: The

system samples 60 pulses / s for a scan range of 15 ps, whereas a scan range of 200 ps corresponds to 6 pulses / s. The 50 ps traces as shown in Figure 2 (b) are recorded at 22.7 Hz.

The effective scanning speed also depends on the travel distance. The highest rate of 1200 ps / s is attained for the maximum scan range of 200 ps, whilst a 15 ps range is scanned at 900 ps / s. The effective sampling time per step is  $\sim 25$  fs, with even shorter sampling intervals at the turning points of the voice coil. This precise timing resolution gives rise to the high accuracy of the time scale, which results in superior PDR values when multiple traces are averaged.

## **Terahertz antennas**

The photoconductive emitter employs a high-mobility InAlAs/InGaAs multilayer heterostructure (MLHS) as described in [19][20]. The receiver is based on an LT-grown Beryllium doped InAlAs/InGaAs MLHS [21][22] with short carrier lifetime. A strip-line antenna geometry with a 100  $\mu\text{m}$  photoconductive gap was chosen for the emitter, and a dipole geometry with 10  $\mu\text{m}$  gap for the receiver. Both transmitter and receiver feature a mesa-structured gap region as detailed in [13].

The antennas are packaged into compact housings (25 mm diameter) with single-mode, polarization-maintaining fiber pigtailed which guarantee stable optical excitation.

## **Impact of jitter on the SNR**

In THz-TDS, various noise effects compromise the signal quality [23]–[25]. Noise contributions include optical and electronic effects [26], [27], laser intensity variations [28], and jitter noise [29], [30]. In the past a lot of effort has been put into reducing electronic detector noise, which played a dominant role in the SNR budget [26], [31]. In this section, we are going to discuss the effect of jitter noise, which has an equally significant impact on the attainable SNR level [25], [29], [32], [33].

Generally, “jitter” denotes a deviation from true periodicity of an assumed periodic signal. In THz-TDS, the terahertz pulse is optically sampled at the detector antenna. More precisely, the terahertz transient is reconstructed from amplitude data acquired in discrete time delay steps. Timing jitter in THz-TDS systems results from a plurality of effects. Whilst contributions that plague free-space laser configurations (e.g., acoustic vibrations of opto-mechanical components, or refractive index fluctuations of air [34]) are largely avoided in our fiber-based design, the timing accuracy of the delay stage itself needs to be taken into account. More specifically, any linear translation stage has a limited length resolution and positional accuracy. Depending on the implementation, the actual position of the delay can differ from the set point by several micrometers [35], [36]. As the optical path length counts two-fold in a delay line with retroreflector, a length difference of only one micrometer already translates into a timing error of 6.6 fs, and the accumulated error can exceed several 10 fs.

Any uncertainty in the time axis leads directly to an uncertainty of the amplitude and thus reduces the dynamic range of the signal. This effect is illustrated in

Figure 3. For reasons of clarity a half-wave of a sinusoidal signal  $A(t) = \sin(2\pi\nu_{THz}t)$  with  $\nu_{THz} = 480$  GHz is shown, which corresponds to the PDR frequency of our system. It is evident that a time-domain jitter  $dt$  results in an amplitude uncertainty  $dA$ . The derivative  $dA/dt$  of the sine wave yields  $2\pi\nu\cos(2\pi\nu t)$ . The amplitude uncertainty reaches maximum values at the zero crossings of  $A(t)$ , i.e. at  $t = k / 2\pi\nu$  with  $k = 0, 1, 2$ , etc. The “worst-case” amplitude error is given by  $dA = 2\pi\nu_{THz}dt$  [33] and the dependence of the dynamic range on the timing jitter can be written [37]

$$\text{DynamicRange}_{\text{jitter}} = -20 \log(2\pi\nu_{THz}dt). \quad (\text{Eq. 2})$$

We note that the absolute value of the PDR depends on a plurality of other factors, such as available terahertz power, the sensitivity of the receiver and electronic noise in the readout circuit. However, Eq. 2 allows us to quantify the influence of the timing jitter in otherwise identical setups.

The system described here determines the delay position with an uncertainty below 400 nm, and thus achieves a time resolution of 1.3 fs. This is an improvement of more than one order of magnitude, compared to the 10 fs level inferred from [35], [36]. Using Eq. 2, we conclude that the precision of the delay stage improves the PDR by more than 17 dB.

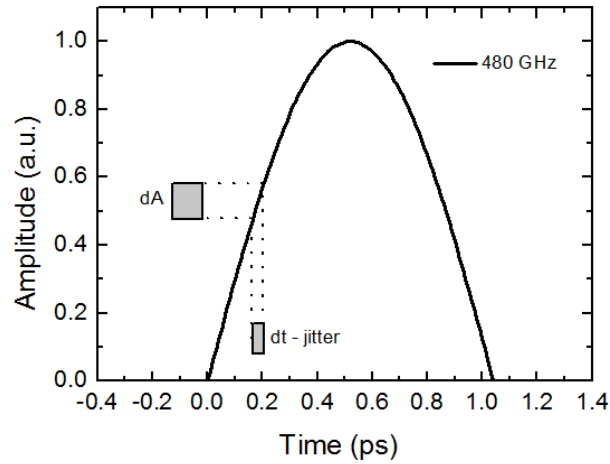


Figure 3: Effect of timing jitter on the signal amplitude.

## Application examples

### Terahertz spectroscopy

To demonstrate the suitability of our system for terahertz spectroscopy, we used three different polymer samples: high density polyethylene (HDPE, thickness 1.93 mm), polyamide (PA, 1.07 mm) and E540i<sup>1</sup>, a liquid-crystal polymer (LCP, 2.05 mm). The emitter / receiver modules, optics and the samples themselves were kept in a sealed box, which was purged with dry air to minimize absorption effects by water vapor. Refractive index values and absorption coefficients of the materials were obtained by comparing a reference pulse and a sample pulse, with 1000 averages per trace (measurement time = 44 s). Figure 4 shows a typical trace of a reference pulse in dry air (black solid line), together with pulses which propagated through the LCP sample in ordinary (dashed red line) and extraordinary direction (dashed dotted green line). The orientational order of the LCP molecules gives rise to anisotropic properties: The extraordinary refractive index is higher than the ordinary refractive index [38], [39] and consequently, the pulse undergoes a larger time shift in the case of extraordinary polarization. Note that the pulse amplitudes are nearly identical for both polarizations, indicating similar absorption coefficients.

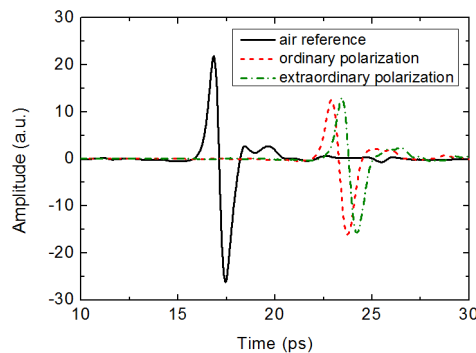


Figure 4: Pulse shift of an anisotropic liquid crystal polymer (LCP) sample.

For extraction of the material parameters we used a quasi-space algorithm [40]. Refractive indices and absorption coefficients are shown in Figure 5 (a) and (b), respectively. The strong absorption of the terahertz wave in the LCP and PA samples at high frequencies lowers the dynamic range and consequently restricts the frequency span useable for analysis to  $\sim 2$  THz.

A nonpolar polymer, HDPE exhibits the lowest absorption (dashed blue line). For this sample almost the full bandwidth of the system is exploited. The absorption coefficient remains  $< 0.1 \text{ cm}^{-1}$  for frequencies below 1 THz, and increases slightly towards higher frequencies (approx.  $1 \text{ cm}^{-1}$  @ 2 THz). The refractive index of 1.53 shows no dispersion over the entire frequency range investigated. In contrast to HDPE, PA is a polar plastic. Our measurements yield a higher, more rapidly increasing absorption coefficient (dotted green line). The refractive index of PA is 1.71 at 0.5 THz and decreases very slightly towards higher frequencies. Our results for PA and HDPE are in very good agreement with literature data [41].

---

<sup>1</sup> E540i is a trademark of TICONA.

The refractive indices of the LCP show a distinct anisotropy: at 0.5 THz, values for ordinary and extraordinary polarization amount to 1.86 and 2.03, respectively. The dispersive feature at around 1.2 THz corresponds to a distinct absorption peak, as seen in Fig. 5 (b). Note that at higher frequencies, the absorption coefficients follow different trends: The ordinary parameter rises faster than the extraordinary parameter. The absorption peak itself is caused by Talcum, a filling material, which is commonly added to LCP samples [42].

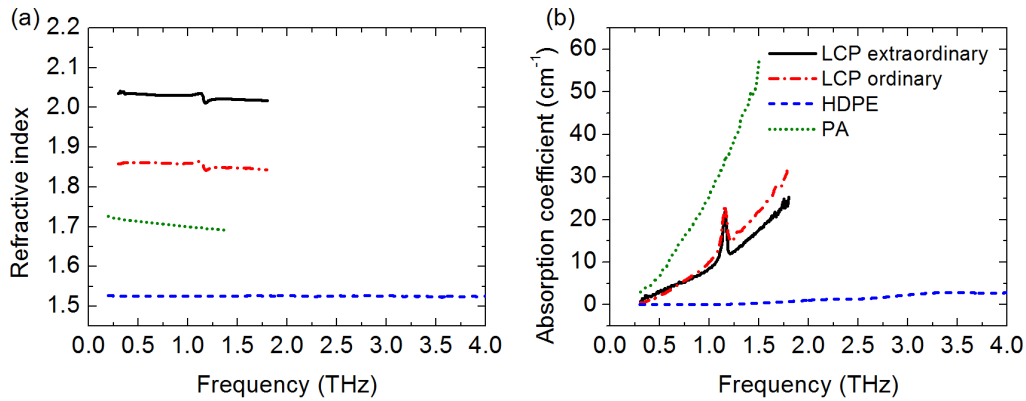


Figure 5: (a) Refractive indices and (b) absorption coefficients of high-density polyethylene (HDPE), polyamide (PA) and a liquid-crystal polymer (LCP) for ordinary and extraordinary polarization.

## Terahertz imaging

Besides terahertz spectroscopy, our system also lends itself for terahertz imaging. For proof-of-principle experiments, two test samples - a mail envelope with an enclosed birthday card featuring a built-in sound chip, and a polyamide step wedge - were mounted on an XY-scanner and moved through the focus of the terahertz beam. Figure 6 shows a photograph of the red envelope that contained the birthday card, and the corresponding terahertz image. The size of the scanned area was 150 mm x 60 mm and the step size was 0.5 mm. The XY-scanner moved at a speed of 3 mm / s, resulting in a total measurement time just below two hours. The terahertz image clearly reveals the electronic board, and the speaker at the center of the envelope.

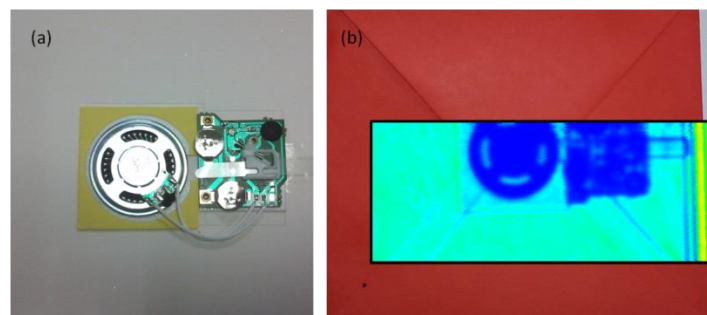


Figure 6: (a) Constituent parts of the birthday card: loudspeaker and circuit board. (b) Photograph and overlay terahertz image of the envelope.

Figure 7 shows a photograph of the polyamide step wedge and a 100 mm x 40 mm terahertz image. The scan speed was 2 mm / s, the step size was 0.3 mm and the total measurement time was 65 min. Red and blue colors denote sample regions with highest and lowest transmission, respectively, which correspond to the thinnest and

thickest sections of the step wedge. The two dark-blue spots reveal air bubbles, which are not visible from the outside. This result demonstrates the suitability of the system for non-destructive testing.

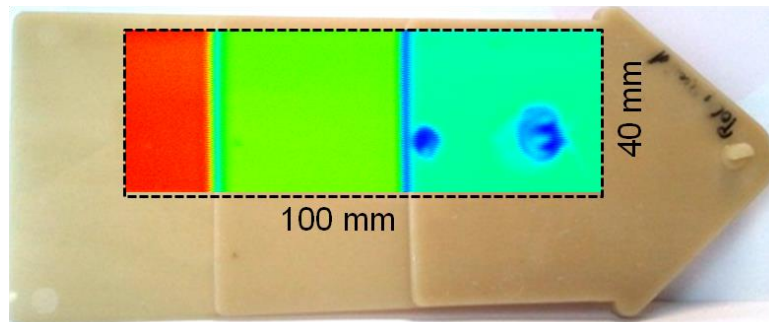


Figure 7: Photograph and overlay terahertz image of a polyamide step wedge.

## Conclusion and Outlook

In conclusion we have designed and characterized a compact, fiber-coupled terahertz time-domain spectrometer operating at an excitation wavelength of  $1.5 \mu\text{m}$ . The system combines mature telecom technology and photoconductive switches based on InAlAs/InGaAs multi-layer heterostructures. Owing to a highly precise mechanical delay stage, the spectrometer offers an outstanding dynamic range, along with a broad bandwidth and high measurement speed. Data acquisition rates range from 6 pulses / s to 60 pulses / s for sampling times of 200 ps and 15 ps, respectively. A precise reconstruction of the time axis reduces the timing jitter to approx. 1.3 fs, which translates into a peak dynamic range of 90 dB and an overall bandwidth of more than 4.5 THz, within a measurement time of less than one minute.

## Acknowledgement

The authors would like to thank Nicola Kocic of the Süddeutsche Kunststoffzentrum (SKZ) for providing the polyamide sample.

## References

- [1] D. Saeedkia, Ed., *Handbook of terahertz technology for imaging sensing and communications*. Woodhead Publishing Series in Electronic and Optical Materials, 2013.
- [2] M. van Exter, C. Fattinger, and D. Grischkowsky, "Terahertz time-domain spectroscopy of water vapor," *Opt. Lett.*, vol. 14, pp. 1128–1130, 1989.
- [3] D. Grischkowsky, S. Keiding, M. van Exter, and C. Fattinger, "Far-infrared time-domain spectroscopy with terahertz beams of dielectrics and semiconductors," *J Opt Soc Am B*, vol. 7, pp. 2006–2015, 1990.
- [4] P. U. Jepsen, D. G. Cooke, and M. Koch, "Terahertz spectroscopy and imaging – Modern techniques and applications," *Laser Photonics Rev.*, vol. 5, pp. 124–166, 2011.
- [5] M. Zalkovskij, C. Z. Bisgaard, A. Novitsky, R. Malureanu, D. Savastru, A. Popescu, P. U. Jepsen, and V. Lavrinenko, "Ultrabroadband terahertz spectroscopy of chalcogenide glasses," *Appl. Phys. Lett.*, vol. 100, p. 031901, 2012.
- [6] S. Tani, F. Blanchard, and K. Tanaka, "Ultrafast carrier dynamics in graphene under high electric field," *Phys. Rev. Lett.*, vol. 109, p. 166603, 2012.
- [7] C. H. Zhang, G. F. Zhao, B. B. Jin, Y. Y. Hou, H. H. Jia, J. Chen, and P. H. Wu, "Terahertz imaging on subcutaneous tissues and liver inflamed by liver cancer cells," *Terahertz Sci. Technol.*, vol. 5, no. 3, pp. 114–123, 2012.
- [8] H.-B. Liu, H. Zhong, N. Karpowicz, Y. Chen, and X.-C. Zhang, "Terahertz Spectroscopy and Imaging for Defense and Security Applications," *Proc. IEEE*, vol. 95, no. 8, pp. 1514–1527, Aug. 2007.

- [9] M. C. Beard, G. M. Turner, and C. A. Schmuttenmaer, "Terahertz spectroscopy," *J. Phys. Chem. B*, vol. 106, pp. 7146–7159, 2002.
- [10] J. A. Zeitler, P. F. Taday, D. A. Newnham, M. Pepper, K. C. Gordon, and T. Rades, "Terahertz pulsed spectroscopy and imaging in the pharmaceutical setting - A review.," *J. Pharm. Pharmacol.*, vol. 59, pp. 209–223, Feb. 2007.
- [11] C. A. Schmuttenmaer, "Exploring Dynamics in the Far-Infrared with Terahertz Spectroscopy," *Chem. Rev.*, vol. 104, pp. 1759–1779, 2004.
- [12] D. M. Mittleman, M. Gupta, R. Neelamani, R. G. Baraniuk, J. V. Rudd, and M. Koch, "Recent advances in terahertz imaging," *Appl. Phys. B*, vol. 68, pp. 1085–1094, 1999.
- [13] H. Roehle, R. J. B. Dietz, H. J. Hensel, J. Böttcher, H. Künzel, D. Stanze, M. Schell, and B. Sartorius, "Next generation 1.5  $\mu\text{m}$  terahertz antennas : mesa-structuring of InGaAs / InAlAs photoconductive layers," *Opt. Express*, vol. 18, pp. 2296–2301, 2010.
- [14] B. Sartorius, H. Roehle, H. Künzel, J. Böttcher, M. Schlak, D. Stanze, H. Venghaus, and M. Schell, "All-fiber terahertz time-domain spectrometer operating at 1.5  $\mu\text{m}$  telecom wavelengths," *Opt. Express*, vol. 16, no. 13, pp. 9565–9570, 2008.
- [15] D. M. Leitner, M. Gruebele, and M. Havenith, "Solvation dynamics of biomolecules: modeling and terahertz experiments.," *HFSP J*, vol. 2, no. 6, pp. 314–323, Dec. 2008.
- [16] D. Molter, F. Ellrich, T. Weinland, S. George, M. Goiran, F. Keilmann, and R. Beigang, "High-speed terahertz time-domain spectroscopy of cyclotron resonance in pulsed magnetic field," *Opt. Express*, vol. 18, no. 25, pp. 26163–26168, 2010.
- [17] N. Krumbholz, T. Hochrein, N. Vieweg, I. Radovanovic, I. Pupeza, M. Schubert, K. Kretschmer, and M. Koch, "Degree of Dispersion of Polymeric Compounds Determined With Terahertz Time-Domain Spectroscopy," *Polym Eng Sci*, vol. 51, pp. 109–116, 2011.
- [18] D. H. Auston, K. P. Cheung, and P. R. Smith, "Picosecond photoconducting Hertzian dipoles," *Appl. Phys. Lett.*, vol. 45, p. 284, 1984.
- [19] R. J. B. Dietz, M. Gerhard, D. Stanze, M. Koch, B. Sartorius, and M. Schell, "THz generation at 1.55  $\mu\text{m}$  excitation : six-fold increase in THz conversion efficiency by separated photoconductive and trapping regions," *Opt. Express*, vol. 19, pp. 25911–25917, 2011.
- [20] R. J. B. Dietz, B. Globisch, M. Gerhard, A. Velauthapillai, D. Stanze, and M. Schell, "64  $\mu\text{W}$  pulsed terahertz emission from growth optimized InGaAs/InAlAs heterostructures with separated photoconductive and trapping regions," *Appl. Phys. Lett.*, vol. 103, no. 6, p. 061103, 2013.
- [21] B. Globisch, R. J. B. Dietz, D. Stanze, T. Göbel, and M. Schell, "Carrier dynamics in Beryllium doped low-temperature-grown InGaAs/InAlAs," *Appl. Phys. Lett.*, vol. 104, p. 172103, Apr. 2014.
- [22] R. J. B. Dietz, B. Globisch, H. Roehle, D. Stanze, T. Göbel, and M. Schell, "Influence and adjustment of carrier lifetimes in photoconductive pulsed terahertz detectors based on InGaAs/InAlAs: Towards 6 THz bandwidth and 90 dB dynamic range," *Submitt. to Opt. Express*.
- [23] P. U. Jepsen and B. M. Fischer, "Dynamic range in terahertz time-domain transmission and reflection spectroscopy.," *Opt Lett*, vol. 30, no. 1, pp. 29–31, Jan. 2005.
- [24] W. Withayachumnankul, B. M. Fischer, H. Lin, and D. Abbott, "Uncertainty in terahertz time-domain spectroscopy measurements," *J Opt Soc Am B*, vol. 25, pp. 1059–1072, 2008.
- [25] W. Withayachumnankul, H. Lin, S. P. Micken, B. M. Fischer, and D. Abbott, "Analysis of Measurement Uncertainty in THz-TDS," *Proc SPIE*, vol. 6593, pp. 659326–659326–18, May 2007.
- [26] M. van Exter and D. Grischkowsky, "Characterization of an optoelectronic terahertz beam system," *IEEE Trans. Microw. Theory Tech.*, vol. 38, pp. 1684–1691, 1990.
- [27] L. Duvillaret, F. Garet, and J.-L. Coutaz, "Influence of noise on the characterization of materials by terahertz time-domain spectroscopy," *J Opt Soc Am B*, vol. 17, pp. 452–460, 2000.
- [28] H. A. Haus and A. Mecozzi, "Noise of mode-locked lasers," *IEEE J. Quantum Elect.*, vol. 29, pp. 983–996, 1993.
- [29] A. Wojdyla and G. Gallot, "Phase noise investigation in terahertz Time-Domain Spectroscopy measurements," *Proc IRMMW*, 2013.
- [30] N. Cohen, J. W. Handley, R. D. Boyle, S. L. Braunstein, and E. Berry, "Experimental Signature of Registration Noise in Pulsed Terahertz Systems," *Fluct Noise Lett*, vol. 6, no. 0, pp. L77–L84, 2006.
- [31] E. Castro-Camus, L. Fu, J. Lloyd-Hughes, H. H. Tan, C. Jagadish, and M. B. Johnston, "Photoconductive response correction for detectors of terahertz radiation," *J. Appl. Phys.*, vol. 104, no. 5, p. 053113, 2008.
- [32] X. Xu, X. Wang, and L. Wang, "Deviation of optical constants extracted in terahertz transmission spectroscopy.," *Appl. Opt.*, vol. 45, no. 4, pp. 648–52, Feb. 2006.
- [33] J. Letosa, M. García-Gracia, J. M. Forniés-Marquina, and J. M. Artacho, "Performance Limits in TDR Technique by Monte Carlo Simulation," *IEEE T Magn*, vol. 32, pp. 4–7, 1996.
- [34] S. M. Rytov, Y. A. Kravtsov, and V. I. Tatarskii, *Principles of statistical radiophysics 4. Wave propagation through random media*. Springer Verlag, 1989.
- [35] M. Theuer, R. Beigang, and D. Grischkowsky, "Highly sensitive terahertz measurement of layer thickness using a two-cylinder waveguide sensor," *Appl. Phys. Lett.*, vol. 97, no. 7, p. 071106, 2010.

- [36] C. D. Stoik, "Nondestructive evaluation of aircraft composites using terahertz time domain spectroscopy," *PhD Thesis, Air Force Inst. Technol.*, 2008.
- [37] L. Wu, "Optimierung des Signal-Rausch-Abstands von AD-Wandlern," *Elektron. Ind.*, vol. 11, pp. 50–52, 2010.
- [38] N. Vieweg, B. M. Fischer, M. Reuter, P. Kula, R. Dabrowski, M. a. Celik, G. Frenking, M. Koch, and P. U. Jepsen, "Ultrabroadband terahertz spectroscopy of a liquid crystal," *Opt. Express*, vol. 20, no. 27, pp. 28249–28256, Dec. 2012.
- [39] N. Vieweg and A. Deninger, "Terahertz waves and liquid crystals: prospects and challenges," *Proc. SPIE*, vol. 8642, p. 86420, 2013.
- [40] M. Scheller, C. Jansen, and M. Koch, "Analyzing sub-100-  $\mu\text{m}$  samples with transmission terahertz time domain spectroscopy," *Opt. Commun.*, vol. 282, pp. 1304–1306, 2009.
- [41] R. Piesiewicz, C. Jansen, S. Wietzke, D. Mittleman, M. Koch, and T. Kürner, "Properties of Building and Plastic Materials in the THz Range," *Int J Infrared Milli Terahz Waves*, vol. 28, pp. 363–371, 2007.
- [42] U. A. Khan, N. Nguyen, and M. N. Afsar, "Millimeter and submillimeter-wave dielectric measurements of household powders using fourier transform spectroscopy," *IEEE T Instrum Meas*, vol. 57, no. 2, pp. 286 – 293, 2008.



**Paper VIII:**

**Optics Letters, vol. 39, no. 22, pp. 6482–6485, 2014**



# All fiber coupled THz-TDS system with kHz measurement rate based on electronically controlled optical sampling

Roman J.B. Dietz<sup>1,\*†</sup>, Nico Vieweg<sup>2,†</sup>, Thomas Puppe<sup>2,†</sup>, Armin Zach<sup>2</sup>, Björn Globisch<sup>1</sup>, Thorsten Göbel<sup>1</sup>, Patrick Leisching<sup>2</sup> and Martin Schell<sup>1</sup>

*Fraunhofer Institute for Telecommunications, Heinrich Hertz Institute, Einsteinufer 37, 10587 Berlin, Germany*  
*TOPTICA Photonics AG, Lochhamer Schlag 19, 82166 Gräfelfing, Germany*

<sup>†</sup> Authors with equal contribution

\*Corresponding author: Roman.Dietz@hhi.fraunhofer.de

Received Month July, 2013; revised Month X, XXXX; accepted Month X, XXXX; posted Month X, XXXX (Doc. ID XXXXX); published Month X, XXXX

We demonstrate a completely fiber coupled THz time-domain spectrometer system based on electronically controlled optical sampling with two erbium-doped femtosecond fiber lasers at a central wavelength of 1560 nm. The system employs optimized InGaAs/InAlAs photoconductive antennas for THz generation and detection. With this system we achieve measurement rates of up to 8 kHz and up to 180 ps scan range. We further achieve 2 THz spectral bandwidth and a dynamic range of 76 dB at only 500 ms measurement time.

*OCIS Codes: (300.6495) Spectroscopy, terahertz, (040.2235) Far infrared or terahertz.*

Steady progress of terahertz (THz) technologies, especially employing 1.55  $\mu\text{m}$  fiber lasers and InGaAs-based photoconductive antennas (PCA) has led to reliable and easy-to-handle THz systems within recent years. Potential applications for scientific and industrial applications are e.g. THz imaging, spectroscopy, chemical sensing or nondestructive testing [1–5]. Nevertheless, up to now, the vast majority of THz systems and devices are still driven by scientific research interests. As a consequence, system size and cost as well as measurement speeds have been less important than flexibility and spectroscopic performance. In the future, however, for widespread industrial applications of THz-time domain spectroscopy (TDS), the systems will have to be robust, compact, highly cost efficient, and measurement speed will have to increase to several kHz from today's several Hz. Furthermore, some promising applications for THz-TDS, such as multilayer thickness determination, require the recording of several reflected THz pulses and therefore long time delay scan ranges of several hundred picoseconds. Yet, measurement rates in the kHz range with hundreds of picoseconds of time delay are almost impossible to obtain with linear or rotary mechanical stages, due to the inertia of the involved moving masses and restrictions to reasonable sizes. Hence one has to utilize electro-optically controlled time delays, i.e. systems based on changing the repetition rate of the pulse laser source, which are able to fulfill the aforementioned technical requirements. Several methods have been proposed for this purpose, i.e. asynchronous optical sampling (ASOPS) [6,7], optical sampling by cavity tuning (OSCAT) [8,9] and electrically controlled

optical sampling (ECOPS) [10–12]. All three techniques have their respective advantages and disadvantages.

The main advantage of OSCAT is the use of only one laser source instead of two, as it is the case for ECOPS and ASOPS. However, OSCAT requires a very long fiber in either the pump or probe arm to obtain a sufficient scanning range. This inevitably deteriorates the laser pulse shape in the respective arm which limits the obtainable THz bandwidth. ASOPS allows for a scan range determined by the laser repetition frequency and at the same time for scan rates of several kHz. A drawback of ASOPS is the fixed scan range. In Terahertz TDS, a scan range of several hundreds of ps, e.g. 400 ps, are sufficient for almost every application, while the typical values are mostly in the range of 100 ps. Unfortunately, in ASOPS systems which employ compact and cost-efficient fiber lasers with repetition rates of 100 MHz or 250 MHz the scan ranges are fixed to 10 ns and 4 ns, respectively. As a consequence, the systems produce a lot of measurement dead time and thus exhibit a decreased measurement time efficiency of less than 10 %. In other words, ASOPS systems employing 100 MHz or 250 MHz lasers partly lose the advantage of the high scan speeds, as signal averaging for increased signal to noise ratios consume much more time than systems featuring flexible scan ranges. An alternative is to use 1 GHz laser oscillators, that would reduce the scan range to at least 1 ns. Yet, as cost-efficient and robust gigahertz-fiber-laser are not commercially available, one has to employ expensive and complex 1 GHz-Titanium sapphire laser systems [6,7]. Such systems additionally require much more expensive and bulky free space optics, since mature

and cost-efficient 1.55  $\mu\text{m}$  fiber components cannot be employed.

Thus, we believe that ECOPS offers the largest flexibility, as it allows for both an adjustable scan range and for scan rates of several kHz. By using ECOPS instead of ASOPS, the authors of [11] found a reduction of the measurement time of a THz TDS system by a factor of 50 for 100 MHz lasers. Furthermore, employing cost efficient erbium-doped fiber laser at 1560 nm emission mitigates the cost increase due to the necessity of two lasers. In this paper we present the first all fiber-coupled ECOPS based THz-TDS system operating at 1560 nm. With this system we obtain measurement rates of up to 8 kHz and up to 180 ps of time delay scan range.

The presented system consists of two erbium-doped fiber oscillators (TOPTICA FemtoFErb 1560) which are passively mode-locked by a semiconductor saturable absorber mirror and emit at a center wavelength of 1560 nm. The lasers yield optical pulse durations of < 100 fs with approx. 80 mW average power at a repetition frequency of 100 MHz.

To employ the ECOPS principle, one of the lasers (laser 1) comprises a piezo-electric crystal within the oscillator cavity to electronically control the cavity length. For this purpose there is a very short free space part inside the oscillator, where the light is coupled out of the fiber oscillator and directed onto a mirror attached to the piezo crystal. The second laser (laser 2) has a fixed cavity length. The repetition frequency of both lasers can be slowly adjusted by oscillator temperature. The repetition frequency  $f_1$  of laser 1 is then phase-locked to the repetition frequency  $f_2$  of laser 2 by electronically controlling the piezo displacement by the use of a high bandwidth, 21 bit digital controller (TOPTICA DigiLock 110). By additionally imposing a periodical, e.g. sinusoidal, modulation onto the piezo crystal, the phase difference  $\Delta\Phi(t)$  between the two lasers frequencies can be modulated around its zero position. Thus the laser pulses of laser 1 exhibit a time delay with respect to the pulses of laser 2 which is given by  $\tau(t)=\Delta\Phi(t)/2\pi f$ . [10,11].

Since the system targets very high measurement rates, the THz emitter and detector have to be chosen carefully in order to obtain sufficiently high measurement signal strengths. Considering a 200 ps scan range with a 50 fs delay time resolution at 2 kHz measurement rate, the measurement bandwidth of the detection electronics has to be at least 8 MHz. This sets an upper limit to the amplification that can be used in the detection electronics. For the generation and detection of the THz radiation we therefore employed highly efficient photoconductive antennas (PCA) based on InGaAs/InAlAs heterostructures. The emitter PCAs were based on a InGaAs/InAlAs heterostructures optimized for high THz powers due to increased carrier mobility and which have been shown to exhibit output powers of up to 64  $\mu\text{W}$  [13,14]. The detector PCAs were made from low

temperature grown (LTG) beryllium doped InGaAs/InAlAs heterostructures, with short carrier lifetimes of a few hundred femtoseconds, which enable high THz bandwidth and dynamic range [15,16]. Both emitter and detector feature a mesa-design of the photoconductive gap to further improve their performance [17] and were packaged into fiber coupled housings for an improved stability of the optical alignment. The combination of these PCAs yields detector current signals of up to 1  $\mu\text{A}$  and therefore supports the aforementioned low amplification requirement formidably. The detector current was amplified using a transimpedance amplifier with a 3 dB bandwidth of 3.5 MHz and an amplification factor of  $10^5$ . The amplified signal was then digitized with a sampling rate of 21 MS/s.

To build a completely fiber coupled THz-TDS system, both lasers comprised an internal pre-compensation of the dispersion of 6 m of SMF 28 fiber, by employing dispersion compensating fiber. The pulse widths of both lasers after the complete fiber length (i.e. at emitter and receiver position) were approximately 140 fs.

Since  $\Delta\Phi(t)$  is modulated in a sinusoidal manner, a linear time axis had to be extracted from the measurement data. The control loop reacts on the applied modulation frequency and its error signal follows the sinusoidal modulation, yet with a certain phase offset and superimposed higher harmonics of the modulation frequency. The error signal was used as a measure of the actual delay timing of the system. First a sinusoidal model function, together with its 3rd and 5th harmonics, was used to fit the measured error signal. The measurement time axis was then replaced by the y-axis of the fit function. Subsequently, the new time axis and signal data were interpolated to obtain equidistant time steps. The exact scale of the linear time axis was then obtained by measuring the THz transmission through a 500  $\mu\text{m}$  thick silicon wafer, which served as a Fabry-Perot etalon for the THz beam, generating one transmitted THz pulse followed by multiple reflected THz pulses that are spread equidistant in time.

The measurement records both the back and the forth motion of the phase difference  $\Delta\Phi(t)$ , i.e. of the time delay, and thus we measure two THz pulse traces for each piezo oscillation cycle. At a scan rate of e.g. 1 kHz we thus obtain a measurement rate of 2 kHz.

An example of two pulse traces measured with the ECOPS system at measurement rates of 2 kHz and 8 kHz (inset) is shown in Fig. 1. The displayed pulse traces are single pulse traces and hence correspond to total measurement times of 500  $\mu\text{s}$  and 125  $\mu\text{s}$ , respectively. For the 2 kHz measurement rate, it was possible to obtain a scan range of up to 180 ps. For 8 kHz measurement rate, the overall time delay was limited to approximately 20 ps, due to limitations of the piezo crystal. However, a delay time of 20 ps equals 6 mm in air and is thus long enough for measurements of e.g. thin films and coatings.

The different appearance of the THz pulses is mostly due to the different time scales, except for a small oscillation observed in front of the main pulse in the 2 kHz measurement. This feature originates from a second optical excitation of the detector caused by a reflection of the unabsorbed portion of the optical excitation pulse at the interface of PCA chip and SI-lens, which then excites the PCA detector for a second time. This second excitation of the detector results in a pre-pulse in the TDS signal, due to the convolutional nature of TDS measurements. These pre-pulses are significantly increased if the back-side of the PCA chip (wafer) is polished. For the measurements of this publication we used different, but similarly grown wafers, to build several fiber-coupled detectors. Some of the wafers were polished (to be able to perform additional pump probe measurements) some of the wafers were not polished. In case of the 2 kHz measurement the detector chip was polished and thus there is a pre-pulse in the TDS trace, whereas the detector PCA used in the 8°kHz measurement was not polished. However, this pre-pulse oscillation has no spectroscopic significance and can therefore be completely ignored.

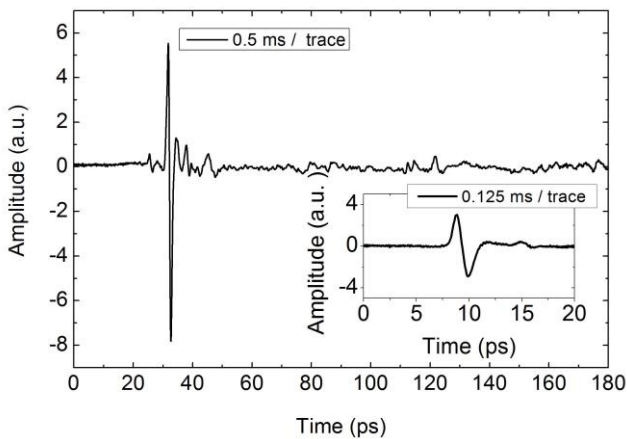


Fig. 1. Single THz pulse traces obtained with the ECOPS system at measurement rates of 2 kHz and 8 kHz (inset).

The Fourier spectrum obtained from averaging 1000 pulse traces recorded at 2 kHz is shown in Fig. 2(a). For a total measurement time of 500 ms at 2 kHz, i.e. an average over 1000 traces, the system reaches a dynamic range (DR) of approx. 76 dB. In this case the usable THz bandwidth is in excess of 2 THz, as illustrated by the clearly resolved water vapor absorption lines in the spectrum of Fig 2(a). For a single recorded pulse trace at 2 kHz, i.e. 500  $\mu$ s measurement time, the dynamic range was still as high as 47 dB [Fig. 2(b)]. The DR shows a logarithmic behavior as a function of the number of averages, as indicated by the linear fit to the logarithmic plot of Fig. 2(b).

It should be noted that the THz bandwidth of the present system is still lower than values that have previously been demonstrated with equal PCAs and lasers using a high precision mechanical delay, which

reached up to 6 THz [16,18]. There are two major influences that limit the THz bandwidth in the present system. The first is due to an insufficiently optimized fiber delivery that resulted in a broadening of the laser pulse width of 140 fs with additional small leading or trailing pulses and which in turn reduces the THz bandwidth [19]. The pulse length can be further optimized in future systems to yield pulse widths <100 fs.

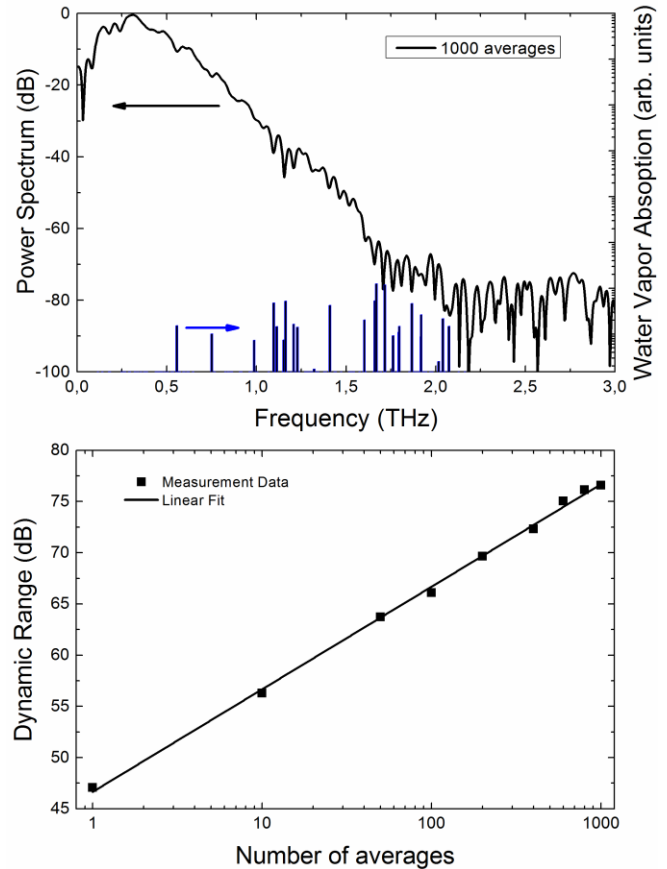


Fig. 2.(a) Fourier spectrum for the pulse trace shown in Fig.1 recorded at 2 kHz measurement rate and averaged over 1000 single traces together with water vapor absorption lines. (b) The dependence of the dynamic range on the number of averaged pulse traces at 2 kHz measurement rate (full symbols) and a linear fit to the logarithmic plot (solid line).

The second influence is the timing jitter of the laser pulses, i.e. fluctuation of their time position, due to variations of the laser repetition rates with respect to each other. The total static timing jitter of two oscillators, measured with a balanced optical cross-correlator [20] integrated from 10 Hz (1 kHz) to the Nyquist frequency, is <40 fs (<20fs) in the static case, i.e. without phase modulation. The dynamic jitter over the course of one piezo oscillation, i.e. with phase modulation, was estimated from comparing arbitrary single THz pulse traces to be in the range of 50 fs. The fluctuations within one oscillation period are correspondingly lower. We are confident that the jitter can be further reduced by employing an improved mechanical mounting of the piezo crystal. Furthermore there are several options to further

improve the frequency lock of the lasers, such as the use of higher harmonics of the error signal [11], which has not yet been employed in the present publication. Considering that the employed PCA antennas generally allow for much higher THz bandwidths [16], we assume that above improvements should help to allow for bandwidth in excess of 4 THz.

However, the presented system already outperforms the previously demonstrated fiber-laser based ECOPS systems in terms of jitter by more than a factor of 3 and increases the maximum measurement speed by more than a factor of 10 [10,12]. Additionally, it features a much more compact and robust laser design as well as a complete fiber-coupled delivery. When compared to the large and expensive Ti:Sapphire laser system with 20 fs laser pulses and free-space optics of [11], we are able to obtain the same bandwidth and dynamic range for half the measurement time at even higher measurement rate and longer scan range. In summary, we attribute the good performance to the combination of the high THz signal of the PCAs with of improved stability of the laser system, which is due to a more robust laser design and high precision control electronics.

In conclusion we have demonstrated an all-fiber-coupled ECOPS based THz-TDS system employing high performance InGaAs/InAlAs heterostructure PCAs with maximum measurement rates of up to 8 kHz. We have shown that a THz bandwidth of approx. 2 THz with a dynamic range of 76 dB is obtainable for measurement times as low as 500 ms at 2 kHz measurement rate with a total scan range of 180 ps. With such compact, robust and fast measurement systems at hand the widespread employment of THz technology for industrial applications comes within reach.

This work was in part funded by the “Zentrales Innovationsprogramm Mittelstand” of the German Federal Ministry of Economic Affairs and Energy under grant numbers KF2110318 AB1 and KF2806204 AB1.

## References

1. P. U. Jepsen, D. G. Cooke, and M. Koch, "Terahertz spectroscopy and imaging - Modern techniques and applications," *Laser Photon. Rev.* 5, 124–166 (2011).
2. W. Chan and M. Moravec, "Terahertz imaging with compressed sensing and phase retrieval," *Opt. Lett.* 33, 974–976 (2008).
3. M. Walther, B. Fischer, and A. Ortner, "Chemical sensing and imaging with pulsed terahertz radiation," *Anal. Bioanal. Chem.* 397, 1009–1017 (2010).
4. M. Hangyo, T. Nagashima, and S. Nashima, "Spectroscopy by pulsed terahertz radiation," *Meas. Sci. Technol.* 13, 1727 (2002).
5. C. Stoik, M. Bohn, and J. Blackshire, "Nondestructive evaluation of aircraft composites using transmissive terahertz time domain spectroscopy," *Opt. Express* 16, 17039–17051 (2008).
6. A. Bartels, A. Thoma, and C. Janke, "High-resolution THz spectrometer with kHz scan rates," *Opt. Express* 14, 430–437 (2006).
7. G. Klatt, R. Gebbs, C. Janke, T. Dekorsy, and A. Bartels, "Rapid-scanning terahertz precision spectrometer with more than 6 THz spectral coverage," *Opt. Express* 17, 22847–54 (2009).
8. T. Hochrein, R. Wilk, M. Mei, R. Holzwarth, N. Krumbholz, and M. Koch, "Optical sampling by laser cavity tuning," *Opt. Express* 18, 1613–7 (2010).
9. R. Wilk, T. Hochrein, M. Koch, M. Mei, and R. Holzwarth, "Terahertz spectrometer operation by laser repetition frequency tuning," *J. Opt. Soc. Am. B* 28, 592 (2011).
10. F. Tauser, C. Rausch, J. H. Posthumus, and F. Lison, "Electronically controlled optical sampling using 100 MHz repetition rate fiber lasers," in *SPIE Proc. SPIE 6881, Commercial and Biomedical Applications of Ultrafast Lasers VIII* (2008), Vol. 688100.
11. Y. Kim and D.-S. Yee, "High-speed terahertz time-domain spectroscopy based on electronically controlled optical sampling," *Opt. Lett.* 35, 3715–7 (2010).
12. S. Kray, F. Spöler, T. Hellner, and H. Kurz, "Electronically controlled coherent linear optical sampling for optical coherence tomography," *Opt. Express* 18, 9976–90 (2010).
13. R. J. B. Dietz, M. Gerhard, D. Stanze, M. Koch, B. Sartorius, and M. Schell, "THz generation at 1.55  $\mu\text{m}$  excitation : six-fold increase in THz conversion efficiency by separated photoconductive and trapping regions," *Opt. Express* 19, 122–126 (2011).
14. R. J. B. Dietz, B. Globisch, M. Gerhard, A. Velauthapillai, D. Stanze, H. Roehle, M. Koch, T. Göbel, and M. Schell, "64  $\mu\text{W}$  pulsed terahertz emission from growth optimized InGaAs/InAlAs heterostructures with separated photoconductive and trapping regions," *Appl. Phys. Lett.* 103, 061103 (2013).
15. B. Globisch, R. J. B. Dietz, D. Stanze, T. Göbel, and M. Schell, "Carrier dynamics in Beryllium doped low-temperature-grown InGaAs/InAlAs," *Appl. Phys. Lett.* 104, 172103 (2014).
16. R. J. B. Dietz, B. Globisch, H. Roehle, D. Stanze, T. Göbel, and M. Schell, "Influence and adjustment of carrier lifetimes in InGaAs/InAlAs photoconductive pulsed terahertz detectors : 6 THz bandwidth and 90dB dynamic range," *Opt. Lett.* 22, 615–623 (2014).
17. H. Roehle, R. J. B. Dietz, H. J. Hensel, J. Böttcher, H. Künzel, D. Stanze, M. Schell, and B. Sartorius, "Next generation 1.5 microm terahertz antennas: mesa-structuring of InGaAs/InAlAs photoconductive layers," *Opt. Express* 18, 2296–301 (2010).
18. N. Vieweg, F. Rettich, A. Deninger, H. Roehle, R. Dietz, T. Göbel, and M. Schell, "Terahertz-time domain spectrometer with 90 dB peak dynamic range," *J. Infrared, Millimeter, Terahertz Waves* 1–10 (2014).
19. L. Duvillaret, F. Garet, and J.-L. Coutaz, "Influence of noise on the characterization of materials by terahertz time-domain spectroscopy," *J. Opt. Soc. Am. B* 17, 452 (2000).
20. J. Kim, J. Chen, J. Cox, and F. Kärtner, "Attosecond-resolution timing jitter characterization of free-running mode-locked lasers," *Opt. Lett.* 32, 3519–21 (2007).

**Paper IX:**

**J. Infrared, Millimeter, Terahertz Waves, vol. 34, no. 3-4,  
pp. 231-237, 2013**



# Low temperature grown Be-doped InGaAs/InAlAs photoconductive antennas excited at 1030 nm

R. J. B. Dietz<sup>a</sup>, R. Wilk<sup>b</sup>, B. Globisch<sup>a</sup>, H. Roehle<sup>a</sup>, D. Stanze<sup>a</sup>, S. Ullrich<sup>a</sup>, S. Schumann<sup>c</sup>, N. Born<sup>c</sup>, M. Koch<sup>c</sup>, B. Sartorius<sup>a</sup> and M. Schell<sup>a</sup>

<sup>a</sup>Fraunhofer Institute for Telecommunications, Heinrich-Hertz-Institute, Berlin, Germany

<sup>b</sup>Menlo Systems GmbH, Martinsried, Germany

<sup>c</sup>Department of Physics, Philipps-Universität Marburg, Marburg, Germany

Email: Roman.Dietz@hhi.fraunhofer.de

**Abstract**—We demonstrate pulsed THz emission and detection in low temperature (LT) MBE grown Be-doped InGaAs/InAlAs multi-nanolayer structures for an excitation wavelength of 1030 nm. We obtained spectra with a bandwidth of up to 3 THz. Furthermore, we performed differential transmission experiments to investigate the material's relaxation time constants.

Terahertz (THz) technology is a rapidly developing field. In particular time-domain terahertz spectroscopy (THz TDS) [1-3] is a promising technique for which many applications are foreseen which range from industrial inspection [4-6], moisture mapping [7,8], investigation of cultural heritage [9], plant physiology [10] to medical diagnosis [11]. To further foster THz TDS, photoconductive THz emitters and detectors which can be excited at the telecom wavelength [12-14] are desired. In combination with 1550 nm femtosecond fiber lasers, cost-effective and mobile THz TDS systems [15] can be built. This is mostly due to the availability of competitive laser sources, easy fiber delivery and dispersion compensating fibers for dispersion management. However, Ytterbium-doped femtosecond fiber lasers operating at a center wavelength of approx. 1030 nm offer higher powers as compared to their 1550 nm counterparts. Hence, they are an interesting candidate for high power photoconductive terahertz generation. Recently, it was demonstrated that GaAsBi can be used as a photoconductive material at this wavelength [16]. An alternative material could be Be-doped LT-grown InGaAs/InAlAs based multi-nanolayer structures (MNLS). Antennas based on this material have been successfully demonstrated to operate with an excitation wavelength of 1550 nm [13,15].

In this paper, we evaluate the potential of MBE grown  $\text{In}_{0.53}\text{Ga}_{0.47}\text{As}/\text{In}_{0.52}\text{Al}_{0.48}\text{As}$  MNLS lattice matched to InP as a photoconductive material for 1030 nm excitation. The structure was made of 100 periods of a 12 nm InGaAs layer followed by an 8 nm InAlAs layer. The samples were grown at a substrate temperature of approx. 130 °C following an in-situ annealing step at 500 °C for 60 min. The band-gap (valence to first sub-band) of the InGaAs layers is approx. 0.76 eV ( $\approx 1630$  nm). The band-

gap of the InAlAs layers is approx. 1.47 eV ( $\approx 850$  nm), i.e. transparent for 1030 nm excitation. After growth the material was processed with mesa-type strip-line antennas with 25  $\mu\text{m}$  gap and mesa-type dipole antennas with 10  $\mu\text{m}$  gap, for emitter (Tx) and detector (Rx) respectively [13]. Additionally, the antennas were packaged into fiber-coupled modules to ensure precise and stable optical coupling of the antennas, with a laser spot size on the semiconductor gap of approx. 10  $\mu\text{m}$ . The packaged antennas performance was subsequently examined in a THz TDS setup with a mode-locked femtosecond ytterbium-doped fiber oscillator laser by Menlo Systems (Orange Laser Head N Sync with Yb-Compressor) as excitation source. In addition, using the same laser, differential transmission experiments were performed on similar MNLSs in order to investigate the trapping and relaxation dynamics of the material. Furthermore, we compare these results with results obtained from similar experiments, for which the excitation source was a femtosecond Erbium-doped fiber laser with a center wavelength of 1550 nm. For the TDS measurements at 1550 nm we used fiber-coupled modules with standard SMF28 fiber. The PCAs that were built into the Tx module for 1550 nm excitation came from the same wafer as the PCAs employed in the Tx module for 1030 nm excitation. The same was the case for the Rx modules.

Fig. 1 shows the normalized THz pulse traces obtained for excitation of the fibre coupled modules with 1030 nm and 1550 nm. In both cases the respective excitation power was chosen in a way that the incident photon density was  $1.65 \times 10^{14} \text{ cm}^{-2}$ , i.e. 5 mW for the 1030 nm excitation and 3.32 mW for the 1550 nm excitation, for both receiver and emitter. The optical pulse lengths were approx. 120 fs for the 1030 nm and 90 fs for the 1550 nm excitation. The applied emitter bias was chosen to be 20V in both cases.

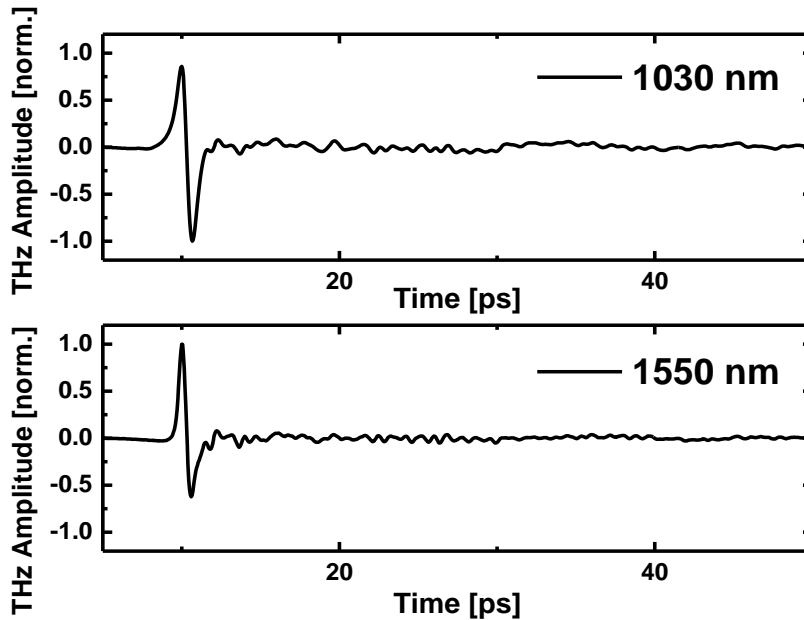


Fig. 1: THz TDS pulse traces for 1030 nm and 1550 nm wavelength excitation of Be-doped annealed MNLS grown at  $T_s=130^\circ\text{C}$

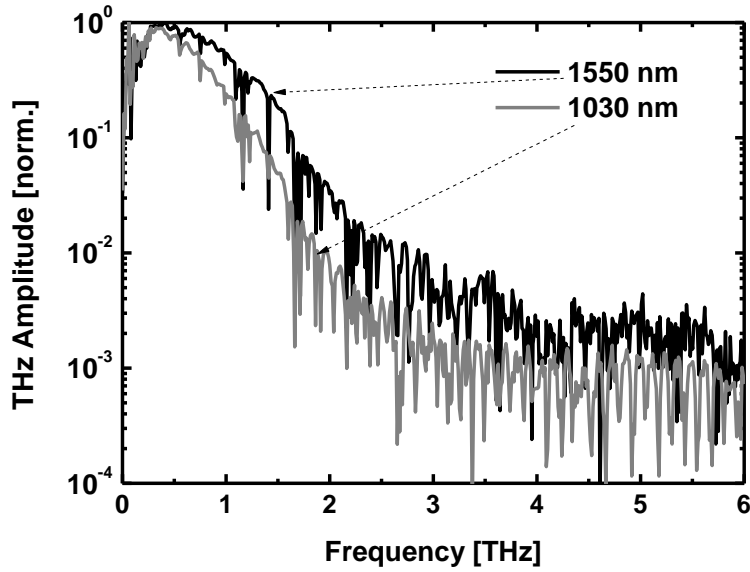


Fig. 2: Corresponding normalized FFT Spectrum for the pulses in Fig.2 for excitation with 1030 nm and 1550 nm wavelength.

Fig. 2 shows the normalized FFT spectra obtained from the corresponding pulses. Both spectra clearly exceed 3 THz of bandwidth. However, the spectrum obtained for the 1030 nm excitation shows a stronger decrease of amplitude over frequency than in case of 1550 nm excitation. The slightly longer excitation pulse length in case of the 1030 nm laser might have a part in this behavior. Additionally, the cross section for carrier trapping into defect states could be reduced for electrons with higher energies. Since an excitation with 1030 nm results in hot electrons with energies well above the conduction band edge, this might have an impact. The matter will be further discussed below.

To evaluate the overall THz TDS performance of the antennas at 1030 nm we measured the detected THz signal in dependence on the applied emitter bias from 1 up to 20 Volts (Fig.3). The incident photon density was kept at a value of approx.  $1.65 \times 10^{14} \text{ cm}^{-2}$ . In both cases, one can note a threshold like behavior for lower bias voltages and a slightly super linear behavior for higher voltages. However, for the 1030 nm excitation the detected THz signal at the detector is more than one order of magnitude, i.e. 35 times, higher as compared to the 1550 nm excitation.

A possible contribution to this increase is the strongly enhanced absorption of 1030 nm wavelength in the InGaAs nano-layers compared to 1550 nm excitation, i.e. a factor of  $\approx 4-5$  [17]. We assume a linear dependence between incident photon density and generated carrier density, as well as a linear dependence between the carrier density and the generated THz emission on the emitter side, as well as on the THz sensitivity on detector side. Under these assumptions the higher absorption contributes multiplicatively to the detected THz signal resulting in a signal increase up to a factor of 25. For the pulses centered at 1550 nm, the estimated average absorption depth is  $1.30 \mu\text{m}$ . Since the overall InGaAs width is  $100 \times 12 \text{ nm} = 1.2 \mu\text{m}$ , approx. 40% of the light passes the MNLS without being absorbed. For the 1030 nm excitation the absorption depth is approx.  $0.3 \mu\text{m}$ , so practically all of the

photons are absorbed over a short distance within the sample, thus generating a higher carrier density as compared to 1550 nm excitation. This suggests that the THz performance is not only dependent on the absolute amount of generated carriers but rather the carrier density.

On the other hand, since the valley separation between  $\Gamma$ -valley and L-valley in InGaAs at 300 K is approx. 0,55 eV [18], we would expect the probability for inter-valley scattering processes to increase within the applied bias field range for hot electrons, i.e. 1030 nm excitation (1.2 eV). Intervalley scattering reduces the average electron mobility due to the strongly increased effective mass in the L-valley, i.e.  $0.29 \times m_0$  compared to  $0.041 \times m_0$  [19]. The lower mobility in turn should reduce the THz emission efficiency. However, this effect is in contradiction with the observed monotonic increase of the THz signal over the complete applied bias field range. Furthermore, the devices show the same qualitative behavior for both wavelengths. This leads to the assumption that intervalley scattering does not affect the THz generation efficiency. Nevertheless, additional measurements have to be conducted in order to further investigate the origin of the increased efficiency.

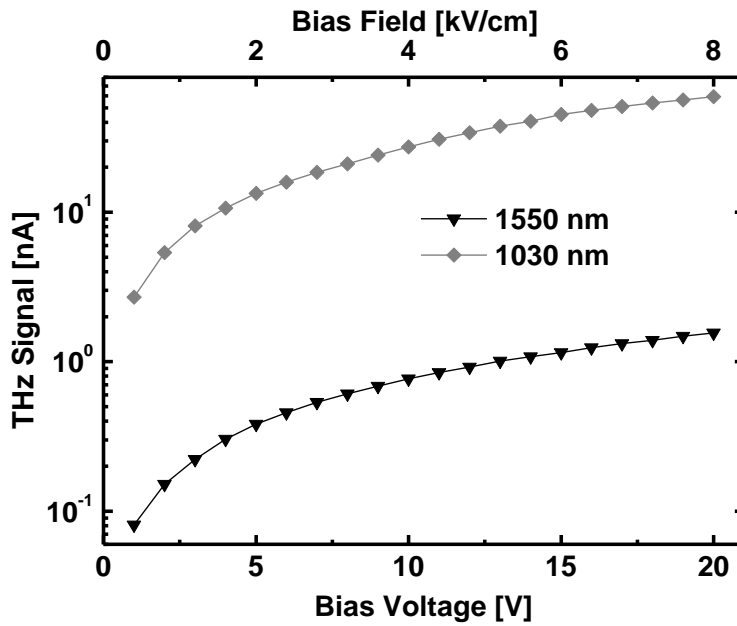


Fig. 3: Detected THz signal amplitude in dependence on the emitter bias voltage for 1550 nm and 1030 nm wavelength excitation and an incident photon density on receiver and emitter of  $1.65 \times 10^{14} \text{ cm}^{-2}$  for both wavelengths.

To further investigate the carrier trapping and recombination dynamics we performed differential transmission experiments using the abovementioned lasers as excitation source. The differential transmission (DT) data obtained from a MLNS sample, similar to the THz antenna material, for 1550 nm and 1030 nm, and at two different pump powers for each wavelength is depicted in Fig.4 and Fig.5. The values for the probe powers were chosen such that they correspond to equal photon densities for the respective wavelengths, i.e.  $\approx 5 \times 10^{13} \text{ cm}^{-2}$ . The same holds true for the lower pump

power value for the respective wavelength. In case of the higher pump power we were limited by the experimental setup, nevertheless reaching comparable excitation densities. A significant increase in the carrier relaxation time is visible when excited with 1030 nm as compared to an excitation with 1550 nm. For all DT measurements we see two decay components in our signal. A fast decay component on a timescale of several hundred femtoseconds to picoseconds and a long decay component on the picosecond to tens of picoseconds range. Both decay components are dependent on the excitation wavelength. In order to obtain quantitative figures, i.e. decay time constants, we applied a simple bi-exponential fit to our measurement data. The results are given in Table. 1.

	<b>1 mW Pump; 1550 nm</b>	<b>8 mW Pump; 1550 nm</b>	<b>1.5 mW Pump; 1030 nm</b>	<b>10 mW Pump; 1030 nm</b>
$\tau_1$ [ps]	<b>0.23 ± 0.001</b>	<b>0.27 ± 0.002</b>	<b>1.2 ± 0.08</b>	<b>2.2 ± 0.08</b>
$\tau_2$ [ps]	<b>2.7 ± 0.07</b>	<b>3.5 ± 0.09</b>	<b>32 ± 1.3</b>	<b>51 ± 0.5</b>

Tab. 1: Time constants resulting from a bi-exponential fit function fitted on to measured differential transmission data of Fig. 4 and Fig. 5.

The short time constant  $\tau_1$  is interpreted as the time constant for an electron to get trapped from the conduction band (CB) into a LT-growth related trap state, e.g.  $\text{As}_{\text{Ga}}$  defect states. The increase of  $\tau_1$  for increasing pump power can be explained by partial trap filling at higher excitation densities. Once traps states are partially filled the probability of an electron being trapped into an empty trap state is reduced. Hence, it takes longer for the absorption to recover due to Pauli blocking from electrons remaining in the CB. As mentioned above, an increase of  $\tau_1$  from 0.23 – 0.27 ps to 1.5 - 2.2 ps is visible when switching from 1550 nm to 1030 nm excitation. This supports our assumption that the trapping time for hot electrons is increased compared to that of electrons energetically close to the band edge. Even though the carrier densities at 1030 nm excitation are 4-5 times higher than for 1550 nm at equal photon densities due to the stronger absorption, the rather strong increase of  $\tau_1$  for 1030 nm compared to 1550 nm, even at low pump photon densities, suggests that partial trap filling isn't the only reason for this increase. It is more reasonable to assume that the capture cross section of the trap states is reduced for electrons with higher energies. These findings of an increase in trapping time for higher electron energies is also supported by a trend suggested by results obtained from differential transmission measurements on comparable samples [20]. Additionally, an elevated trapping time is in agreement with the reduced THz bandwidth in our TDS measurements, as compared to a 1550 nm excitation.

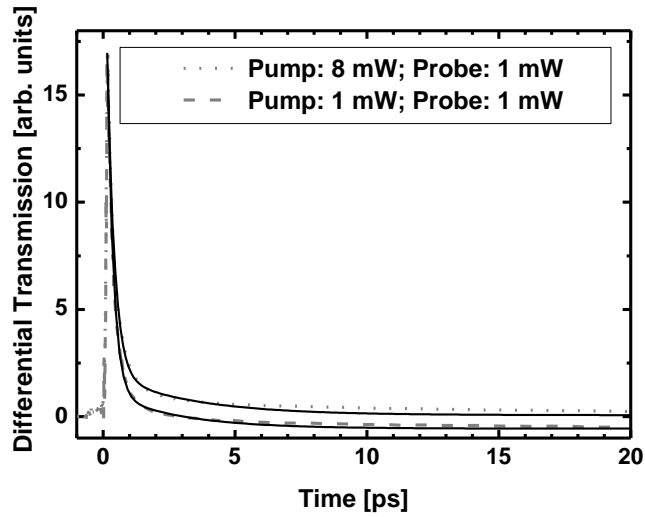


Fig. 4: Differential transmission data for an excitation with 1550 nm wavelength at two different pump powers. The black curves are obtained from bi-exponential fit functions.

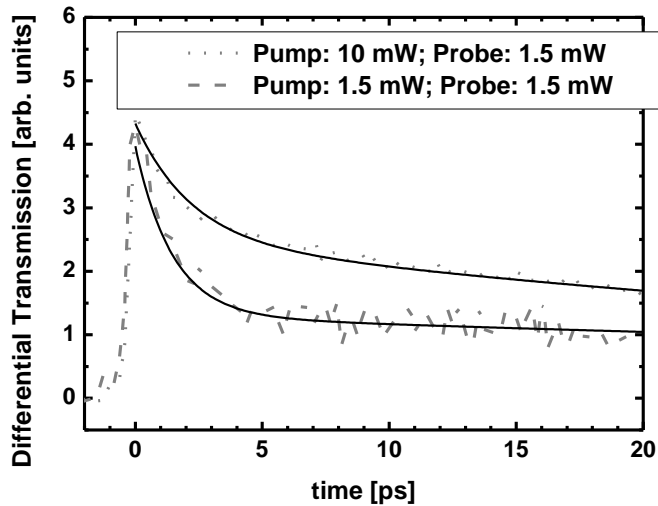


Fig. 5: Differential transmission data for excitation with 1030 nm wavelength at two different pump powers. The black curves are obtained from bi-exponential fit functions.

The longer time constant  $\tau_2$  is mostly governed by the life time of an electron populating a trap state before recombining with a hole in the valence band (VB). In case of the 1550 nm excitation and high pump fluence a slowly decaying positive signal component is visible. This originates from Pauli blocking by carriers remaining in the CB due to highly populated trap states. In this case the second decay is governed by the recombination time instead of the trapping time and is independent on the CB population which leads to a slow decay of the DT signal. This is further increased in the 1030 nm excitation case because of the increased absorption and thus higher carrier densities. However, the difference of  $\tau_2$  for 1550 nm compared to 1030 nm excitation can't be explained in this simple picture. For 1550 nm excitation and lower pump powers the signal decays to a negative value which is

assumed to be induced absorption from trapped electrons. However the extremely long recovery time of this negative signal cannot be consistently explained assuming just one trap state, considering the signal decay of  $\tau_2$  at higher pump fluence. The same behavior has been found in LT-GaAs samples [21]. Since the recovery of the induced absorption takes places on a time scale much longer than the one of interest, we follow the approach given in Ref. [21] and use the value of the decayed signal as a baseline for our fit. However, a more sophisticated model and a rate-equation-based fit-routine would be beneficial in order to get a better understanding of the behavior.

In summary, we examined Be-doped MBE LT-grown InGaAs/InAlAs MNLS under 1030 nm femtosecond excitation. The differential transmission signals show an increased carrier trapping time compared to an excitation with 1550 nm. However, THz emission and detector sensitivity increased by more than an order of magnitude while maintaining broadband spectral characteristics. This might be interesting for THz applications where strong signals are necessary in order to obtain shorter measurement times, e.g. in-line production control. In conclusion, the material system poses another promising candidate for high power and high speed THz TDS systems that are based on Ytterbium-doped fiber lasers.

## REFERENCES

- [1] J. P. Laib and D. M. Mittleman, „Temperature-Dependent Terahertz Spectroscopy of Liquid n-alkanes”, *Journal of Infrared, Millimeter and Terahertz Waves*, **31**, 1015 (2010)
- [2] P. Uhd Jepsen und H. Merbold, „Terahertz Reflection Spectroscopy of Aqueous NaCl and LiCl Solutions”, *Journal of Infrared, Millimeter and Terahertz Waves*, **31**, 430 (2010)
- [3] J. Lloyd-Hughes, T.-I. Jeon, “A review of the terahertz conductivity of bulk and nano-materials”, *Journal of Infrared, Millimetre and Terahertz Waves*, **33**, 871 (2012)
- [4] N. Krumbholz, T. Hochrein, N. Vieweg, T. Hasek, K. Kretschmer, M. Bastian, M. Mikulics, and M. Koch, “Monitoring Polymeric Compounding Processes Inline with THz Time-Domain Spectroscopy”, *Polymer Testing*, **28**, 30 (2009)
- [5] T. Yasui, T. Yasuda, K. Sawanaka, and T. Araki, “Terahertz paintmeter for noncontact monitoring of thickness and drying progress in paint film”, *Applied Optics*, **44**, 6849 (2005)
- [6] M. Yamashita, K. Kawase and C. Otani, T. Kiwa, and M. Tonouchi “Imaging of large-scale integrated circuits using laser terahertz emission microscopy”, *Optics Express*, **13**, 115 (2005)
- [7] J. F. Federici, “Review of Moisture and Liquid Detection and Mapping using Terahertz Imaging”, *Journal of Infrared, Millimetre and Terahertz Waves*, **33**, 97 (2012)
- [8] C. Jördens, S. Wietzke, M. Scheller, and M. Koch, “Investigation of the water absorption in polyamide and wood plastic composite by terahertz time-domain spectroscopy”, *Polymer Testing*, **29**, 209 (2010)
- [9] J.B. Jackson, J. Bowen, G. Walker, J. Labaune, G. Mourou, M. Menu, K. Fukunaga, "A Survey of Terahertz Applications in Cultural Heritage Conservation Science," *IEEE Transactions on Terahertz Science and Technology*, **1**, 220 (2011)
- [10] C. Jördens, M. Scheller, B. Breitenstein, D. Selmar, and M. Koch, “Evaluation of the Leaf Water Status by means of the Permittivity at Terahertz Frequencies”, *Journal of Biological Physics*, **35**, 255 (2009)
- [11] E. Jung, H. Park, K. Moon, M. Lim, Y. Do, H. Han, H. J. Choi, B.-H. Min, S. Kim, I. Park, H. Lim, “THz Time-Domain Spectroscopic Imaging of Human Articular Cartilage”, *Journal of Infrared, Millimetre and Terahertz Waves*, **33**, 593 (2012)
- [12] M. Suzuki and M. Tonouchi, “Fe-implanted InGaAs terahertz emitters for 1.56  $\mu\text{m}$  wavelength excitation”, *Applied Physics Letters* **86**, 051104 (2005)
- [13] H. Roehle, R. J. B. Dietz, H. J. Hensel, J. Böttcher, H. Künzel, D. Stanze, M. Schell, and B. Sartorius, “Next generation 1.5  $\mu\text{m}$  terahertz antennas: mesa-structuring of InGaAs/InAlAs photoconductive layers,” *Optics Express*, **18** (3). 2296 (2010)
- [14] J. Mangeney, “THz Photoconductive Antennas Made From Ion-Bombarded Semiconductors”, *Journal of Infrared, Millimetre and Terahertz Waves*, **33**, 244 (2012)
- [15] N. Krumbholz, C. Jansen, M. Scheller, T. Müller-Wirts, S. Lübbecke, R. Holzwarth, R. Scheunemann, B. Sartorius, H. Roehle, D. Stanze, J. Beckmann, L. von Chrzanowski, U. Ewert, and M. Koch, “Handheld Terahertz Spectrometer for the Detection of Liquid Explosives”, *Proceedings of SPIE - The International Society for Optical Engineering* **7485** (2009)
- [16] A. Arlauskas, P. Svidovsky, K. Bertulis, R. Adomavicius, and A. Krotkus, “GaAsBi Photoconductive Terahertz Detector Sensitivity at Long Excitation Wavelengths”, *Applied Physics Express*, **5**, 022601 (2012)
- [17] S. Adachi, *Physical Properties of III-V Semiconductor compounds*. John Wiley and Sons. (1992)
- [18] K. Y. Cheng, A. Y. Cho, S. B. Christman, T. P. Pearsall, and J. E. Rowe, Measurement of the Gamma-L separation in  $\text{Ga}_{0.47}\text{In}_{0.53}\text{As}$  by ultraviolet photoemission”, *Appl. Phys. Lett.* **40**, 423 (1982)
- [19] T.P. Pearsall, *GaInAsP Alloy Semiconductors*. John Wiley and Sons, (1982)
- [20] P. W. Juodawlkis, D. T. McInturff, and S. E. Ralph, “Ultrafast carrier dynamics and optical nonlinearities of low-temperature-grown InGaAs/InAlAs multiple quantum wells”, *Applied Physics*, **69**, 4062 (1996)
- [21] T. S. Sosnowski, T. B. Norris, H. H. Wang, P. Grenier, J. F. Whitaker, and C. Y. Sung, “High-carrier-density electron dynamics in low-temperature-grown GaAs”, *Appl. Phys. Lett.* **70**, 3245 (1997)

**Paper X:**

**J. Infrared, Millimeter, Terahertz Waves, vol. 36, no. 1, pp. 60–71,  
2015**



# Low temperature grown photoconductive antennas for pulsed 1060 nm excitation: Influence of excess energy on the electron relaxation

R. J. B. Dietz<sup>a</sup>, A. Brahm<sup>b,c</sup>, A. Velauthapillai<sup>d</sup>, A. Wilms<sup>b</sup>, C. Lammers<sup>d</sup>, B. Globisch<sup>a</sup>, M. Koch<sup>d</sup>, G. Notni<sup>b</sup>, A. Tünnermann<sup>b,c</sup>, T. Göbel<sup>a</sup> and M. Schell<sup>a</sup>

<sup>a</sup>Fraunhofer Institute for Telecommunications, Heinrich-Hertz-Institute, Berlin, Germany

<sup>b</sup>Fraunhofer Institute for Applied Optics and Precision Engineering, Jena, Germany

<sup>c</sup>Institute of Applied Physics, Abbe Center of Photonics, Friedrich-Schiller University Jena, Germany

<sup>d</sup>Department of Physics, Philipps-Universität Marburg, Marburg, Germany

Email: Roman.Dietz@hhi.fraunhofer.de

**Abstract**—We investigate properties of MBE grown photoconductive terahertz (THz) antennas based on the InGaAs/InAlAs/InP material system aimed for an excitation wavelength of approx. 1060 nm. Therefore, we analyze several different approaches concerning growth parameters, layer and material compositions as well as doping. The carrier dynamics are probed via transient white-light pump-probe spectroscopy as well as THz Time Domain Spectroscopy (TDS) measurements. We find that the electron capture probability is reduced for higher electron energies. By adjusting the material band gap this can be resolved and lifetimes of 1.3 ps are obtained. These short lifetimes enable the detection of THz TDS spectra with a bandwidth exceeding 4 THz.

Since the advent of the first THz TDS system [1], there have been many developments concerning new photoconductive materials [2]–[9] as well as other generation and detection techniques [10]–[12]. To a great part these developments were spurred by demands from basic research of THz-matter interactions in semiconductor physics [13]–[17] and chemistry [18]–[21]. However, apart from basic research, numerous promising out-of-lab applications for THz TDS have been identified such as industrial non-destructive inspection [22]–[24] and moisture mapping [25], [26]. Therefore, attempts have been made to build reliable and cost efficient THz TDS systems based on photoconductive THz emitters and detectors which can be excited at the telecom wavelength of 1.5  $\mu\text{m}$  [4]–[7], [9], [27]–[30]. This choice of wavelength is due to the availability of competitive laser sources and fiber optic components at 1550 nm. Nevertheless, Ytterbium-doped femtosecond fiber lasers operating at a center wavelength of approx. 1030-1060 nm can be built with much higher output powers compared to their 1550 nm counterparts. Thus, they offer another prospective choice for efficient and stable THz TDS systems with high power photoconductive terahertz generation and/or multi-channel arrays driven by one laser source, which allow for significant measurement time reduction in imaging and tomography applications [31]. However, concerning the development of photoconductive materials that are optimized for this wavelength, so far there has been only very little research. Amongst the investigated materials were GaAsBi [32], [33] and  $\text{In}_{0.3}\text{Ga}_{0.7}\text{As}$  grown on GaAs substrates [34]. More recently a proof-of-principle demonstration with Be-doped low temperature grown (LTG) InGaAs/InAlAs multi-layer heterostructures has been performed, which were originally designed for 1550 nm wavelength excitation [35]. The results of [35] indicated that the carrier capture time of conduction band (CB) electrons into gallium antisite ( $\text{As}_{\text{Ga}}$ ) defect states, is significantly increased for hot electrons, e.g. 1030 nm excitation, as compared to an excitation close to the band edge, e.g. 1550 nm wavelength, where carrier lifetimes of <200 fs have been achieved [29]. In this paper we further investigate the influence of the excess electron energy on the capture process as well as the potential of optimization of InP based photoconductors for 1060 nm

excitation wavelength.

To investigate the carrier capture process in dependence of the electron excess energy, four samples with different band gap energies were grown lattice matched to an InP:Fe substrate via molecular beam epitaxy (MBE). Two samples are based on Be-doped LTG InGaAs/InAlAs heterostructures with different InGaAs layer thicknesses, i.e. sub-band energies. The other two samples are based on quaternary bulk InAlGaAs layers, with and without Be-doping. The growth temperature of all samples was chosen to be approx. 130 °C, to obtain non-stoichiometric growth, i.e. incorporation of excess arsenic, which results in the formation of arsenic anti-site defects ( $As_{Ga}$ ) [36], [37]. After growth all samples were in-situ annealed at 500 °C for 60 min.

The first sample (HHI33252) consisted of 100 periods of a 12 nm  $In_{0.53}Ga_{0.47}As$  layer followed by a 8 nm  $In_{0.52}Al_{0.48}As$  layer and serves as a reference sample, since its layer composition and growth parameters resemble that of the samples investigated in Ref. [35].

The second heterostructure sample (HHI33253) features a shifted band-gap with respect to sample HHI33252. This was achieved by reducing the  $In_{0.53}Ga_{0.47}As$  layer thicknesses from 12 nm to 3 nm and thus shifting the first sub-band energy to approx. 0.94 eV, i.e. 1300 nm wavelength. The overall InGaAs thickness of sample HHI33253 was kept equal to HHI33252, i.e. 1.2  $\mu m$ , by growing 400 periods. To limit the overall growth stack height, the  $In_{0.52}Al_{0.48}As$  layer thickness was also reduced from 8 nm to 4 nm. The InGaAs layer thickness of 3 nm is a trade-off between sub-band energies shifted towards the higher energies and sufficiently high carrier mobility. The latter is important for the purpose of building photoconductive antennas (PCA) for THz detection with sufficient detector currents. The reduction of the mobility for thinner layers is due to the increasing influence of interface roughness scattering on the InAlAs layer boundaries, which becomes already evident in case of the 3 nm InGaAs layers of sample HHI33253 from the reduction of the Hall mobility by a factor of 2.5 as compared to sample HHI33252 (cf. Table 1).

The two quaternary samples, HHI33251 and HHI33284, were grown with a composition of  $In_{0.52}Al_{0.28}Ga_{0.20}As$ , which results in a band gap energy of approx. 1.1 eV, i.e. 1120 nm wavelength.

Samples HHI33252, HHI33253 and HHI33284 were additionally Be-doped with a concentration of  $4 \times 10^{18} \text{ cm}^{-3}$  to raise the amount of ionized  $As_{Ga}$  defects, which increases the electron capture cross section as compared to neutral  $As_{Ga}$  [29], [36]. As shown in Ref. [29], the holes are captured by Be-dopants and the subsequent electron-hole recombination then occurs between bound electrons in  $As_{Ga}$  defects and holes bound to Be-dopants on the order of several tens of picoseconds. Furthermore, the amount of ionized  $As_{Ga}$  defects can be assumed equal to the Be-doping concentration.

In case of LTG InGaAs/InAlAs heterostructures, the Be-doping also strongly reduces the residual carrier concentration. The energy levels of the  $As_{Ga}$  defects in LTG InGaAs are close to the conduction band (CB) [36], [38]. In scanning tunneling microscopy measurements of  $As_{Ga}$  defects in LTG-InGaAs, Grandidier et al. measured a band of mid-gap states at energies of around 150 meV below the CB. They attributed this to a combination the two ionization transitions of the  $As_{Ga}$  defect, i.e. neutral to singly charged (0,+) and singly to doubly charged (+,++). The transfer to the singly charged state was associated with an activation energy of 32 meV, corresponding to a ionization energy of roughly 91 meV in uncompensated LTG InGaAs, which has previously been determined from temperature dependent Hall measurements by Künzel et al. [38]. The double charge state was assumed to have an energy of 230 meV. In the following we will for simplicity assume the defect energy of the  $As_{Ga}$  defect in LTG  $In_{0.53}Ga_{0.47}As$  to be at its averaged value of 150 meV. Hence without counter Be-doping there would be a significant amount of thermally excited carriers in the CB.

Considering that the electron Bohr radius for an electron bound to a singly charged state is approx. 15 nm, the energetic position of the  $As_{Ga}$  defects with respect to the valence band (VB) is assumed to be shifted in the case of sample HHI33253 due to the confinement of the quantum wells. The fact that the residual carrier concentration of HHI33253 does not change significantly as compared to sample HHI33252 supports this assumption (cf. Table 1). Hence, the energy level of the  $As_{Ga}$  defects in sample HHI33253 are also approx. 150 meV below the CB edge of the first sub-band.

Concerning the energy levels of the  $As_{Ga}$  defects in the quaternary samples the following inference can be applied: The energetic position of the  $As_{Ga}$  defect with respect to the valence band (VB) maximum in  $In_xGa_{1-x}As$  was found to be only very weakly dependent on the Indium content  $x$  of the samples [39], [40]. Hence, considering that the energy levels of the  $As_{Ga}$  defect in  $In_{0.53}Ga_{0.47}As$  are approx.  $0.76\text{ eV}-0.15\text{ eV}=0.61\text{ eV}$  above the VB, the energy level of the  $As_{Ga}$  defects in  $In_{0.52}Al_{0.28}Ga_{0.20}As$  can be estimated to be at approx. 0.5 eV below the CB edge. The validity of this assumption is supported by the residual carrier concentration of the two quaternary samples, which are found to be very low, even without Be-doping. This suggests that the defect energy is situated in a mid-gap position and thermal excitation is low.

Sample	Structure	Periods	Growth Temperature [°C]	Be-Doping [ $cm^{-3}$ ]	Resistivity [ $\Omega cm$ ]	Mobility [ $cm^2/Vs$ ]	Residual Carrier conc. [ $cm^{-3}$ ]
HHI33252	12 nm $In_{0.53}Ga_{0.47}As$ / 8 nm $In_{0.52}Al_{0.48}As$	100	130	$4 \times 10^{18}$	850	308	$2.39 \times 10^{13}$
HHI33253	3 nm $In_{0.53}Ga_{0.47}As$ / 4 nm $In_{0.52}Al_{0.48}As$	400	130	$4 \times 10^{18}$	7285	127	$6.72 \times 10^{12}$
HHI33251	1.2 $\mu m$ $In_{0.52}Al_{0.28}Ga_{0.20}As$	bulk	130	-	8238	1130	$6.7 \times 10^{11}$
HHI33284	1.2 $\mu m$ $In_{0.52}Al_{0.28}Ga_{0.20}As$	bulk	130	$4 \times 10^{18}$	29050	331	$6.5 \times 10^{11}$

Table 1: Growth parameters and hall data of the four samples studied.

To experimentally verify the band gap positions of the four samples, we performed linear absorption measurements [Fig. 1]. All four samples show a broadened band edge, with an Urbach-like absorption tail arising from disorder due to band tail states [41]. This is a typical feature of LTG semiconductors. The absorption edge of sample HHI33252 and HHI33253 are found to be at approx. 1600 nm and 1300 nm, respectively. The samples HHI33251 and HHI33284 both have an absorption edge at 1100 nm, which is in good agreement with the value calculated for this alloy composition. Additionally, sample HHI33284 shows a slightly increased absorption broadening at the band edge as compared to samples HHI33251, which we assumed to be due to additional band tail states that are induced by the Be-doping.

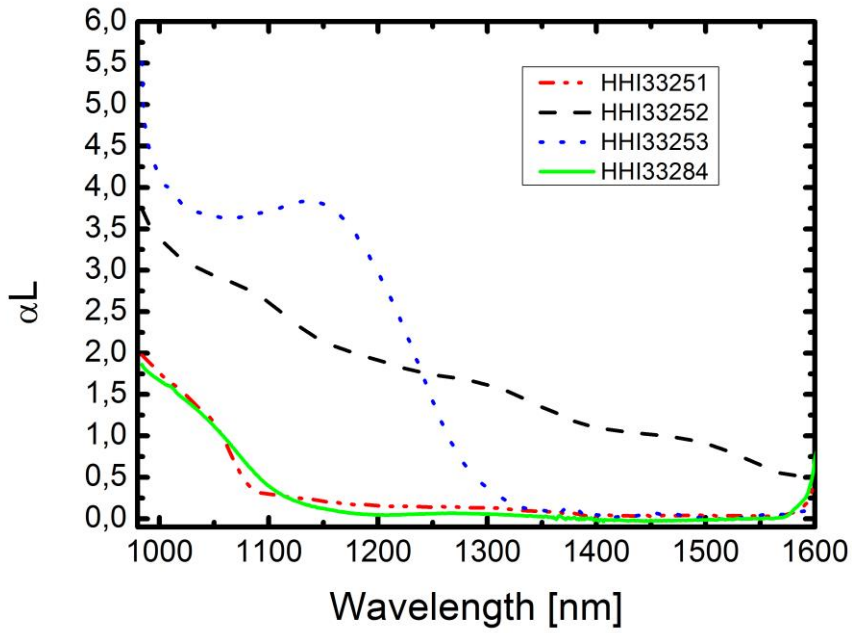


Fig. 1: Linear absorption spectra of the samples given in Table 1.

## Transient white-light pump-probe spectroscopy: Results

To investigate the ultrafast carrier dynamics of the material we used transient white-light pump-probe (TWPP) spectroscopy. The pump beam was generated by a tunable optical parametric amplifier (OPA) which provides a transform-limited 80 fs pump pulse. A white-light super-continuum, generated by self-phase modulation in a sapphire-crystal, was used as the probe pulse. The wavelength of the pump pulse can be continuously tuned by the OPA, while the broad white-light enabled the monitoring of the full spectral range of interest. Thus the experiment yields the differential transmission spectra revealing the pump-induced change in absorption as a function of energy and time. The light source for both pump- and probe-pulses was a 1 kHz regenerative Ti:Sapphire amplifier with 100 fs pulse width. The resulting temporal resolution of the setup was sub-50-fs. All measurements were performed at room temperature. Due to the optical elements used and the intrinsic chirp of the white-light, a chirp correction was performed by using coherent oscillations and the multi-photon absorption features in the signals. Thereby we can eliminate artifacts and study the ultrafast response of the system over a broad spectral range. A linear stage, combined with a beam-stabilization, was used to set the time delay between pump- and probe-pulse. The TWPP measurements for samples HHI33252 and HHI33253 were performed at pump wavelengths of 1060 nm and 1250 nm, whereas samples HHI33251 and HHI33284 were measured only for 1060 nm pump due to their higher band gap energy. The average power of the pump beam was 15  $\mu\text{W}$  for both pump wavelengths. The pump beam was focused on a 260 $\mu\text{m}$  spot, which results in photon densities of  $1.5 \times 10^{14} \text{ cm}^{-2}$  and  $1.77 \times 10^{14} \text{ cm}^{-2}$  for 1060 nm and 1250 nm wavelength, respectively.

It should be noted that the induced carrier densities differ due to the different absorption coefficients of the samples as well as for the two different wavelengths [cf. Fig. 1]. This fact is especially significant for the 1060 nm excitation of samples HHI33252 and HHI33253, where the absorption lengths are only 415 nm and 330 nm,

respectively. Since the time scales of interest are on the order of a few picoseconds, carrier diffusion is negligible and there is a persistent density gradient towards the depth of the samples. The densities in the top layers of the samples are approx.  $4 \times 10^{18} \text{ cm}^{-3}$ , i.e. not higher than the assumed concentration of ionized  $\text{As}_{\text{Ga}}$  defects, and hence strong trap saturation should not occur. However, the influence of partial trap filling cannot be ruled out. The carrier densities in case of 1250 nm excitation of HHI33252 and HHI33253, as well as the 1060 nm excitation of samples HHI33284 are on the order of  $1 \times 10^{18} \text{ cm}^{-3}$  and thus well below the density of available ionized  $\text{As}_{\text{Ga}}$  defects.

The TWPP results of all four samples are shown in Fig. 2 a)-f). The vertical axis shows the time delay between pump and probe pulses and the horizontal axis shows the spectral components of the white light probe pulse. The color map value indicates the normalized differential transmission signal, where a positive color map value corresponds to an induced transmission and a negative color map value corresponds to an induced absorption.

Due to the high carrier densities of  $\geq 10^{18} \text{ cm}^{-3}$ , all samples exhibit an ultra-fast thermalization of the optically induced carriers into a hot carrier population via carrier-carrier scattering on a time scale of approx. 50-100 fs. After this initial thermalization of the carriers with each other, the relaxation of the carrier population depends on the sample and the excitation wavelength. Since the density of states (DOS) in the CB is smaller than in the VB, the differential transmission signals are dominated by the electron population. We will therefore limit most of the discussion to the dynamics of the CB electrons.

For an excitation wavelength of 1060 nm of sample HHI33252 [Fig. 2a)] and after the initial thermalization, the majority of the electron population relaxes towards the band edge via longitudinal optical (LO) phonon emission, on a time scale of approx. 1.6 ps. There appears to be a small delay of the electron relaxation at the intersubband transition from the second to the first subband, where the relaxation via phonon emission is inhibited by the k-vector and energy conservation. The relaxation of the electrons towards the band edge results in a very strong transmission signal for probe wavelengths close to the band edge due to lower DOS and the resultant strong Pauli blocking. The electron population at the band edge then subsequently decays on a time scale of 1.8-2 ps via non-radiative capture into defect states.

For the excitation of sample HHI33252 with 1250 nm pump wavelength [Fig. 2b)], the change of the transmission signal is much less pronounced than for the 1060 nm excitation. This can be attributed to the lower absorption coefficient for 1250 nm light and hence a lower initial electron density, as elaborated above. After the excitation there is again an ultra-fast thermalization of the electrons into a hot electron population with a subsequent relaxation via electron-phonon (e-ph) scattering, i.e. LO-phonon emission. The maximum of the differential transmission appears at around 1375 nm probe wavelength. This can be in part assigned to the aforementioned delayed electron relaxation at the intersubband transition. However, a part of the electrons appears to be captured into defect states already before relaxing to the band-edge via LO-phonons emission. The non-radiative decay of the remaining electron population, which has relaxed to the band edge, has a time constant of 1.3 ps-1.6 ps.

For sample HHI33253 at a pump wavelength of 1060 nm [Fig. 2c)] and after initial electron-electron thermalization, the majority of the electron population relaxes towards the band gap via LO-phonon emission on a time scale of 300 fs before being capture by a defect state.

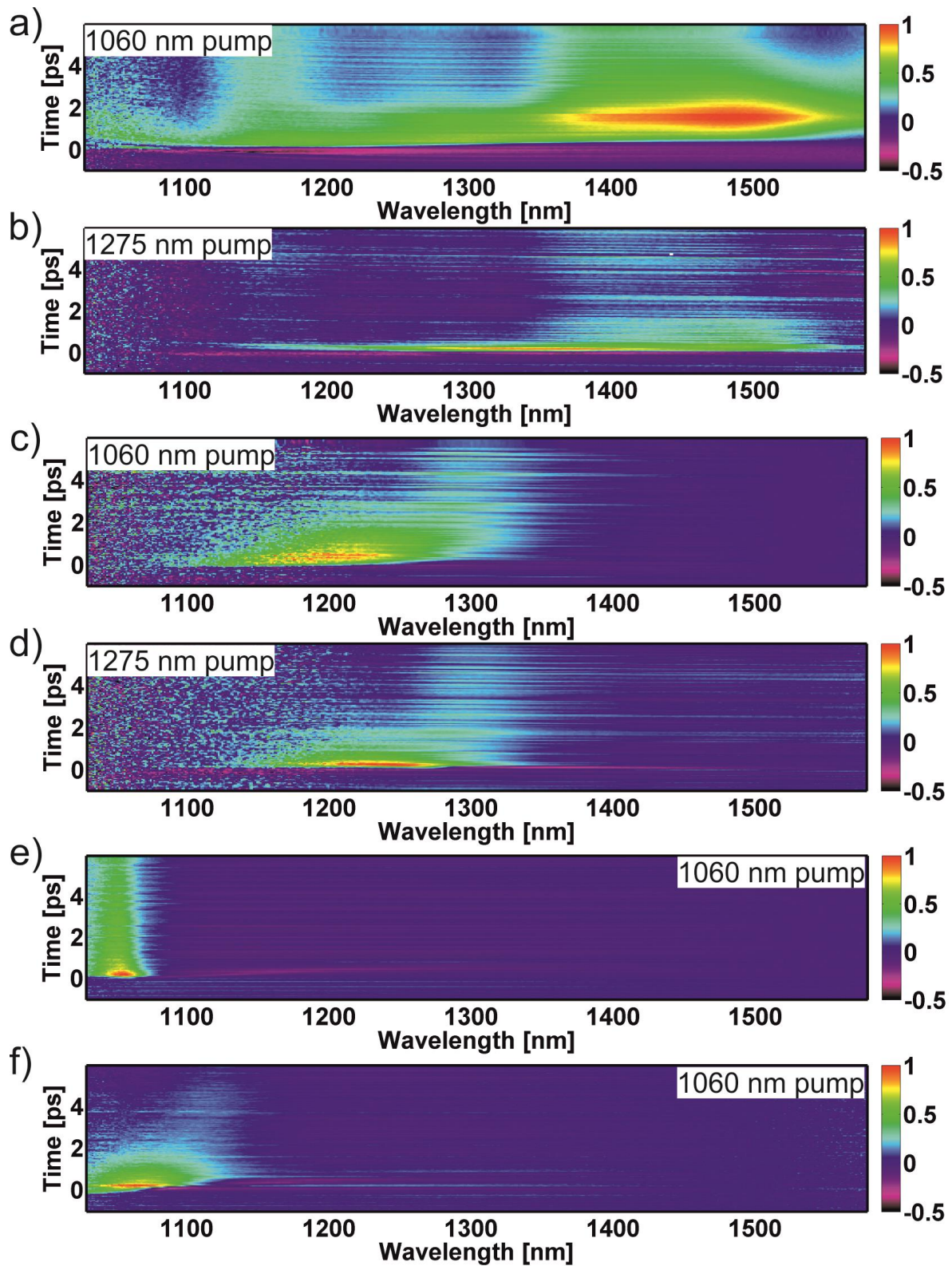


Fig. 2: TWPP spectra obtained for samples HHI33252 (a, b), HHI33253 (c, d), HHI33251 (e) and HHI33284 (f). The horizontal axis is the probe wavelength, the vertical axis is the time delay between pump and probe pulse and the color map gives the differential transmission signal, where a positive value corresponds to increased transmission.

At 1250 nm pump wavelength [Fig. 2d)], i.e. for excitation at the band edge, the excited electron population forms a cold Fermi distribution due to the lack of excess energy. The cold electron population is subsequently broadened due to the redistribution of electrons via electron-electron (e-e) and e-ph scattering on a time scale of 300 fs, which results in a partial decrease of the transmission signal. This decrease due to electron redistribution is superimposed by the electron capture process into  $As_{Ga}$  defects with a time constant of approx. 1.3 ps. For both excitation wavelengths there is a long lived transmission signal from band tail states around 1300 nm which will be discussed later.

For sample HHI33251 [Fig. 2e)], we observe an initial short decay of the signal on a time scale of 300 fs, followed by a longer decay component on a time scale of 3 ps. The initial short signal decay is again due to a redistribution of the electrons via e-e and e-ph scattering. The second decay component of the TWPP signal is due to electron capture into  $As_{Ga}$  defects. The  $As_{Ga}$  defects in this sample are mostly neutral since the sample is not Be-doped, which explains the rather long decay time of 3 ps. However, the decay is much shorter than the one observed in undoped or moderately doped InGaAs/InAlAs heterostructures [29].

In case of sample HHI33284 excited at 1060 nm [Fig. 2f)], the carrier density is also redistributed via e-e and e-ph scattering, again on a time scale of approx. 300 fs. The transmission signal of this sample is much broader compared to sample HHI33251. This is attributed to the higher amount of band tail states, caused by the Be-doping, which becomes occupied due to the e-e and e-ph scattering. The subsequent decay due to the carrier capture time into defect states in this sample is found to be approx. 1.3 ps.

There is another prominent difference between samples HHI33251 and HHI33284. The latter shows an increased transmission in the band tail at approx. 1120 nm wavelength while the former does not. This feature is similar to the slow decay component of sample HHI33253 at a probe wavelength of 1300 nm. Considering that the Be-dopants in the initial state are negatively ionized, some of the pump photons are absorbed by the electrons bound to Be-dopants leaving a hole at the Be-dopant. We assume that the observed change of the transmission signal is caused by the bleaching of this absorption. The bleaching is then persistent until an electron from an  $As_{Ga}$  defect recombines with the hole bound to the Be-dopant, which has been found to take place on the order of several picoseconds [29].

The most interesting and consistent feature of the TWPP measurements, where the electrons exhibit a significant amount of excess energy, is the finding that the relaxation via phonon emission appears to have a higher probability than the capture process of hot electrons into defect states. The LO-phonon emission time for a room temperature phonon occupation number  $N_{ph} \approx 0.4$  is approx. 300 fs [42]. The electron capture process into  $As_{Ga}$  defects for samples equal to HHI33252 and near band edge excitation, i.e. 1550 nm, has previously been found to take place on the same time scale, e.g.  $\approx 200$  fs [29]. To understand the findings of our measurements it is therefore mandatory to consider the dependence of the LO-phonon emission probability and the electron capture cross section on the electron energy. Since the exact description of both processes is highly involved and thus beyond the scope of this publication, we will discuss this in a merely qualitative way.

Each electron hole-pair produces a number  $n_{ph,LO} = E_c / E_{ph,LO}$  of LO-phonons, where  $E_c$  is the excess carrier energy and  $E_{ph,LO}$  is the LO-phonon energy. Assuming that the lifetime of a LO-phonon at room temperature is equal to values found for GaAs, i.e. 4 ps [43], the relaxation of the hot electron population via-LO-phonon emission produces a non-thermal phonon distribution with a large phonon occupation number  $N_{ph} \gg 1$  for small k-vector LO-phonons [42]. The elevated phonon occupation number increases the probability of re-absorption of phonons by electrons, which leads to an inhibition of the electron energy relaxation, i.e. the formation of a phonon

bottleneck. Hence, higher electron energies should increase the energy relaxation time via phonon emission. However, we do not observe a significant increase of the carrier relaxation time within the first picosecond of the carrier energy relaxation. This is most probably due to k-vector and energy conservation as well as the non-thermal characteristics of the phonon distribution. The quadratic dispersion relation of the CB electrons prevents electrons that are already relaxed to lower band states from re-absorbing a previously emitted phonon with a smaller k-vector [44]. An inhibited carrier relaxation is only visible in case of the 1060 nm excitation of sample HHI33252 [cf. Fig. 2a)], i.e. very high excess energies. As visible from the measurement, part of the electrons occupy high band states for times  $>2\text{ps}$  after the excitation by the pump pulse. Even though a significant part of carriers is already captured by defect states at this time, the influence of Pauli blocking is still not negligible. We therefore attribute this persistent high band state electron occupation to a combination of Pauli blocking and phonon re-absorption by electrons in higher band states.

The energy dependence of the capture cross section, within the scope of non-radiative multi phonon emission (NMPE), has been worked out in detail by Pässler [45]. As shown in [45] the dependence of the capture cross section on the electron energy  $E$  is governed by the depth  $E_D > 0$  and the charge of the defect state as well as on the lattice relaxation energy  $A$ , i.e. the energy difference between the initial and final state of the lattice in the NMPE process. In the cases of weak ( $\ln(A/(E + E_D)) < 0$ ) or intermediate ( $\ln(A/(E + E_D)) \approx 0$ ) electron-lattice coupling and attractive defect potentials the capture cross section is a monotonically declining function of the electron energy  $E$ . In contrast, for a strong electron-lattice coupling ( $\ln(A/(E + E_D)) > 0$ ) there is a maximum of the capture cross section for a certain value of  $E > 0$  in dependence of the exact coupling strength. The capture cross section is also dependent on the lattice temperature and hence the phonon occupation number. The exact dependence is complicated and also dependent on  $A$ ,  $E_C$  and  $E$ . Yet, in most cases the cross section is increased for higher phonon numbers, i.e. lattice temperature [46].

The TWPP measurements indicate that the electron capture probability is reduced at higher electron energies. This is the case for all samples and, hence, defect state energies. We therefore conclude that the electron-lattice coupling of  $\text{As}_{\text{Ga}}$  defects in all our samples is situated in the weak or intermediate regime.

## Terahertz time domain spectroscopy measurements

In order to investigate how carrier relaxation influences the behavior of the PCAs made from the four samples, the samples were structured with mesa-type dipole antennas [47] with a gap size of 10  $\mu\text{m}$  and employed as PCA detectors in a TDS setup. For THz generation, strip-line antennas with 400  $\mu\text{m}$  gap size made from sample HHI33253 were used. The antennas were excited with an ytterbium doped fiber laser with a center wavelength of approx. 1030 nm and 100 fs pulse width at a repetition rate of 20 MHz. The optical powers at the PCA antennas were chosen to be 3 mW and 75 mW for the detector and the emitter, respectively. The obtained THz TDS pulse traces and corresponding Fourier spectra are shown in Fig. 3 and Fig. 4, respectively. The pulse trace of sample HHI33252 is broadened as compared to the traces of the other samples and hence the bandwidth is limited to 3 THz. As has been shown by several authors, the detectable bandwidth in THz-TDS is greatly influenced by the time-dependence of the conductivity in the receiver [30], [48], [49]. An ideal THz PCA detector for high bandwidth THz detection features an almost delta function like time dependency of the photo-conductivity. Since holes have a much bigger effective mass they can be neglected in the discussion, and the duration of the photoconductivity is defined by the electron lifetime. In case of sample HHI33252 excited at 1060 nm wavelength, there is a significant photoconductivity over a time duration of  $> 7$  ps, i.e. from the point in time of the optical excitation over the phonon relaxation to the band edge and until the majority of the electrons ( $>99\%$ ) have left the CB due to non-radiative capture into  $\text{As}_{\text{Ga}}$  defects. Therefore, the low THz bandwidth of sample HHI33252 can be attributed to the prolonged carrier relaxation time of the high excess energy electrons. The pulse trace of sample HHI33253 is significantly shorter than the pulse trace of sample HHI33252 and hence the bandwidth is increased up to 4 THz as expected from the shorter carrier lifetime. Interestingly, the quaternary samples do not exhibit equally high bandwidth as the sample HHI33253. The Be-doped sample HHI33284 shows a better frequency roll-off behavior in the low frequency range as compared to the un-doped sample HHI33251, which can be attributed to the shorter carrier capture time of approx. 1.3 ps of sample HHI33284, as compared to the 3 ps of sample HHI33251.

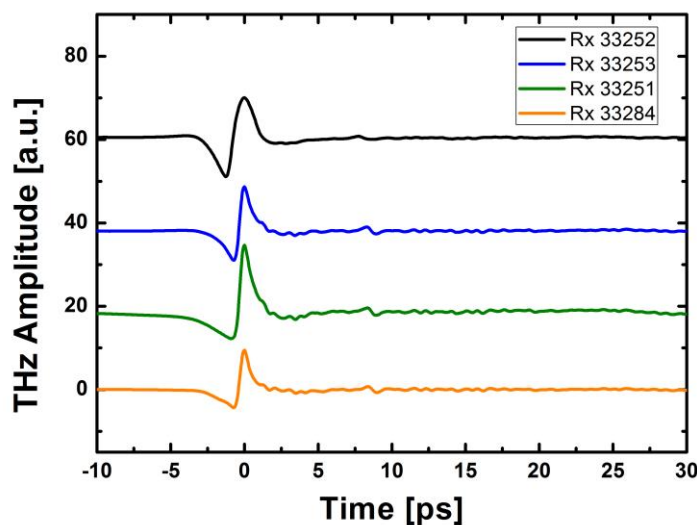


Fig. 3: THz-TDS pulse traces obtained for dipole PCA detectors made from the four samples and a 400  $\mu\text{m}$  strip-line antenna as emitter. The optical power was 3 mW and 75 mW for the detectors and the emitter, respectively. The emitter was biased with 200 V. The lock-in integration time was 300 ms per time delay step of 30 fs.

However, the amplitude of the frequency components above 2 THz of sample HHI33284 are reduced as compared to the spectra obtained with sample HHI33251, which is in contradiction with what would be expected from the shorter carrier lifetime. We assume that the spectral dip at 2.2 THz and the low signal amplitude at higher frequencies in part originate from a minor misalignment in the THz beam path. Nevertheless, we cannot rule out that there is an influence of more complex electron transport phenomena in the presence of the THz field which are not covered by the TWPP measurements. An indication for a more complex carrier relaxation behavior in the presence of electrical field is the elevated noise floor, i.e. the spectral amplitude above approx. 4 THz, of samples HHI33251 and HHI33284 as compared to the two heterostructure samples. This elevated noise floor can be attributed to Nyquist noise and is indicative of a high average conductivity in the sample [30]. However, a high average conductivity is in contradiction with the short carrier lifetimes obtained from the TWPP measurements and the high dark resistivity of the hall measurements. To resolve this matter and to determine the potential of LTG InAlGaAs as PCA material for 1060 nm excitation wavelength, further measurements have to be performed in the future to determine the time resolved conductivity, e.g. optical pump THz-probe measurements. Hence, at this point InGaAs/InAlAs heterostructure samples with thin InGaAs layers of approx. 3 nm, e.g. HHI33253, are the most promising choice for InP-based broadband THz PCA detector materials at an excitation wavelength of 1060 nm.

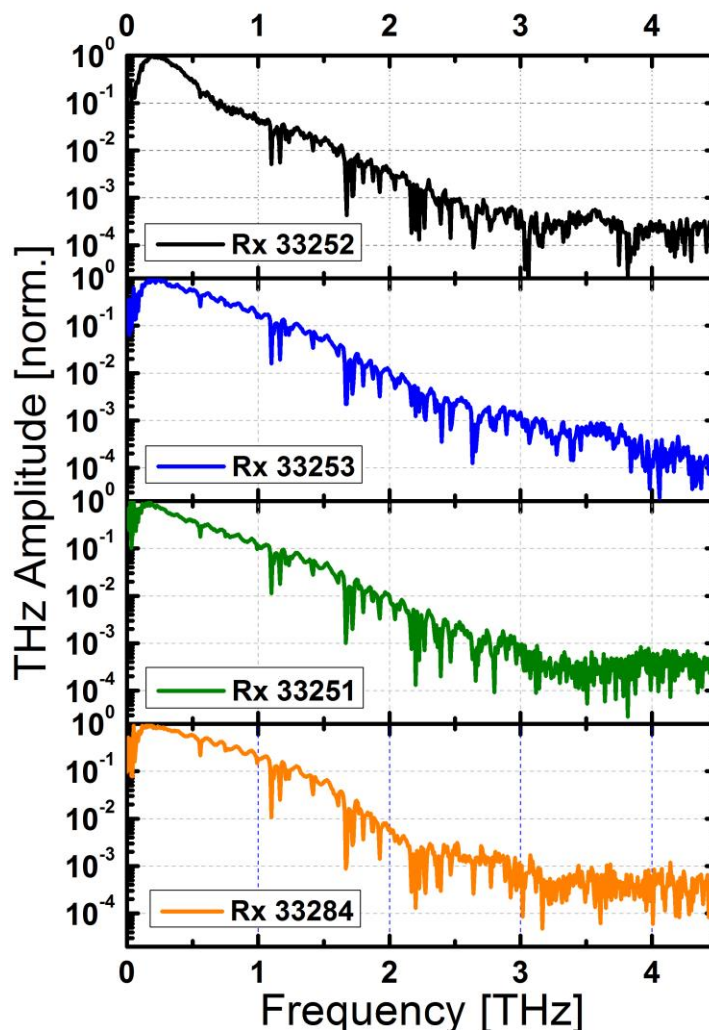


Fig. 4: THz TDS Fourier spectra obtained from the pulse traces shown in Fig. 3.

In conclusion, we investigated a set of LTG bulk and heterostructure III-V samples to study the influence of excess carrier energy on the electron relaxation and capture process. Our data indicate that the capture process of electrons into  $\text{As}_{\text{Ga}}$  defects for electrons with higher band energies is reduced compared to electrons with near-band-gap energies. As a consequence, the energy relaxation towards the band gap via LO-phonon emission becomes more likely than direct electron capture. Therefore, hot electrons significantly prolong the conductivity of the samples, which reduces the detectable THz bandwidth when employed as a material for PCA detectors in THz-TDS. We have shown that this can be resolved by shifting the band gap towards higher energies. For lattice matched growth on InP, this was achieved either by employing a quaternary alloy composition, i.e. InAlGaAs, or by employing InGaAs/InAlAs heterostructures with thin InGaAs layer thicknesses, e.g. 3 nm. We demonstrated that with such a band gap optimized InGaAs/InAlAs heterostructure based PCA detector, THz bandwidths of up to 4 THz can be achieved.

The Marburg group acknowledges financial support from the German Science Foundation (DFG: GRK 1782).

## References

- [1] D. H. Auston, K. P. Cheung, and P. R. Smith, "Picosecond photoconducting Hertzian dipoles," *Appl. Phys. Lett.*, vol. 45, no. 3, p. 284, 1984.
- [2] F. W. Smith, H. Q. Le, V. Diadiuk, M. A. Hollis, A. R. Calawa, S. Gupta, M. Frankel, D. R. Dykaar, G. A. Mourou, and T. Y. Hsiang, "Picosecond GaAs-based photoconductive optoelectronic detectors," *Appl. Phys. Lett.*, vol. 54, no. 10, p. 890, 1989.
- [3] J. Sigmund, C. Sydlo, H. L. Hartnagel, N. Benker, H. Fuess, F. Rutz, T. Kleine-Ostmann, and M. Koch, "Structure investigation of low-temperature-grown GaAsSb, a material for photoconductive terahertz antennas," *Appl. Phys. Lett.*, vol. 87, no. 25, p. 252103, 2005.
- [4] J. Mangeney, N. Chimot, L. Meignien, N. Zerounian, P. Crozat, K. Blary, J. F. Lampin, and P. Mounaix, "Emission characteristics of ion-irradiated  $\text{In}_{0.53}\text{Ga}_{0.47}\text{As}$  based photoconductive antennas excited at 1.55  $\mu\text{m}$ ," *Opt. Express*, vol. 15, no. 14, pp. 8943–50, Jul. 2007.
- [5] M. Suzuki and M. Tonouchi, "Fe-implanted InGaAs terahertz emitters for 1.56  $\mu\text{m}$  wavelength excitation," *Appl. Phys. Lett.*, vol. 86, no. 5, p. 051104, 2005.
- [6] M. Suzuki and M. Tonouchi, "Fe-implanted InGaAs photoconductive terahertz detectors triggered by 1.56  $\mu\text{m}$  femtosecond optical pulses," *Appl. Phys. Lett.*, vol. 86, no. 16, p. 163504, 2005.
- [7] A. Schwagmann, Z.-Y. Zhao, F. Ospald, H. Lu, D. C. Driscoll, M. P. Hanson, A. C. Gossard, and J. H. Smet, "Terahertz emission characteristics of ErAs:InGaAs-based photoconductive antennas excited at 1.55  $\mu\text{m}$ ," *Appl. Phys. Lett.*, vol. 96, no. 14, p. 141108, 2010.
- [8] O. Hatem, J. Cunningham, E. H. Linfield, C. D. Wood, A. G. Davies, P. J. Cannard, M. J. Robertson, and D. G. Moodie, "Terahertz-frequency photoconductive detectors fabricated from metal-organic chemical vapor deposition-grown Fe-doped InGaAs," *Appl. Phys. Lett.*, vol. 98, no. 12, p. 121107, 2011.
- [9] B. Sartorius, H. Roehle, H. Künzel, J. Böttcher, M. Schlak, D. Stanze, H. Venghaus, and M. Schell, "All-fiber terahertz time-domain spectrometer operating at 1.5  $\mu\text{m}$  telecom wavelengths," *Opt. Express*, vol. 16, no. 13, pp. 9565–9570, 2008.
- [10] L. Xu, X.-C. Zhang, and D. H. Auston, "Terahertz beam generation by femtosecond optical pulses in electro-optic materials," *Appl. Phys. Lett.*, vol. 61, no. 15, p. 1784, 1992.
- [11] Q. Wu and X.-C. Zhang, "Free-space electro-optic sampling of terahertz beams," *Appl. Phys. Lett.*, vol. 67, no. 24, p. 3523, 1995.
- [12] P. Jepsen, C. Winnewisser, M. Schall, V. Schyja, S. R. Keiding, and H. Helm, "Detection of THz pulses by phase retardation in lithium tantalate," *Phys. Rev. E*, vol. 53, no. 4, pp. 3052–3054, 1996.
- [13] R. H. M. Groeneveld and D. Grischkowsky, "Picosecond time-resolved far-infrared experiments on carriers and excitons in GaAs-AlGaAs multiple quantum wells," *J. Opt. Soc. Am. B*, vol. 11, no. 12, p. 2502, Dec. 1994.
- [14] R. Kaindl, M. Carnahan, D. Hägele, R. Lövenich, and D. S. Chemla, "Ultrafast terahertz probes of transient conducting and insulating phases in an electron-hole gas," *Nature*, vol. 423, p. 734, 2003.

- [15] S. Leinß, T. Kampfrath, K. v. Volkman, M. Wolf, J. Steiner, M. Kira, S. Koch, A. Leitenstorfer, and R. Huber, "Terahertz Coherent Control of Optically Dark Paraexcitons in Cu<sub>2</sub>O," *Phys. Rev. Lett.*, vol. 101, no. 24, p. 246401, Dec. 2008.
- [16] D. Golde, M. Wagner, D. Stehr, H. Schneider, M. Helm, A. M. Andrews, T. Roch, G. Strasser, M. Kira, and S. W. Koch, "Fano Signatures in the Intersubband Terahertz Response of Optically Excited Semiconductor Quantum Wells," *Phys. Rev. Lett.*, vol. 102, p. 127403, 2009.
- [17] B. Ewers, N. S. Köster, R. Woscholski, M. Koch, S. Chatterjee, G. Khitrova, H. M. Gibbs, a. C. Klettke, M. Kira, and S. W. Koch, "Ionization of coherent excitons by strong terahertz fields," *Phys. Rev. B*, vol. 85, no. 7, p. 075307, Feb. 2012.
- [18] T. M. Korter and D. F. Plusquellic, "Continuous-wave terahertz spectroscopy of biotin: vibrational anharmonicity in the far-infrared," *Chem. Phys. Lett.*, vol. 385, no. 1–2, pp. 45–51, Feb. 2004.
- [19] V. Křesálek and T. Gavenda, "Using Terahertz Spectroscopy for Observing the Kinetics of Recrystallisation of Polybutene-1," *J. Infrared, Millimeter, Terahertz Waves*, vol. 34, no. 2, pp. 187–193, Jan. 2013.
- [20] W. Qiao, K. Yang, A. Thoma, and T. Dekorsy, "Dielectric Relaxation of HCl and NaCl Solutions Investigated by Terahertz Time-Domain Spectroscopy," *J. Infrared, Millimeter, Terahertz Waves*, vol. 33, no. 10, pp. 1029–1038, Jun. 2012.
- [21] H. Zhang, K. Siegrist, D. F. Plusquellic, and S. K. Gregurick, "Terahertz spectra and normal mode analysis of the crystalline VA class dipeptide nanotubes," *J. Am. Chem. Soc.*, vol. 130, no. 52, pp. 17846–57, Dec. 2008.
- [22] C.-C. Chen, D.-J. Lee, T. Pollock, and J. F. Whitaker, "Pulsed-terahertz reflectometry for health monitoring of ceramic thermal barrier coatings," *Opt. Express*, vol. 18, no. 4, pp. 3477–86, Feb. 2010.
- [23] W. L. Chan, J. Deibel, and D. M. Mittleman, "Imaging with terahertz radiation," *Reports Prog. Phys.*, vol. 70, no. 8, pp. 1325–1379, Aug. 2007.
- [24] C. Jansen, S. Wietzke, O. Peters, M. Scheller, N. Vieweg, M. Salhi, N. Krumbholz, C. Jördens, T. Hochrein, and M. Koch, "Terahertz imaging: applications and perspectives," *Appl. Opt.*, vol. 49, no. 19, pp. E48–57, Jul. 2010.
- [25] J. F. Federici, "Review of Moisture and Liquid Detection and Mapping using Terahertz Imaging," *J. Infrared, Millimeter, Terahertz Waves*, vol. 33, no. 2, pp. 97–126, Jan. 2012.
- [26] D. Banerjee, W. von Spiegel, M. D. Thomson, S. Schabel, and H. G. Roskos, "Diagnosing water content in paper by terahertz radiation," *Opt. Express*, vol. 16, no. 12, pp. 3003–3006, 2008.
- [27] R. J. B. Dietz, M. Gerhard, D. Stanze, M. Koch, B. Sartorius, and M. Schell, "THz generation at 1.55  $\mu\text{m}$  excitation : six-fold increase in THz conversion efficiency by separated photoconductive and trapping regions," *Opt. Express*, vol. 19, no. 27, pp. 122–126, 2011.
- [28] R. J. B. Dietz, B. Globisch, M. Gerhard, A. Velauthapillai, D. Stanze, H. Roehle, M. Koch, T. Göbel, and M. Schell, "64  $\mu\text{W}$  pulsed terahertz emission from growth optimized InGaAs/InAlAs heterostructures with separated photoconductive and trapping regions," *Appl. Phys. Lett.*, vol. 103, no. 6, p. 061103, 2013.
- [29] B. Globisch, R. J. B. Dietz, D. Stanze, T. Göbel, and M. Schell, "Carrier dynamics in Beryllium doped low-temperature-grown InGaAs/InAlAs," *Appl. Phys. Lett.*, vol. 104, no. 17, p. 172103, Apr. 2014.
- [30] R. J. B. Dietz, B. Globisch, H. Roehle, D. Stanze, T. Göbel, and M. Schell, "Influence and adjustment of carrier lifetimes in InGaAs/InAlAs photoconductive pulsed terahertz detectors : 6 THz bandwidth and 90dB dynamic range," *Opt. Express*, vol. 22, no. 16, pp. 615–623, 2014.
- [31] A. Brahm, A. Wilms, R. J. B. Dietz, T. Göbel, M. Schell, G. Notni, and A. Tünnermann, "Multichannel terahertz time-domain spectroscopy system at 1030 nm excitation wavelength," *Opt. Express*, vol. 22, no. 11, p. 12982, May 2014.
- [32] A. Bic, K. Bertulis, and A. Krotkus, "Optoelectronic terahertz radiation system based on femtosecond 1  $\mu\text{m}$  laser pulses and GaBiAs detector," *Electron. Lett.*, vol. 44, no. 19, 2008.
- [33] V. Pačebutas, a. Bičiūnas, S. Balakauskas, a. Krotkus, G. Andriukaitis, D. Lorenc, a. Pugžlys, and a. Baltuška, "Terahertz time-domain-spectroscopy system based on femtosecond Yb: fiber laser and GaBiAs photoconducting components," *Appl. Phys. Lett.*, vol. 97, no. 3, p. 031111, 2010.
- [34] I. Hinkov, G. Harzendorf, S. Kluska, B. Hinkov, K. Kamaruzaman, R. Beigang, J. Heinrich, S. Hoefling, and A. Forchel, "Generation of terahertz pulsed radiation from photoconductive emitters using 1060 nm laser excitation," in 15th International Conference on Terahertz Electronics. IRMMW-THz. Joint 32nd International Conference on, 2007, pp. 1–2.
- [35] R. J. B. Dietz, R. Wilk, B. Globisch, H. Roehle, D. Stanze, S. Ullrich, S. Schumann, N. Born, M. Koch, B. Sartorius, and M. Schell, "Low Temperature Grown Be-doped InGaAs/InAlAs Photoconductive Antennas Excited at 1030 nm," *J. Infrared, Millimeter, Terahertz Waves*, vol. 34, no. 3–4, pp. 231–237, Mar. 2013.
- [36] B. Granddier, H. Chen, R. M. Feenstra, D. T. McInturff, P. W. Juodawlkis, and S. E. Ralph, "Scanning tunneling microscopy and spectroscopy of arsenic antisites in low temperature grown InGaAs," *Appl. Phys. Lett.*, vol. 74, no. 10, p. 1439, 1999.
- [37] H. Künzel, J. Böttcher, R. Gibis, H. Hoenow, and C. Heedt, "Low-temperature MBE of AlGaInAs lattice-matched to InP," *J. Cryst. Growth*, vol. 127, no. 1–4, pp. 519–522, Feb. 1993.
- [38] H. Künzel, J. Böttcher, R. Gibis, and G. Urmann, "Material properties of Ga<sub>0.47</sub>In<sub>0.53</sub>As grown on InP by low-temperature molecular beam epitaxy," *Appl. Phys. Lett.*, vol. 61, no. 11, p. 1347, 1992.
- [39] A. Mircea, A. Mitonneau, J. Hallais, and M. Jaros, "Study of the main electron trap in Ga<sub>1-x</sub>In<sub>x</sub>As alloys," *Phys. Rev. B*, vol. 16, no. 8, pp. 3665–3675, Oct. 1977.

- [40] A. Irvine and D. Palmer, "First observation of the EL2 lattice defect in indium gallium arsenide grown by molecular-beam epitaxy," *Phys. Rev. Lett.*, vol. 68, no. 14, pp. 2168–2171, 1992.
- [41] F. Urbach, "The long-wavelength edge of photographic sensitivity and of the electronic absorption of solids," *Phys. Rev.*, vol. 92, p. 1324, 1953.
- [42] S. E. Esipov and Y. B. Levinson, "The temperature and energy distribution of photoexcited hot electrons," *Adv. Phys.*, vol. 36, no. 3, pp. 331–383, Jan. 1987.
- [43] J. Kash, J. Tsang, and J. Hvam, "Subpicosecond time-resolved Raman spectroscopy of LO phonons in GaAs," *Phys. Rev. Lett.*, vol. 54, no. 19, pp. 2151–2154, 1985.
- [44] W. Pötz and P. Kocevar, *Hot Carriers in Semiconductor Nanostructures*. Elsevier, 1992, pp. 87–120.
- [45] R. Pässler, "Nonradiative multiphonon capture of thermal and hot carriers by deep traps in semiconductors for the alternative regimes of small and large lattice relaxation," *Czechoslov. J. Phys.*, vol. 34, pp. 377–401, 1984.
- [46] H. Goto, Y. Adachi, and T. Ikoma, "Carrier capture by multiphonon emission at extrinsic deep centers induced by self-trapping in GaAs," *J. Appl. Phys.*, vol. 54, no. 4, p. 1909, 1983.
- [47] H. Roehle, R. J. B. Dietz, H. J. Hensel, J. Böttcher, H. Künzel, D. Stanze, M. Schell, and B. Sartorius, "Next generation 1.5  $\mu\text{m}$  terahertz antennas: mesa-structuring of InGaAs/InAlAs photoconductive layers.," *Opt. Express*, vol. 18, no. 3, pp. 2296–301, Feb. 2010.
- [48] L. Du villaret, F. Garet, J.-F. Roux, and J.-L. Coutaz, "Analytical modeling and optimization of terahertz time-domain spectroscopy experiments, using photoswitches as antennas," *IEEE J. Sel. Top. Quantum Electron.*, vol. 7, no. 4, pp. 615–623, 2001.
- [49] E. Castro-Camus, L. Fu, J. Lloyd-Hughes, H. H. Tan, C. Jagadish, and M. B. Johnston, "Photoconductive response correction for detectors of terahertz radiation," *J. Appl. Phys.*, vol. 104, no. 5, p. 053113, 2008.



**Paper XI:**

**Optics Express, vol. 22, no. 11, p. 12982, 2014**



# Multichannel Terahertz Time-Domain Spectroscopy System at 1030 nm

Anika Brahm,<sup>1,2\*</sup> Annika Wilms,<sup>1</sup> Roman J. B. Dietz,<sup>3</sup> Torsten Göbel<sup>3</sup>, Martin Schell<sup>3</sup>,  
Gunther Notni<sup>1</sup>, and Andreas Tünnermann<sup>1,2</sup>

<sup>1</sup> Fraunhofer Institute for Applied Optics and Precision Engineering (IOF), Albert-Einstein-Straße 7, 07745 Jena, Germany

<sup>2</sup> Institute of Applied Physics, Abbe Center of Photonics, Friedrich-Schiller-Universität Jena, Max-Wien-Platz 1, 07743 Jena, Germany

<sup>3</sup> Fraunhofer Institute for Telecommunications, Heinrich-Hertz-Institut, Einsteinufer 37, 10587 Berlin Germany  
[\\*Anika.Brahm@iof.fraunhofer.de](mailto:Anika.Brahm@iof.fraunhofer.de)

**Abstract:** We present Terahertz (THz) imaging with a 1D multichannel Time-domain spectroscopy (TDS) system which operates with femtosecond fiber laser system at 1030 nm. The emitter and detector are photoconductive antennas made of InGaAs/InAlAs based on multi layer heterostructures (MLHS). We characterized the THz optics and the resolution of the system. The performance is demonstrated by the multichannel imaging of two samples. A simultaneous measurement of 15 THz pulses with a pixel pitch of 1 mm increases the measurement speed of the TDS system by factor 15.

©2014 Optical Society of America

**OCIS codes:** (110.6795) Terahertz Imaging; (040.1240) Arrays; (040.2235) Far infrared or terahertz; (300.6495) Spectroscopy, terahertz.

---

## References and links

1. C. Jansen, S. Wietzke, O. Peters, M. Scheller, N. Vieweg, M. Salhi, N. Krumbholz, C. Jördens, T. Hochrein, and M. Koch, "Terahertz imaging: applications and perspectives", *Appl. Opt.* **49**, E48-E57 (2010).
2. D. M. Mittleman, M. Gupta, R. Neelamani, R. G. Baraniuk, J. V. Rudd, and M. Koch, "Recent advances in terahertz imaging", *Appl. Phys. B* **68**, 1085-1094 (1999).
3. D. M. Mittleman, R. H. Jacobsen, and M. C. Nuss, "T-Ray Imaging", *IEEE J. Sel. Top. Quantum Electron.* **2**, 679 - 692 (1996).
4. B. Sartorius, H. Roehle, H. Künzel, J. Böttcher, M. Schlak, D. Stanze, H. Venghaus, and M. Schell, "All-fiber terahertz time-domain spectrometer operating at 1.5  $\mu\text{m}$  telecom wavelengths", *Opt. Express* **16**, 9565-9570 (2008).
5. R. Wilk, S. Kocur, T. Hochrein, M. Mei, and R. Holzwarth, "Imaging with THz OSCAT spectrometer", in 36th International Conference on Infrared, Millimeter and Terahertz Waves (IRMMW-THz), 2011.
6. M. Haaser, Y. Karrout, C. Velghe, Y. Cuppok, K. C. Gordon, M. Pepper, J. Siepmann, T. Rades, P. F. Taday, and C. J. Strachan, "Application of terahertz pulsed imaging to analyse film coating characteristics of sustained-release coated pellets", *Int. J. Pharm.* **457**, 521 - 526 (2013).
7. A. Redo-Sanchez, N. Laman, B. Schulkin, and T. Tongue, "Review of Terahertz Technology Readiness Assessment and Applications", *J. Infrared Millimeter Waves* **34**, 500-518 (2013).
8. X. C. Zhang, "Terahertz wave imaging: horizons and hurdles", *Phys. Med. Biol.* **47**, 3667-3677 (2002).
9. M. Tonouchi, "Cutting-edge terahertz technology", *Nat. Photonics.* **1**, 97-105 (2007).
10. M. Herrmann, M. Tani, K. Sakai, and M. Watanabe, "Towards multi-channel time-domain terahertz imaging with photoconductive antennas", in International Topical Meeting on Microwave Photonics, 2002.
11. B. Pradarutti, R. Müller, W. Freese, G. Matthäus, S. Riehemann, G. Notni, S. Nolte, and A. Tünnermann, "Terahertz line detection by a microlens array coupled photoconductive antenna array", *Opt. Expr.* **16**, 18443-50 (2008).
12. S. Wohnsiedler, M. Kolano, J. Klier, M. Herrmann, J. Jonuscheit, R. Beigang, E. Peytavit, and J. - Lampin, "Multichannel THz imaging using arrays of photoconductive antennas", in 35th International Conference on Infrared Millimeter and Terahertz Waves (IRMMW-THz), 2010.
13. A. Brahm, S. Scharnowski, B. Pradarutti, G. Matthäus, C. Brückner, S. Riehemann, S. Nolte, G. Notni, and A. Tünnermann, "128 channel THz ultrashort pulse system", in the European Quantum Electronics Conference in Lasers and Electro-Optics Conference on, 2009.

14. C. Gerth, R. J. B. Dietz, T. Göbel, M. Schell, A. Brahm, G. Notni, and A. Tünnermann, "Highly Efficient Terahertz Photoconductive Switch at 1060nm Excitation Wavelength", in 38th International Conference on Infrared, Millimeter, and Terahertz Waves (IRMMW-THz), 2013.
  15. R. J. B. Dietz, R. Wilk, B. Globisch, H. Roehle, D. Stanze, S. Ullrich, S. Schumann, N. Born, M. Koch, B. Sartorius, and M. Schell, "Low Temperature Grown Be-doped InGaAs/InAlAs Photoconductive Antennas Excited at 1030 nm", *J. Infrared Millimeter Waves* **34**, 231-237 (2013).
  16. R. J. B. Dietz, M. Gerhard, D. Stanze, M. Koch, B. Sartorius, and M. Schell, "THz generation at 1.55  $\mu\text{m}$  excitation: six-fold increase in THz conversion efficiency by separated photoconductive and trapping regions", *Opt. Express* **19**, 25911-25917 (2011).
  17. R. J. B. Dietz, B. Globisch, M. Gerhard, A. Velauthapillai, D. Stanze, H. Roehle, M. Koch, T. Göbel, and M. Schell, "64  $\mu\text{W}$  pulsed terahertz emission from growth optimized InGaAs/InAlAs heterostructures with separated photoconductive and trapping regions", *Appl. Phys. Lett.* **103**, 061103-061103 (2013).
  18. H. Roehle, R. J. B. Dietz, H. J. Hensel, J. Böttcher, H. Künzel, D. Stanze, M. Schell, and B. Sartorius, "Next generation 1.5  $\mu\text{m}$  terahertz antennas: mesa-structuring of InGaAs/InAlAs photoconductive layers", *Opt. Express* **18**, 2296-2301 (2010).
  19. C. Brückner, B. Pradarutti, S. Riehemann, G. Notni, and A. Tünnermann, "Design of a THz optics for a 128 channel THz imaging system", in 34th International Conference on Infrared, Millimeter, and Terahertz Waves (IRMMW-THz), 2009.
  20. A. Brahm, M. Müller, C. Gerth, and G. Notni, "Development of a multichannel lock-in amplifier for Terahertz time-domain systems", in 37th International Conference on Infrared, Millimeter, and Terahertz Waves (IRMMW-THz), 2012.
  21. J. Dai, J. Zhang, W. Zhang, and D. Grischkowsky, "Terahertz time-domain spectroscopy characterization of the far-infrared absorption and index of refraction of high-resistivity, float-zone silicon", *J. Opt. Soc. Am. B* **21**, 1379-1386 (2004).
  22. J. M. Khosrofiyan, and B. A. Garetz, "Measurement of a Gaussian laser beam diameter through the direct inversion of knife-edge data", *Appl. Opt.* **22**, 3406-3410 (1983).
  23. J. Magnes, D. Odera, J. Hartke, M. Fountain, L. Florence, and V. Davis, "Quantitative and Qualitative Study of Gaussian Beam Visualization Techniques", arXiv:physics/0605102 v1 (2006).
  24. B. Pradarutti, C. Rau, G. Torosyan, R. Beigang, and K. Kawase, "Plasmonic response in a one-dimensional periodic structure of metallic rods", *Appl. Phys. Lett.* **87**, 204105 (2005).
  25. B. Dörband, H. Müller, and H. Gross, *Handbook of Optical Systems, Metrology of Optical Components and Systems*, 5 (John Wiley Sons, 2012).
- 

## 1. Introduction

Terahertz (THz) radiation gives an opportunity to perform non-destructive spectroscopy, imaging or tomography measurements in a large variety of the applications fields such as quality control, security technologies, biosensor, medical imaging or communication technologies [1,2]. The advantages of THz time-domain spectroscopy (TDS) systems have led to a rapid proliferation of researchers studying properties and phenomena in the frequency range between far-infrared and microwave radiation [3]. The increased industrial interest in THz imaging or tomography measurements has pushed the development of imaging systems based on the principle of THz TDS [4-6]. Today several companies such as Toptica (Germany), TeraView (U.K.) Picometrix (U.S.), Zomega (U.S.), Menlo Systems (Germany) or Advantest (Japan) provide commercial TDS systems with several of specifications and application purposes [7]. Nevertheless, these systems are limited to a single pixel detection, e.g. with a photoconductive antenna. Thus, THz TDS imaging measurements often imply sample scanning in the focus of a THz beam path and a measurement requires from several minutes till hours. The measurement time also depends on the sample size, scan parameters and data acquisition techniques [8,9]. Therefore, the development of multichannel systems to speed up the measurement in THz TDS systems provides an opportunity for significant improvement.

Herrmann et al. presented an electronic circuit for the simultaneous readout of 8 photoconductive antenna signals (low temperature grown (LT)-GaAs). They performed a multichannel measurement after placing the detector array in the expanded THz beam behind the THz optics [10] which was rather configured for a one channel system. Pradarutti et al. presented the functionality of a 16 channel detector antenna made of LT-GaAs operating at 530 nm wavelength excited with the frequency doubled radiation of an ultrashort pulse fiber laser [11]. The antenna was also placed in an expanded THz beam behind the THz optics, but

additionally illuminated with the use of a micro lens array. The development of a multichannel emitter array with horn-type photoconductive switches was shown in [12].

In [13] we presented a first bigger concept of a multichannel TDS system based on fs fiber laser (1060 nm) and specially designed THz optics which generates and images a THz line focus to overcome optical aberrations in the THz beam path. The efficiency of LT-InGaAs in combination with 1060 nm excitation wavelength was too weak to overcome the absorption and reflection losses in the optical system. Therefore, it was necessary to carry on the investigation of broadband, sensitive and efficient THz emitter and detector material for 1030/1060 nm central wavelengths [14-15]. The combination of high power ultrashort pulse fiber lasers and efficient scalable detector and emitter antennas are the basis for future developments of fast compact multichannel TDS systems.

In this paper we present the first 1D multichannel THz TDS system with 15 detection channels operating at 1030 nm laser wavelength. The experimental setup of the THz system and single components of the THz and infrared optics are described in section 2. In section 3 we show the characterization of the beam profile in the THz line focus and 15 THz pulses, which were measured simultaneously with the detector array. Furthermore, we determined the resolution and the beam quality of the detector channels with a knife edge method along the optical axis in the THz focus and a second measurement of a metallic sample with different gaps up to 100  $\mu\text{m}$ . In section 4 we demonstrate the results of the first THz multichannel imaging measurements where we used a metallic Siemens star and a plastic pump wheel as samples. The conclusion is presented in section 5.

## 2. Experimental setup

The experimental setup of the multichannel THz system is shown in Fig. 1. It consists of an ytterbium (Yb)-doped ultrashort pulses fiber laser system with a passively mode locked oscillator from Active Fiber Systems GmbH. The oscillator operates at a wavelength of 1030 nm with an average output power of 100 mW, a pulse repetition rate of 20 MHz and pulse duration of 250 fs. The amplifier is an Yb-doped rod-type fiber with a length of 80 cm and a mode field diameter of 50  $\mu\text{m}$ . The wavelength of the pump laser is 976 nm. The pulse compression is realized after the amplification. Thus, the fiber laser system receives an average output power of about 4.5 W and generates laser pulses with 94 fs width, 20 MHz repetition rate and energies of about 223 nJ.

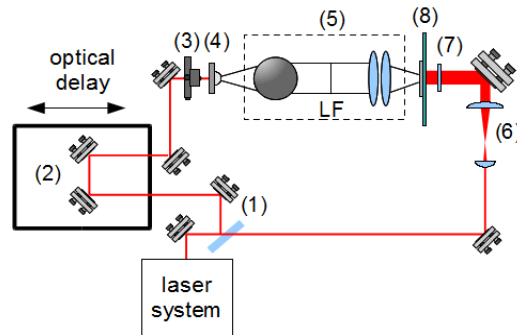


Fig. 1. Experimental setup of the multichannel THz TDS system: (1) Beam splitter (90:10), (2) Optical delay stage, (3) Aspheric lens, (4) THz emitter, (5) THz optics, (6) Telescope, (7) Cylinder lens, (8) THz detector.

The laser radiation is split into a pump beam which leads to the THz emitter and a probe beam for the THz detection beam path. A beam splitter and filters are used to reduce the laser power of 4.5 W and to avoid the destruction of the emitter and detector material. A motorized stage creates an optical delay for the time resolved measurement of the THz pulses. The photoconductive emitter based on a molecular beam epitaxy grown high mobility InGaAs/InAlAs multi layer heterostructures (MLHS). The MLHS consists of 100 periods of a

8 nm thick InAlAs layer followed by a 12 nm InGaAs layer grown lattice matched on an InP substrate at a growth temperature of approximately 400°C [16,17]. The antenna structure is a 400 μm gap mesa-structured stripline antenna [18]. The emitter is illuminated with 80 mW focused by an aspheric lens ( $f=15.29$  mm), and biased with  $\pm 125$  V at 1100 Hz. The silicon lens on the THz emitter is a hyper hemispherical lens made of high-resistive float zone (HRFZ) silicon with a diameter of 6 mm, radius of 3 mm and thickness of 3.45 mm. The THz optics consists of a 90° off-axis parabolic mirror with an effective focal length of 127 mm and a 76.2 mm free aperture, which collimates the radiation of the THz emitter. A cylindrical mirror, which was made by ultra-precision turning, with an effective focal length (EFL) of 127 mm and an aperture of 76.2 mm generates a line focus (LF) in the THz beam path. Two aspheric Zeonex480R® lenses with diameters of 76.2 mm and thicknesses of about 20 mm image the THz line focus to the detector.

A cylindrical HRFZ silicon lens was placed in front of the THz detector antenna to focus the THz radiation on the photoconductive antenna. The lens has a radius of 6.3 mm and a thickness of 6 mm. The imaging part of the THz optics has been designed to be diffraction limited up to the wavelength of 600 μm for a field of 31.75 mm. The imaging scale is -1 in horizontal direction. Detailed description of the imaging part of the THz optics was presented in [19]. The arrangement of the optical components is shown in Fig. 2.

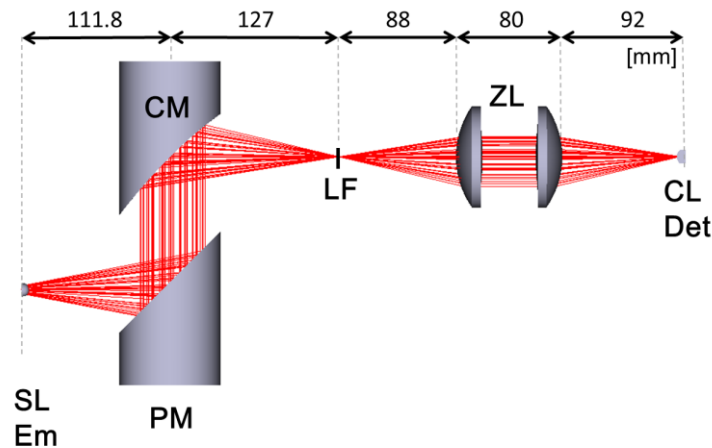


Fig. 2. Setup of the THz optics: SL Em – THz emitter with silicon lens, PM – parabolic mirror, CM – cylinder mirror, LF – THz line focus, ZL – Zeonex® lenses, CL Det – THz detector and silicon cylinder lens.

A telescope in the detector beam path, which consists of two cylinder lenses with focal lengths of  $f_1=12.7$  mm and  $f_2=100$  mm, forms about 350 mW of the laser power into a line focus. A third cylinder lens ( $f_3=12.7$  mm) focuses the laser radiation on the detector gaps.

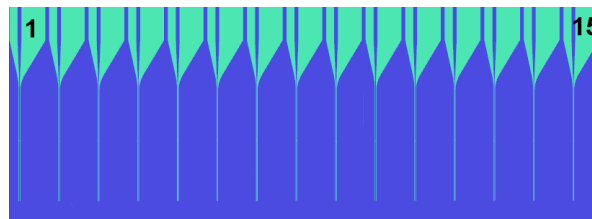


Fig. 3. Photoconductive detector array with 15 dipole antennas.

The THz detector material is made of Be-doped LT-grown (130°C) InGaAs/InAlAs MLHS [18]. The detector consists of 15 dipole antennas with a total length of 15 mm (see Fig. 3). The distance between each channel is 1 mm and the gap size of each structure is 7.5 μm.

The detector output is connected transimpedance amplifiers. A scalable multichannel lock-in amplifier (LIA), which was presented in [20], is used for the measurements. Several channels can be readout almost simultaneously due to the multiplexing technology, triggering and data acquisition program.

THz imaging and tomography measurements can be performed by placing a sample on motorized stages into the line focus of the THz optics.

### 3. Characterization of the THz system

#### 3.1 THz line focus

In order to characterize the beam profile of the THz line focus we used a fiber coupled detector unit to analyze the optical design of the THz beam path. The detector is a photoconductive antenna made of Be-doped LT-grown InGaAs/InAlAs based MNLS with a gap distance of 5  $\mu\text{m}$ . The detector unit consists of a hyper hemispherical lens with a diameter of 10 mm, a thickness of 6.12 mm and a radius of 5 mm to focus the THz radiation on the gap. The maximum THz pulse amplitude values and the position of the THz pulses were extracted to characterize the full width at half maximum (FWHM) of the line focus and the optical delay of the pulses. Fig. 4 shows the results of the measurements at a distance of 106 mm from the cylindrical mirror. The distance was chosen to be shorter than the effective focal length (127 mm) of the cylinder mirror due to the silicon lens placed in front of the fiber coupled detector. The lens shortens the focal length and therefore, we calculated the optimal position with optical design software (Zemax). Furthermore, the values of the measured THz focus must be understood as an approximation, since the silicon lens on the detector averages the THz radiation over a defined solid angle.

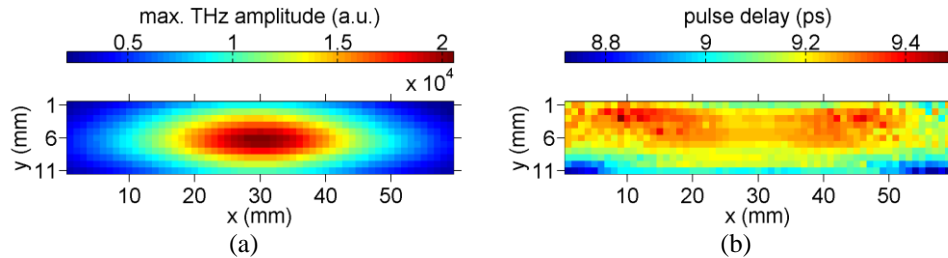


Fig. 4. Beam profile of the THz line focus: (a) Values of the maximum THz pulse amplitude; (b) Time delay of the THz pulses.

The FWHM of the THz focus was measured to be about 37 mm in the x direction (horizontal) and 10 mm in y direction (vertical) relatively to the optical axis of the THz beam path. Fig. 4b shows the temporal deviations of the THz pulses with the range in the whole measurement area of about  $\pm 0.39$  ps ( $\pm 0.117$  mm) and in the middle horizontal direction of about  $\pm 0.13$  ps ( $\pm 0.039$  mm). The time shift is introduced by the optical aberrations of the parabolic and cylindrical mirror as well as the position errors of the emitter in front of the 90° off-axis parabolic mirror.

#### 3.2 THz pulse measurement

Fig. 5 shows a THz measurement over the time window of 40 ps, performed with 15 detection channels. The scan was executed with an optical delay of 1 ps/s and LIA averaging time of 10 ms. The pulses are shifted by 2 ps for a better overview and normalized to the measured currents. Due to the imaging optics each THz pulse represents a point at the horizontal THz line focus with a lateral shift of 1 mm. The maximum amplitude values and positions of the THz pulses vary between the THz detector channels, which was expected after the optical design and system characterization in 3.1 (compare Fig. 4). The signal to noise ratio of the maximum THz pulse amplitude in the middle of the detector (channel 8 and 9), measured with

an LIA averaging time of 30 ms, was estimated to be about 39 dB. In the edge regions of the detector array we measured a signal to noise ratio of about 35 dB at 30 ms LIA average time.

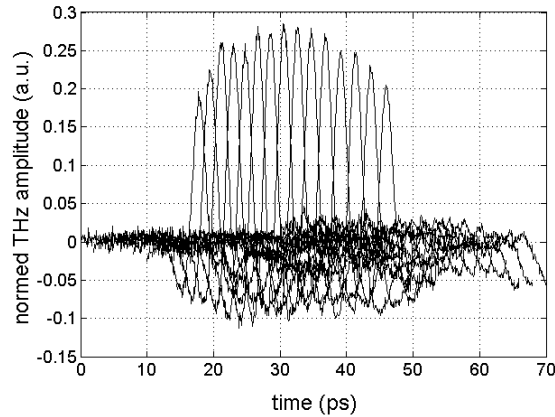


Fig. 5. THz measurement with 15 detector channels: The pulses are shifted by 2 ps for a better overview.

Fig. 6 demonstrates the amplitude maxima and its positions (time) of 15 measured THz pulses compared to simulation data, which was obtained with the optical design software (Zemax). First, we simulated the intensity profile behind the cylindrical silicon lens in horizontal direction (Fig. 6a). The simulation was normalized to the maximum amplitudes of the pulses for a better comparison. The measurement and simulation match well together and exhibit their maximum values in the middle of the detector antenna. The amplitude values decrease to the edge region by about 34%, which depends on the irradiation pattern of the emitter. Further, we compared the position of the maximum pulse amplitudes with the simulation of field of curvature. Channel 1 and 15 are delayed by about 1.5 ps relative to channel 8 in the middle. The simulated curve agrees quite well to the measured values and the delay between channel 1 and 15 compared to channel 8 is only about 0.93 ps. Possible reasons for the discrepancy could be optical aberrations introduced by the THz optics, the IR telescope optics or adjustment errors of the THz system.

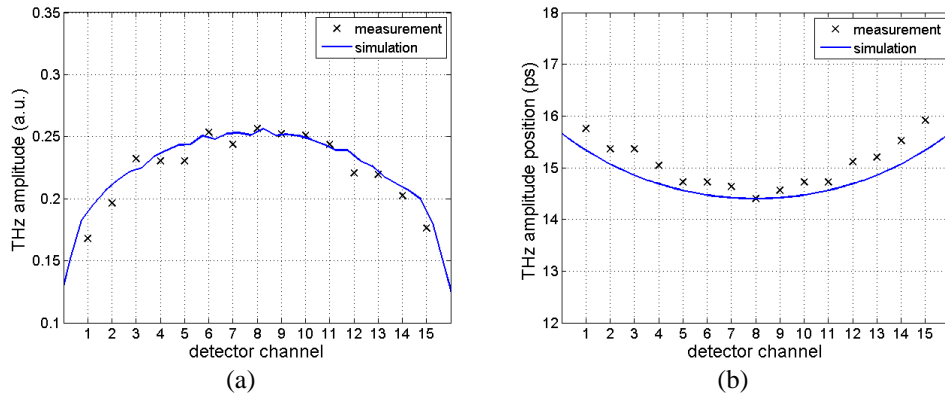


Fig. 6. Extracted values of the THz pulses: (a) Maximum THz amplitude values, (b) Position of the maximum THz amplitude.

Fig. 7 presents the THz signal measured with channel 8 (black line) in more detail. It was scanned with a time window of 40 ps, an optical delay velocity of 1 ps/s and LIA averaging time of 10 ms. The main pulse at 9 ps is followed by a second pulse at 36 ps, which must be introduced by the THz optics of the system (Fig. 7a). We compared the THz signal of channel

8 to an earlier measurement (red line) with a standard one channel TDS system at 1030 nm, which was presented in [14]. The emitter and detector in the one channel TDS system were made of the same material. The THz optics consisted of two 90° off-axis parabolic mirrors (EFL = 101.6 mm), as well as hyper hemispherical silicon lenses that are placed in front of the emitter and detector antennas. According to the graph, the multichannel signal is 500 times lower compared to the one channel TDS system. Fig. 7b shows the normed spectra of both pulse measurements, where the TDS reference is shown 500 times greater. The spectrum of channel 8 was calculated with the Fourier transform of the time window from 0 to 30 ps to avoid oscillations caused by the second pulse. The spectral bandwidth reaches up to 0.8 THz instead of almost 3 THz of the one channel TDS system.

There are various reasons for the relative low THz signals and the spectral bandwidth limitations in the multichannel TDS system. For example, the emitter generates a THz line focus with a FWHM diameter of about 37 mm (compare section 3.1), but each detector channel can only capture a small part of it (compare section 3.3). Furthermore, the two Zeonex480R® lenses absorb the THz radiation (e.g. 0.15 cm<sup>-1</sup>, @1 THz) and the refractive index of about 1.52 generates reflection losses at the surfaces. The cylindrical silicon lens, which is placed in front of the detector array, limits the focusing of the THz radiation to the vertical direction (see Fig. 2) and parts of the THz radiation are reflected because of the high refractive index step between air and HRFZ silicon (3.417) [21].

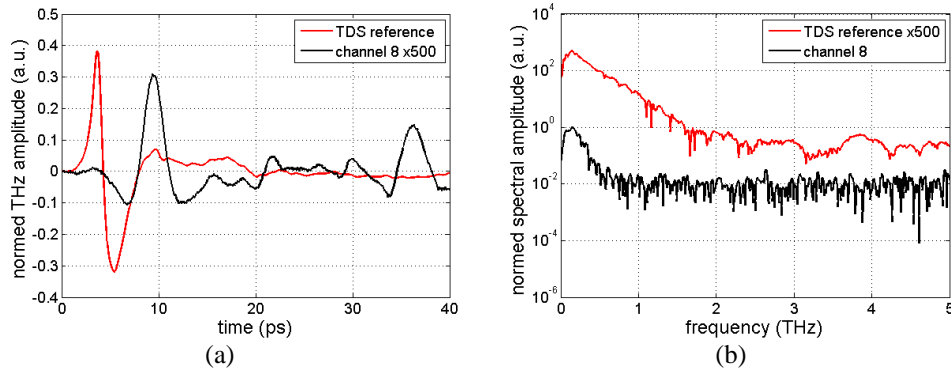


Fig. 7. THz signals of channel 8 and a one channel TDS system (TDS reference): (a) The THz pulse of channel 8 is shown 500 times larger for a better comparison to the TDS reference, (b) Normed spectra of channel 8 and the one channel TDS system.

### 3.3 Resolution of the multichannel TDS system

The THz optics image only a part of the THz line focus on each detector channel. We characterized the THz beam path with the knife edge method [22] to define the local full width at half maximum (FWHM) beam waists and depth of focus for each detector channel. Fig. 8 shows maxima of the THz pulse amplitude in the line focus of the THz optics. During the measurement a metal blade was shifted vertical and horizontal with a step width of 0.3 mm. The amplitudes of the pulses decrease, if the metal blade hits the focus. With the adaptation of the integration of the Gaussian beam function [23] it is possible to calculate the beam waists at the measured focus positions to the measured curvatures. As expected, the vertical knife edge measurement shows equal curvatures for the detector channels. The amplitude differences are caused by the THz beam profile (see Fig. 4). In contrast, the horizontal measurements show the curvatures shifted by 1mm in horizontal direction, which corresponds to the geometrical distances of 1 mm between the detector channels. Again the maximum amplitude values are varying because of the THz beam profile.

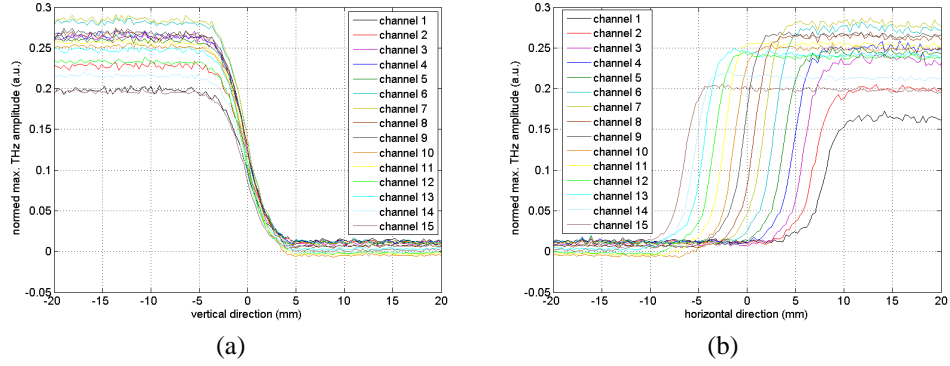


Fig. 8. Knife edge measurement in the line focus of the THz optics: (a) Maximum pulse amplitudes in vertical direction, (b) maximum pulse amplitudes in horizontal direction.

The value of the FWHM beam diameter in vertical direction is about 3.3 mm for the maximum THz pulse amplitude in the focus of the THz optics and is uniform for all detector channels. The vertical depth of focus is about 27 mm. In the horizontal direction the part of the THz line focus, which is detected by each detector channel, has a FWHM beam diameter of about 2.7 mm and is also uniform for each detector. The horizontal depth of focus is about 25 mm. Fig. 9 shows the beam profiles recorded by the channel 8 representative for the multichannel detector array along the optical axis of the THz beam path. The negative axis is in the emitter and the positive axis in the detector direction. The focus between vertical and horizontal beam profile is shifted by about 5 mm, which is caused by the astigmatism of the THz optics.

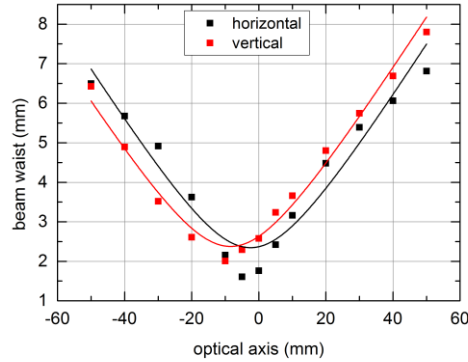


Fig. 9. Measured beam profiles (dotted) of channel 8 and fit functions of a Gaussian beam waist (line).

Despite the FWHM beam diameters greater than 2 mm, the time resolved measurement of THz pulses enables the detection with remarkable resolutions. To provide a proof, we measured a metallic sample with gaps of different distances from 5 mm to 100  $\mu\text{m}$  (see Fig. 10a). The sample was placed in the focus of the THz beam path and scanned with a step width of 100  $\mu\text{m}$  in the horizontal and vertical direction. The results of the maximum amplitudes are shown in Fig. 10b recorded with channel 8, which is representative for the multichannel detector. It can be shown, that the resolution in the horizontal scan direction is much better than in the vertical direction, because the 100  $\mu\text{m}$  gap is still resolvable, whereas the vertical direction only resolves a gap up to 500  $\mu\text{m}$ . This can be caused by the smaller focus diameter in horizontal direction, the astigmatism, as well as effects of sub-wavelengths phenomena on small structures in combination with the polarization of the electromagnetic field [24].

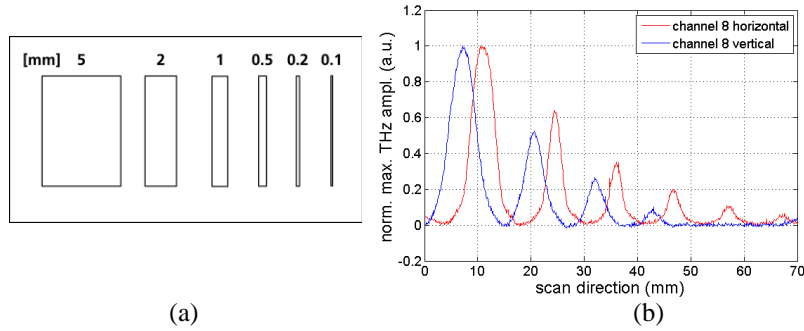


Fig. 10. Resolution measurement: (a) Metallic sample with different gap sizes from 5 mm to 100  $\mu\text{m}$ ; (b) Measurement results of channel 8 and 13 for a horizontal scan direction with step width of 0.1 mm.

#### 4. THz Multichannel Imaging

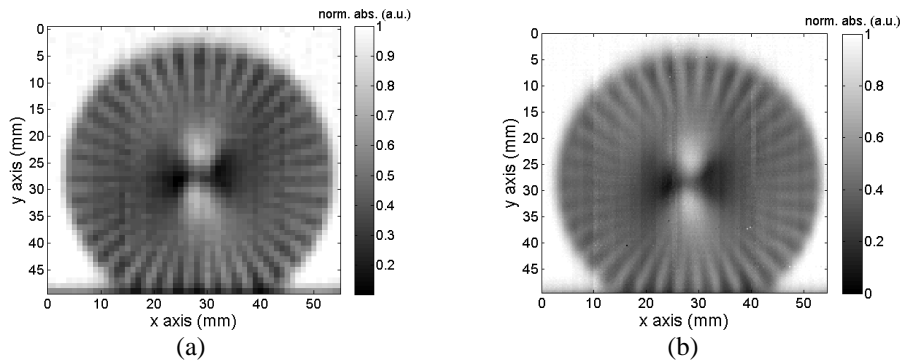


Fig. 11. THz imaging of a metallic Siemens star: (a) THz absorption image with a scan resolution of 1 mm in x and y direction; (b) THz absorption image with a scan resolution of 250  $\mu\text{m}$  in x and y direction.

Fig. 11 shows the measurement results of a metallic Siemens star. The images were generated with a normalization of the pulse amplitudes to the reference values of each detector. That overcomes inconsistencies of the changing beam profile (Fig. 6a), which would disturb the image quality. The reference values were achieved from a measurement without a sample. Firstly, we scanned an image area of  $60 \times 50 \text{ mm}^2$  with a pixel resolution of 1 mm. In x direction 4 measurement steps with a step width of 15 mm were used because of the 15 detection channels. The THz pulses with a time window of 8 ps were scanned with an optical delay of 3.3 ps/s and LIA averaging time of 10 ms. Further, the net measurement time, which depends only on the measurement of the time window with a certain velocity and on no processing time, was reduced to 13 minutes instead of almost 2 hours with conventional one channel detection (Fig. 11a). Secondly, we performed a measurement over the same area of  $60 \times 50 \text{ mm}^2$  with a higher pixel resolution of 250  $\mu\text{m}$  in x and y direction, which amounts to 48000 measurement points. A time window of 7 ps was scanned with 3.3 ps/s and LIA averaging time of 10 ms. The net measurement time took about 1.8 hours instead of 28 hours and the image was used to determine the resolution of the THz imaging system. The Siemens star has an outer diameter of about 50 mm and consists of a pattern of 32 metallic spokes which become wider as they get further from the center of the star. The structures can be resolved to the inner diameter of about 24 mm in x direction and 26 mm in y direction. Thus, the spatial resolution of the multichannel system is about 1.05 mm in horizontal (x) and 1.13 mm in vertical (y) measurement direction, which corresponds to a spatial frequency of about 0.47 LP/mm (x) and 0.44 LP/mm (y). The vertical orientated sectors have a higher transmission area (70-80%), whereas the horizontal sectors show an absorption behavior. This

effect is based upon the polarization dependency of the transmission at sub-wavelength structures [25], which has already been observed at the resolution sample of Fig. 10a.



Fig. 12. Picture of a pump wheel made of plastic.

A pump wheel made of plastics was the second sample measured with the multichannel THz TDS system (Fig. 12). An image area of  $60 \times 45 \text{ mm}^2$  was scanned with a pixel resolution of 1 mm. The x axis was scanned in 4 steps with a width of 15 mm provided by the 15 detection channels. We measured each THz pulse with a time window of 40 ps, optical delay of 3.3 ps/s and LIA averaging time of 10 ms. Overall the net measurement time took about 36 minutes instead of about 9 hours due to a one channel detector with identical measurement parameters.

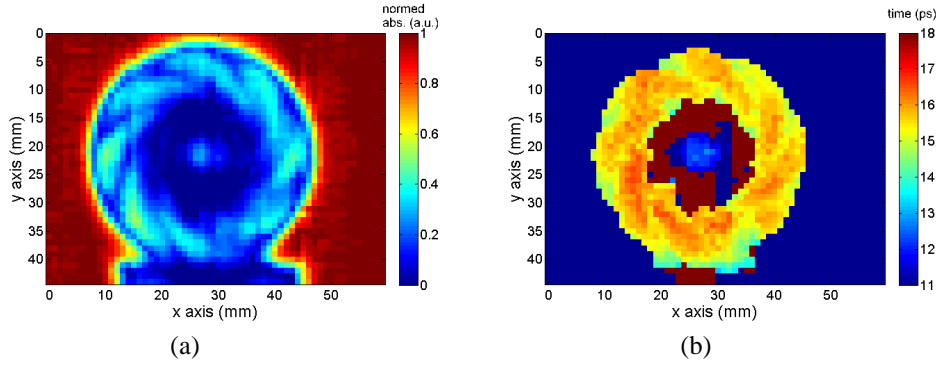


Fig. 13. Pump wheel made of plastic: (a) Extraction of the maximum THz pulse amplitude, (b) Extraction of the time information of the maximum THz pulse amplitude.

Fig. 13 shows the normalized THz absorption image obtained from the maximum THz pulse amplitudes (Fig. 13a) and the image of the time values extracted from their positions in the time domain (Fig. 13b). The time positions were also normalized to a reference measurement to overcome time shifts in the THz image caused by the field curvature which was shown in Fig. 6b. In the middle of the pump wheel there is a metallic ring part, where no transmission takes place. Therefore, the absorption is zero and the time image shows noise values. More importantly, the parts of the blades and their cavity can be resolved and thus, provide us information about the sample and production process. For example, on the left side the blades have a higher absorption, which could be determined from the greater time shift at those positions. Whereas, the absorption in the space between the blades on the left side is lower than the blades on the right side.

## 5. Conclusion

We presented the first multichannel THz TDS system which operates at 1030 nm with an Yb-doped ultrashort pulse fiber laser and a photoconductive antenna array. The THz optics consists of parabolic and cylindrical mirrors and creates a THz line focus with a FWHM diameter of 37 mm in horizontal and 10 mm in vertical direction. Aspheric lenses made of Zeonex480R<sup>®</sup> image the pulses onto a 15 mm long detector array with a cylindrical HRFZ silicon lens for the focusing. We measured 15 channels simultaneously with a lateral

resolution of 1 mm and a signal to noise ratio of about 39 dB in the middle and 35 dB at the edge of the detector array with multichannel lock-in technology. Compared to a one pixel TDS system the measurement time has been decreased by a factor of 15. The spectrum of the THz pulses ranges from 0.1 to 0.8 THz, which offers the potential for further improvements, e.g. by applying antireflection structures on THz optics, as well as the development of more efficient THz emitter and detector material at 1030 nm. It is also possible to adapt the THz optics to only one aspheric Zeonex<sup>®</sup> lens in combination with the development of a spherical silicon lens array. Thus the bandwidth and THz signals could be increased similar to one channel TDS systems.

The spatial resolution of the multichannel TDS system was determined with the multichannel measurement of a Siemens star and is about 1.05 mm in horizontal and 1.13 mm in vertical direction, which corresponds to the spatial frequencies of about 0.47 LP/mm (x) and 0.44 LP/mm (y).

The combination of a high-power fiber laser at 1030 nm and photoconductive detector arrays made of InGaAs/InAlAs based on MLHS offers the potential for faster and powerful multichannel TDS systems. Currently, the system works with almost 10% of the laser power, which provides the opportunity to use more than 15 detector channels, e.g. in two dimensions or to excite an array of emitter structures. Thus, the measurement time for THz imaging or tomography could be shortened even more drastically.

### **Acknowledgement**

This work was supported by the FhG internal program under grant no. MEF 620033. The authors would like to thank T. Schreiber (Fraunhofer IOF) and J. Limpert (IAP Jena) for the support of the fiber laser system, as well as W. Buß and M. Müller (Fraunhofer IOF) for developments at the electronic part of the THz system.